



Lidar observations of the Fe layer and temperatures in the polar mesopause region

by
Timo P. Viehl

This scientific report has been accepted as a dissertation at the
Faculty of Mathematics and Natural Sciences, University of Rostock, Germany.

Reviewer: Prof. Dr. Franz-Josef Lübken
Leibniz-Institute of Atmospheric Physics (IAP), University of Rostock,
Kühlungsborn, Germany

Prof. Dr. Otto Schrems
Alfred-Wegener-Institute (AWI), Helmholtz-Centre for Polar and Marine Research,
Bremerhaven, Germany

Submitted: 28 October 2016
Public defence: 27 January 2017



*Science is the one human activity that is truly progressive.
The body of positive knowledge is transmitted from generation to generation.*

—Edwin P. Hubble, 1936

Preface

The region of the upper mesosphere and lower thermosphere (MLT) has unique physical and chemical characteristics. MLT observations at polar regions, in particular, allow drawing far-reaching conclusions about the physics and chemistry of the whole system of Earth's atmosphere. Recent international and national programmes such as SCOSTEP's scientific project "Role of the Sun and the Middle Atmosphere in Climate" (ROSMIC) or the Leibniz Association's Senate Competition project "Mixing and Turbulence in the Mesosphere and Lower Thermosphere" (MaTMeLT) emphasise the importance of such investigations.

Of particular interest in these middle atmospheric research programmes are the coupling of atmospheric layers and the role of the upper layers in global climate models. The quantification of the solar variability and its importance for long-term variations in the middle atmosphere, trends in the thermal and dynamical structure, as well as atmospheric composition, can provide crucial information to the overall system of the atmosphere.

High-resolution observations, as presented in this thesis, provide insights into the dynamical coupling of atmospheric layers through gravity waves and tides, the effects of middle atmospheric circulation on the lower atmosphere, and trends in dynamic coupling. Such observations help to determine to what extent the middle atmosphere can have an influence on the climate through a change in dynamics, the radiative budget, and chemistry, or how it can be used as a proxy to monitor lower atmospheric processes and anthropogenic climate change.

This thesis presents results obtained from high-resolution lidar observations at polar latitudes, which are of particular importance for the whole system of Earth's atmosphere. Their exemplary location in the global circulation, as well as a lack of observations due to the inaccessibility and difficult environmental conditions, place the polar regions among the last frontiers in atmospheric science.

Observations with the mobile IAP Fe lidar provide temperatures, metal layer densities, and aerosol data in the particularly inaccessible MLT region. The continuous observations are among the most accurate measurements with high resolution in the middle and upper atmosphere. Modern resonance lidar systems can be further used to study a variety of other topics, such as the mixing of trace species. Although mesospheric metals have been observed by different means for several decades, some aspects of their dynamics and chemistry are still unknown. Several dynamical and chemical features of the MLT region (in particular at polar latitudes) and the whole atmosphere will in the near future be understood significantly better through an enhanced understanding of the mesospheric metals. The results of this thesis enable to understand the physics and chemistry of the MLT region better and to improve the knowledge about the middle atmosphere in the global context.

An integral part of the doctoral research summarised in this thesis has been the preparation and execution of two major measurement campaigns with the mobile IAP Fe lidar to Antarctica and the Arctic. In addition to the expeditionary preparation in Germany and Australia, this involved two journeys to Antarctica, including three summer seasons and one winter (a total of around 22 months) at Davis Station. On one hand, such measurement campaigns require routine observations, instrument and infrastructure maintenance and improvement, and ongoing data analyses. On the other hand it is necessary for all expeditioners at a mid-sized station with year-round personnel such as Davis to help out with other experiments and projects, and to keep the general station alive.

The expeditions have not only been truly invaluable experiences but yielded a series of new insights and surprising observations. The analyses of the observations are still ongoing, but several important results have already been published in peer-reviewed journals. 9 of these articles are cumulatively submitted in this thesis. The *Manuscripts* of the publications are an integral part of this doctoral research.

This thesis additionally provides a review of the scientific subject and the results. The *Introduction* gives an overview of middle atmospheric science related to this work (Section 1), summarises important aspects about mesospheric metals and the Fe layer in particular (Section 2), describes the instrument and its capabilities (Section 3), and gives a brief overview of the measurement campaigns conducted (Section 4).

The *Summary of Results* describes the methods and results of the studies, and puts them into the context of the relevant literature. Sections 5 to 8 primarily deal with the chemistry of the mesospheric metals. Sections 9 to 11 discuss the influence of ice particles, temperatures, and transport on the Fe layer. Sections 12 and 13 present observations and model calculations of thermal tides in temperatures and metal densities in the MLT region. Sections 14 to 18 reveal insights into the coupling of atmospheric layers. These observations enable a new understanding of the winter to summer transition of the MLT region at polar latitudes. Together, these results obtained by a single instrument (as well as the comparison of the datasets with other instruments and models) have significantly enhanced our understanding of the chemistry and the dynamics of the MLT region. They have additionally provided new insights into the coupling of atmospheric layers, as well as hemispheric differences of the atmosphere.

Selected *Further Results* of the measurement campaigns, which have not yet been published, are briefly discussed in Sections 19 to 24, and concluded by an *Outlook* of ongoing and future measurements, as well as some important technical developments. A list of abbreviations, measurement statistics, chemical rate coefficients relevant to the mesospheric Fe layer, and copyright licenses are given in the *Appendix*. *References* are listed in the back of the thesis.

It is not possible to personally acknowledge all helping hands of the polar expeditions leading to the results presented here. The most significant contributions are summarised in the *Acknowledgement*.

Timo P. Viehl
October 2016



Table of Contents

Preface	III
Table of Contents	V
Short Summary of Papers	VII
Introduction	1
1 Earth's atmosphere	1
2 Mesospheric metals	7
3 The mobile IAP Fe lidar	12
4 Measurement campaigns	17
Summary of Results	21
5 Bottomside extension of the Fe layer during daylight	21
6 Photolysis of FeOH and reactions with H	22
7 Depletion of FeOH during sunlit periods	25
8 Definition of the metal layer bottomside	25
9 Uplift of the Fe layer	26
10 Seasonal influence of ice particles on the Fe layer	28
11 Temperature dependence of mean Fe density around summer solstice	29
12 First measurements of thermal tides in the Antarctic summer mesopause region	31
13 Tides in metal layers: comparison of lidar observations and a 3D atmospheric chemistry model	33
14 Gravity wave activity in the middle atmosphere	35
15 Ice particles and temperatures after the winter/summer transition in the Antarctic MLT	37
16 Stratospheric winds and mesospheric ice particles	39
17 Elevated Summer Mesopause	40
18 Definition of the summer season in the polar MLT	43
Further Results and Outlook	45
19 MLT temperature climatology for the austral polar region	45
20 Constant Fe tides in the polar MLT	47
21 The mesospheric Fe layer in Antarctica and the Arctic	48
22 Intraday variability of the Fe layer and short term influence of ice particles	49
23 Lidar observations of meteor smoke particles	50
24 Comparison of Fe lidar and OH spectrometer temperature observations	51
25 Outlook	53
Appendices	55
Appendix A: Abbreviations	57
Appendix B: Rate coefficients	59
Appendix C: Measurement statistics	60
Appendix D: Copyright licenses	61
Manuscripts	63
Viehl et al. [2016a]: The photolysis of FeOH and its effect on the bottomside of the mesospheric Fe layer	65

Viehl et al. [2015]: Summer time Fe depletion in the Antarctic mesopause region	75
Viehl et al. [2016b]: Corrigendum to “Summer time Fe depletion in the Antarctic mesopause region” . .	81
Lübken et al. [2011]: First measurement of thermal tides in the summer mesopause region at Antarctic latitudes	83
Feng et al. [2015]: Diurnal variation of the potassium layer in the upper atmosphere	87
Kaifler et al. [2015]: LIdar observations of gravity wave activity in the middle atmosphere over Davis (69°S, 78°E), Antarctica	95
Morris et al. [2012]: Experimental evidence of a stratospheric circulation influence on mesospheric temperatures and ice-particles during the 2010–11 austral summer at 69°S	111
Lübken et al. [2014]: Winter/summer mesopause temperature transition at Davis (69°) in 2011/2012 . .	119
Lübken et al. [2015]: Winter/summer transition in the Antarctic mesopause region	125
Contribution to the Manuscripts	141
Declaration	143
References	145
Acknowledgment	159

Short Summary of Papers

This thesis is submitted as a cumulative work of papers published in peer-reviewed journals. The following pages give a short overview of the contributing papers authored by the candidate. Citations to these papers are given in **bold** throughout the text. The manuscripts are part of this thesis and collected on pages 63 to 141.

Viehl et al. [2016a]

The photolysis of FeOH and its effect on the bottomside of the mesospheric Fe layer

Viehl, T. P., J. M. C. Plane, W. Feng, and J. Höffner
Geophys. Res. Lett., 43, 1373–1381, (2016)

Lidar observations of a mesospheric metal are for the first time combined with quantum chemical calculations and a 3D atmospheric chemistry model to derive an unknown photolysis rate. The inclusion of this photolysis rate leads to a considerable improvement in the ability of atmospheric chemistry models to describe the diurnal behaviour of the Fe layer. The results explain the regular bottomside extension of the Fe layer in the MLT region which is primarily caused by the direct photolysis of FeOH. Reactions of FeOH with H play a subordinate role. FeOH is depleted during polar summer. This may have implications for the formation and composition of meteor smoke particles.

Viehl et al. [2015]

Summer time Fe depletion in the Antarctic mesopause region

Viehl, T. P., J. Höffner, F.-J. Lübken, J. M. C. Plane, B. Kaifler, and R. J. Morris
J. Atmos. Solar-Terr. Phys., 127, 97–102, (2015)

Ice particles were previously thought to be a major cause of the seasonal change in Fe densities at polar latitudes. Lidar and radar observations at Davis, Antarctica show an anti-correlation of ice particle occurrence and Fe density. The centroid altitude of the Fe layer rises due to a dynamic uplift of the whole layer by vertical winds and not due to a scavenging effect of ice particles at lower altitudes. The temperature dependence of mean Fe densities during a very

strong and unexpected depletion observed around summer solstice suggests that gas-phase chemical reactions have a dominating effect. An attempt is made to explain the substantial depletion around summer solstice with a simplified gas-phase chemistry partitioning between Fe and FeOH.

Viehl et al. [2016b]

Corrigendum to: Summer time Fe depletion in the Antarctic mesopause region, by Viehl et al. [2015]

Viehl, T. P., J. Höffner, F.-J. Lübken, J. M. C. Plane, B. Kaifler, and R. J. Morris
J. Atmos. Solar-Terr. Phys., 142, 150–151, (2016)

Due to a mathematical error, **Viehl et al. [2015]** incorrectly concluded that a simple gas phase chemistry scheme could explain the strong Fe depletion at Antarctic latitudes around the summer solstice. The correction of the mistake can no longer justify this conclusion, under the assumptions and simplifications made. Hence, vertical and horizontal transport must explain the depletion, also shown in the observed uplift of the layer. Simulations with an atmospheric chemistry model support this new interpretation.

Lübken et al. [2011]

First measurements of thermal tides in the summer mesopause region at Antarctic latitudes

Lübken, F.-J., J. Höffner, T. P. Viehl, B. Kaifler, and R. J. Morris
Geophys. Res. Lett., 38, L24806, (2011)

Measurements with the mobile IAP Fe lidar have detected thermal tides in the summer polar mesopause region. These tides are much larger than existing model simulations predict, with modulations in temperature up to ± 6 K and Fe number densities up to $\pm 40\%$. Temperature tides show a semidiurnal and diurnal structure at different altitudes. In Fe densities, a strong diurnal tidal component seems to dominate at all altitudes. The downward tidal phase progression in temperatures and Fe densities is similar and correspond to vertical wavelengths of 30 km and 36 km, respectively.

Feng et al. [2015]

Diurnal variation of the potassium layer in the upper atmosphere

Feng, W., J. Höffner, D. R. Marsh, M. P. Chipperfield, E. C. M. Dawkins, T. P. Viehl, and J. M. C. Plane
Geophys. Res. Lett., 42, 3619–3626, (2015)

Measurements of K atoms in the MLT at mid-latitudes in Kühlungsborn, Germany are compared to the 3D atmospheric chemistry model WACCM-K. Amplitude and phase of the diurnal and semidiurnal tide are captured well, even though some discrepancies between the model and the observations persist. The temperature influence is presumably not significant because of the chemistry of K. However, direct temperature comparisons are not yet possible.

Kaifler et al. [2015]

Lidar observations of gravity wave activity in the middle atmosphere over Davis (69°S, 78°E), Antarctica

Kaifler, B., Lübken, F.-J., J. Höffner, R. J. Morris, and T. P. Viehl
J. Geophys. Res.: Atmos., 120, 4506–4521, (2015)

Lidar observations in the stratosphere and the upper mesosphere and lower thermosphere (MLT) region at Davis, Antarctica are used to investigate gravity wave activity. The gravity wave potential energy density (GW-PED) has a large seasonal variation with a semiannual oscillation in the MLT, consistent with selective critical-level filtering in the lower stratosphere. The identical structure of the MLT and stratosphere suggest that the wind field near the tropopause level controls the gravity wave flux reaching the MLT region.

Morris et al. [2012]

Experimental evidence of a stratospheric circulation influence on mesospheric temperatures and ice-particles during the 2010–2011 austral summer at 69°

R. J. Morris, J. Höffner, F.-J. Lübken, T. P. Viehl, B. Kaifler, and A. R. Klekociuk
J. Atmos. Solar-Terr. Phys., 89, 54–61, (2012)

First IAP Fe lidar temperature measurements in the mesopause region at Davis, Antarctica are compared to the occurrence of ice particles detected as polar mesosphere summer echoes (PMSE) and the breakdown of the polar vortex. The timing of the annual breakdown of the southern polar stratospheric vortex seems to influence mesopause temperatures and the formation of

PMSE early in the austral summer. Temperatures below mesopause altitudes in the 2010/2011 austral summer were unusually high.

Lübken et al. [2014]

Winter/summer mesopause temperature transition at Davis (69°S) in 2011/2012

Lübken, F.-J., J. Höffner, T. P. Viehl, B. Kaifler, and R. J. Morris
Geophys. Res. Lett., 41, 5233–5238, (2014)

Quasi-continuous Fe lidar measurements at Davis, Antarctica are presented for the austral summer season 2011/2012. Mesopause altitudes and temperatures are similar to the Northern Hemisphere (NH) after the initial transition from the winter to the summer state. A significant elevation of the mesopause for a short period around the solstice follows the initial downward shift of the mesopause during the winter/summer transition. The mesopause is then higher and colder than typical NH values by ~4 km and 10 K. Individual profiles show temperatures as low as 100 K. The temperature transition strongly correlates with zonal winds in the stratosphere. However, the impact of stratospheric winds on the occurrence of ice particles seems to be more complicated than previously assumed.

Lübken et al. [2015]

Winter/summer transition in the Antarctic mesopause region

Lübken, F.-J., J. Höffner, T. P. Viehl, E. Becker, R. Latteck, B. Kaifler, D. J. Murphy, and R. J. Morris
J. Geophys. Res.: Atmos., 120, 12,394–12,409, (2015)

Temperature data obtained by the IAP Fe lidar in the Antarctic MLT are of unprecedented accuracy and resolution, and available for three consecutive seasons with a surprisingly different summer mesopause structure. The analysis of MF radar winds and PMSE ice particle detection shows that the occurrence of an 'elevated summer mesopause' (ESM) in some years is not only caused by changing breakdown conditions of the polar vortex, as previously thought. In such years, mesospheric winds are also shown to be relevant for the propagation of gravity waves and the subsequent shift in temperatures. Furthermore, comparison with results of a general circulation model shows that the filtering of gravity waves alone cannot explain the ESM. It is important to take the spectrum of gravity waves into account to explain this feature of the MLT region.

Introduction

The following Sections 1 to 4 give a brief introduction in the scientific subject of this thesis, some technical details of the instrument and the data retrieval, and basic information about the two measurement campaigns to the polar regions of both hemispheres during which the observations were obtained. For more comprehensive information refer to the cited literature.

1 Earth's atmosphere

The atmospheric region of the upper mesosphere and lower thermosphere (MLT) has unique physical characteristics. Observations at polar latitudes allow drawing interesting conclusions about the physics and chemistry of the whole atmosphere. However, accurate observations with high resolution are challenging and still rare in the polar MLT region.

Earth's atmosphere can be divided into different altitude layers in relation to several physical characteristics. A common classification can be carried out according to the temperature structure. With increasing altitude, these layers are the troposphere, stratosphere, mesosphere, and thermosphere, which are separated by the tropopause, stratopause, and mesopause (Figure 1; for more details see [Houghton \[2002\]](#), [Schumann \[2012\]](#), [Brekke \[2013\]](#), or other atmospheric physics textbooks). The region of the stratosphere and mesosphere is often called the "middle atmosphere".

The wider area around the mesopause between approximately 70 km and 110 km altitude is referred to as the region of the upper mesosphere and lower thermosphere (MLT). For meteoroids entering Earth's atmosphere, air densities in the MLT become sufficiently large (around 0.001 hPa) to evaporate material through frictional heating. This evaporation creates layers of metal atoms such as the iron (Fe) layer. The Fe layer usually occurs between around 75 km and 100 km altitude and can occasionally extend down below 70 km and up to above 120 km altitude (see Figure 1 and Section 2).

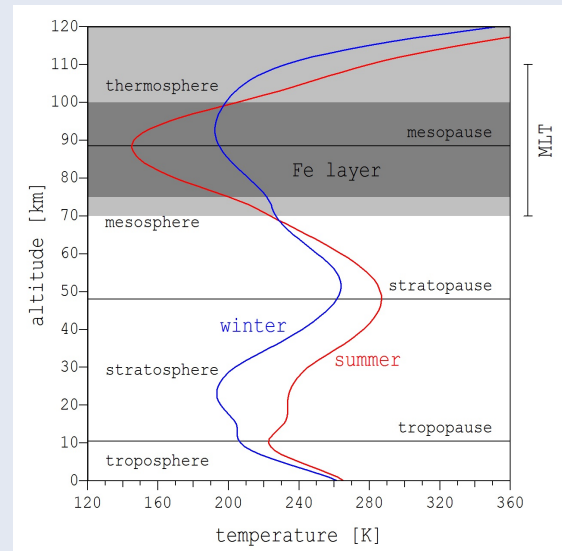


Figure 1: Earth's atmosphere. Different altitude levels can be classified according to the temperature structure. During summer (red), temperatures at the mesopause are lower than during winter (blue). Layers of metal atoms such as Fe are created through meteoric ablation in the region of the upper mesosphere and lower thermosphere (MLT) between approximately 75 and 100 km altitude (dark grey). The Fe layer can occasionally extend down below 70 km; Fe atoms are further observed in sporadic layers in the thermosphere above 100 km (light grey). Temperature data from NRLMSISE-00 [[Picone et al., 2002](#)]. CC BY 4.0

The MLT further exhibits a variety of unique physical and chemical processes and is therefore of particular interest for a broad branch of modern atmospheric research [[Smith, 2012](#)]. For example, temperatures in the MLT are generally lower during summer than during winter. This phenomenon is important for the understanding of the whole Earth atmosphere's dynamics. The polar MLT is also the home of the highest clouds on Earth (NLC, see Section 1.3). A potential extension of these ice clouds to lower latitudes as well as an increase in their brightness has been proposed as an indicator for a cooling of the MLT as well as an increase in water vapour levels through the photolysis of enhanced levels of methane (CH_4) [e.g., [DeLand and Thomas, 2015](#); [Berger and Lübken, 2015](#); [Hervig et al., 2016](#)]. Both phenomena are directly linked to an increase

in greenhouse gases, which are associated with global warming in the troposphere.

1.1 The MLT region

Several reviews have outlined the current knowledge about the MLT and list open scientific questions [e.g., [Becker, 2012](#); [Feofilov and Kutepov, 2012](#); [Sinnhuber et al., 2012](#); [Smith, 2012](#); [Plane et al., 2015](#)]. The following sections summarise important physical and chemical aspects and concepts of the MLT which are relevant for this thesis.

Temperature anomaly

Temperatures in the polar summer MLT are lower than during winter although the solar irradiance is higher (Figures 1 & 2). In fact, temperatures during summer deviate by more than 100 K from a hypothetical state of radiative equilibrium of the atmosphere in which dynamical factors are neglected. Temperatures around summer solstice can fall below 100 K (-173°C) [e.g., [Lübken et al., 2014](#)], making the polar summer MLT the coldest naturally occurring place on Earth. The low summertime temperatures are caused by atmospheric waves which break in the mesopause region and cause a strong upwelling at polar latitudes (Section 1.2).

Major reactive chemical species

Solar electromagnetic radiation and energetic particles cause the photolysis and photoionisation of atmospheric constituents in the MLT and the higher atmosphere. Atomic oxygen (O) is the most important reactant in the MLT. Atomic O is created through the photolysis of the oxygen molecule (O_2) in the UV band below 242 nm, as well as through collisions with cosmic particles with energies larger than 5.2 eV. The concentration of atomic O controls many important chemical reactions in the MLT region, either directly, or indirectly through removal of ozone (O_3) or by controlling the creation of the odd-hydrogen (HO_x) radicals atomic hydrogen (H), hydroxyl (OH), and hydroperoxyl (HO_2).

The rate-determining step of the removal of atomic O is given through the recombination forming O_3 in collisions with O_2 . This reaction is pressure dependent as it needs a moderating third body to carry excess collision energy and hence varies with $[\text{O}_2]^2$ at its low-pressure limit [[Plane et al., 2015](#)].

The pressure range at higher MLT altitudes above ~ 90 km (<0.001 hPa) is too low for an efficient formation of O_3 . Any O_3 found in this pressure range was primarily formed at lower altitudes and transported upwards through diffusive processes.

Atomic O has a pronounced diurnal variation below 80 km altitude, where it essentially disappears at night. However, there is nearly no diurnal variation above 84 km, where the time constant for the removal exceeds 12 h due to the low pressure and hence comparatively low amounts of molecular oxygen [O_2] [[Plane et al., 2015](#)]. The exact representation of this atomic O shelf is important for atmospheric models analysing chemical reactions and the radiative budget in the MLT [e.g., [Feofilov and Kutepov, 2012](#); [Viehl et al., 2016a](#)]. The absence of daytime photolysis causes a 10-fold increase of [O_3] throughout the MLT during the night [[Plane et al., 2015](#)]. The increase of [O] and the decrease of [O_3] with altitude causes an inversion of the ratio [O]/[O_3] at around 75 km, with [O]/[O_3] then rapidly increasing from ~ 10 at 80 km to $\sim 100,000$ at 110 km altitude.

The large-scale upwelling at the summer poles (see Figure 2) transports minor constituents such as methane (CH_4) to the upper atmosphere. The photolysis of CH_4 by Lyman- α radiation at 121.6 nm (penetrating down to about 80 km altitude) and subsequent reaction with O_2 is the primary source of water vapour (H_2O) in the MLT region. As a result of the seasonal cycle of the residual meridional circulation and CH_4 upwelling, [H_2O] in the MLT increases by a factor of 3 from winter to summer and allows for sufficient growth of mesospheric ice particles during the summer months.

In the MLT, atomic H is primarily created through photolysis of H_2O at wavelengths shorter than 240 nm, as well as through the reaction of atomic O with H_2O . The resulting diurnal variation of atomic H largely follows the variation of atomic O at daytime concentrations of roughly [H]/[O] ~ 0.01 at around 80 km and [H]/[O] ~ 0.0003 at around 90 km. Particularly on a seasonal level, [H] further follows [H_2O] with a maximum in summer, at ratios of [H]/[H_2O] between ~ 1 and 10 000 throughout the MLT, increasing to higher altitudes [[Plane et al., 2015](#)].

Figure 5 on page 10 and the reactions in Appendix B show the importance of O, H, and O_3 to the chemistry of the Fe layer (also see Section 2.3).

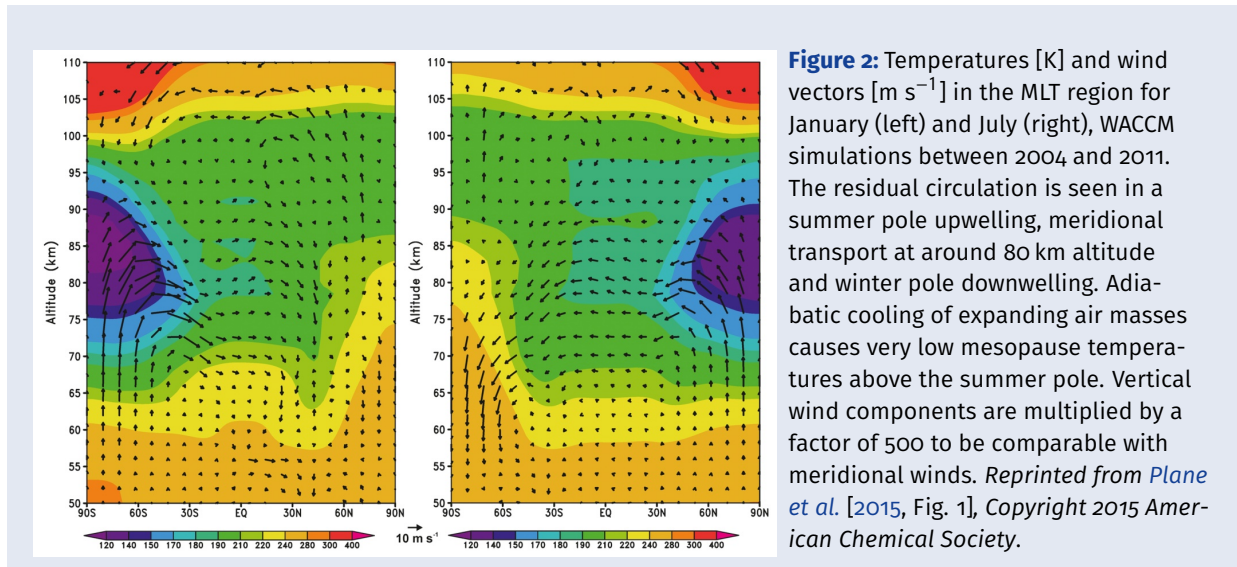


Figure 2: Temperatures [K] and wind vectors [m s^{-1}] in the MLT region for January (left) and July (right), WACCM simulations between 2004 and 2011. The residual circulation is seen in a summer pole upwelling, meridional transport at around 80 km altitude and winter pole downwelling. Adiabatic cooling of expanding air masses causes very low mesopause temperatures above the summer pole. Vertical wind components are multiplied by a factor of 500 to be comparable with meridional winds. Reprinted from *Plane et al.* [2015, Fig. 1], Copyright 2015 American Chemical Society.

1.2 Important waves in the MLT

Various atmospheric wave phenomena are important for the dynamic state of the MLT region [e.g., *Holton, 2004; Smith, 2012*]. For the scope of this thesis, gravity waves and thermal tides are of particular importance. The knowledge about both wave phenomena grows continuously and cannot be summarised here in its entirety. The following only lists some basic principles relevant to the discussions and conclusions in this thesis.

Gravity waves

Gravity waves are transversal atmospheric waves, with buoyancy acting as the restoring force. In the MLT, they are usually observed as variations in temperature, winds, or the movement of tracers such as ice particles or gradients in mesospheric metal layers. *Fritts and Alexander* [2003] have compiled a comprehensive review of gravity waves and their dynamics in the middle atmosphere.

Gravity waves are excited, for example, when air parcels are vertically displaced in the atmosphere and then restored in statically unstable conditions (i.e. the real atmospheric temperature gradient dT/dz is larger than the adiabatic lapse rate). Gravity waves, therefore, have intrinsic periods larger than the Brunt-Väisälä period, which depends on the temperature gradient and is around 5 min to 10 min throughout the middle atmosphere. On the other end of the spectrum, gravity waves are restricted to periods lower than the Coriolis parameter [e.g., *Fritts and Alexander, 2003*], which is around 13 h at 69° latitude. This shows that gravity

waves can have a broad range of wavelengths and phase speeds. Typically, gravity waves have horizontal wavelengths between 100 km and 10 000 km, vertical wavelengths between 4 km and 20 km, and phase speeds between 20 m/s and 200 m/s.

Most atmospheric gravity waves are generated in the troposphere through flow over topographic features, convection, geostrophic adjustment, or wind shear [*Becker, 2012*]. However, secondary gravity waves can also be generated throughout the middle atmosphere, in particular through wave-wave interactions and wave breaking.

Gravity waves can propagate horizontally and vertically, transporting energy and momentum over large distances. When gravity waves propagate upwards, their amplitudes increase with decreasing air density, conserving the energy of the wave. Gravity waves are therefore more pronounced throughout the middle atmosphere than in the troposphere. Typical temperature disturbances of gravity waves are less than ± 1 K in the troposphere but can reach more than ± 20 K in the MLT.

With growing amplitudes and disturbances of the background temperature, gravity waves can become unstable. This occurs once the temperature gradient reaches the adiabatic temperature gradient and buoyant oscillations are no longer possible. When propagating upwards, gravity waves will therefore always break once they have reached regions of sufficiently low densities. This is commonly the case at MLT altitudes.

From the dispersion relation of gravity waves it follows that the vertical wavelength m is not only proportional to the Brunt-Väisälä frequency N but also to the difference between the background wind u

and the phase speed c , with $m = N/(c-u)$ [Fritts and Alexander, 2003]. This means that the wind field in the middle atmosphere has a significant influence on the breaking and filtering of gravity waves.

The turbulent dissipation of gravity waves in the troposphere and stratosphere is small. However, gravity wave breaking significantly affects the sensible heat budget of the MLT, where the effect is as strong as the net radiative heating [Lübken, 1997].

The largest effect of gravity waves in the MLT, however, is their influence on the momentum budget. The resulting residual meridional circulation from the summer to the winter pole causes the low temperatures during the polar summer [Lindzen, 1981]: winds in the polar middle atmosphere are predominantly eastward during winter. Gravity waves with eastward phase speeds are therefore mainly filtered before they reach the MLT. During the winter/summer transition, the zonal-mean zonal winds decrease and become westward. Gravity waves with eastward phase speeds can then propagate through the middle atmosphere and break in the MLT after becoming unstable. Gravity waves with westward phase speeds are simultaneously filtered in the lower middle atmosphere. The deposition of eastward momentum therefore dominates in the summer MLT. This momentum deposition exerts an eastward drag on the zonal wind. The Coriolis force deflects the resulting zonal wind equatorwards and induces a meridional flow from the summer to the winter pole. A strong upwelling compensates the associated mass flux at the summer pole. Rising air masses experience adiabatic expansion due to the exponentially decreasing air pressure. The resulting strong adiabatic cooling causes the low temperatures observed (Figure 2).

Atmospheric thermal tides

Thermal tides are large scale oscillations of the atmosphere, excited by the periodic diurnal change of solar irradiance around the globe [Lindzen and Chapman, 1969]. Tides are observable as variations in temperature, pressure, and horizontal and vertical winds. Although the Moon and the Sun exert a measurable gravitational force on Earth's atmosphere, these gravitational tidal effects are much smaller than tidal effects generated by solar heating. In this thesis, the term "tides" therefore only refers to solar thermal tides. Tidal oscillations have periods which are subharmonics of a solar day and

can be grouped into two categories: migrating and non-migrating tides.

Migrating tides have the same phase speeds as Earth's angular velocity. To a stationary observer on the ground they appear to be travelling with the Sun, with their phases depending only on the local solar time but not on longitude. The frequencies of migrating tides equal their zonal wavenumbers, i.e. the 24 h (diurnal) tide has the wavenumber 1, the 12 h (semidiurnal) tide has the wavenumber 2, and so on. Migrating tides are excited by solar absorption of sources independent of longitude, such as tropospheric H_2O or stratospheric O_3 [e.g., Smith et al., 2003b; Smith, 2012]. The local generation of tides in the MLT region is assumed to be small compared to the upwards propagating tidal components generated in the troposphere [Smith et al., 2003b].

Non-migrating tides are excited by sources with an anisotropic longitudinal distribution, like convective latent heat release over tropical land masses. They can be further excited through non-linear wave-wave interactions, e.g., between quasi-stationary planetary waves and migrating tides [e.g., Hagan and Forbes, 2002, 2003]. The periods of non-migrating tides are also subharmonics of the solar day. However, they can have arbitrary wavenumbers and propagate westwards, eastwards at a phase speed different than the Earth's angular velocity, or be stationary.

Contrary to individual gravity waves, tides are globally present and not significantly affected by mean winds [Lindzen, 1981]. In the middle atmosphere, tidal variations in temperature and wind can be substantial and need to be taken into account in global models. Tides interact with other waves such as gravity waves, the Quasi-Biennial Oscillation, or the El Niño-Southern Oscillation [e.g., McLandress, 2002; Gurubaran et al., 2005]. Upward propagating tides transport energy and momentum to the MLT. Tides can furthermore lead to significant observational biases for observations restricted to certain local times.

Importantly for the MLT, tides change the vertical temperature gradient of the atmosphere and horizontal wind speeds. These changes affect the breaking conditions for gravity waves and cause an additional influence on the global meridional circulation [e.g., Fritts and Vincent, 1987; Mayr et al., 2005b; Senf and Achatz, 2011]. In particular, gravity waves with eastward phase speeds, which are re-

sponsible for the residual meridional circulation, can break well below the mesopause region during the eastward tidal phase of the zonal wind [Becker, 2012].

Observations by Pancheva *et al.* [2002] show that the dominating modes of the vertical wavelength of the semidiurnal tide are at least 35 km long. The vertical wavelength of the diurnal tide is shorter and only around 25 km long [Smith, 2012]. Shorter vertical wavelengths correspond to stronger gradients in temperature and winds. The diurnal tide is therefore expected to interact more strongly with gravity waves than the semidiurnal tide.

1.3 Ice particles in the MLT

Ice particles can form in the MLT when sufficient water vapour and nuclei for heterogeneous nucleation are present, and the temperature drops below the frost point (around 145 K). A common hypothesis for the source of condensation nuclei is the nucleation of meteor smoke particles (MSP) from meteoric material (see Section 2.3). During the polar summer months, water vapour and MSP are assumed to be present in sufficient quantities. The sole criterion for ice particle formation is therefore determined by absolute temperature. Water ice particles can nucleate around MSP under these conditions, forming the highest clouds in Earth's atmosphere at around 83 km altitude [e.g., Hervig *et al.*, 2001; Rapp and Thomas, 2006].

Noctilucent Clouds / Polar Mesospheric Clouds

In-situ observations of mesospheric ice particles are technically challenging and only possible with sounding rockets. Knowledge about the ice particles in the MLT has primarily been achieved through observations in the optical range. The best-known phenomenon related to ice particles in the MLT are noctilucent clouds (NLC). When ice particles grow to sufficient sizes (>20 nm), they reflect light in the visible spectrum at sufficient amounts to be detected by various means.

The clouds are high enough to reflect light of the Sun behind the horizon to a ground observer at mid-latitudes during conditions of twilight and darkness (solar elevation between -5 and -15°), illuminating them in the night sky (Figure 3). NLC were first observed and reported two years after

the eruption of Krakatoa by Leslie [1885] and systematically studied by Jesse [1896].

When viewed from space, it becomes apparent that NLC are formed above the summer pole and extend equatorward, reaching mid-latitudes only under favourable conditions. Clouds of ice particles in the polar mesopause region have hence also become known as Polar Mesospheric Clouds (PMC). Studies by Baumgarten *et al.* [2012] have shown quantitatively that PMC and NLC describe the same ice particles, observed by different means.

On short time-scales, mesospheric ice particles act as nearly passive tracers when displaced vertically or horizontally. The formation conditions and the vertical displacement have been employed to study MLT dynamics (through gravity wave analyses) and temperatures [e.g., Baumgarten and Fritts, 2014].

Polar Mesosphere Summer Echoes

A further phenomenon related to mesospheric ice particles are Polar Mesosphere Summer Echoes (PMSE). These strong echoes observed with VHF radars are caused by small-scale structures in electron densities on the order of the radar's Bragg scale ($d = \lambda/2$). PMSE require the combined effect of neutral air turbulence, free electrons and charged ice particles [e.g., Rapp and Lübken, 2004; Lübken, 2013].

Turbulence can create lasting structures in mesospheric ice particle layers. The ice particles can be charged through uptake of free electrons. The presence of comparatively heavy charged ice particles reduces the diffusivity of the considerably lighter electrons. The resulting electron density structures constitute irregularities in the radar refractive index. Radio waves are reflected from the created structures like a grating when the Bragg condition is fulfilled.

Ice particles causing PMSE can usually be smaller than NLC particles and hence be subvisible to satellites or ground-based observers. While NLC usually occur around 83 km altitude (the lower part of the super saturated MLT region), PMSE can extend up to 94 km altitude where they are formed before sedimenting and growing through condensation growth. The reduced diffusivity decouples active neutral air turbulence and the irregularities in electron number density on temporal scales. PMSE therefore last for much longer than the turbulence creating the structures until the ice particles evaporate.



Figure 3: Noctilucent cloud (NLC) observed in north-eastern direction above Rostock, Germany (54°N , 12°E) on 10 July 2015 at 23:46 LT, solar elevation -12.3° . NLC are ice clouds formed in the MLT region at around 83 km altitude during the summer months when temperatures fall below $\sim 145\text{ K}$. When ice particles have grown to radii $\gtrsim 20\text{ nm}$ they can reflect light from the sun below the horizon to a ground observer at mid-latitudes, making them shine at night. CC BY-NC 4.0

The radar echoes associated with PMSE hence give an indication of temperatures below the frost point, even in the absence of other observations. It must be noted though that low temperatures are only a necessary, but not sufficient, criterion for the observation of PMSE. The absence of PMSE must therefore not necessarily mean that temperatures are too high, but could be caused by a lack of free electrons or turbulence.

Observations of mesospheric ice particles are presumably the longest lasting observations in the MLT region. Trends analyses of their occurrence rates and geographic extension can, therefore, be used to study the long-term evolution of temperatures in the upper middle atmosphere [e.g., [DeLand et al., 2006, 2007](#)]. Observations of the onset of ice particles in early summer measured as PMC or PMSE have furthermore been used to investigate the transition from the winter to the summer state of the polar MLT [e.g., [Karlsson et al., 2011](#)]. However, as Sections 15 to 18 of this thesis show, processes are more complicated than previously assumed.

Heterogeneous chemistry of mesospheric ice

Ice particles in the MLT region interact with ambient chemical species. They can act as catalysts and change the composition of trace species, in particular of oxidants such as atomic O, O_3 , and HO_x [[Thomas, 1991](#)]. Most importantly in the scope of this thesis, ice particles heterogeneously inter-

act with the gas-phase mesospheric metal layers and can cause a scavenging uptake effect, lowering metal atom densities [e.g., [Plane et al., 2004](#); [Lübken and Höffner, 2004](#); [Gardner et al., 2005](#)].

[Gardner et al. \[2011\]](#) proposed this interaction as a qualitative explanation for differences in Fe layer observations at two Antarctic stations. However, to employ mesospheric metal layers for analytic purposes, the uptake effect needs to be quantitatively understood. Changes in metal layer densities can otherwise not be attributed to transport and dynamic displacements, temperature dependent (homogenous) gas-phase chemistry, or interactions with reactive species and charge transfer effects.

Laboratory and model investigations indeed point to discrepancies to the reported Fe layer depletions. The uptake coefficient of Fe atoms (but not K and Na atoms) on cubic ice has been shown to decrease at very low temperatures [[Murray and Plane, 2005](#)], and a dominating effect of transport processes for the seasonal variation of the mesospheric Na layer has been shown in model calculations [[Marsh et al., 2013b](#)]. Observations by [Viehl et al. \[2015, 2016b\]](#), presented in Sections 9 to 11 of this thesis, investigate these effects further and conclude that the ice particle uptake effect is negligible for the mesospheric Fe layer.

2 Mesospheric metals

Layers of metal atoms are created in the MLT region as a result of meteoric ablation. They can be efficiently probed by resonance lidars to determine ambient temperatures with high accuracy and resolution. The observation of metal densities further allows the investigation of the physics and chemistry of the MLT region, providing information about cosmic dust input, middle atmosphere dynamics, ionospheric physics, fundamental chemical reactions, and the formation of meteor smoke particles influencing the nucleation of clouds in the middle atmosphere. It is important to understand the morphology and the chemical properties of the metal layers in more detail to achieve these goals.

When meteoroids enter Earth's atmosphere, they vaporise in the altitude region of the MLT due to frictional heating. The process of thermal ablation creates layers of the elements most prevalent in cosmic dust particles (the metals Fe, Mg, Na, K, and Ca as well as the metalloid Si) in atomic form [e.g., [Vondrak et al., 2008](#)].

J. M. C. Plane and coworkers have published a series of comprehensive reviews of mesospheric metal studies since 1991 [[Plane, 1991, 2003](#); [Plane et al., 2015](#)]. The following sections give a brief summary of some important aspects of the origin, chemistry, physics, and observations of mesospheric metals with an emphasis on the Fe layer.

History of observation

Discovered by [Slipher \[1929\]](#) through the Na *D*-line emissions ($3^2P_J - 3^2S_{1/2}$) at 589 nm in the atmospheric nightglow, mesospheric metals were first studied with photometers [[Hunten, 1954](#); [Hunten and Godson, 1967](#)] and then with resonance lidar systems (historically called “laser radars”) [[Bowman et al., 1969](#)]. Lidars proved to be advantageous due to their much higher spatial and temporal resolution as well as longer possible measurement durations than passive photometers, which can only operate during twilight. Moreover, lidar systems soon became able to determine temperatures through the probing of the metal atoms' hyperfine structure, and the derivation of the Doppler broadening of the resonance lines [[Gibson et al., 1979](#); [Fricke and](#)

[von Zahn, 1985](#); [Neuber et al., 1988](#)]. A prime objective since then has been to develop more sophisticated lidar systems and acquire even more precise temperature measurements. Today, resonance lidar systems are the most accurate instruments for continuous MLT temperature measurements with high temporal and spatial resolution [e.g., [Lübken et al., 2015](#)].

2.1 Scientific interest

Several scientific topics and physical properties are related to the observations of mesospheric metals. Some important aspects are summarised here. In summary, the investigation of the metal layers can significantly improve our understanding of the thermal, chemical, and dynamic state of the MLT region, and thus the whole atmosphere. Furthermore, many interactions with the neutral and ionised atmosphere, as well as cosmic influences, can be investigated. However, a more detailed understanding of all processes involved is required. Parts of this thesis aim to improve our knowledge of the MLT region by gaining new insights about the mesospheric metal layers.

MLT temperatures

A major driver in the development of resonance metal lidars has been the need to derive temperatures in the otherwise inaccessible but important MLT region of the atmosphere. These temperature measurements have been very successful and provided deep insight into the structure of the MLT region and its dynamics [e.g., [von Zahn et al., 1996b](#); [Lautenbach et al., 2008](#); [Lübken et al., 2011](#); [Kopp et al., 2015](#)].

Cosmic dust evolution and atmospheric input

By comparing the abundances of various metals in the MLT, the composition and evolution of cosmic dust can be investigated. Lidar flux measurements of mesospheric metals are a promising approach to determine the absolute amount of meteoric input [[Gardner et al., 2014](#); [Huang et al., 2015](#)]. However, these measurements require certain assumptions concerning the unknown vertical eddy diffusion coefficient, mean vertical winds, and the technical performance of the laser. Additionally, small metal layer density fluctuations on the order of

the laser sampling frequency can cause non-linear deviations from the mean state. An improved understanding of these processes is required.

MLT dynamics

Metal densities can be observed with much higher sensitivity and over a much larger altitude range than temperatures or winds in the MLT region. Metal layers have therefore been used to investigate transport processes and wave phenomena [e.g., *Eska and Höffner, 1998; Fricke-Begemann et al., 2002; Fricke-Begemann and Höffner, 2005; Marsh et al., 2013b; Suzuki et al., 2013*] and have revealed unexpectedly strong tidal variations [*Lübken et al., 2011*], see Section 12.

Gravity wave analyses in the MLT have been successfully performed using NLC observations [*Kaifler et al., 2013; Ridder et al., 2016*]. However, these ice clouds are only available during the 2 or 3 coldest summer months. In contrast, it is possible to observe metal layers all year round, and the bottom-side of the metal layers is very sensitive to gravity wave distortions [*Viehl et al., 2016a*].

Lidar observations of metal layers can therefore significantly increase the capabilities to study dynamic features. However, metal atoms are not passive tracers but are subject to a variety of temperature-dependent chemical reactions (see review by *Plane et al. [2015]* and the following Sections). It is therefore necessary to gain a thorough understanding of these chemical processes through laboratory studies and combining lidar density observations with the appropriate theoretical modelling.

Abundances of important reactive species

Mesospheric metals interact with reactive species such as atomic O and O₃. These species are important for the radiative budget of the MLT but cannot be easily measured [*Feofilov and Kutevov, 2012*]. By observing metal densities, and combining the observations with model calculations, it might in the future be possible to derive concentrations of atomic O and O₃. Calculating the abundances in this way would improve the understanding of the representation of reactive species in models as well as the influence on the radiative budget of the MLT.

Nucleation of meteor smoke particles

Some of the metal compounds chemically created in the MLT condensate to so-called meteor smoke particles (MSP). These particles are slowly transported to the surface of the Earth and act as nuclei for clouds in the middle atmosphere [e.g., *Hunten et al., 1980; Megner and Gumbel, 2009*]. The formation of MSP is still not well understood, but the investigation of the metal layers is a crucial step in the process [*Plane et al., 2015*].

Ionosphere physics

Ionised metal species are strongly related to sporadic E layers (E_S) in the ionosphere [*Delgado et al., 2012*]. E_S are thought to be constituted from positively charged Fe and Mg ions, interacting with the Earth's magnetic field and gravity waves or wind shear [*MacDougall et al., 2000*]. These transient ionisation enhancements influence long distance HF radio communication and can also have an effect on the transmission of GPS signals. However, the formation process of E_S is not yet well understood. The phenomenon cannot be predicted accurately, although a relationship to solar thermal tides is known [e.g., *Haldoupis et al., 2004; Pignatelli et al., 2014*]. Sporadic layers appear in Fe lidar observations. Sporadic or sudden Fe layers (Fe_S) have been observed to occur with surprising regularity by the mobile IAP Fe lidar at Davis, Antarctica (69°S). The phenomenon has also been observed at ALOMAR, Norway (69°N), but less often. This is briefly addressed in Section 25.

Chemical reaction rates

The metal layers experience a variety of changes through different interactions (chemistry and photochemical effects, ionisation, transport dynamics). This allows investigation of chemical reactions by analysing high-resolution observations. *Viehl et al. [2016a]* correlate the change in an external variable (solar insolation) with observed changes in metal layer density. The authors thereby derive chemical reaction rate coefficients which had so far not been deducted successfully in laboratory studies, see Sections 5 & 6.

2.2 Origin

Mesospheric metals are created by the meteoric ablation of cosmic dust particles (meteoroids). The two primary cosmic dust sources are collisions between asteroids in the asteroid belt between Mars and Jupiter as well as the sublimation of comets approaching the Sun [Cepilecha *et al.*, 1998]. The exact amount of the daily cosmic dust input into the Earth's atmosphere is unknown and current estimations range from $5 \times 10^3 \text{ kg d}^{-1}$ to $2.7 \times 10^5 \text{ kg d}^{-1}$ globally [Plane, 2012]. However, it is known that the constant background stream of sporadic meteoroids entering the atmosphere every second causes a much larger average mass influx than even strong meteor showers such as the Perseids and Leonids [Höffner *et al.*, 1999; Höffner and Friedman, 2004; Nesvorný *et al.*, 2010]. Most of these constantly entering small meteoroids have masses in the range of 10^{-12} g to 1 g . Of those, particles of around $10 \mu\text{g}$ and a diameter of $\sim 200 \mu\text{m}$ provide the largest contribution to the daily mass input [Plane, 2012].

Meteoroids entering the atmosphere exhibit very high velocities between 11.5 km s^{-1} for particles in the same orbit as the Earth, and 72.5 km s^{-1} for particles in a retrograde orbit [Baggaley, 2002]. Significant frictional heating due to collisions with air molecules then occurs at these velocities when the particles encounter pressures of $\sim 0.001 \text{ hPa}$ at around 90 km altitude. Temperatures above the melting point of $\sim 1800 \text{ K}$ are reached, causing the particles to evaporate and create layers of atomic metals [Vondrak *et al.*, 2008]. Particles with a mass of less than 10^{-5} g fully ablate in this process, and only larger particles are deposited on the surface as meteorites [Flynn, 2002].

A variety of meteorites are found on Earth, but it is generally assumed that a majority of the meteoroids entering the atmosphere have a composition of ordinary chondrites similar to the orthosilicate olivine, i.e. a complete solid solution from forsterite (Mg_2SiO_4) to fayalite (Fe_2SiO_4) [Anders and Ebihara, 1982; Plane, 2012]. Hence, the metals Fe and Mg (as well as the metalloid Si) are expected to be the most abundant ablated species in the MLT region, with important minor constituents Al, Ca, Na, Cr, K, Mn, and Ni at a mass ratio of 5–10% relative to Si [Alpers, 1993a]. Element ratios satisfactorily matching some of these model predictions have been found in various studies [Plane, 2003].

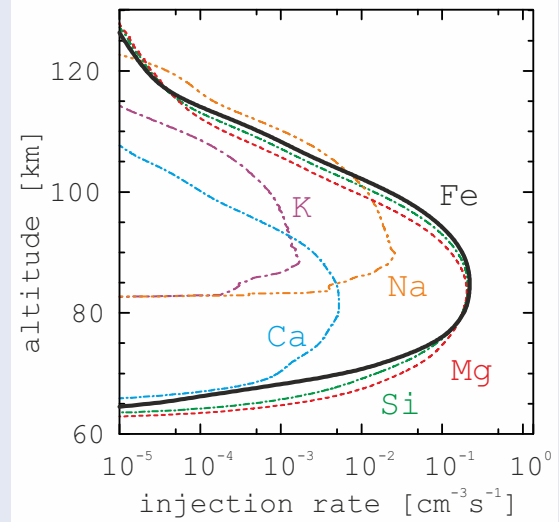


Figure 4: Model calculations of total meteoric injection rates for a distribution of chondritic meteoroids. The most abundant species are Fe, Mg, and Si. The peak of Fe ablation is calculated to occur around 85 km altitude. Adapted from Vondrak *et al.* [2008, Fig. 11], CC BY 3.0.

Figure 4 shows results of the Chemical Ablation Model (CABMOD) by Vondrak *et al.* [2008] for expected meteoric injection rates of chondritic meteoroids with masses from $5 \times 10^{-18} \text{ g}$ to $5 \times 10^{-3} \text{ g}$ entering the atmosphere at velocities of 11.5 km s^{-1} to 72.5 km s^{-1} . The peak injection rates of the abundant elements are calculated to occur around 85 km altitude. The shape of the resulting atomic layers will have a slightly different altitude distribution, as the elements are not only subject to dynamic transport and mixing processes, but also to rapid chemical reactions [e.g., Alpers *et al.*, 1993b].

2.3 Chemistry

Nearly all results presented in this thesis have been obtained from the analysis of Fe lidar observations. A brief introduction to the basic gas-phase chemistry of mesospheric Fe (see Figure 5) will allow a better understanding of these results. The following simplified discussion follows a more detailed analysis by Plane *et al.* [2015] and focusses on the aspects relevant to this work.

Laboratory studies have provided a broad insight into many of the relevant reactions shown in Figure 5 and determined most of the reaction rate coefficients [e.g., Plane, 2003; Self and Plane, 2003]. The important rate coefficients corresponding to the reactions are listed in Appendix B on page 59.

recombination can then create sudden enhancements in density [MacDougall et al., 2000; Bones et al., 2015]. However, for a given set of atmospheric conditions, mean abundances can be calculated by 3D atmospheric chemistry models employing the reaction rate coefficients in Appendix B.

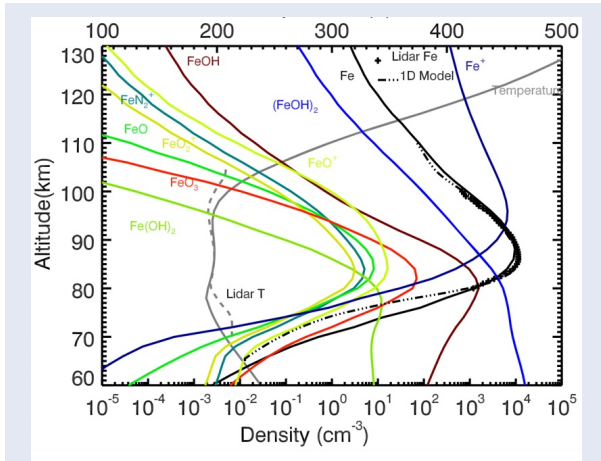


Figure 6: Number densities of Fe, Fe⁺, and important oxides and hydroxides. Below 90 km altitude, FeOH is the dominant reservoir from which Fe can be released. At higher altitudes Fe⁺ dominates. Model output of WACCM-Fe. Reproduced from Feng et al. [2013, Fig. 5], CC BY 3.0

Figure 6 shows mid-latitude model calculations by the Fe chemistry version of the Whole Atmosphere Community Climate Model (WACCM-Fe) which was developed by Feng et al. [2013]. The peak of the Fe layer (black) occurs around 87 km altitude. Above the peak of the layer, Fe⁺ (navy blue) is the dominant species. Below the layer peak, FeOH (maroon) is the main reservoir from which Fe can be released, exceeding the abundance of FeO₃ (red) by at least an order of magnitude. The creation of the dimer (FeOH)₂ (medium blue) is parameterised to occur with high efficiency upon every collision of two FeOH molecules. The model treats the dimer as an inert sink, accumulating to lower altitudes.

Although the chemistry of other meteoric metals is similar to Fe in many respects, some aspects differ considerably, in particular for K [Plane et al., 2014]. However, only Section 13 of this thesis briefly deals with K and a detailed understanding of its chemistry is not required in that context. For an in-depth discussion of K and other FeOH metals refer to the review by Plane et al. [2015] and the references therein.

Meteor smoke particles

Figure 5 shows that the nucleation of stable metal oxides and hydroxides (orange boxes) balances the meteoric input of the metal layers. Such particles formed from meteoric metals have become known as “meteor smoke particles” (MSP) [Hunten et al., 1980]. MSP are important as nucleation seeds for polar mesospheric clouds in the mesopause region [Turco et al., 1982; Gumbel and Megner, 2009; Saunders et al., 2010]. On average, it takes the particles around 4 years to reach the Earth surface [Plane et al., 2015]. During winter, however, the residual circulation can rapidly funnel MSP down to the stratosphere, where they reside in the air masses encircled by the polar vortex. Primarily within the stratospheric polar vortex, the particles are thought to interact with sulphuric acid and nitric acid, removing the vapours from the gas phase [Mills et al., 2005; Saunders et al., 2012; Frankland et al., 2015]. Hence, MSP may be not only important condensation nuclei for polar mesospheric ice particles (e.g., noctilucent clouds) but also for polar stratospheric clouds (nacreous clouds).

While investigating MSP nucleation pathways for Fe species, Saunders and Plane [2006] note that FeOH can be oxidised by O₃ to form anhydrous iron(III) oxide-hydroxide (FeOOH), see Section 7. The crystalline form α-FeOOH (goethite) has been identified by Rietmeijer [2001] as one of the most plausible candidates for MSP. Fe can also form α-Fe₂O₃ (hematite) and add to silica particles and be heterogeneously oxidised to FeSi₂O₆ (pyroxene) and Fe₂SiO₄ (fayalite) [Self and Plane, 2003]. A possible further sink for Fe is the dimerisation of FeOH, whereafter (FeOH)₂ could be picked up by other embryonic MSP.

However, several factors about the nucleation of MSP are still largely unknown. For example, the oxidation of FeOH to form goethite has not yet been investigated under laboratory conditions. A better understanding of these processes is required and can be achieved through further laboratory studies and via the comparison of lidar observations and 3D model calculations.

2.4 Spectral properties and observations

Even the more abundant mesospheric metals have relatively low absolute number densities of around $5 \times 10^2 \text{ cm}^{-3}$ to $5 \times 10^4 \text{ cm}^{-3}$ compared to the am-

bient atmosphere ($\sim 6 \times 10^{14} \text{ cm}^{-3}$ to $1 \times 10^{12} \text{ cm}^{-3}$ in the MLT between 75 km and 110 km altitude). However, their extremely large resonant scattering cross-sections allow efficient detection with ground-based lidar systems [Alpers *et al.*, 1990; Gardner, 2004]. Atomic Fe is particularly suited for year-round observation for a variety of reasons:

First, Fe exhibits high abundances in the MLT region, matched only by Mg and Si [Plane, 1991]. Second, the lower atmosphere is relatively transparent for the strong Fe resonance lines at 386 nm and 372 nm with a transmissivity of around 35%. In contrast, the resonance lines of Mg at 285 nm or 203 nm, and Si at 251 nm or 221 nm are located in the Hartley bands. They are fully absorbed by atmospheric O_3 and can only be observed from satellites [Alpers, 1993a; Langowski *et al.*, 2015]. Third, the linewidth of the resonance scattering of Fe is a lot narrower than the dominant resonance lines of Na at 589 nm or K at 770 nm, for three reasons: (a) the Doppler broadening is wavelength dependent and hence comparatively smaller at lower wavelengths, (b) Fe exhibits a much narrower hyperfine structure than the alkali metals, and (c) the isotope broadening is weaker for Fe [e.g., Lautenbach and Höffner, 2004; Höffner and Fricke-Begemann, 2005]. Narrower optical filters can therefore be used to observe Fe, which reduces the solar background detected and increases the overall daytime signal-to-noise ratio (SNR) of Fe over Na and K. Finally, the Fe resonance at 386 nm is located in a particularly deep Fraunhofer line, at which the solar flux is considerably low. This further reduces the solar background and increases the SNR, in particular during daylight conditions [Höffner and Lautenbach, 2009].

The peak scattering cross-section of Fe is approximately an order of magnitude lower than that of Na [Gardner, 2004]. However, because of the reasons listed above, Fe can be observed with a much higher SNR overall. The mesospheric Fe layer has consequently been investigated by several ground-based lidar systems, providing a variety of insights into the physics and chemistry of the MLT region [e.g., Alpers *et al.*, 1990; Lautenbach *et al.*, 2005; Gardner *et al.*, 2011; Chu *et al.*, 2011b; Viehl *et al.*, 2015].

While Fe is particularly suited to determine temperatures throughout the full diurnal and seasonal cycle, other metals (mainly Na and K) have also been observed with lidar instruments in order to

obtain density and night-time temperature measurements [e.g., Clemesha *et al.*, 1982; von Zahn and Höffner, 1996a; Höffner and Friedman, 2005; Höffner and Lübken, 2007]. Additionally, satellite observations of metal densities (Na, Mg, and K) became available through analyses of OSIRIS/ODIN as well as GOMOS and SCIAMACHY/Envisat measurements [Fussen *et al.*, 2004; Scharringhausen *et al.*, 2008; Dawkins *et al.*, 2014; Langowski *et al.*, 2015]. These observations can provide a unique near-global image of the metal layers and continuous climatological records. However, a fundamental limitation of satellite observations is their reduced vertical and temporal resolution. Several satellite experiments such as OSIRIS/ODIN can provide individual profiles with higher resolution, but published global data is often limited to a spatial resolution of about 10° (geographical) and ~ 1.7 km vertically, as well as 1-month averages [e.g., Fussen *et al.*, 2010].

The best overall picture of the mesospheric metals can, therefore, be obtained by combining high-resolution lidar measurements with global-scale satellite observations, and by interpreting the observations with models such as WACCM-Fe [Feng *et al.*, 2013].

3 The mobile IAP Fe lidar

The mobile IAP Fe lidar is an instrument for middle atmospheric temperature, metal atom density, and aerosol measurements. The main operational principle is based on an Alexandrite ring laser system scanning the Doppler broadened Fe resonance line at 386 nm. The precise high-power laser, a narrow field-of-view, and high-resolution optical filters allow high accuracy observations of MLT temperatures, Fe densities, and NLC in full daylight.

The Leibniz-Institute of Atmospheric Physics at the University of Rostock (IAP) in Kühlungsborn, Germany, has developed and operates a transportable Fe resonance lidar (mobile IAP Fe lidar) for MLT research. Measurements with this system provide the primary dataset analysed in this thesis. This section briefly summarises some technical details about the system and the data retrieval.

The first transportable lidar of this kind has been built into an insulated single customised 20' shipping container suitable for polar expeditions (Fig-



Figure 7: The mobile IAP Fe lidar at Davis, Antarctica (69°S) in March 2011. The system is housed in a single insulated 20' container, designed to be transported to remote polar regions. CC BY-NC 4.0

ure 7) at the University of Bonn in 1989. Since then it has continuously undergone a series of substantial and incremental improvements [e.g., Höffner, 1994; Schmitz, 1994; von Zahn and Höffner, 1996a]. The system has been operated by IAP since 1994 and measuring on an Fe line since 2004 [Lautenbach and Höffner, 2004]. Nearly background-free MLT measurements with high accuracy are possible due to the unique combination of diffraction limited high power laser, active beam stabilisation, narrow telescope field of view, and narrowband detection optics as well as real-time signal processing.

3.1 Laser system

At its core the system uses an Alexandrite ring laser with two flash lamp pumped chambers operating at 33 Hz pulse repetition rate [e.g., Schmitz, 1994; Schmitz et al., 1994] (see Figure 8 for a simplified schematic). The unidirectional Q-switched laser achieves a spectral bandwidth of less than 20 MHz with nearly 100% of the pulses in TEM₀₀ mode [Lautenbach and Höffner, 2004]. The fundamental wavelength of the Alexandrite ring laser is tuned to 771.9820 nm (in air; hereafter: 772 nm) by injection seeding of a tunable distributed feedback (DFB) diode laser.

An external-cavity Lithium triborate (LBO) non-linear crystal is then used as a frequency doubling unit, generating the second harmonic wavelength. The lidar can thereby probe the $a^5D_4 \rightarrow z^5D_4^0$ transition of the neutral Fe atom at 385.9910 nm (in air; hereafter: 386 nm) [Lautenbach and Höffner,

2004]. The mobile IAP Fe lidar can be operated at pulse energies between 100 and 140 mJ. Measurements are commonly performed at around 120 mJ to optimise between signal strength and optical deterioration.

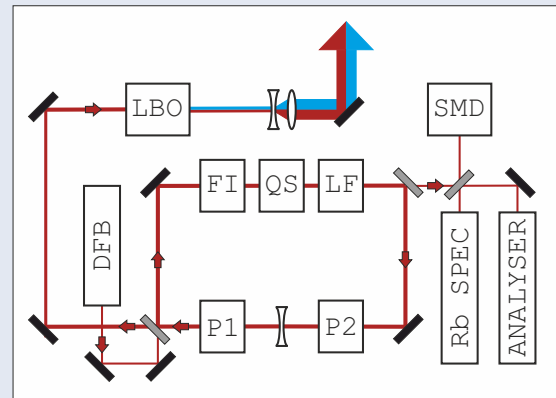


Figure 8: Simplified schematic of the mobile IAP Fe lidar's Alexandrite ring laser system at 772 nm with two pump chambers (P1 & P2), Faraday isolator (FI), Q-switch (QS) with single mode device (SMD), and a Lyot filter (LF) for intra-cavity mode tuning. The ring laser is injection seeded by a distributed feedback (DFB) laser. A spectrum analyser system examines each pulse and compares the frequency to a Rb saturation spectroscopy. An LBO crystal is used for the second harmonic generation to the Fe resonance line at 386 nm. CC BY 4.0

The DFB seeder laser is then continuously scanned in a range of ± 600 MHz (± 1.2 pm at 772 nm) to probe the Doppler broadening of the resonance scattering on the order of the FWHM of the Fe line width (± 1000 MHz, i.e. ± 0.5 pm at 386 nm) [Höffner and Lautenbach, 2009]. Due to effects inherent to all solid state laser systems (e.g., thermal lensing), the resulting frequency of the ring laser differs from the injection seeded frequency. A patented spectrum analyser system therefore measures the frequency and the mode structure of each laser pulse in real time [Höffner, 2015]. Each emitted pulse is compared to a compact Rubidium saturation spectroscopy unit with a resolution better than 100 kHz ($\ll 0.0002$ pm at 772 nm) and the signal recorded. The signals of pulses not in TEM₀₀ mode are discarded from the measurements.

The pulsed laser is vertically emitted into the atmosphere. A telescope retrieves the scattered light and transmits it to a detection bench. The altitude resolution is given by the time delay of the light detection, with photons from the MLT region arriving approximately 0.5–0.7 ms after their emission.

3.2 Telescope

The system is equipped with a Newtonian telescope composed of a purpose made 80 cm parabolic primary mirror with a focal ratio of $f/2.4$ and a flat secondary mirror with $R \approx 90\%$. The primary mirror is made from Aluminium coated Zerodur with $R \approx 86\%$ at both 386 nm as well as 772 nm and a surface quality better than $\lambda/10$, enabling good preservation of the Gaussian beam. The retrieved light is directly focussed into an optical fibre at the focal point of the telescope and guided to the detection bench (right panel of Figure 9).

An additional camera system operating at $f \neq 1$ behind the secondary mirror uses $\sim 10\%$ of the signal to determine the walk-off of the laser beam in the field of view (FOV). The offset is fed back to a piezo mounted mirror of the main laser. This setup can stabilise the laser at the pulse repetition rate of 33 Hz and minimise the impact of tropospheric turbulence and other disturbances on the signal [Eixmann et al., 2015].

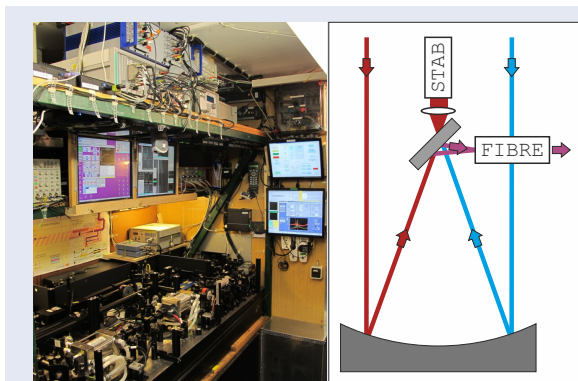


Figure 9: (left) Interior of the mobile IAP Fe lidar container: the Alexandrite ring laser table and electronics system shelf. (right) Schematic of the Newtonian telescope system. Both wavelengths are directly focussed into an optical fibre. A camera system behind the secondary mirror analysis about 10% of the detected light to stabilise the laser in the field-of-view. CC BY 4.0

The telescope's narrow FOV of $\sim 60 \mu\text{rad}$ is an essential component of the system's daylight capability as it reduces the total background radiation received [Höffner and Lautenbach, 2009]. It is furthermore optimised to the divergence of the diffraction limited laser. This results in the highest signal-to-noise ratio (SNR) possible with the outgoing laser power. A further reduction of FOV and laser divergence would decrease the signal strength due to

seeing which depends on atmospheric turbulence and cause local saturation in the Fe layer [Alpers, 1993a]. The telescope system is nearly fully made from carbon fibre materials to eliminate deforming by temperature variations.

3.3 Detection bench

The optically sealed detection bench comprises a spectral beam splitter and two separate detection branches for the UV and IR signals at 386 nm and 772 nm (Figure 10). Both branches use two narrowband plane-parallel Fabry-Perot interferometers (etalons) with high finesse to separate the retrieved signal from direct and diffuse solar as well as other optical background radiation [Höffner and Lautenbach, 2009]. The FWHM of the etalons are 10 600 MHz and as 4 200 MHz at 386 nm (~ 5.3 pm and 2.1 pm), as well as 2 600 MHz and 500 MHz at 772 nm (~ 5.2 pm and 1 pm). Additionally, interference filters with a bandpass of < 0.3 nm are used at the detectors.

The narrow FOV of the telescope results in a small divergence of the collimated signal, allowing to parallelise the beam to a width of less than 18 mm and hence an overall very compact and efficient construction of the detection optics. The near-Gaussian beam quality results in an efficiency of the etalons' transmission and reflectivity of more than 98%. The etalons are equipped with thermally stable Zerodur spacers and are pressure stabilised to the respective central frequencies. The IR channel additionally contains an actively stabilised confocal Fabry-Perot interferometer (CFPI) with a free spectral range of ~ 1000 MHz and a finesse 40 designed to detect aerosols with high precision [Viehl, 2010].

High-performance photomultiplier tubes (PMT) and avalanche photodiodes (APD) in Geiger-mode detect the UV and IR signals, respectively [Höffner and Lautenbach, 2009]. The PMTs and APDs are specifically chosen to exhibit a dark count rate of less than 20 Hz. Hence, at an altitude resolution of 200 m and a pulse repetition rate of 33 Hz the dark count rate accounts for less than 0.1 counts per altitude bin and 4 000 pulses (~ 2 min). The detectors are read out by a purpose built counter and electronics system designed by IAP operating at 6 MHz. The system creates around 50 MB of data per second overall which is compressed during the hard drive writing process by a specifically devel-

oped and patented packing algorithm to data files of around 4 MB per 2-Minute integration [Höffner, 2015]. A mechanical shutter wheel (chopper) with 4 wings rotating at ~ 8000 rpm blocks the strong Rayleigh and Mie signals of the lowest 14–20 km to avoid blurring of the sensitive detectors. The current setup of the chopper limits the overall detection altitude to ~ 208 km. The data algorithm, however, currently only analyses files up to ~ 145 km.

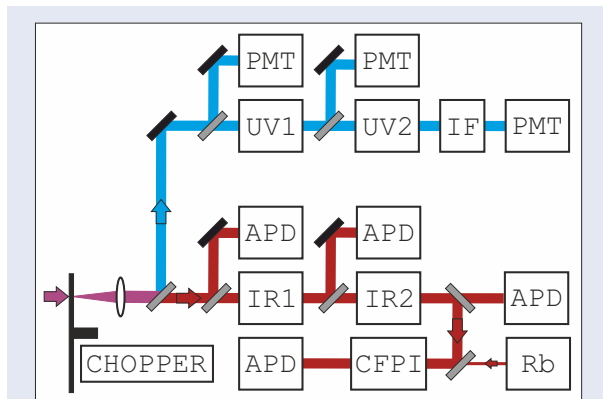


Figure 10: Simplified schematic of the detection bench of the mobile IAP Fe lidar. A chopper wheel blocks the high signal of the lower atmosphere before the parallelised beam is split into a UV and an IR branch. Both branches contain two etalons (UV1/2, IR1/2) as well as several single photon detectors (PMTs, APDs) to analyse each etalon’s filter curve. The UV branch has an additional flip mirror interference filter (IF) for daytime operation. The IR branch uses as narrow confocal etalon (CFPI) stabilised to a Rb saturation spectroscopy for high-resolution aerosol detection. CC BY 4.0

Contrary to common Rayleigh-Mie-Raman (RMR) lidar systems, the Rayleigh scattering of the neutral atmosphere (predominantly of N_2 and O_2) is currently not used to determine temperatures with the mobile IAP Fe lidar. While this is technically possible and has been successfully demonstrated by Kaifler [2014], the spectral properties of the laser and the detection bench are not optimised for this purpose. However, the exponentially decreasing Rayleigh signal in the middle atmosphere is indirectly used as an intensity reference for the resonance backscatter from the Fe layer and the Mie scatter of aerosols in the lower stratosphere.

3.4 Fe density retrieval

The retrieved lidar signal power needs to be compared to the outgoing laser power, as well param-

eters of atmospheric transmission and atomic backscatter, to determine absolute Fe densities in the MLT region. As Alpers [1993a] has shown, the Rayleigh signal in the stratosphere can be used to normalise the outgoing laser intensity. This approach simplifies the wavelength dependent lidar equation, as terms of the transmissivity of the atmosphere and the outgoing laser power can be substituted by a term dependent on the Rayleigh signal, assuming hydrostatic equilibrium. The detected background intensity is simultaneously determined at altitudes well above the Fe layer. With the approach described by Alpers [1993a], the Fe density can then be deduced from the lidar equation considering the remaining geometric factor and atomic physical factors including Hanle effect, Zeeman effect, Stark effect, and isotopic effect. Metal lidars may suffer from the so-called “saturation effect” and resonant extinction when stimulated emission of an already excited Fe atom occurs or emitted photons are reabsorbed within the metal layer [e.g., Simonich and Clemesha, 1983]. However, while these effects need to be considered for other metals such as K, they are negligible for Fe at the power densities of the mobile IAP Fe lidar [von der Gathen, 1990; Alpers, 1993a].

The measurement uncertainty depends on several factors, including atmospheric seeing and the intensity of the atmospheric (mainly solar) background radiation. However, it is roughly equal for different densities at different altitudes within the Fe layer. Typical uncertainties of the Fe density retrieval are on the order 2–5% at 1 km resolution and 15 min integration.

The altitude resolution is given by the time of flight measurement. The uncertainty of the altitude resolution mainly depends on the trigger of the counter electronics as well as detector dead time and is a lot smaller than 25 m.

3.5 Temperature retrieval

The mobile IAP Fe lidar determines MLT temperatures by spectrally scanning the Doppler broadened resonance scattering of atoms in the Fe layer. The raw data of 4000 laser pulses (i.e. ~ 2 min integration at 33 Hz) is integrated at an altitude resolution between 200–1000 m. Although the main isotope ^{56}Fe accounts for 91.72% of the abundance, the isotopes ^{54}Fe , ^{57}Fe , and ^{58}Fe also need to be considered when analysing the combined spec-

tral shape of the resonance scattering [Lautenbach and Höffner, 2004]. The filter function of each etalon is determined during each measurement by the mobile IAP Fe lidar at stratospheric altitudes [Höffner and Lautenbach, 2009]. With the knowledge of the combined theoretical spectrum of the 4 Fe isotopes, the laser linewidth as well as the filter function, the Doppler broadening can then be deconvoluted, giving a direct measure of the kinetic temperature of the metal atoms [Höffner and Fricke-Begemann, 2005]. As local thermodynamic equilibrium (LTE) can be assumed to exist throughout the atmosphere up to the turbopause at around 107 km, this temperature corresponds to the neutral gas temperature at the respective altitude. Potential deviations from the LTE as well as the hyperfine structure and the observed isotope composition as well as higher order effects like the relaxation pathway can be detected and considered by the algorithm through the spectral analysis and comparison with a theoretical model.

The photon statistic of the temperature retrieval depends on several factors, including the outgoing laser power, the atmospheric seeing, and the absolute density of the Fe layer. The uncertainty at the peak of the layer will therefore always be lower than at the layer's edges. Typical uncertainties within the RMS width of the layer are on the order 0.5–1 K for mean daily temperatures and 2–5 K after 1-hour integration [e.g., Lautenbach and Höffner, 2004; Viehl et al., 2015]. A comparative study of Fe and K lidars [Lautenbach et al., 2005] and comparison of K lidars and falling spheres released from sounding rockets [Höffner and Lübken, 2007] as well as a comparison with SOFIE temperature observations by the AIM satellite [Stevens et al., 2012] have shown the validity of the temperature soundings. The low uncertainty and high spatial and temporal resolution make the mobile IAP Fe lidar the most accurate temperature sounding instrument for the polar MLT region, in particular during the crucial summer months with 24 h sunlight [Lübken et al., 2015].

3.6 Aerosol retrieval

The mobile IAP Fe lidar can observe aerosols by detecting and analysing the fundamental Alexandrite wavelength at 772 nm and determining the peak of the Mie scattering. Light of this wavelength is always simultaneously emitted, as the extra-cavity

frequency conversion to 386 nm is never fully efficient.

Contrary to the UV wavelength, the IR line does not exhibit resonance scattering but only Rayleigh and Mie scattering (in this context the term “Rayleigh scattering” is used for the small particle approximation of the Mie theory while “Mie scattering” refers to the aerosol scattering of particles [e.g., van de Hulst, 1981]). As Viehl [2010] has shown, the separation of the much narrower and more intense Mie scattering (“Mie peak”) from the broader Rayleigh background can be performed by employing a very narrow band CFPI. The CFPI can be stabilised to the same Rb saturation spectroscopy that is used to analyse the frequency of the emitted laser pulse (see Section 3.1).

Using this method, common NLC can be detected within 1 integrated profile (i.e. 2 min of observations). The system can detect very faint NLC at 15 or 30 minute integration time. The probability of missing an average NLC with a mean brightness of $\ll 1 \times 10^{-10} \text{ m}^{-1} \text{ sr}^{-1}$ and lasting for more than 10 minutes can be approximated to be less than 0.01 %

In addition to the analysis at 772 nm, it is further possible to deconvolve the components of Rayleigh, resonance, and Mie scattering of the retrieved spectra at 386 nm and determine aerosol backscatter from this wavelength at MLT altitudes. As both signals are independently recorded and analysed, they can provide an independent confirmation of each other. The Mie scattering of the NLC at 386 nm is higher than at 772 nm, and less influenced by thin tropospheric clouds. However, the detection with the CFPI at 772 nm has a much larger SNR through the much stronger background suppression. The high SNR makes the detection of (a) smaller particles and especially (b) under unfavourable measurements conditions such as strong solar background or unfavourable atmospheric viewing more accurate and efficient on the IR wavelength. The aerosol (NLC) data presented in this thesis has been obtained with the CFPI at 772 nm.

4 Measurement campaigns

The mobile IAP Fe lidar has been in operation at Davis, Antarctica (69°S) from 2010–2012 and at ALOMAR, Norway (69°N) from 2008–2009 and again since 2014. The measurements have yielded a dataset of more than 4 800 hours of temperature and Fe density observations with unprecedented resolution and accuracy. This unique dataset and the co-located operation of further instruments present a rare opportunity to study the polar MLT region.

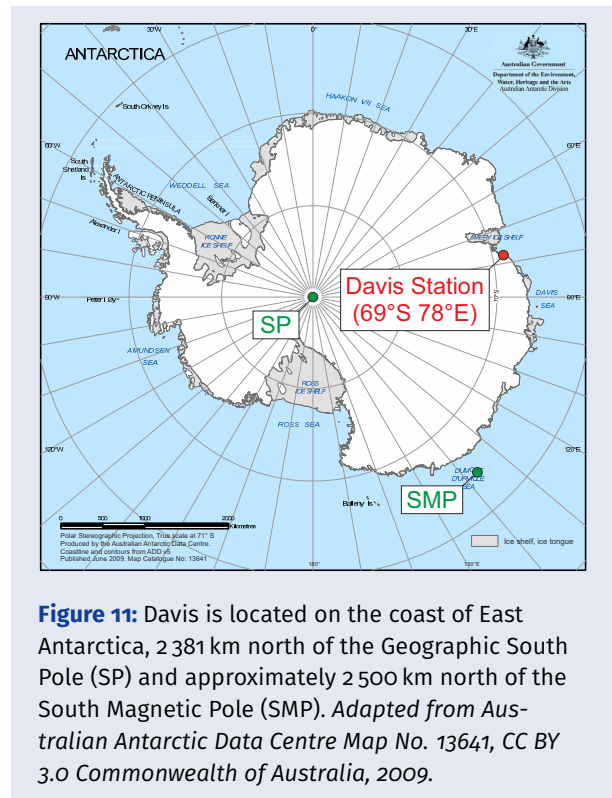
The emphasis of this thesis lies on the analysis of a new and unique set of lidar observations and their comparison with other instruments and model studies. This section provides an overview of the two measurement campaigns, conducted respectively in opposing polar regions, during which the lidar data discussed in this thesis has been obtained.

4.1 Davis, Antarctica (69°S)

Davis is an Antarctic research station with year round personnel, very good infrastructure for operating a containerised instrument as well as technical and scientific support allowing continuous measurements. The mobile IAP Fe lidar was transported to Davis ($68^{\circ}34'35''\text{S}$, $78^{\circ}58'20''\text{E}$) in 2010. It was operated there for slightly more than two years in close collaboration with the Australian Antarctic Division (AAD). Additionally, several other instruments for middle atmospheric research are stationed at Davis. The resulting joint datasets of various physical parameters can provide invaluable insights for the understanding of the atmosphere at different altitude levels.

Co-located instruments

Among the instruments operated at Davis are two radars: a VHF mesosphere-stratosphere-troposphere (MST) radar providing PMSE observations at 55 MHz [e.g., [Morris et al., 2004](#); [Alexander et al., 2013](#)], and an MF radar providing middle atmosphere wind data at 1.94 MHz [e.g., [Murphy et al., 2006](#); [Morris et al., 2006](#); [Murphy et al., 2012](#)]. Furthermore, a Lowe digisonde continuously records sporadic E and F layers in the ionosphere as well as electron density profiles from about 90 km upwards.



The AAD has been operating a Rayleigh-Mie-Raman (RMR) lidar at Davis since 2005 [e.g., [Kleociuk et al., 2008](#)]. The AAD RMR lidar has been recording temperature and aerosol data from the troposphere up to the upper mesosphere. It has been providing valuable statistics about the occurrence of ice particles in the mesopause region (NLC) and the stratosphere (Junge layer and Polar Stratospheric Clouds) as well as allowing temperature and gravity wave analyses [e.g., [Alexander et al., 2011](#)]. As for most RMR lidars, the temperature retrieval does not cover the mesopause region due to the exponential decrease of neutral air density and the resulting loss of signal towards higher altitudes. A combination of RMR and metal resonance lidars therefore enables the investigation of the full temperature structure from the ground to the lower thermosphere. Moreover, MLT temperature observations as provided by the mobile IAP Fe lidar can improve the temperature retrieval of RMR systems by setting an accurate initial temperature for the downward integration [[Gerding et al., 2008](#)].

Further instruments installed at Davis are a scanning Czerny-Turner hydroxyl (OH) spectrometer (providing average temperatures in the OH layer around 87 km during dark hours) [e.g., [French and Kleociuk, 2011](#)] as well as a narrow-field Fabry-Perot spectrometer (providing neutral thermo-

spheric winds from observations of the Doppler shift of auroral emissions) [e.g., [Dhadly et al., 2015](#)]. The Space Weather Services section of the Australian Bureau of Meteorology (BOM) monitors the geomagnetic activity with the Southern Hemisphere Imaging Riometer Experiment (SHIRE) and a magnetometer at Davis [e.g., [Morris et al., 2005](#)]. The BOM also launches standardised weather balloons with radiosondes twice a day and operates two weather stations at Davis and at Woop Woop, about 35 km from Davis on the Antarctic plateau. A host of further experiments are conducted at Davis but have no direct relation to the middle atmospheric measurements presented here.

Mobile IAP Fe lidar campaign

The mobile IAP Fe lidar was shipped to Hobart, Tasmania (43°S) in August 2010 and loaded on board the Australian icebreaker Aurora Australis in October 2010. After a 4 week journey through the Southern Ocean, the system was set up at Davis (69°S) in November and December 2010, commencing first measurements in the MLT region on 14 December 2010 [[Lübken et al., 2011](#)]. Measurements continued for more than 2 years until the end of the Antarctic summer season 2012/2013. The very successful first part of the campaign with considerably more measurement hours than expected resulted in stronger than usual deterioration of several laser components. Major maintenance on the main Alexandrite laser became necessary during the 2012 winter. No measurements were therefore obtained between June–September 2012. With this exception, the mobile IAP Fe lidar was in continuous operation whenever tropospheric weather permitted, performing the last measurements on 31 December 2012 [[Lübken et al., 2015](#)].

The dataset obtained at Davis includes around 2 900 hours of high resolute temperature and Fe density measurements in the MLT region. Figure 42 in Appendix C shows the distribution of measurements throughout the year and hours of the day. All months of the year were covered during the campaign, with a minimum of 129 hours obtained in September and a maximum of 381 hours in January, averaging around 241 hours per month. A slight minimum of observations is apparent in the early morning hours, mainly due to tropospheric weather conditions and, to a smaller extent, due to opera-



Figure 12: Unloading of the 20' shipping container of the mobile IAP Fe lidar from the Australian icebreaker RSV Aurora Australis onto the fast ice at Davis, Antarctica (69°S , 78°E). Photo courtesy of Dr J. Höffner.

tor fatigue management considerations. However, a substantial amount of measurements has been obtained throughout all hours of the day, enabling representative full diurnal analyses for all months.

Although it had been planned to recover the instrument and the operator after the 2012 SH winter in November 2012, an unusually warm spring, as well as high quantities of dust, deteriorated the fast ice much quicker than usual. Additionally, the Aurora Australis encountered unexpectedly heavy pack ice which delayed progress. By the time of the ship's arrival, the fast ice had deteriorated to such an extent that no heavy cargo could be loaded. Weighing around 9 000 kg, the mobile IAP Fe lidar could not be transported to the icebreaker by alternative helicopter slinging or other means. Hence, the lidar container could only be recovered nearly 4 months later in the middle of summer once the sea ice had cleared, which gave the opportunity for an unplanned third season of measurements. As Section 17 shows, this turned out to be a scientifically very fortuitous coincidence, as the third season in a row showed a markedly different temperature structure in the MLT region compared to the previous two years [[Lübken et al., 2015](#)].

In early February, the mobile IAP Fe lidar container was transported to the Aurora Australis via barge transfer and shipped back to Australia and then further to Kühlungsborn, Germany, where it arrived for maintenance at IAP on 12 June 2013.

4.2 ALOMAR, Norway (69°N)

After thorough maintenance and upgrade of several infrastructure components, the mobile IAP Fe lidar container was transferred to the Arctic Lidar Observatory for Middle Atmosphere Research (ALOMAR) in northern Norway in June 2014. ALOMAR is located on top of the Ramnan mountain on the island of Andøya (69°16'42"N, 16°00'31"E), 2 303 km south of the Geographic North Pole and approximately 2 700 km south of the North Magnetic Pole.



Figure 13: The mobile IAP Fe lidar container at the Arctic Lidar Observatory for Middle Atmosphere Research (ALOMAR) on Andøya, Norway (69°N, 16°E). Measurements at similar latitudes in the Arctic and Antarctica allow a unique comparison of the differences and similarities of both hemispheres. *Photo courtesy of R. Wörl.*

Co-located instruments

ALOMAR is mainly operated by personnel of the Andøya Space Centre (ASC) in Andenes, Norway. The observatory houses several instruments for middle atmosphere research. The largest and likely most visible instrument at ALOMAR is the steerable double-beam ALOMAR RMR lidar with two 1.8 m Cassegrain-design primary mirrors and a dual Nd:YAG laser system. The ALOMAR RMR lidar has been employed to study middle atmosphere temperatures, NLC properties, stratospheric winds, and gravity waves [e.g., [Schöch et al., 2008](#); [Baumgarten et al., 2012](#); [Hildebrand et al., 2012](#); [Baumgarten et al., 2015](#)]. Further instruments at ALOMAR include an ozone lidar as well as a Na lidar [e.g., [Dunker et al., 2015](#)]. ASC personnel allow year-round operation of the instruments. Observations are routinely conducted and supported by staff and students of

IAP, in particular at nighttime and during the summer months crucial for NLC observations.

ASC further operates a facility to launch atmospheric sounding rockets. Sounding rocket campaigns studying the dynamics and chemistry of the MLT are frequently conducted [e.g., [Lübken, 1999](#); [Rapp et al., 2012](#)]. Lidar and rocket-borne measurements have also been combined to validate new measurement techniques and to provide more accurate observations overall [e.g., [Lübken et al., 2016](#)]. Further important instruments for middle atmospheric research have been built close to ALOMAR and are operated by IAP personnel. The Middle Atmosphere ALOMAR Radar System (MAARSY) is a very recent and modern VHF radar operating at 53.3 MHz. It is set up as an active phased array antenna comprised of 433 three-element Yagi antennas and provides, amongst other measurements, PMSE data. The narrow-beam Saura MF radar system operating at 3.17 MHz provides wind and turbulence parameters between 50 km and 94 km at an altitude resolution of 1–1.5 km. Similarly to Davis, the combined dataset of various instruments at ALOMAR results in unique opportunities for atmospheric research.

Mobile IAP Fe lidar campaign

Figure 42 in Appendix C shows the measurement statistics of the mobile IAP Fe lidar at ALOMAR, combined for the years 2008–2009 as well as since July 2014. During the first deployment of the lidar in 2008–2009, around 400 hours of observations were obtained at ALOMAR. Since July 2014, an additional 1 500 hours of Fe density and temperature observations have been acquired, adding to a total of around 4 800 hours in both hemispheres. The measurement uncertainties at ALOMAR are equal to those from the observations at Davis, Antarctica. As for the measurements in Antarctica, the statistics show a small decline in observations during the early morning hours. Similarly to the conditions at Davis, this is mainly caused by tropospheric weather. However, on some occasions, measurements efforts were hampered, as the system cannot be operated entirely autonomously at ALOMAR due to aviation safety considerations and technical challenges. As ASC operators or IAP personnel are not always available, especially during weekends, public holidays and at night, valuable measurement opportunities are so far occasionally missed.

Summary of Results

The following Sections 5 to 18 summarise the main results of this thesis published in peer-reviewed journals. The individual chapters give an overview of the previously existing knowledge, the methods and results of the studies, and the insights gained from the analyses. Where applicable, some open questions or relations to other studies are briefly mentioned. Citations to papers authored by the candidate are given in **bold**. For further details refer to the manuscripts reprinted on pages 63 to 141.

5 Bottomside extension of the Fe layer during daylight

The mesospheric Fe layer shows a pronounced extension of the bottomside during periods of daylight. Observations of this extension in both hemispheres are quantitatively analysed. A lower limit to the reaction creating Fe at the bottomside is derived. The analysis suggests that only the direct photolysis of FeOH can be fast enough to explain the observations.

A regular downward extension of the mesospheric Fe layer has been observed at ALOMAR, Norway and McMurdo, Antarctica [Yu et al., 2012]. The phenomenon is caused by solar irradiance: whenever the MLT region is sunlit (solar elevation $\gtrsim -5^\circ$), the Fe layer shows a pronounced downward extension of the bottomside (Figure 14). Yu et al. [2012] analyse the altitude change $\frac{\Delta z}{\Delta t}$ of a defined bottomside contour at different times of the year and demonstrate that this effect depends on the timing of the solar irradiation. Self and Plane [2003] show that iron(II) hydroxide (FeOH) is a significant reservoir for Fe at the respective altitudes below 90 km (see Section 2). It is further known that FeOH can react with H to form Fe [Plane et al., 1999]. Based on these principles, Yu et al. [2012] give a qualitative explanation of a possible chemical nature of the bottomside extension, suggesting that the photolytic creation of H in the MLT and reaction with FeOH could cause the observed behaviour.

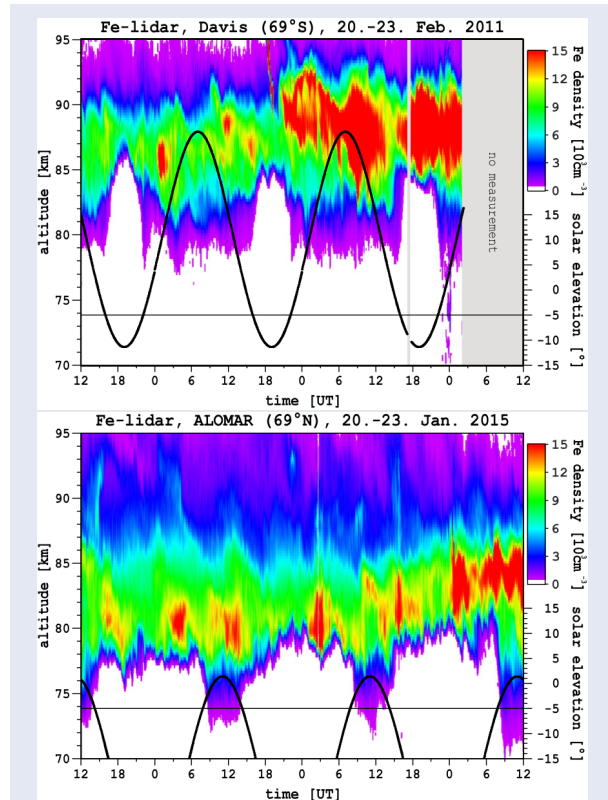


Figure 14: The Fe layer at Davis, 69°S (top) and ALOMAR 69°N (bottom) during 3 cycles of sunrise and sunset. The bottomside of the Fe layer is extended whenever the MLT region is sunlit. Reprinted with permission from Viehl et al. [2016a, Fig. 1], Copyright 2016 John Wiley & Sons, Inc.

A different quantitative approach can be made to analyse the effect in more detail. Viehl et al. [2016a] investigate the rate of increase $\frac{\Delta[\text{Fe}]}{\Delta t}$ at each altitude rather than the altitude change of the defined bottomside contour, thereby quantifying the rate of increase of Fe at the respective time of apparent sunrise. An example of the analysis is shown in Figure 15. As Viehl et al. [2016a] show, a first approximation to the reaction creating Fe can then be derived by assuming a full conversion of the reservoir FeOH to Fe. However, Fe is not only created but simultaneously rapidly oxidised via O_3 and O_2 to FeO, FeO₂ and FeO₃, which then react with H₂O and H to Fe(OH)₂ and ultimately back to FeOH again. The rate determined from the observations, therefore, sets a lower limit to the rate of the reaction producing Fe.

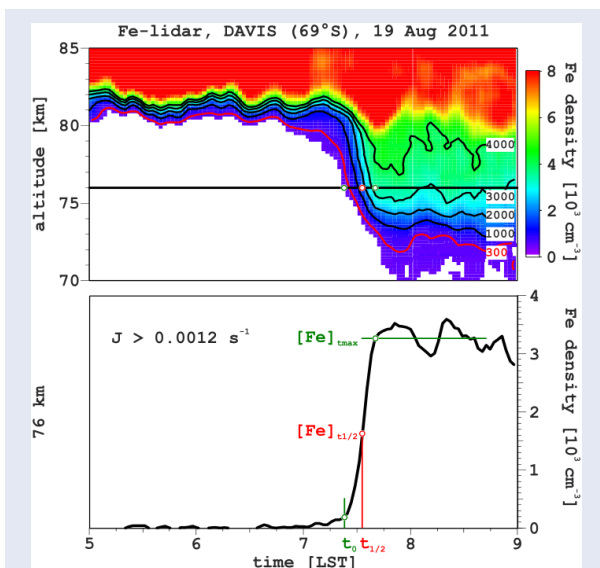


Figure 15: Analysis of the bottomsides extension. The observed rate of increase sets a lower limit to the photolysis coefficient. Reprinted with permission from [Viehl et al., 2016a, Fig. 2] Copyright 2016 John Wiley & Sons, Inc.

Viehl et al. [2016a] analyse all available cases of the bottomsides extension observed at Davis (69°S) and ALOMAR (69°N), averaging the rates of increase obtained at all altitudes and days to average out the influence of gravity waves, which could distort the analysis through quick vertical transport and temperature changes. The analysis yields a rate of increase larger than $(1.2 \pm 0.4) \times 10^3 \text{ s}^{-1}$ and shows that there is no discernible difference between the hemispheres [Viehl et al., 2016a]. This rate is a lot faster than what was expected of both the reactions of FeOH with H as well as the direct photolysis of FeOH. However, it was so far not possible to measure the photolysis rate $J(\text{FeOH})$ under laboratory conditions. A value much larger than the low level of $J = 1 \times 10^{-5} \text{ s}^{-1}$ hitherto assumed is well possible. On the other hand, a discussion in the literature shows uncertainty regarding the reaction rate coefficients and relative importance of the reactions $\text{FeOH} + \text{H} \longrightarrow \text{Fe} + \text{H}_2\text{O}$ and $\text{FeOH} + \text{H} \longrightarrow \text{FeO} + \text{H}_2$ [Jensen and Jones, 1974; Rumminger et al., 1999; Self and Plane, 2003]. However, even the fastest assumptions don't seem to be able to reproduce the observations as the modelling work by Feng et al. [2013] shows. Hence, after the analysis of the lidar observations, it appears more likely that the direct photolysis of FeOH causes the bottomsides extension instead of the reaction of FeOH with photolytically created atomic H.

A further indication of the relative dominance of the direct photolysis of FeOH over the reactions with H is the diurnal cycle of atomic H in the polar summer MLT region. While H is mainly created through photolysis of H_2O at sunrise, its abundance increases until sunset and only slowly decreases thereafter with sufficient H for potential reaction with FeOH remaining for several hours. As the bottomsides extension rapidly retracts at sunset, the diurnal cycle of H argues against a dominating contribution of the reactions of FeOH with H. However, the abundance of ozone which is responsible for the oxidation of Fe simultaneously increases at sunset. As all reaction rates depend on the abundances of several non-steady species, only a full chemical model including all reactions and abundances such as presented by Feng et al. [2013] can quantitatively examine the relative importances adding to the observed effect.

Section 6 examines the possible pathways from FeOH to Fe closer and gives new insights on their importance for the Fe chemistry in the MLT region.

6 Photolysis of FeOH and reactions with H

The combination of mesospheric lidar observations, quantum chemical calculations, and 3D atmospheric modelling is used to derive a photolysis rate. Two previously not well-known reaction rate coefficients are re-evaluated. Implementation of the new photolysis rate and reaction rate coefficients markedly improves the modelling of the mesospheric Fe layer.

Laboratory studies have provided a broad insight into the gas phase metal chemistry of the MLT region [e.g., Helmer et al., 1998; Rollason and Plane, 2000; Self and Plane, 2003; Vondrak et al., 2006]. However, not all molecules have a suitable electronic transition for probing with laser-induced fluorescence, which means that some important and relevant reactions with metal-containing species cannot be directly investigated in the laboratory. The recent use of photo-ionisation combined with Time-of-Flight mass spectrometry has enabled some new species to be detected, and their kinetics studied directly [Goméz-Martín et al., 2015]. Nevertheless, the photolysis rate of FeOH cannot currently be examined with either technique. It had been assumed to be negligible and set to a low

level of $J(\text{FeOH}) = 1 \times 10^{-5} \text{ s}^{-1}$ in atmospheric model calculations [Feng et al., 2013; Plane et al., 2015].

Analyses performed by Viehl et al. [2016a] show both that the photolysis of FeOH most likely causes the bottomsides extension and that the photolysis rate seems to be larger than $(1.2 \pm 0.4) \times 10^{-3} \text{ s}^{-1}$ (Section 5). Subsequently, Viehl et al. [2016a] perform quantum chemical calculations to test this assumption and to determine a plausible value of the photolysis rate. The range-separated CAM-B3LYP functional introduced by Yanai et al. [2004] is used with the 6-311+g(2d,p) basis set to optimise the geometry of FeOH in the Gaussian 09 suite of programs [Frisch et al., 2009]. The time-dependent density functional method [Scalmani et al., 2006] is then used to compute the necessary energy transitions to calculate the photolysis cross section shown in Figure 16. The thermodynamic threshold for FeOH had been determined to be at around 370 nm [Schröder, 2008].

However, Viehl et al. [2016a] point to two pieces of evidence that the broad band between ~ 300 nm and 400 nm most likely does not lead to photolysis. First, FeOH has a very similar absorption cross section to iron(I) chloride (FeCl) for which experimental data is available for comparison and which, moreover, is electronically analogous. It has been observed that FeCl does not photolyse between 315 nm and 400 nm, but to produce fluorescence instead [Delaval et al., 1980; Lei and Dagdigian, 2000]. Second, the Mulliken electron populations show that the excited states of FeOH remain ionic like the ground state until the 8th and higher states which are covalent in nature and more likely to dissociate. This transition is calculated to occur at 300 nm [Viehl et al., 2016a].

Allowing for a slight red-shift for internal excitation, Viehl et al. [2016a] then integrate over the absorption cross section and the solar flux from 150 nm to 305 nm, yielding a photolysis rate of $J(\text{FeOH}) = (6 \pm 3) \times 10^{-3} \text{ s}^{-1}$. This is more than 500 times faster than previously assumed [Plane et al., 2015]. However, it is only about 5 times larger than the lower limit set by the analysis of lidar observations (Section 5) and hence constitutes a reasonable result which can be tested further.

Viehl et al. [2016a] employ a recent 3D global atmospheric chemistry model to test the implications of the newly determined photolysis rate. On the basis of the Whole Atmosphere Community Climate Model (WACCM), Feng et al. [2013] have de-

signed WACCM-Fe for the global investigation of the mesospheric Fe layer. The background chemistry scheme is based on that of Kinnison et al. [2007] with the addition of more than 120 gas phase reactions [Plane et al., 2015]. The model further considers the meteoric input through a combination of a cosmic dust astronomical model with a chemical ablation model [Fentzke and Janches, 2008; Plane, 2004; Vondrak et al., 2008]. More information on the model can be found in Marsh et al. [2013a, b].

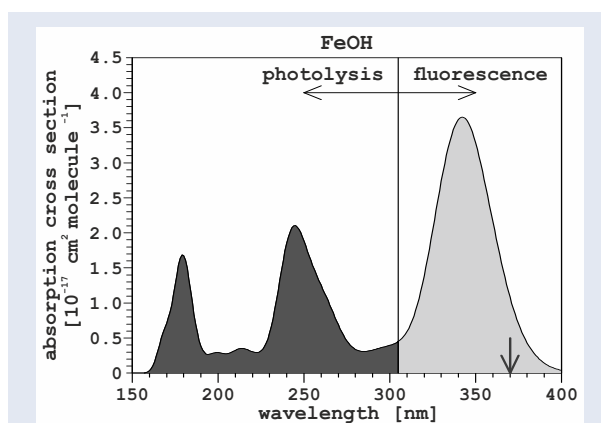


Figure 16: Absorption cross section of FeOH as calculated by hybrid TD/CAM-B3LYP density functional theory. Wavelengths shorter than 305 nm lead to photolysis. Reprinted with permission from Viehl et al. [2016a, Fig. 3], Copyright 2016 John Wiley & Sons, Inc.

Viehl et al. [2016a] use the method of Merkel et al. [2009] to increase the vertical resolution of WACCM-Fe in the MLT region from ~ 3.5 km to ~ 0.5 km. This is an important step to give a more accurate representation of the crucial distribution of atomic H and O at the bottomsides of the Fe layer.

The results of the model simulations are compared to lidar observations (black) in Figure 17. The existing model run by Feng et al. [2013] shows a slight increase in Fe density during the day (red). However, absolute daytime densities are underestimated compared to observations and high Fe levels are predicted during the night, when no Fe is observed by lidar. The increased model resolution employed by Viehl et al. [2016a] results in a more pronounced daytime enhancement and nighttime depletion (orange). Nevertheless, the timing of the observed increase is not captured well. When employing a photolysis rate of $J(\text{FeOH}) = 6 \times 10^{-3} \text{ s}^{-1}$ (cyan and blue), the sudden increase of Fe at sunrise is captured very well by the model. The good agreement in the comparison of lidar and mod-

elling work shows that the calculations performed by [Viehl et al. \[2016a\]](#) were reasonable and seemed to have produced the correct value for the photolysis rate. Hence, the novel combination of quantum chemical calculations and comparison of a global 3D atmospheric model with mesospheric Fe lidar measurements was successfully used to determine the photolysis rate of FeOH.

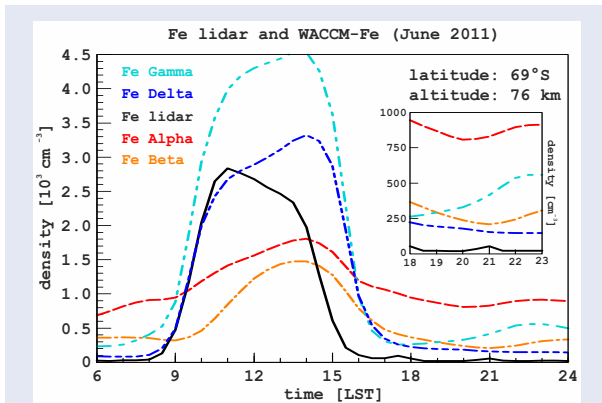


Figure 17: Various WACCM-Fe model runs compared to lidar observations (black). Previous model runs underestimated the increase at sunrise and predicted high Fe densities during nighttime periods (red and orange). With the implementation of a new photolysis rate of FeOH deduced from quantum chemical calculations and lidar observations, the representation of the increase at sunrise as well as the absolute abundance of Fe is markedly improved (cyan and blue). The use of two new rate coefficients for reactions of FeOH with H reproduces the low nighttime densities observed (blue). Adapted with permission from [Viehl et al. \[2016a, Fig. 4\]](#), Copyright 2016 John Wiley & Sons, Inc.

However, the model still shows discrepancies to the observed metal layer which can be investigated further. As it turns out, the high nighttime densities of Fe calculated by the model and shown in Figure 17 are nearly exclusively caused by the reactions of FeOH with H (cyan). [Viehl et al. \[2016a\]](#) review the dispute about these reactions mentioned in Section 5. Reinterpreting the results from flame and modelling work by [Jensen and Jones \[1974\]](#) and [Rumminger et al. \[1999\]](#) as well as the results summarised by [Self and Plane \[2003\]](#), an alternative interpretation of the data is drawn. Instead of adopting a single very high coefficient $k_{12a} = 3.0 \times 10^{-10} \exp(-1264/T)$ [[Feng et al., 2013](#)] and neglecting k_{12b} , the rate coefficient $k_{12a} = 2.0 \times 10^{-12} \exp(-600/T)$ can be taken from [Jensen and Jones \[1974\]](#) while the pre-exponential factor and activation energy

can be altered slightly from $k_{12b} = 5.0 \times 10^{-11} \exp(-800/T)$ to $k_{12b} = 6.0 \times 10^{-11} \exp(-1200/T)$ [[Viehl et al., 2016a](#)]. The changes to k_{12b} are modest when considering the extrapolation over the wide temperature range from the flame work (>2000 K) and the reactions at typical MLT temperatures between 135 K and 250 K.

When employing both reactions with the described rate coefficients (blue) instead of only considering the presumed $k_{12a} = 3.0 \times 10^{-10} \exp(-1264/T)$ (cyan), [Viehl et al. \[2016a\]](#) find a considerable improvement of the Fe layer description (see inlay in Figure 17). Some discrepancies persist in the evening hours. These may be caused by an incorrect representation of [H] and [O] in WACCM or by a further overestimation of k_{12a} and k_{12b} . However, to reduce the rate coefficients further would have been incompatible with the flame work by [Jensen and Jones \[1974\]](#) and beyond the scope of the paper. More laboratory work regarding these reactions is required.

Indeed, [Viehl et al. \[2016a\]](#) point out that the high spatial and temporal resolution of a resonance metal lidar puts a stringent test to 3D atmospheric chemistry models. If all reactions rates were known precisely from laboratory measurements, the comparison of lidar observations and model predictions could provide valuable information about the overall validity of the transport processes of the model as well as the distribution of the crucial reactants H and O. These reactants, in turn, are of high importance for the abundances of O_3 , CO_2 , and other species that are crucial for the energy budget of the middle atmosphere.

The analysis by [Viehl et al. \[2016a\]](#) shows that $J(\text{FeOH})$ is more than 2 orders of magnitude larger than previously assumed. To the knowledge of the authors, this is the first time a mesospheric metal was used to determine a photolysis rate in a “natural laboratory” by the novel combination of techniques. A re-evaluation of reaction rate coefficients discussed in the literature allows slight changes to the rate coefficient of the reaction $\text{FeOH} + \text{H} \rightarrow \text{FeO} + \text{H}_2$ and results in a significantly improved representation of the mesospheric Fe layer in a 3D climate chemistry model. The bottomside extension shown in Figure 14 can now be explained by the photolysis of FeOH and not by reaction of FeOH with atomic H. The strong importance of photodissociative processes influences the overall diurnal behaviour of the Fe layer and hence tidal effects as reported by [Lübken et al. \[2011\]](#).

7 Depletion of FeOH during sunlit periods

Mesospheric FeOH is nearly entirely photolysed whenever sunlight is present. FeOH can therefore not be a major reservoir for Fe in the polar summer MLT region. This may have consequences for the formation and composition of meteoric smoke particles.

As discussed in Sections 2 and 5, FeOH is assumed to be the primary reservoir of Fe below 95 km [Plane, 2003; Self and Plane, 2003]. Figure 18 compares two high resolution WACCM-Fe model simulations without (run Beta) and with (run Delta) the implementation of the new rate coefficients determined in Section 6. The strongly increased photolysis leads to a nearly complete depletion of FeOH whenever sunlight is present. This changes the equilibrium between Fe and its reservoir species in the summer polar mesopause region [Viehl et al., 2016b].

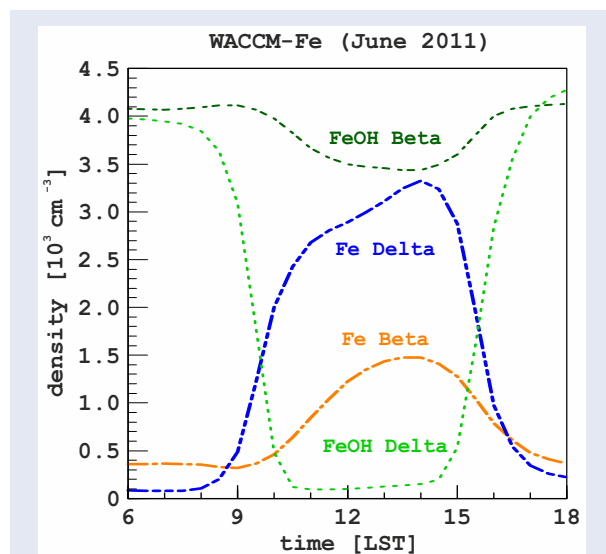


Figure 18: WACCM-Fe calculations of Fe and FeOH. After implementing the new photolysis rate, FeOH is now calculated to be nearly fully photolysed whenever sunlight is present. This may have implications for the formation and composition of MSP. CC BY 4.0

The nucleation of meteor smoke particles (MSP) balances the meteoric input creating the metal layers in the MLT region. Viehl et al. [2016a] note that FeOH can be oxidised by O_3 to form FeOOH. Rietmeijer [2001] has shown that the crystalline form goethite (α -FeOOH) is a plausible candidate for MSP. As the polar summer mesosphere is continuously sunlit, FeOH is unlikely to be present in

significant concentrations and hence goethite is unlikely to be formed. Fe can still add to silica particles and be oxidised heterogeneously and form hematite (α -Fe₂O₃), pyroxene (e.g., FeSi₂O₆) or fayalite (Fe₂SiO₄) which removes Fe and balances the input [Self and Plane, 2003; Plane et al., 2015]. However, Saunders and Plane [2006] note that goethite and hematite are the most likely stable solid species. The composition of meteoric smoke particles created in the summer polar regions could differ from regions with considerable periods of darkness. The unavailability of FeOH in the sunlit MLT hence changes the overall composition of expected MSP [Viehl et al., 2016a].

Johnson [2001] proposed that the input of meteoric Fe into the oceans might play an important role for the fertilisation of phytoplankton. A modelling study by Dhomse et al. [2013] indicated that this could indeed be the case for the Southern Ocean, resulting in a significant impact on ocean productivity and hence global CO₂ drawdown. A recent idea has been to couple a whole atmosphere model of meteoric metals to an ocean biogeochemistry model to evaluate these processes [Plane et al., 2015]. The changed speciation of MSP which can be expected from the results of Viehl et al. [2016a] could potentially influence the solubility and availability of Fe in this process.

8 Definition of the metal layer bottomsides

The Fe layer's dependence on chemical reactions leads to ambiguous definitions of the layer bottomsides. Care needs to be taken when defining and comparing absolute values.

Höffner and Friedman [2004] define the mesospheric metal layer "topside" as the metal and ion layers above 110 km. While analysing the diurnal behaviour of the Fe layer, Yu et al. [2012] define the "bottomside" of the layer as the lower 300 cm⁻³ contour and investigate its altitude variation with time. That study concluded that the time lag observed was in accordance with a time delay of the first solar insolation at different altitudes during dawn. Although the conclusion of a seasonal dependence is still valid in this case, Viehl et al. [2016a] note that care needs to be taken when defining the bottomside in such a way.

The photolysis causing the bottomside extension is a first order reaction. The observed rate of increase will hence depend on the photolysis rate and the abundance of the photolysed species [Viehl *et al.*, 2016a]. Both [FeOH] and subsequently [Fe] show a strong altitude dependence, with higher densities generally at higher altitudes throughout the bottomside extension.

The same absolute amount of [Fe] will therefore generally be reached more quickly at higher altitudes, even if solar irradiance simultaneously sets in at all altitudes. The altitude variation of the bottomside will therefore vary with the definition of different absolute values (compare, e.g., the different contours in the upper panel of Figure 15).

This effect can be significant on time scales comparable to the reaction rates. An alternative approach is to define the bottomside as a set fraction of the maximum density reached at each altitude, e.g., $\frac{1}{10}$ [Fe]_{max}(*z*) or similar. However, a suitable definition will depend on the application, and a set contour may well be used for time scales a lot larger than the rates of the chemical reactions.

9 Uplift of the Fe layer

The Fe layer at Davis (69°S) shows an uplift during the summer months. This uplift appears to be dynamically induced and not caused by the uptake on ice particles at lower altitudes. Very low densities are observed around summer solstice and coincide with very low mesopause temperatures.

Measurements with the mobile IAP Fe lidar at Davis (69°S) show that the Fe layer in the MLT is at significantly higher altitudes around summer solstice than during the rest of the year [Viehl *et al.*, 2015]. The centroid altitude of the layer (grey line in the upper panel of Figure 19) increases from around 85 km in September to over 90 km in December and then decreases towards 85 km in late March again. Moreover, not only the centroid altitude but the whole layer including the upper and lower edge (centroid altitude $\pm 0.5 \times$ RMS width) follows this behaviour. The shift is distinctively observable at the 2 000 cm⁻³ and 4 000 cm⁻³ contours between October and February in Figure 19.

These observations question previous explanations of high Fe layer centroid altitudes at polar latitudes

and differences between the two Antarctic stations Rothera (68°S) and the South Pole, which were attributed to the uptake of Fe atoms on ice particles at lower altitudes [Gardner *et al.*, 2011]. The measurements at Davis, the South Pole, and Rothera can only be compared to a certain extent, as a harmonic fit has been applied to the latter datasets (see Feng *et al.* [2013, Fig. 9] for a direct comparison). However, general features in the observations by Gardner *et al.* [2005, 2011] are comparable to the observations by the IAP Fe lidar at Davis.

The Fe layer's centroid altitude at the South Pole and Rothera was observed to rise while the layer width decreased, similarly to the upper panel in Figure 19. NLC were observed at some distance below the main layer on several days. As several studies had reported an uptake of metal atoms on ice particles, Gardner *et al.* [2011] concluded the metal atoms in the lower part of the Fe layer at Antarctic latitudes had been removed by ice particles and the centroid altitude hence had been shifted upwards. Gaps between the observed large ice particles and the layer were explained by the presumed presence of small, sub-visible ice particles.

However, the altitude increase of the upper boundary of the layer observed at Davis, as well as the early onset of the uplift at low altitudes (in areas with temperatures too high for ice formation), suggest that the summertime upwelling at polar latitudes and the related meridional transport, as well as the temperature dependent metal chemistry, cause the overall uplift [Viehl *et al.*, 2015, 2016b; Plane *et al.*, 2015].

A similar point was made by Marsh *et al.* [2013b] in a modelling study of the global Na layer when comparing their results to lidar observations at the South Pole. Calculations with the global 3D atmospheric chemistry model WACCM-Na showed the uplift of the Na layer at polar latitudes during summer. The authors note that contrary to 1D model explanations of Na lidar observations [Gardner *et al.*, 2005], the PMC uptake was not included in their model and hence not necessary to explain this behaviour. However, Marsh *et al.* [2013b] argue that the average altitude of the Na layer is higher than the Fe layer. The scavenging uptake effect might therefore not be relevant for the Na layer, but possibly for the lower Fe layer. Feng *et al.* [2013] hence include the uptake effect in WACCM-Fe with an ice particle parameterisation as described by Merkel *et al.* [2009].

The summertime increase of the centroid altitude and the simultaneous decrease of RMS width seems to be a global phenomenon at polar latitudes in both hemispheres [Feng et al., 2013, Fig. 15]. However, Viehl et al. [2016b] show new WACCM-Fe calculations for the months December and January with and without the inclusion of the uptake on ice particles and find no overall effect during the time of the uplift. The observed uplift and the model results provide strong evidence that the influence of ice particles is less relevant to the metal layers than assumed from singular 1D observations [e.g., Plane et al., 2004; Gardner et al., 2005]. It is important to consider the lower contribution of an ice uptake when evaluating the dynamics of 3D atmospheric chemistry models.

Although the uplift of the neutral atomic Fe layer might be qualitatively explained by the dynamical uplift of the residual circulation in the summer polar regions [Viehl et al., 2016b], the net vertical displacement or an average vertical wind cannot be easily deduced from Fe density observations. Fe atoms in the MLT region are not passive tracers but subject to changing temperature dependent chemical equilibria with reservoir species and ionisation processes at different altitudes [Plane et al., 2015]. In fact, the conversion from Fe to Fe⁺ through charge transfer with NO⁺ and O₂⁺ on the topside of the layer should be increased in the sunlit polar summer MLT and suppress an uplift [Viehl et al., 2015]. Moreover, the altitude region between ~90 km to 97 km, in which the increased altitude of the upper side of the layer is observed, has generally much lower temperatures during summer than during winter. As shown by Plane et al. [2015], a temperature decrease should move the chemical equilibrium from Fe towards the reservoir species.

These ion-molecule and neutral gas phase chemistry considerations make the observations of the elevated mid-summer Fe layer all the more striking. A quantification of the mean vertical uplift of the neutral atmosphere from Fe layer observations requires detailed 3D atmospheric chemistry modelling to separate transport and temperature-dependent gas phase and ion-molecule chemistry.

Indeed, the largest discrepancies between current WACCM-Fe simulations and lidar observations persist in the upper part of the polar MLT region, where the model predicts an “hourglass shape” of the Fe layer [Feng et al., 2013, Fig. 9]. However, this

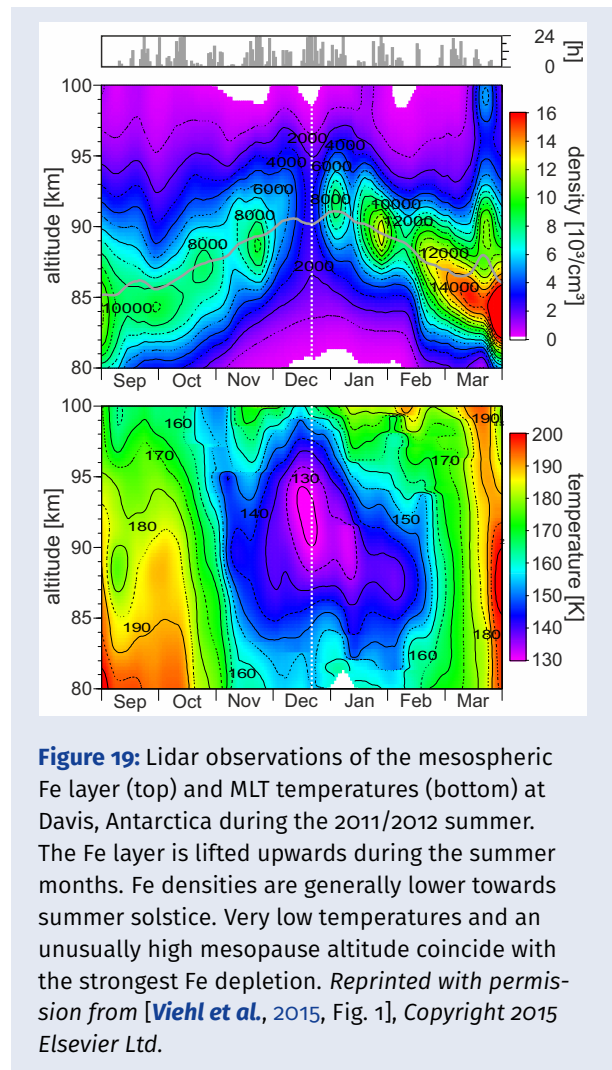


Figure 19: Lidar observations of the mesospheric Fe layer (top) and MLT temperatures (bottom) at Davis, Antarctica during the 2011/2012 summer. The Fe layer is lifted upwards during the summer months. Fe densities are generally lower towards summer solstice. Very low temperatures and an unusually high mesopause altitude coincide with the strongest Fe depletion. Reprinted with permission from [Viehl et al., 2015, Fig. 1], Copyright 2015 Elsevier Ltd.

depression of the upper edge in the modelling results has not been observed. This may be caused by the known misrepresentation of summer polar MLT temperatures in WACCM changing the chemical reaction rates [Smith, 2012], a potentially incomplete understanding of dynamical processes [Becker, 2012], or uncertainty about the amount of important reactive trace species such as NO⁺ and atomic O [Pedatella et al., 2014]. In fact, due to the increasing knowledge about the metal layer chemistry [Plane et al., 2015], resonance metal lidar observations in the MLT can provide invaluable means to investigate the results of these influences in 3D atmospheric chemistry models. The measurements hence improve the overall understanding of the physics and chemistry of the MLT region.

A further result by Viehl et al. [2015] shown in Figure 19 is the overlap of extremely low Fe densities of less than 1 000 cm⁻³ and very low summer mesopause temperatures at unusually high altitudes around the summer solstice. This behaviour

had not been observed before and is unknown in the Northern Hemisphere [Lübken *et al.*, 2014]. The coupling of low densities and low temperatures as well as the dynamics of this “elevated summer mesopause” will be analysed in more detail in Sections 11 and 17. The following Section 10 further investigates observations of the occurrence of ice particles and Fe densities.

10 Seasonal influence of ice particles on the Fe layer

Fe column densities at Davis (69°S) show a pronounced seasonal cycle with a minimum around the summer solstice. Simultaneous lidar and radar measurements of ice particles show surprisingly anti-correlated features, in particular in December and January.

Lidar observations by Viehl *et al.* [2015] show that the uptake of ice particles does not seem to cause the uplift of the Fe layer (Section 9). However, an overall depleting effect through ice particles might nevertheless be possible. Indeed, several observational studies had reported simultaneous observations of the depletion of metal atoms (Fe, Na, and K) and the occurrence of ice particles measured with radars as polar mesosphere summer echoes (PMSE) or lidars as noctilucent clouds (NLC). However, the duration of the reported Fe depletion by Plane *et al.* [2004] was comparatively short and the vertical extent limited. Model calculations suggesting a depleting effect of PMCs on the Fe layer at the South Pole were only one-dimensional and had to make a series of assumptions Gardner *et al.* [2005]. Reports by She *et al.* [2006] and Thayer and Pan [2006] for Na were not made on seasonal scales. The observations of a seasonal depletion reported by Lübken and Höffner [2004] were limited to K. The data set obtained by the mobile Fe lidar at Davis [Viehl *et al.*, 2015] allows a seasonal analysis of the Fe layer and includes an unprecedented amount of measurements during the technically challenging sunlit summer period. Furthermore, the collocated measurements by the Davis MST radar allow the detection of PMSE. The observation of PMSE is a strong indication of the presence of ice particles, including small, sub-visible particles not detectable by optical instruments [Rapp and Lübken, 2004].

Figure 20 shows the occurrence of ice particles observed as PMSE (blue) and as NLC (red) as well as Fe column density (black) in the years 2011–2012. A general decrease of Fe column densities is observed from August onwards. During the onset period of ice particle occurrence in mid-November, the decrease pauses, even though a decline due to the uptake on ice particles would have been expected and was observed for K at Spitsbergen (78°N) [Lübken and Höffner, 2004]. Moreover, during the period of lowest Fe densities, nearly no NLC were observed at Davis which means the advected ice particles had not lasted long enough to grow to radii >20 nm. The most striking feature of Figure 20 however is the substantial increase in Fe column densities in late December and early January, when NLC were observed to occur 42.5% of the time during 94 h of lidar observation. In contrast, Fe densities were lowest before solstice when no NLC were observed during 130 h of observations during 9 days. Additionally, nearly no PMSE occurred during a local Fe minimum in February.

In summary, Fe column densities are generally lowest during the summer months, when temperatures are lowest, and ice particles can nucleate. However, several striking and unexpected anti-correlated features emerge when the behaviour of the Fe layer column densities before, during, and after the ice particle season are compared in more detail. The timing of onset and disappearance of ice particles does not coincide with drops and increases in Fe column density.

Raizada *et al.* [2007] have shown that a depletion at any altitude of the metal layer should affect the overall layer and therefore the column density. If ice particles were an important factor determining the behaviour of the Fe layer as suggested in a comparison of two Antarctic stations [Gardner *et al.*, 2011], the occurrence of ice particles would therefore necessarily need to lead to lower Fe column densities. A drop in Fe column densities at the beginning of the ice particle season, as well as a rapid recovery of the Fe layer towards then end, would be expected. However, such features are not observed. Furthermore, the increase of column densities during mid-summer contradicts the predictions of this hypothesis. Neither the meteoric Fe input [Feng *et al.*, 2013] nor the temperature dependence of the Fe chemistry during at low mid-summer temperatures [Plane *et al.*, 2015] can explain a sufficient increase to compensate a potential depleting effect

of ice particles. This anti-correlated behaviour of ice particle occurrence and Fe depletion reported by [Viehl et al. \[2015\]](#) is the first observational evidence that heterogeneous removal on ice particles is no dominant cause of the seasonal variation of Fe densities at Antarctic latitudes.

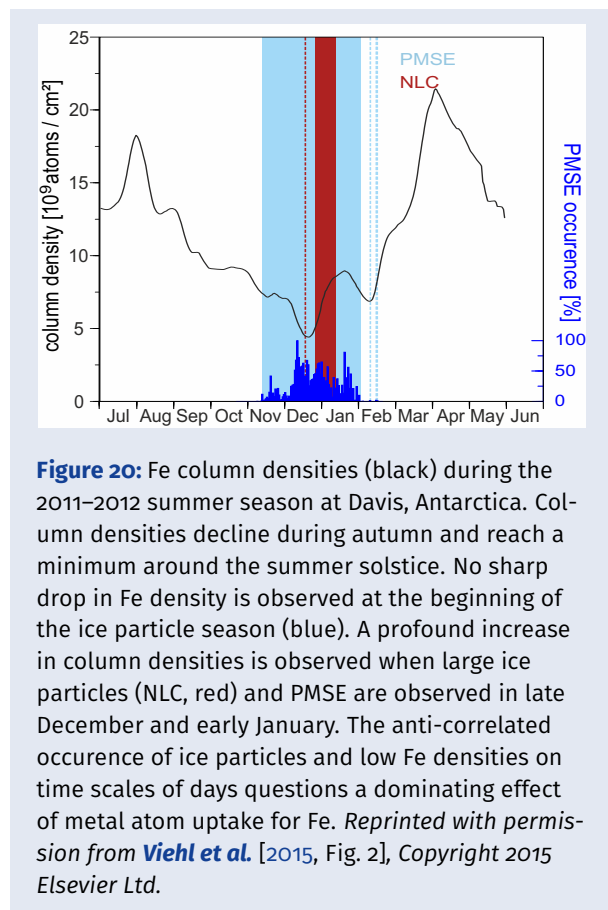


Figure 20: Fe column densities (black) during the 2011–2012 summer season at Davis, Antarctica. Column densities decline during autumn and reach a minimum around the summer solstice. No sharp drop in Fe density is observed at the beginning of the ice particle season (blue). A profound increase in column densities is observed when large ice particles (NLC, red) and PMSE are observed in late December and early January. The anti-correlated occurrence of ice particles and low Fe densities on time scales of days questions a dominating effect of metal atom uptake for Fe. Reprinted with permission from [Viehl et al. \[2015, Fig. 2\]](#), Copyright 2015 Elsevier Ltd.

A possible explanation for the different behaviour of K and Fe on a seasonal scale might be the dimensionless uptake coefficients of the metal atoms on ice. [Murray and Plane \[2005\]](#) have shown that while they are larger than 0.05 and likely to be unity for K and Na, the uptake coefficient rapidly decreases towards 3×10^{-3} for Fe at temperatures below 135 K. These temperatures are common in the Antarctic MLT region around summer solstice and necessary for ice nucleation at this altitude [e.g., [Viehl et al., 2015](#); [Lübken et al., 2015](#)]. Future studies will have a closer look at the intraday variability of the Fe layer and the interaction with ice particles observed as PMSE and NLC, see Section 22. It may thereby be possible to quantify the heterogeneous removal for Fe and explain how an uptake effect might influence the layer locally [[Plane et al., 2004](#)] while not being able to proceed to alter the layer on seasonal scales.

11 Temperature dependence of mean Fe density around summer solstice

The temperature dependence of the Fe layer is analysed during a period of substantial Fe depletion around the summer solstice. The high correlation between Fe densities and temperatures during mid-summer seems to be caused by the upwelling and divergence of adiabatically cooled Fe-poor air masses in polar regions.

The chemistry of the metal layers in the MLT region is temperature dependent (see Section 2). Low temperatures shift the equilibrium from Fe towards its oxides and hydroxides, so lower Fe densities are generally expected at lower temperatures [[Plane et al., 2015](#)]. Figure 19 on page 27 showed a very strong depletion of Fe around summer solstice which coincided with very low temperatures. Ice particles had previously been held responsible for strong summer time depletions in the MLT region, but [Viehl et al. \[2015\]](#) show strong evidence against this assumption, see preceding Sections 9 and 10. A general change from high to low densities from winter to summer can be explained by meridional transport [Marsh et al. \[2013b\]](#). However, transport calculations have so far not predicted the substantial depletion observed in Fe in the few weeks around summer solstice. To further investigate the strong depletion, [Viehl et al. \[2015\]](#) analyse the temperature dependence of the daily mean Fe densities during a ± 40 day period around summer solstice in the 2011/12 season.

An Arrhenius-type plot of $\ln([\text{Fe}])$ over T^{-1} in Figure 21 shows a nearly linear relation, suggesting the importance of chemical reactions in this process. [Viehl et al. \[2015, Sec. 3.3\]](#) then assume a temperature dependent partitioning between Fe and the assumed main reservoir FeOH and deduce an equation which can be fitted to the observations. The resulting fit satisfactorily reproduces the observations for approximate values of main atmospheric constituents. [Viehl et al. \[2015\]](#) then conclude that temperature-dependent chemistry can explain the strong depletion around the summer solstice.

However, in a corrigendum to the publication [Viehl et al. \[2016b\]](#) show that this conclusion was invalid for two reasons. First, the bottomside analysis by [Viehl et al. \[2016a\]](#) revealed that the reservoir FeOH

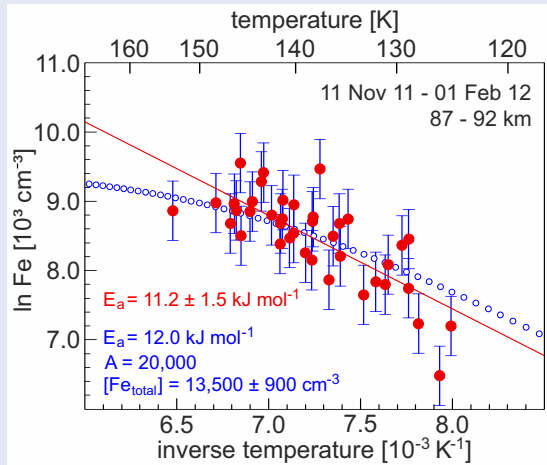


Figure 21: Fe lidar observations of the temperature dependence of daily mean Fe densities (red dots) in a period of ± 40 days around the summer solstice. The approximate linearity in an Arrhenius type plot suggests the importance of chemical reactions (red line). An attempt to fit the data assuming a temperature dependent chemical equilibrium between Fe and FeOH seems successful (blue curve), but was only possible due to a mathematical error. Reprinted with permission from [Viehl et al. \[2015, Fig. 3\]](#), Copyright 2015 Elsevier Ltd.

is nearly fully depleted in the polar summer MLT region. A temperature-dependent partitioning between Fe and FeOH as assumed by [Viehl et al. \[2015\]](#) therefore seems to be a questionable simplification as the equilibrium will shift to all other reservoir species (FeO_2 , FeO_3 and others) as well as atomic Fe. The assumptions and simplifications made are hence no longer good estimates. Second, the fit obtained through the analysis in [Viehl et al. \[2015, Sec. 3.3\]](#) (blue curve in Figure 21) only matched the observations (red dots) due to an unfortunate mathematical error. [Viehl et al. \[2016b\]](#) correct this mistake and conclude that gas phase chemistry could no longer explain the depletion observed.

[Viehl et al. \[2016b\]](#) then give an alternative explanation of the observations, supported by calculations with WACCM-Fe shown in Figure 22. The temperature dependence simulated with WACCM-Fe [[Feng et al., 2013](#)] is very similar to the observations, albeit at consistently lower absolute densities (black dots). In a comparative run, [Viehl et al. \[2016b\]](#) show results obtained under the same modelling conditions but without the inclusion of the respective PMC uptake modules (red dots). Both runs show the same temperature dependence of [Fe] around the summer solstice. Most strikingly, the

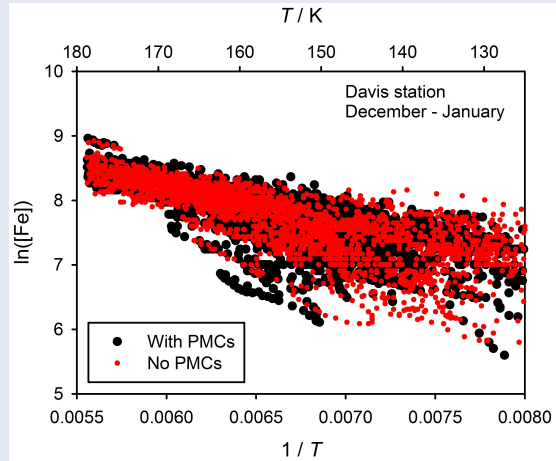


Figure 22: Temperature dependence of atomic Fe calculated by 3D atmospheric chemistry model WACCM-Fe with (black) and without (red) the inclusion of Fe uptake on ice particles. Fe densities are not significantly influenced by the uptake effect. Reprinted with permission from [Viehl et al. \[2016b, Fig. 1\]](#), Copyright 2016 Elsevier Ltd.

linearity does not change at around 135 ± 5 K, which is the approximate frost point temperature at the respective altitude (see [Lübken et al. \[2014\]](#) and cyan lines in the left panel of Figure 36 on page 46). However, a change of the temperature dependence would have been expected if ice particles had a substantial effect on the mean densities, as they would only exist and deplete Fe for temperatures lower than the frost point.

In an additional analysis, [Viehl et al. \[2016b\]](#) compare the temperature dependence of the total amount of all Fe species $[\text{Fe}]_{\text{total}}$, i.e. the combined abundance of Fe and all of its oxides, hydroxides and ionised species. The temperature dependence is nearly identical to Figure 22. Moreover, the fraction of Fe that is present in the atomic form remains constant at around 60% of $[\text{Fe}]_{\text{total}}$ over the whole temperature range. This means that the temperature change does on average not cause a shift from one Fe-containing species to another. The change during the two investigated months December and January is hence a simultaneous change of temperature and $[\text{Fe}]_{\text{total}}$.

As is well known [e.g., [Becker, 2012](#)], the upwelling at polar latitudes during summer is inherently linked to a strong adiabatic cooling effect. Hence, the only possible explanation for the simultaneous observation of low temperatures and low Fe densities is that both are results of the residual circulation [[Viehl et al., 2016b](#)]: when Fe-poor air rises to

the mesopause region, it cools adiabatically and is then transported equatorwards. On the other hand, neither the meteoric input nor the chemical sinks change significantly over the investigated period and can hence not explain this behaviour.

An additional, presumably small uptake effect of Fe atoms and reservoir species on ice particles is not ruled out by this conclusion. However, the occurrence of ice particles at this altitude most likely seems to be a coincidence facilitated through the low temperatures and not a dominant driving factor of the seasonal change [Viehl et al., 2015, 2016b].

12 First measurements of thermal tides in the Antarctic summer mesopause region

Fe lidar measurements at Davis (69°S) reveal the first observations of thermal tides in the polar summer MLT region. Surprisingly, tidal modulations are a lot larger than expected from model calculations. Tides in Fe density have similarities with tides in temperatures and can be observed over a larger altitude range into the lower thermosphere.

Atmospheric tides are present throughout the atmosphere and can play an important role for the thermal and dynamical state of the MLT region. As Lübken et al. [2011] point out, they can significantly modify gravity wave propagation and change composition due to transport. Atmospheric tides interact with gravity waves and larger scale motions, hence influencing wave breaking and the deposition of momentum [e.g., McLandress, 2002; Mayr et al., 2005a, b]. In general, tides may affect the analysis of middle atmospheric trends [Beig et al., 2003]. A precise knowledge of tides is needed to estimate a potential bias of trends in PMC satellite observations which cover only certain local times and change from year to year [DeLand et al., 2007].

Predictions about solar thermal tides in the polar MLT region were rather small with amplitudes around 1–2 K [e.g., Zhang et al., 2010; Achatz et al., 2008]. Measurements were so far mostly limited to radar wind observations [e.g., Oberheide et al., 2006; Hoffmann et al., 2010]. Satellite-borne temperature measurements can provide analyses of thermal tides, even though the slow orbit preces-

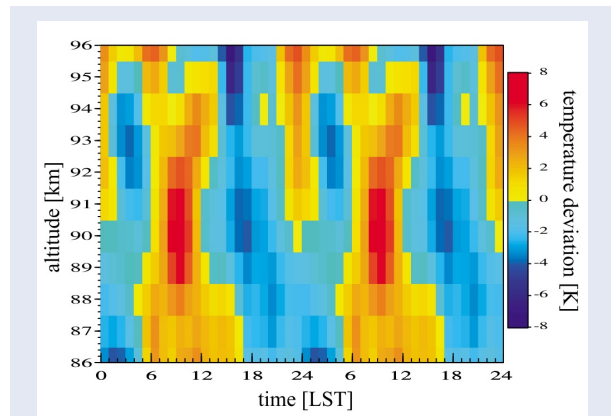


Figure 23: Average MLT temperature deviations from the seasonal mean plotted for a period of two days for better identification of the periodic features. A total of 171 hours of observations obtained during 12 days in January 2011 contribute to this plot. Observed temperature deviations are much stronger than predictions for polar latitudes. Reprinted with permission from Lübken et al. [2011, Fig. 2], Copyright 2011 John Wiley & Sons, Inc.

sion (which requires an integration of several weeks for a full coverage of all local times) may hamper the observations. Nevertheless, satellite analyses have shown strong thermal tides at equatorial and mid-latitudes. During the dark hours of 3 winter months, these observations were shown to be compatible with K lidar soundings [Shepherd and Fricke-Begemann, 2004]. Amplitudes are strong around the equator, but weaker (<3 K) towards the polar circle. No measurements were available in the polar MLT [Forbes and Wu, 2006].

Lübken et al. [2011] report 171 hrs of temperature and Fe density measurements obtained during 12 days of measurement with the mobile Fe lidar at Davis, Antarctica (69°S) between 12–28 January 2011. Figure 23 shows the average temperature deviations in the polar summer MLT region, plotted for a period of 48 days for better visibility of the diurnal and semi-diurnal features. A diurnal variation is observed to dominate below 90 km altitude. Above 90 km, a strong semi-diurnal component becomes apparent. As the data set is large enough and the phase progression in Figure 24 shows consistency with altitude, gravity waves can be ruled out to produce this thermal behaviour due to their random orientation and overall destructive interference. Hence, the features observed by Lübken et al. [2011] indeed have to be attributed to thermal tides and present the first direct observation in the summer polar mesopause region.

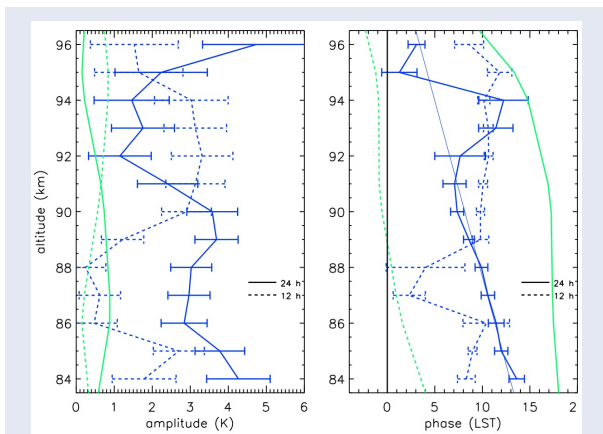


Figure 24: (left) Amplitudes and (right) phases of the diurnal (solid) and semi-diurnal (dotted) tidal components. Fe lidar observations are shown in blue, model predictions are shown in green. Between 84 and 92 km altitude, the phase of the observed diurnal tide can be represented by a vertical wavelength of ~ 30 km. Reprinted with permission from [Lübken et al. \[2011, Fig. 3\]](#), Copyright 2011 John Wiley & Sons, Inc.

The analysis of the amplitude and phase structure of the diurnal and semi-diurnal tide in Figure 24 shows a similar phase of both components at most altitudes, leading to constructive interference. The amplitudes of the tidal modulation sum up to more than ± 6 K, which is considerably larger than what models such as the Global Scale Wave Model (GSWM) had so far predicted [[Zhang et al., 2010](#)]. The observed diurnal tide is out of phase with GSWM, whereas the semi-diurnal tide matches the predicted phase at higher altitudes. The observations by [Lübken et al. \[2011\]](#) show that the global modelling of atmospheric tides is incomplete. Either not all tidal sources are yet well known, or the mathematical theory employed in global models is insufficient. The non-linear interactions of non-migrating tides and planetary waves, as well as gravity waves studied by [Mayr et al. \[2005a, b\]](#) and others, might play a role in explaining the differences between models and the new observations. As a further result of [Lübken et al. \[2011\]](#), Figure 25 shows tidal features in Fe densities. Contrary to temperature measurements, Fe density observations don't require spectral decomposition. Considerably fewer laser pulses per data point are needed to achieve a comparable SNR. Therefore, Fe densities, as well as the tidal signals therein, can be observed in a far larger altitude range (between approximately 75 km and 140 km altitude) than any temperature observation.

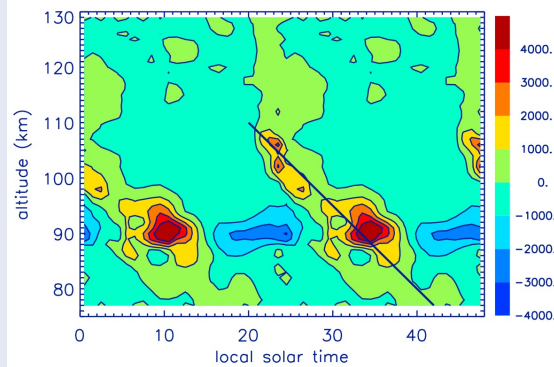


Figure 25: Fe density deviations from the seasonal mean shown for a period of two days. Between 75 km and 110 km altitude, the straight line indicates a phase progression corresponding to a vertical wavelength of ~ 36 km. A diurnal tidal structure dominates this altitude range. Towards higher altitudes, the phase remains constant and shows a stronger semidiurnal component. The Fe layer can be observed over a larger altitude range and with higher accuracy than MLT temperatures. Reprinted with permission from [Lübken et al. \[2011, Fig. 1\]](#), Copyright 2011 John Wiley & Sons, Inc.

The observed tidal modulation of up to $\pm 40\%$ at the peak of the layer is very large and shows a similar tidal structure to the temperature observations. The vertical wavelength of around ~ 36 km observed in Fe density variations below 110 km is similar to the phase progression of approximately ~ 30 km observed in temperatures, see right panel of Figure 24. As temperatures and densities are derived independently from the lidar signal, this is further evidence for the conclusion that tides cause the observed modulations. [Lübken et al. \[2011\]](#) suggest that the temperature variation could have a crucial role for the tidal features observed in Fe densities, as the Fe chemistry is highly temperature dependent. However, the authors further note that other factors such as meteoric input, photochemical effects and transport play crucial roles as well.

Since the publication of [Lübken et al. \[2011\]](#), lidar measurements have covered all months of the year. A full analysis of the data set is currently being performed. Preliminary results in Section 20 show a very constant phase progression in Fe density variations throughout the year. This finding is surprising, as a study about tides in winds at Antarctic latitudes showed strong seasonal variations [[Murphy et al., 2006](#)]. The following section attempts to find an approach to examine various influences on metal layer densities quantitatively.

13 Tides in metal layers: comparison of lidar observations and a 3D atmospheric chemistry model

Lidar observations of K at 54°N are compared to model simulations. WACCM-K captures the general diurnal and semidiurnal variations of the metal layer satisfactorily. Photochemistry can explain most of the variability. Diurnal temperature variations and tidally driven vertical transport appear to play a minor role for K in the MLT region. A similar analysis for Fe at polar latitudes is possible and likely to show a larger temperature impact.

The lidar observations of strong temperature tides described in Section 12 were accompanied by tides in Fe density. While investigating the Na layer, *Clemensha et al. [1982]* found significant semi-diurnal variations at São José dos Campos, Brazil (23°S) as well as a strong diurnal component below 82 km which was attributed to photochemical effects. Later studies by *Zhou et al. [2008]* and *Yu et al. [2012]* report significant diurnal variations of the Fe layer at Arecibo, Puerto Rico (19°N) and McMurdo, Antarctica (78°S), respectively. Those variations are comparable to the tides reported by *Lübken et al. [2011]*. All studies indicate a combination of tidal and photochemical influences. However, direct comparisons of the observed and modelled response of the metal layers to atmospheric tides and the photochemistry in the MLT region had not been undertaken.

In contrast to the other results presented in this thesis focussing on Fe observations at polar latitudes, the analysis of model results by *Feng et al. [2015]* presented in this section were obtained by comparing with K (potassium) densities observed at mid-latitudes in Kühlungsborn, Germany (54°N). There were several motivations for this preference. Compared to the analyses of Na and Fe, no diurnal analysis of K had so far been published. As the seasonal variation of K is considerably different to that of Na and Fe [*Plane et al., 2014*], a fundamental question hence was to investigate the diurnal variation closer and compare it to other metals. Moreover, as *Lübken et al. [2011]* have emphasised, the tidal features observed in Antarctica were considerably larger than predicted by GSWM (see Section 12). It therefore seems plausible to first

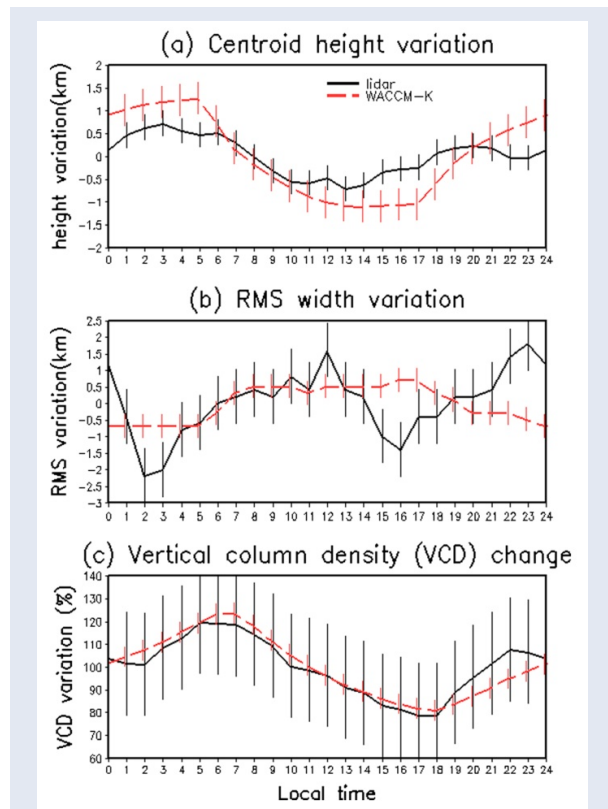


Figure 26: Diurnal variation of (a) centroid altitude, (b) RMS width [km], and (c) vertical column density of the K layer over 24 h. The error bars show the standard deviation of the mean K density. The model (red) reproduces most aspects of the lidar observations (black) reasonably well. Reprinted from *Feng et al. [2015, Fig. 2]*, CC BY 4.0, 2015 John Wiley & Sons, Inc.

compare model results and observations at mid-latitudes (where tidal effects should be stronger) and prove the overall agreement, and then compare at more critical polar latitudes later.

Analogously to WACCM-Fe, WACCM-K has recently been developed to describe the neutral and ion-molecule chemistry of K in the MLT [*Plane et al., 2014*]. Overall, WACCM-K simulates the observed K layer quite well and also captures the large differences between dawn and dusk [*Feng et al., 2015*]. The production and loss of K at the bottomside is comparable to Fe and follows a similar behaviour as analysed by *Viehl et al. [2016a]*, with potassium hydrogen carbonate (KHCO₃) taking the role of FeOH [*Plane et al., 2014*]. Figure 26 compares key parameters of the modelled and observed K layer. *Feng et al. [2015]* discuss which aspects the model over- or underestimates in comparison to the observations. They conclude that the model satisfactorily captures the lidar observations albeit some

differences persist, which may be attributed to the limited measurement statistic of the observations.

Figure 27 shows altitude profiles of the amplitude and phase (diurnal and semidiurnal) of the measured and modelled K density. Although the maximum diurnal and semidiurnal K amplitudes from the model are at similar altitudes to the ones observed, the model largely overestimates the observed diurnal K amplitude maximum. The model captures the observed phase of the diurnal variation well and correctly predicts a phase of the semidiurnal component later than the diurnal component. [Feng et al. \[2015\]](#) then investigate the possible effect of atmospheric thermal tides on the diurnal cycle. The variation of the total density of K-bearing species (which is essentially the sum of K, K^+ and $KHCO_3$) varies as a function of altitude and local time and is almost constant at each altitude. These considerations suggest that vertical transport plays a minor role. [Plane et al. \[2014\]](#) show how K and K^+ follow a diurnal cycle above ~ 87 km, converting into each other through photolysis as well as cluster formation and dissociative recombination. Photochemistry also explains the buildup of neutral K atoms below 87 km from photolysis of $KHCO_3$, similarly to the process described by [Viehl et al. \[2016a\]](#).

The diurnal variation in temperature predicted by WACCM is around 4 K at each altitude between 80 and 100 km, which is comparable to results obtained by RMR and resonance lidar measurements by [Kopp et al. \[2015\]](#). Since the temperature dependencies of the relevant reactions in the K chemistry scheme are comparatively small [[Plane et al., 2014](#)], the diurnal variations in temperature do not play a significant role in the diurnal variation of the K layer [[Feng et al., 2015](#)]. The analysis further shows that the modelled vertical wind at $54^\circ N$ is small and corresponds to a tidally driven displacement of less than 1 km, explaining the near-constant total K density at each altitude. Using known reaction rates from [Plane et al. \[2014\]](#), [Feng et al. \[2015\]](#) show that the lifetime of K is short below 80 km (less than 10 min), although doubling effectively during the day because of the increased concentrations of atomic O and H and decreased O_3 . The lifetime increases to around 1 day at 100 km altitude and becomes even larger in the thermosphere. These lifetime analyses explain why the in-situ photochemistry plays a much larger role for the diurnal variation of K than other tidal effects. Finally,

[Feng et al. \[2015, Fig. 3 \(c\)–\(f\)\]](#) show a comparison of the tidal components in WACCM-K and GSWM. Both models are in good agreement at K hlungsborn (54°), although WACCM underestimates tidal amplitudes in temperature and vertical wind.

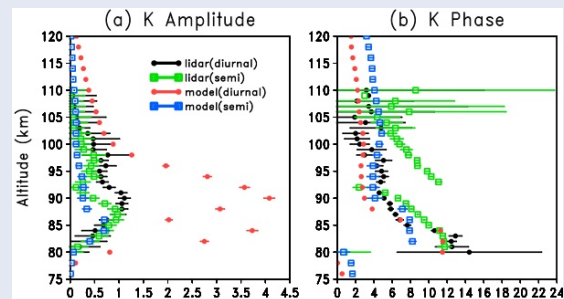


Figure 27: Amplitude and phase of diurnal and semidiurnal tidal phase for potassium lidar observations at K hlungsborn and WACCM-K model simulations. The model strongly over-estimates the diurnal amplitude. However, absolute column densities, the semidiurnal component, and the phase progression of the metal layer are captured satisfactorily. Reproduced from [Feng et al. \[2015, Fig. 3\]](#), CC BY 4.0, 2015 John Wiley & Sons, Inc.

Overall, the analyses by [Feng et al. \[2015\]](#) show that WACCM can be usefully employed to study the tidal behaviour of mesospheric metal layers. Future studies will examine the validity of this analysis at other latitudes and seasons. A detailed comparison of WACCM-Fe simulations and lidar data might hence provide a deeper insight into the causes of the diurnal variations of Fe observed by [L bken et al. \[2011\]](#) and [Yu et al. \[2012\]](#) at polar latitudes. A comparison of the temperature tide with the tidal signature in K lidar data was so far not possible due to instrument limitations, but will be in the upcoming analyses of Fe at polar latitudes. The temperature dependence of the Fe chemistry is larger than for K [[Plane et al., 2015](#)], hence a different result regarding the relative importances of photochemistry, temperature dependent reactions and tidal transport can be expected. Section 20 shows some preliminary results of the analysis of tides in the Fe layer observed with the mobile Fe lidar at Davis, Antarctica with surprisingly constant tidal features during all months of the year.

14 Gravity wave activity in the middle atmosphere

2310 h of lidar observations in the stratosphere and MLT region at Davis (69°S) are used to investigate gravity wave activity. The gravity wave potential energy density (GWPED) shows a considerable seasonal variation with a maximum in winter and a minimum in summer. During winter, the GWPED in the stratosphere and the MLT show a similar behaviour. This suggests that the wind field in the stratosphere controls the gravity wave flux to the MLT.

Gravity waves transport energy and momentum over large vertical and horizontal distances and are important for the global meridional circulation from the summer to the winter pole. Gravity wave studies have been performed through observations with radiosondes, radars, satellites, and various lidars [e.g., [Allen and Vincent, 1995](#); [Zhang, 2004](#); [Alexander and Barnett, 2007](#); [Yamashita et al., 2009](#); [Nicolls et al., 2010](#); [Alexander et al., 2011](#)]. The mobile IAP Fe lidar allows gravity wave analyses of high-resolution temperature data in the Antarctic MLT region and the stratosphere for a full annual cycle [[Kaifler et al., 2015](#)]. These results have already been discussed in full detail in the PhD thesis of [Kaifler \[2014\]](#). The following section presents only a short overview of some important points.

[Kaifler et al. \[2015\]](#) analyse 2310 h of temperature data obtained by the mobile IAP Fe lidar at Davis, Antarctica between January 2011 and April 2012. The study evaluates the Rayleigh scattering in the stratosphere to derive temperatures between 25 km and 55 km in addition to the MLT temperatures obtained from the resonance scattering of the Fe layer. The stratospheric temperature profiles are sampled with 2 km vertical resolution at typical uncertainties of around 2 K at 40 km and 7 K at 55 km altitude in daytime conditions after 1 h integration. The impact of gravity waves can be characterised through the gravity wave potential energy density (GWPED), which is a measure of the potential energy per unit mass derived from the wave-induced temperature perturbation [[Alexander et al., 2011](#)]. An example of this analysis is shown in [Figure 28](#). The left panel shows temperature perturbations from lidar observations with predominantly downward phase progression in the MLT and the stratosphere, which implies an upward transport of en-

ergy. The middle panel in [Figure 28](#) shows hourly perturbation amplitudes from around 0.5 K at 30 km altitude up to 15 K in the MLT. The GWPED calculated from these perturbations is shown in the right panel of [Figure 28](#) and increases with altitude. The general increase of the GWPED up to 40 km in the stratosphere and up to 90 km in the MLT region in this example is an indicator for freely propagating waves. The reduced growth rate towards higher altitudes may be associated with wave breaking.

In a further step, [Kaifler et al. \[2015\]](#) then analyse the seasonal variation of the GWPED. [Figure 29](#) shows the monthly mean GWPED in the stratosphere (blue) and the MLT (red). In the stratosphere, the GWPED shows an apparent maximum during the winter months and a minimum during the summer months, ranging from 0.8 J kg^{-1} to 5.4 J kg^{-1} between 30 km and 40 km. These findings confirm previous results by [Alexander et al. \[2011\]](#), who analysed data from the AAD RMR lidar and gave evidence for conservative wave propagation between 35 km and 39 km altitude. The similar results indicate low seasonal variability. In the MLT region, the GWPED is a lot larger than in the stratosphere (ranging from around 40 J kg^{-1} to above 100 J kg^{-1}) due to the exponential growth of the wave amplitudes and the stronger temperature perturbations. However, the GWPED remains below the growth rate of conservatively propagating waves, indicating energy loss rates on the order of $8\% \text{ km}^{-1}$.

Large fluctuations in the MLT GWPED are observed during mid-summer, which may result from the temperature variability during summer. [Kaifler et al. \[2015\]](#) also note that the altitude range of the temperature derivation in the MLT changes throughout the year as the Fe layer is lifted upwards during the summer months [[Viehl et al., 2015](#)]. [Kaifler et al. \[2015\]](#) further point to the apparent correlation between the GWPED in the stratosphere and MLT region, with the same double peak structure observable during winter ([Figure 29](#)). This correlation is an indication of the coupling between the atmospheric layers, caused by the selective filtering of waves by winds in the middle atmosphere. This coupling should be important at Davis (69°S), as the Antarctic polar vortex is usually strong and persistent during the winter months.

[Figure 30](#) shows the GWPED in the stratosphere, calculated to 14 day means from spring (October 2011) to autumn (March 2012). Further shown are daily

Figure 28: Calculation of the GWPED from temperature perturbations on 15/16 August 2011. (left) Temperature perturbations in the MLT region and the stratosphere. (middle) Hourly perturbation profiles. (right) Mean GWPED (solid) and conservative growth rate (dashed). Reprinted with permission from [Kaifler et al. \[2015, Fig. 1\]](#), Copyright 2015 John Wiley & Sons, Inc.

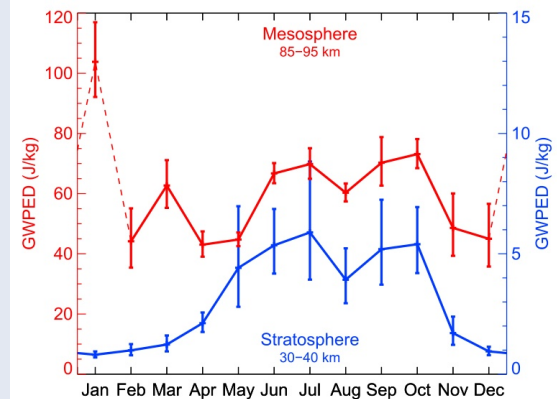
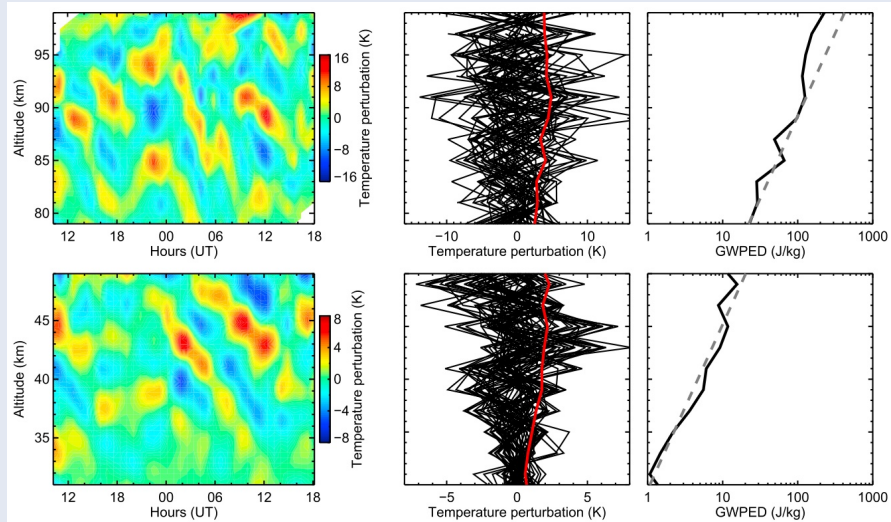


Figure 29: Seasonal variation of GWPED at 69°S. The stratosphere (blue) shows a pronounced double-peak maximum during winter and a minimum around the summer solstice. The MLT region (red) shows a very similar GWPED structure during winter, but a high variability during summer. Vertical bars denote the standard deviation from the mean. Reprinted with permission from [Kaifler et al. \[2015, Fig. 6\]](#), Copyright 2015 John Wiley & Sons, Inc.

mean zonal winds $|u| < 2 \text{ m s}^{-1}$ taken from ECMWF data. The wind reversal associated with the polar vortex breakdown can be seen as the downward progression of the blue shaded area from around 60 km altitude in October to around 20 km altitude in December and January. As a significant result, the GWPED in Figure 30 can be seen to decrease with altitude below the blue shaded area during November and December, which indicates strong wave filtering. From January onwards, the GWPED returns to approximately conservative wave progression conditions.

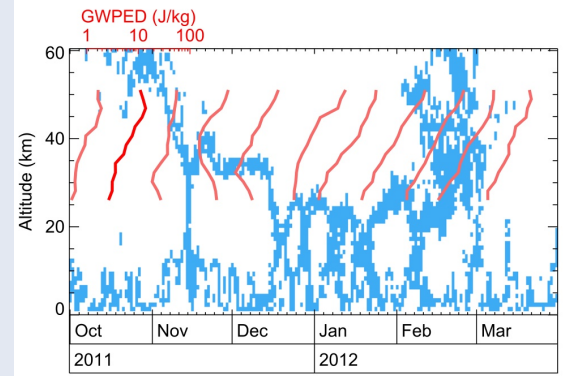


Figure 30: Interaction of gravity waves (GWPED, red) with the stratospheric background wind ($|u| < 2 \text{ m s}^{-1}$, blue). The GWPED is reduced below the set wind level in November and December. Reprinted with permission from [Kaifler et al. \[2015, Fig. 8\]](#), Copyright 2015 John Wiley & Sons, Inc.

Using a simple model, [Kaifler et al. \[2015\]](#) reproduce the observations and conclude that the filtering of gravity waves in the lower stratosphere causes the major seasonal variation of the gravity wave activity at Davis. This is in line with conclusions by [Wilson et al. \[1991\]](#), who made similar observations at mid-latitudes. However, the situation during summer is more complicated than during winter. The reversal of the stratospheric winds after the breakdown of the polar vortex results in a selective filtering of gravity waves with small phase speeds. Waves with large phase speeds therefore have to dominate the MLT region, which results in the semi-annual oscillation reported at high and mid-latitudes in the NH [[Hoffmann et al., 2010](#)].

15 Ice particles and temperatures after the winter/summer transition in the Antarctic MLT

The winter to summer transition of the MLT region at Davis is analysed using observations of ice particles and temperatures. Mesospheric ice particles (observed as PMSE and NLC) were strongly reduced at Davis (69°S) in the austral summer season 2010/2011. PMSE were further observed at unusually high altitudes. Measurements around summer solstice reveal an unexpectedly high mesopause.

The transition from the winter to the summer state of the MLT region is primarily characterised through a pronounced temperature change. Temperatures in the polar MLT are generally lower during summer than during winter. Most prominently, the altitude of the mesopause shifts from around 100 km during winter to around 88 km during summer [Lübken and von Zahn, 1991; She et al., 1993]. These altitude levels are representative for the respective summer and winter hemispheres. The global “two level mesopause” was discovered with an earlier version of the mobile IAP Fe lidar [von Zahn et al., 1996b]. Observations with the mobile IAP Fe lidar at Davis have again challenged our understanding of the MLT temperature structure with the discovery of “mesopause jumps” leading to an elevated summer mesopause [Lübken et al., 2014, 2015]. Section 17 explains the phenomenon in detail and shows why it can only be observed in the Southern Hemisphere. The next two Sections follow the observations leading to the discovery more or less chronologically.

Mesospheric ice particles are an indicator of low summer temperatures in the MLT. Higher summer mesopause temperatures in the Southern Hemisphere (SH) compared to the Northern Hemisphere (NH) have been proposed to explain hemispheric differences in PMSE occurrence through limitations in ice particle formation. In general, mesospheric ice particles in the SH (as observed as PMSE, NLC, or PMC) have lower occurrence rates, occur towards higher altitudes on average, and are more variable than their counterparts in the NH [DeLand et al., 2003; Bailey et al., 2005, 2007; Latteck et al., 2007; Kirkwood et al., 2007, 2008; Klekociuk et al., 2008]. Studies with the Leibniz-Institute Middle Atmosphere Ice (LIMA/ice) model by Lübken and Berger [2007, 2011] reproduce these mean characteristics,

including the seasonal variation and altitude differences. However, these studies focus on multi-year trends and have so far not explained the details of the winter/summer transition process. The observed and modelled connection of the variation in ice particle occurrence to middle atmospheric dynamics as reported by Siskind et al. [2003]; Kirkwood et al. [2008]; Karlsson et al. [2011], and others had so far not been understood in detail.

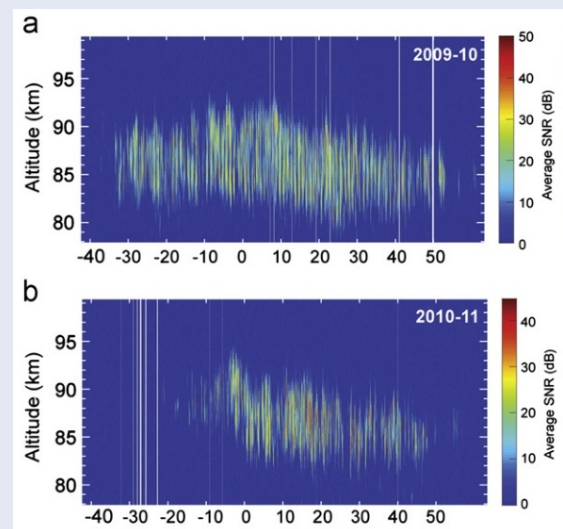


Figure 31: PMSE intensity versus altitude at Davis (69°S) for 2009/2010 (a) and 2010/2011 (b), days relative to solstice. PMSE occurrence was markedly reduced during the austral summer 2010/2011. Significant amounts of PMSE were observed less than 10 days before the summer solstice. The centroid altitude of early PMSE events was significantly higher than on average. Reproduced with permission from Morris et al. [2012, Fig. 1], Copyright 2012 Elsevier Ltd.

Morris et al. [2012] present SH observations of PMSE by the Davis MST radar, and NLC as well as temperatures by the mobile IAP Fe lidar. During the first summer of measurements with the mobile IAP Fe lidar in 2010/2011, the occurrence rate of PMSE was strongly reduced compared to previous years. The first PMSE of the season were observed more than 2 weeks later than in 2009/2010, were unusually faint, and were covering a very limited altitude range (Figure 31). Significant amounts of PMSE were observed a month later than in the preceding year. Overall, the occurrence rate in 2010/2011 was reduced by 59 % compared to 2009/2010. The PMSE centroid altitude throughout the early season was the highest since the MST radar became operational in 2004 (upper panel of Figure 32).

In addition to the PMSE observations, significantly fewer NLC were observed in 2010/2011 compared to previous years [Morris *et al.*, 2012]. The mobile IAP Fe lidar detected NLC only 1.1 % of the time during 322 h of measurement between 18 December 2010 and 8 February 2011. The AAD RMR lidar, on the other hand, had observed NLC at around 19 % of the time during 266 h of measurement at the same location one year earlier between 22 November 2009 and 28 February 2010.

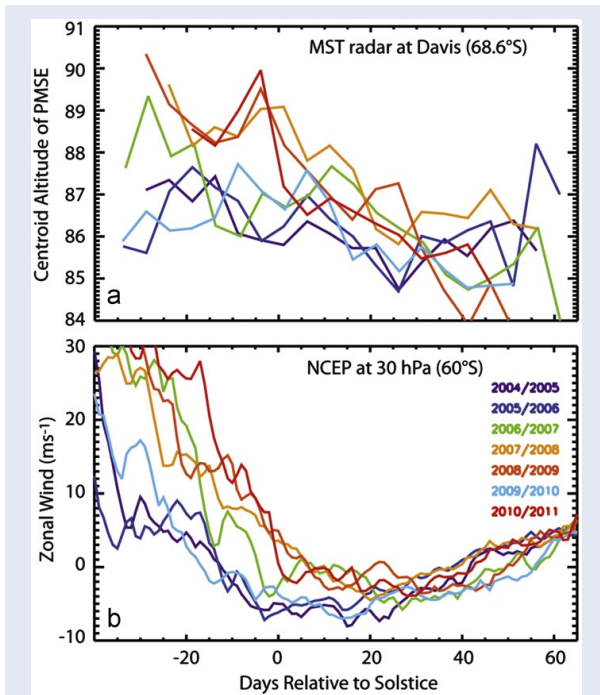


Figure 32: (top) Centroid altitude of PMSE observations during 7 austral summers at Davis, Antarctica (69°S). (bottom) NCEP data of zonal winds in the stratosphere at 30 hPa. The breakdown of the stratospheric polar vortex can be seen in the decrease of the zonal wind. Years with a late polar vortex breakdown are associated with high PMSE early in the season (red and orange). Reprinted with permission from Morris *et al.* [2012, Fig. 6], Copyright 2012 Elsevier Ltd.

This substantial reduction is consistent with strongly reduced PMC observations by the OSIRIS instrument onboard the Odin satellite in the same season [Gumbel and Karlsson, 2011]. Observations with the SOFIE instrument on board the AIM satellite later also revealed a significant (more than sevenfold) reduction in PMC occurrence from around 35 % to less than 5 % in the respective years [Hervig and Stevens, 2014]. These satellite observations are an independent confirmation of the lidar measurements. These reductions argue for either higher av-

erage temperatures at regular PMSE/NLC altitudes, which counteract a long residence time for the ice particles to grow to visibly observable sizes, or for a profound reduction in available water vapour.

First direct temperature observations with the mobile IAP Fe lidar at Davis, Antarctica (69°S) were obtained on 14 December 2010, but only for 1 h. Substantial temperature observations commenced from 18 December 2010 onwards. Morris *et al.* [2012] find that the mesopause was unexpectedly high at around 92 km altitude during these first temperature measurements, with average temperatures as low as 116 K (the results are reproduced in the top panel of Figure 34 on page 41). This mesopause altitude is about 4 km higher and the mesopause temperature ~12 K colder than the climatological mean in the NH [Lübken, 1999]. In 2007/2008, Kirkwood *et al.* [2008] had also found the SH mesopause to be elevated by 3 km compared to earlier seasons, which coincided with a high PMSE layer.

Mesospheric ice particles usually occur at altitudes around 83 km to 92 km. During common (NH) summer conditions, the mesopause is roughly located at around 88 km, in the centre of the ice particle altitude range. The mesopause altitude at Davis early in the summer season was observed to be elevated to altitudes around 92 km. As the mesopause is the point of lowest temperatures, altitudes below the mesopause are comparatively warmer. At common lapse rates of around -5 K km^{-1} , temperatures at altitudes 4 km below the mesopause will be 20 K warmer than the mesopause. Ice nucleation at regular PMSE altitudes can therefore be reduced by increased temperatures. Morris *et al.* [2012] note that this effect alone could explain a large part of the observed anomaly in mesospheric ice particle occurrence.

Furthermore, an altitude increase of 5 km roughly reduces the water vapour available for particle growth by a factor of 10, limiting the growth of all mesospheric ice particles at higher altitudes (see blue lines in the left panel of Figure 36 on page 46). As the optical visibility of NLC ice particles increases with the square of the particle radius, a 5 km increase in altitude, therefore, reduces the optical visibility by two orders of magnitude [Lübken *et al.*, 2014]. The change in average particle sizes resulting from the lower availability of water vapour could explain the observed particular strong reduction of larger ice particles (PMC/NLC) relative to smaller particles observed as PMSE.

16 Stratospheric winds and mesospheric ice particles

Winds in the middle atmosphere control the propagation of gravity waves, thereby influencing the momentum deposition and circulation in the MLT region. The first occurrence of mesospheric ice particles after the winter/summer transition has been associated with the stratospheric polar vortex breakdown (SPVBD). At Davis, the altitude of PMSE early in the season strongly correlates with the timing of the SPVBD. However, observations reveal no good correlation of the SPVBD timing with the first occurrence of small ice particles.

Ice particles observations have been investigated in both hemispheres to study the variability of the winter to summer transition in the MLT as well as the vertical coupling of the atmospheric layers [e.g., Woodman *et al.*, 1999; Siskind *et al.*, 2003; Karlsson *et al.*, 2007; Benze *et al.*, 2012]. Subsequently, Gumbel and Karlsson [2011] note that the very late start of the NLC/PMC season in the SH summer 2010/2011 coincided with a particularly long lasting stratospheric polar vortex. Karlsson *et al.* [2011] investigate the onset of the PMC season in relation to the stratospheric polar vortex breakdown (SPVBD). A good correlation of the timing of the SPVBD and the onset of PMC ice particles as observed by the AIM satellite in the years 2007/2008 to 2009/2010 is found. The correlation is then reproduced with the Canadian Middle Atmosphere Model (CMAM) and explained as being caused by MLT temperature variations through stratospheric wind filtering of gravity waves [Karlsson *et al.*, 2011]. The CMAM simulations show that the mesopause in the SH should be higher, but warmer than in the NH. Kirkwood *et al.* [2008] find this behaviour in analyses of MLS temperature and VHF radar PMSE observations.

Morris *et al.* [2012] extend the analysis and compare PMSE centroid altitudes during the 2010/2011 summer, as well as the 6 previous summers, with stratospheric zonal wind data from NOAA's "National Center for Environmental Prediction" (NCEP) Reanalysis-1 (Figure 32). Summer seasons which experienced an early SPVBD correspond to years in which the centroid altitude of the PMSE layer was comparatively low, at around 85 km to 87 km throughout the season (blue colours in Figure 32). Summer seasons with a later SPVBD on the other

hand show unusually high PMSE centroid altitudes of above 87 km to 90 km early in the season (red colours in Figure 32).

Lübken *et al.* [2014] present wind analyses of "Modern-Era Retrospective Analysis for Research and Application" (MERRA) data [Rienecker *et al.*, 2011], as well as direct observations of PMSE and temperatures (reproduced in the middle panels of Figures 33 and 34). Contrary to the more qualitative analysis of Morris *et al.* [2012], that study uses a more stringent SPVBD criterion at 52 hPa and 69°S, similar to Karlsson *et al.* [2011]. Figure 33 shows several interesting features. First, the SPVBD (red dot) in the first two summer seasons (2010/2011 and 2011/2012) occurred very late in the season around summer solstice, towards the positive standard deviation of the long-term wind observations (black). Second, the zonal-mean zonal wind decreased markedly around 35 days before solstice in 2011/2012 but recovered thereafter (middle panel). Lübken *et al.* [2015] call this behaviour a "quasi-late breakdown". Third, in contrast to the first two seasons, the SPVBD occurred unusually early at around 40 days before summer solstice in the summer season 2012/2013 (bottom panel). From 20 days before summer solstice onwards, the winds in 2012/2013 followed typical NH winds (green).

During the 2011/2012 summer season, PMSE with a mean centroid altitude of 86 km first occurred sparsely on 16 November 2011. As Figure 34 shows, the centroid altitude of the PMSE (red line) then follows the temporal development of the mesopause at a distance of around 3 km to 4 km. PMSE in 2010/2011 and 2011/2012 occur at very high centroid altitudes of above 89 km altitude during the SPVBD at around summer solstice. Note that (charged) ice particles cannot be observed as PMSE a lot higher than 94 km because the increasing kinematic viscosity prevents the creation of turbulent structures, eliminating a necessary criterion for radar detection [Lübken *et al.*, 2009].

However, when comparing wind and PMSE data of all three seasons, Lübken *et al.* [2015] note that stratospheric winds do not necessarily correlate well with the onset of ice particles after the winter/summer transition of the MLT. In the seasons 2011/2012 and 2012/2013, PMSE were first observed at very similar dates, around 40 days before summer solstice. The final SPVBD, however, occurred almost exactly around summer solstice in 2011/2012 but 40 days earlier in 2012/2013.

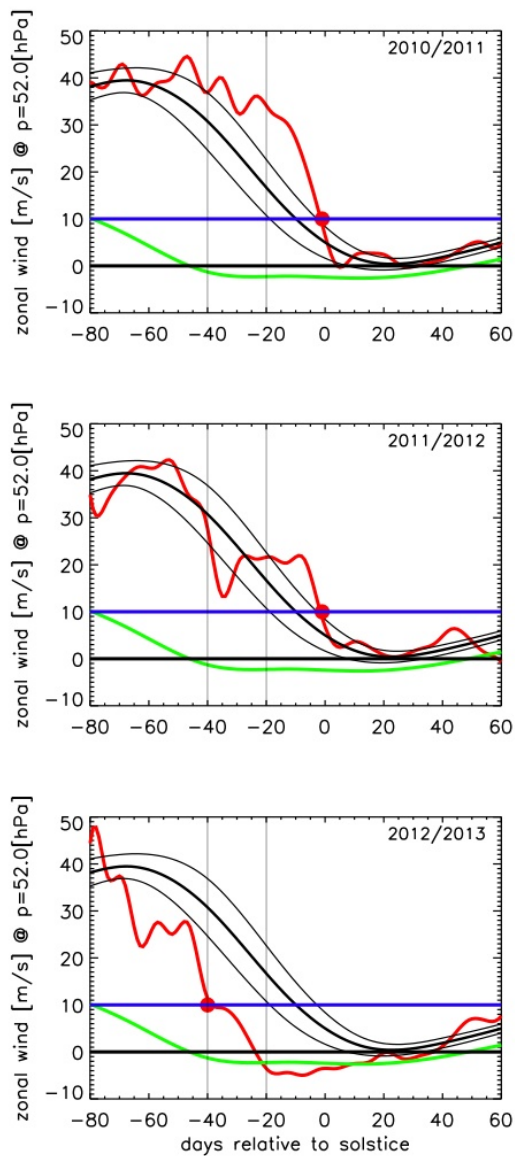


Figure 33: Zonal-mean zonal winds (red) close to 52 hPa at 69°S in the summer months of the years 2010–2013. The stratospheric polar vortex breakdown (SPVBD; red dot) can be characterised to occur when the winds drop below 10 m s^{-1} (blue line). In the years 2010/2011 and 2011/2012, the SPVBD occurred later than the long-term average in the SH (black; mean and standard deviation of anomalies). In contrast, the SPVBD occurred unusually early in 2012/2013. In the NH, average stratospheric winds are less eastward throughout summer (green). Reprinted with permission from [Lübken et al. \[2015, Fig. 9\]](#), Copyright 2015 John Wiley & Sons, Inc.

In summary, the observations at Davis, Antarctica find a correlation of PMSE centroid altitudes during the early summer season with the timing of the reversal of stratospheric winds during the winter/summer transition of the SH. It is obvious from Figure 32 that the PMSE centroid altitude is ele-

vated in years with a late SPVBD, i.e. when the zonal wind change from prevailing westerlies to easterlies (from positive to negative values) occurs late in the SH summer season. However, contrary to previous findings by [Karlsson et al. \[2011\]](#), the timing of the onset of small ice particles as observed as PMSE by the Davis MST radar does not show a good correlation with the SPVBD. This seems to be strongly related to the different temperature structure of the MLT region in the respective years.

17 Elevated Summer Mesopause

Lidar observations at Davis (69°S) reveal unexpected MLT temperatures during the summer months of some years, while other years resemble conditions in the Northern Hemisphere (NH). Under suitable middle atmospheric wind conditions in the Southern Hemisphere (SH), gravity waves can propagate to unusual altitudes where they deposit their momentum. This high altitude momentum deposition causes an increased summertime polar upwelling, leading to an “Elevated Summer Mesopause” (ESM). An ESM has never been observed in the NH and changes the conditions for ice particle growth in the respective years.

The thermal structure of the summer MLT is significantly influenced by breaking gravity waves and the subsequent residual circulation. The circulation change from the winter to the summer state of the upper polar atmosphere requires gravity waves with eastward phase speeds to break in the MLT. The gravity waves relevant for the momentum deposition predominantly originate in the troposphere and propagate upwards through the middle atmosphere. In the middle atmosphere, gravity waves become unstable or are filtered at critical layers when their phase speed and the background wind speed are equal or differ only slightly [e.g., [Fritts and Alexander, 2003](#)]. During winter conditions, the persistent stratospheric polar vortex is characterised through strong eastward winds, prohibiting the propagation of gravity waves with eastward phase speeds. Mesospheric winds are weak during winter, setting a further boundary for gravity waves, as wave breaking can result through dynamic instabilities.

Sections 14 to 16 have already discussed the coupling of lower atmospheric layers to the MLT through

gravity wave filtering due to background winds. Differences between the hemispheres originate through different wind patterns and, to a smaller extent, radiative differences. Calculations with the Canadian Middle Atmosphere Model (CMAM) predict the mesopause in the SH to be higher, but simultaneously warmer, than in the NH [Karlsson *et al.*, 2011]. These calculations had been in line with satellite observations of higher average mesopause temperatures in the SH compared to the NH [e.g., Huaman and Balsley, 1999].

Observations at Davis

Figure 34 summarises the summer MLT temperature observations by the mobile IAP Fe lidar at Davis in the seasons 2010/2011 to 2012/2013, including the results presented by Morris *et al.* [2012] (upper panel), Lübken *et al.* [2014] (middle panel), and new results by Lübken *et al.* [2015] (lower panel). As previously noted, the mesopause altitude in 2010/2011 was unusually high early in the season and declined thereafter. A similar behaviour was observed in 2011/2012. As expected from similar observations in the NH, temperatures throughout the MLT in 2011/2012 drop by around 20 K at all altitudes during the winter/summer transition about 60 to 40 days before the summer solstice. The mesopause altitude (white line in Figure 34) drops to around 89 km at the beginning of summer. This altitude, as well as the absolute temperatures, are similar to common NH summer conditions. Surprisingly, Lübken *et al.* [2014] then observe a very rapid change in mesopause altitude (“mesopause jump”). 20 days after the winter/summer transition of the MLT in 2011/2012, the mesopause altitude increased to nearly 94 km within about 10 days. Interestingly, the temperatures at these “elevated summer mesopause” (ESM) altitudes were only around 120 K, and hence lower than at common summer mesopause altitudes in both the SH and the NH. Shortly before summer solstice, Lübken *et al.* [2014] show lidar temperature observations as low as 100 K (see Figure 36 on page 46).

The surprising behaviour of summer mesopause jumps to an ESM had never been observed in any hemisphere and is in contradiction to previous modelling studies [e.g., Huaman and Balsley, 1999; Lübken and Berger, 2007; Karlsson *et al.*, 2011]. A likely reason that an ESM in the polar summer MLT had never been observed before is that no obser-

vational technique so far had the temporal and spatial resolution of the mobile IAP Fe lidar. This highlights the importance of the technical developments described in Section 3.

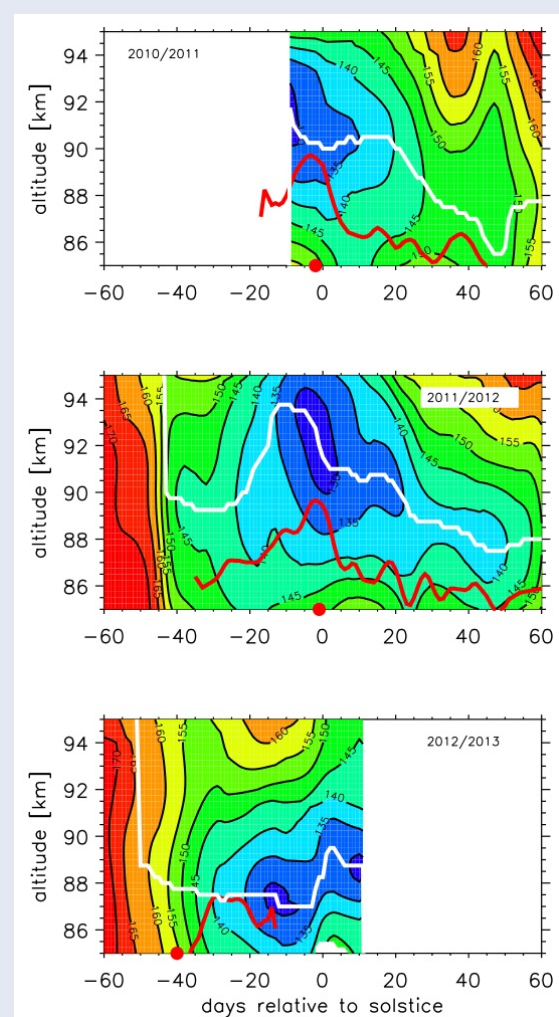


Figure 34: Lidar observations of temperatures (colour scale) in the MLT region at Davis, Antarctica (69°S). The summer mesopause altitude (white line) is elevated shortly before summer solstice when the polar vortex breakdown (red dot) occurs late in the season. The timing of the onset and the mean altitude of PMSE (red line) are also affected by this transition, with PMSE generally following the mesopause altitude. Temperature data are smoothed with Hann filters of 14 days (horizontal) and a 2 km (vertical) width. Reprinted with permission from Lübken *et al.* [2015, Fig. 3], Copyright 2015 John Wiley & Sons, Inc.

After summer solstice, the mesopause altitude steadily decreased in 2010/2011 and 2011/2012, and absolute temperatures were comparable to the NH later in the season [Lübken, 1999; Lübken *et al.*, 2014]. The downward motion of the mesopause can be explained by the effect of interhemispheric cou-

pling in the middle atmospheric circulation [Körnich and Becker, 2010; Becker et al., 2015]. Around 60 days after summer solstice, the MLT experiences the autumn transition and temperatures, as well as the mesopause altitude, then rapidly increase to the winter state (not shown).

To explain the observations and the hemispheric differences, Lübken et al. [2015] investigate zonal MF radar winds obtained at Davis (Figure 35) and compare them to stratospheric winds, as well the correlation with MLT lidar temperatures (Figures 33 and 34). Interestingly, MF radar winds during the ESM period are observed to be much more westward than during non-ESM conditions. Furthermore, westward winds extend to higher altitudes during ESM periods.

Lübken et al. [2015] then use the Kühlungsborn Mechanistic Climate Model (KMCM) by Becker et al. [2015] to reproduce the wind fields and temperatures in the MLT. Comparing both hemispheres, as well as control runs without gravity wave interactions, Lübken et al. [2015] reproduce several features of the MLT temperature structure. The analysis suggests that mesospheric winds above the stratospheric polar vortex change the gravity wave propagation in the years with and without ESM.

Explanation of the ESM

Lübken et al. [2016] have recently presented further correlation analyses of wind fields in the middle atmosphere and MLT temperature changes. In comparing the wave forcing in the SH with the NH, that study provides a comprehensive explanation of the mesopause jumps and the ESM at Davis:

The polar vortex with strong eastward winds is much more persistent in the SH than in the NH and acts as a barrier for gravity waves with eastward phase speeds. The momentum of these waves does not reach the MLT. Occasionally, the SPVBD in the SH occurs as late as 1 or 2 days before summer solstice. Shortly before the SPVBD, gravity waves with large eastward phase speeds can propagate through the stratosphere in the early summer season. Simultaneously, winds in the summer mesosphere are strongly westward. The reduced vertical flux of eastward momentum (compared to mean summer conditions in the NH or later in the SH) results in even stronger westward winds in the upper mesosphere. The strong westward mesospheric winds are a consequence of the reduced gravity

wave flux through strong stratospheric winds and the downward control principle [Haynes et al., 1991; Becker, 2012; Becker et al., 2015]. Gravity waves with high eastward phase speeds can then pass the mesopause region without breaking because the different signs of phase speed and background wind speed lead to large vertical wavelengths and comparatively stable conditions. The wave amplitude increases further with increasing altitude, breaking only at unusually high altitudes in the lower thermosphere at around 95 km. The relative effect of the momentum deposition is stronger at higher altitudes, inducing even stronger eastward winds, a stronger meridional flow through the Coriolis force, and a subsequently even stronger upwelling to higher altitudes. This causes the very low temperatures of the ESM.

As Lübken et al. [2016] note, two important aspects of this explanation are (a) slightly eastward winds which filter gravity waves with low phase speeds, but let waves with high speeds pass to the mesosphere, and (b) strongly westward winds in the mesosphere, enabling the wave propagation to the lower thermosphere. An ESM can therefore only be found if the timing of stratospheric and mesospheric winds is favourable. This condition is never fulfilled in the NH, where the SPVBD occurs early in the season, when mesospheric winds are still in their weak, predominantly eastward winter state. The different stratospheric wind patterns of the hemispheres are therefore responsible for the hemispheric differences observed in the summer polar MLT, including different mesopause altitudes and presumably all observed differences in ice particle occurrence described in Section 15. The importance of gravity waves with large phase speeds for the dynamics of the MLT is in line with the conclusions of Kaifler et al. [2015] about the selective filtering in the stratosphere (see Section 14).

ESM influence on ice particles

The temperature structure of the summer MLT is highly important for the formation of ice particles. The temporal evolution of temperature around the mesopause is consistent with the findings of Section 15 which showed a strong correlation of PMSE centroid altitudes with stratospheric winds. Below the ESM, the sublimation of ice particles is increased, and ice particles occur in the colder regions at higher altitudes. The increased PMSE

centroid altitudes (Section 15) is, therefore, a manifestation and indication of an ESM in certain years.

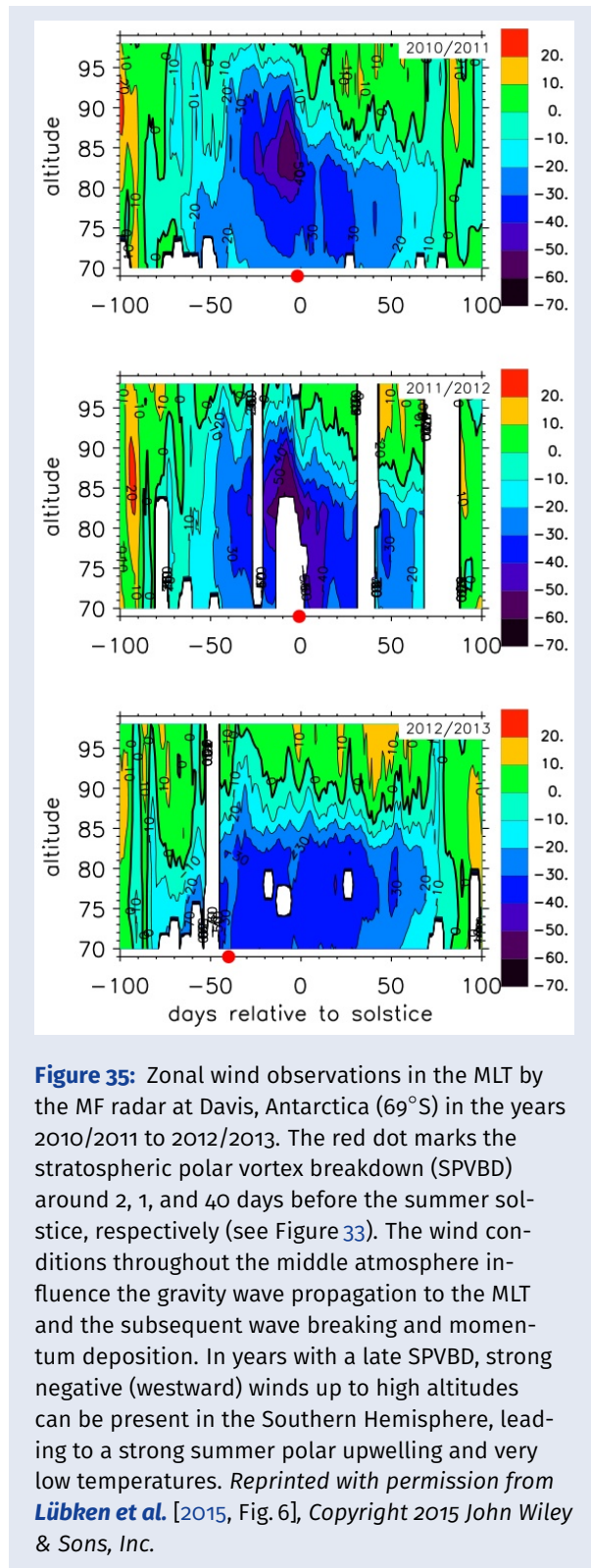


Figure 35: Zonal wind observations in the MLT by the MF radar at Davis, Antarctica (69°S) in the years 2010/2011 to 2012/2013. The red dot marks the stratospheric polar vortex breakdown (SPVBD) around 2, 1, and 40 days before the summer solstice, respectively (see Figure 33). The wind conditions throughout the middle atmosphere influence the gravity wave propagation to the MLT and the subsequent wave breaking and momentum deposition. In years with a late SPVBD, strong negative (westward) winds up to high altitudes can be present in the Southern Hemisphere, leading to a strong summer polar upwelling and very low temperatures. Reprinted with permission from [Lübken et al. \[2015, Fig. 6\]](#), Copyright 2015 John Wiley & Sons, Inc.

As the mesopause altitude decreases to common NH values later in the 2010/2011 season, the temperature lapse rate below the ESM can no longer explain the reduction in ice particle occurrence.

However, [Morris et al. \[2012\]](#) note that the wind pattern observed by the Davis MF radar suggests a warming by a 2-day wave [[Morris et al., 2009](#)]. This, together with strong thermal tides reported by [Lübken et al. \[2011\]](#) (see Section 12) could increase average temperatures and reduce ice particle growth. It may also be speculated that a change in wind and vertical transport later in the season reduced the available water vapour compared to other seasons. More understanding of these processes is required and might in the future be achieved by comprehensive 3D modelling.

18 Definition of the summer season in the polar MLT

In the Southern Hemisphere, the MLT region temperature transition between winter and summer is coupled to the timing of the polar vortex breakdown. The resulting variability has consequences for some MLT investigations such as the interpretation of trends in ice particle occurrence.

The implications of the traditionally defined seasons based on astronomical parameters (i.e., spring and fall equinox as well as summer and winter solstice) for atmospheric research are seldom considered. When investigating the annual cycle of atmospheric parameters, common analyses include mean winter temperature, seasonal average centroid altitude of a metal layer, or days with ice particle occurrence during the summer season.

However, [Lübken et al. \[2015\]](#) point out that the astronomical definition of the “Summer Season” may be misleading in certain situations of atmospheric research. As detailed in the preceding Sections, the MLT temperature transition and the occurrence of ice particles depend on the timing of the SPVBD.

This is of particular importance when statistically comparing the occurrence of ice particles of several years [e.g., [DeLand et al., 2003, 2007](#)]. If an average is given respective to “all days of summer”, the comparison of various years might lead to incorrect interpretations. For such applications, the beginning of the summer state of the polar MLT in the SH might, therefore, be most accurately defined by the timing of the temperature transition, not by a fixed date in the astronomical calendar.

Further Results and Outlook

The measurement campaigns of the mobile IAP Fe lidar have produced an unprecedented dataset with several unexpected new observations. Not all results have yet been published or fully analysed. The following sections give an overview of some preliminary analyses of important observations.

19 MLT temperature climatology for the austral polar region

Lidar observations at Davis, Antarctica (69°S) have yielded around 2900 h of high accuracy temperature measurements in the MLT region. The measurements cover all months of the year and all hours of the day. The resulting dataset is the most comprehensive high-resolution temperature climatology of the austral polar MLT region.

Accurate temperature datasets are essential for understanding Earth's atmosphere. Global reference atmospheres and models provide a broad overview of important aspects [e.g., CIRA-86 and NRLMSISE-00, [Fleming et al., 1990](#); [Picone et al., 2002](#)]. However, these references and predictions do not show short term variations, need observational input, and have to be tested for their accuracy.

Existing datasets

Temperature observations in the polar MLT of the Southern Hemisphere (SH) have been obtained by several means, including measurements by satellites, sounding rockets, OH imagers, meteor radars, and resonance lidars. All observations have their respective strengths and were used for several important studies. However, all observational methods also have their own shortcomings.

Satellite observations such as Aura(EOS)/MLS, TIMED/SABER, and AIM/SOFIE provide a near-global image of MLT temperatures. However, they are particularly limited in their vertical and temporal resolution. For example, the vertical resolution of MLS

temperatures in the MLT region is around 14 km [[Schwartz et al., 2008](#)]. The error of the SABER temperature retrieval can increase from around 1.5–5 K under favourable conditions to 18 K during the polar summer months [[García-Comas et al., 2008](#)]. MLT temperature measurements by the SOFIE experiment are expected to have a precision of ~ 0.2 K and are obtained during 15 sunsets and sunrises per day [[Gordley et al., 2009](#)]. However, the AIM satellite is in a retrograde circular polar orbit and the measurements only take place near the time of local sunrise and sunset [[Russell et al., 2009](#)]. Temperature variations by thermal tides in particular can therefore bias the mean, and a warm bias of 10 K has been observed in comparison to other measurements [[Hervig and Gordley, 2010](#)].

Observations of dynamic features from space are furthermore hampered by the precession of the satellites. In the case of the higher resolution SABER measurements, the precession of the TIMED satellite means that a full 24 h coverage at given point requires an integration of 60 days of observations. Although tidal analysis are still possible with the datasets [e.g., [Zhang et al., 2010](#)], none of these techniques allow to resolve waves on shorter time scales or the highly dynamical features in the MLT region as presented in this thesis.

A resonance lidar climatology at the South Pole has been obtained by [[Pan and Gardner, 2003](#)], covering 26 h of measurements during the crucial summer months November to February (see right panel of [Figure 36](#)). With such little data, a potentially strong bias by gravity wave or tidal activity seems likely. Furthermore, [Lübken et al. \[2015\]](#) point out that those measurements during the summer months did not actually capture the mesopause directly, but interpolated the data above and considerably below the suspected mesopause altitude. Additionally, no observations were made during November at all, leaving quite an important gap of data during the crucial transition time from the winter to the summer state of the Southern Hemisphere. The SH summer months, however, are particularly crucial for many analyses in regards to PMC occurrence or the residual circulation [e.g., [Lübken et al., 2016](#)].

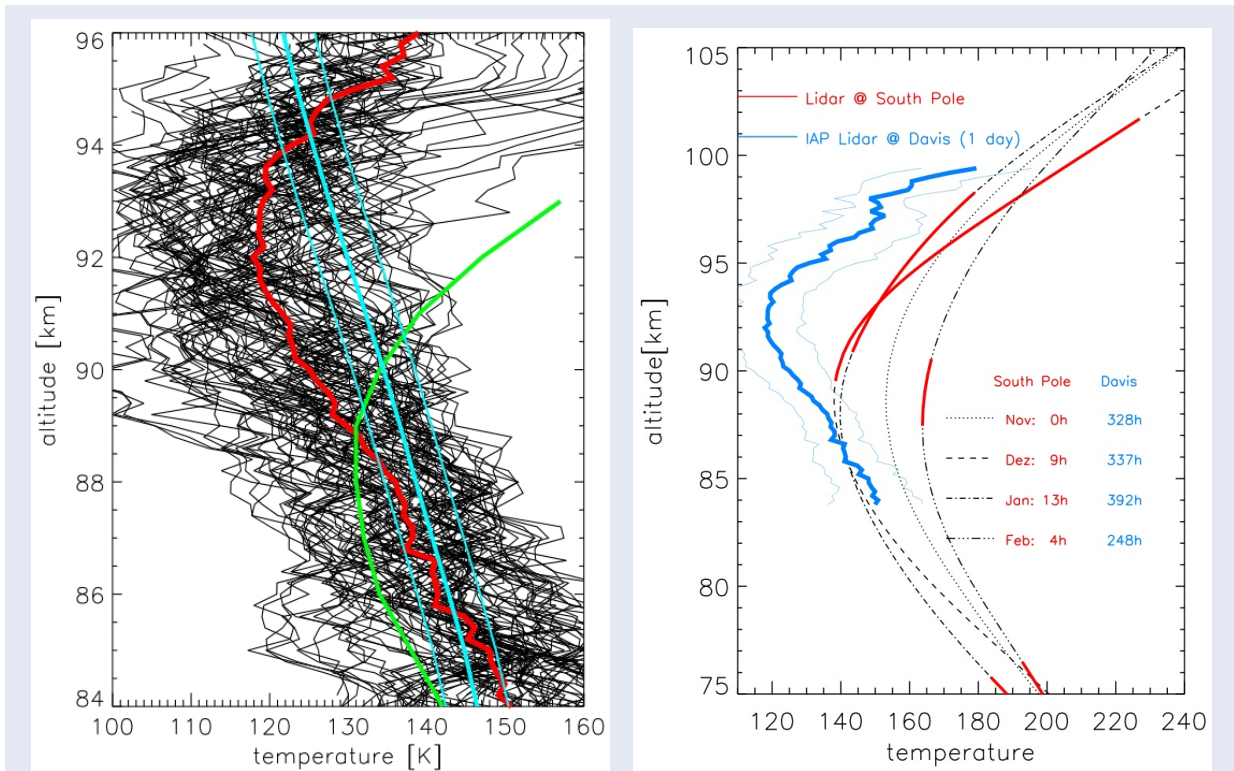


Figure 36: Example measurements of the improved temperature climatology data set obtained by the mobile IAP Fe lidar. (left) 24 h measurement at Davis, Antarctica on 17/18 December 2011: 96 profiles integrated for 1 h every 15 minutes (black), daily mean profile (red) and comparison to climatology of the Northern Hemisphere (green). The mesopause is observed to be high and cold with mean temperatures below the frost point (cyan). Waves cause a high variability throughout the day. (right) Comparison of one day of measurements with the mobile IAP Fe lidar (mean and variance, blue) and previously existing dataset from the South Pole (red). The new dataset contains considerably more hours of measurement throughout the summer months, providing a far more accurate representation of the MLT temperature structure and variability. Reprinted with permission from [Lübken et al. \[2014, 2015\]](#) Copyright 2014 and 2015 John Wiley & Sons, Inc.

New dataset

The new climatology obtained by the mobile IAP Fe lidar at Davis, Antarctica (69°S) covers around 2 893 hours of Fe density and temperature measurements. While observations of at least 129 h were obtained during all months of the year, the dynamic summer months November to February were covered particularly well with at least 248 h and up to 392 h (see Figure 42 on page 60). The new temperature climatology contains 50 times more hours of measurement than the existing lidar climatology by [Pan and Gardner \[2003\]](#) during the crucial summer months. To date, this is the most comprehensive high-resolution temperature dataset of the MLT region in the SH. The observation of the high altitude of the summer mesopause during some years was unexpected and lead to new insights about the atmospheric coupling (see Section 17 as well as [Lübken et al. \[2014, 2015\]](#)).

Figure 36 illustrates some features of this dataset. The new observations have revealed some of the lowest temperature measurements ever obtained in the atmosphere as well as a high temperature variability throughout the day. The left panel in Figure 36 shows all lidar measurements (black) obtained during 24 h, the daily mean temperature profile (red), and a comparison to the NH climatology by [Lübken \[1999\]](#). The right panel in Figure 36 compares the data of this one day (blue) to the existing austral lidar climatology (red and black) by [Pan and Gardner \[2003\]](#). The thin blue lines around the daily mean indicate the high variability throughout one day. This shows that temperature variations can be substantial and need to be taken into account.

Parts of the temperature data covering the summer months have already been published in [[Lübken et al., 2015](#)]. The full climatology is currently being prepared for publication.

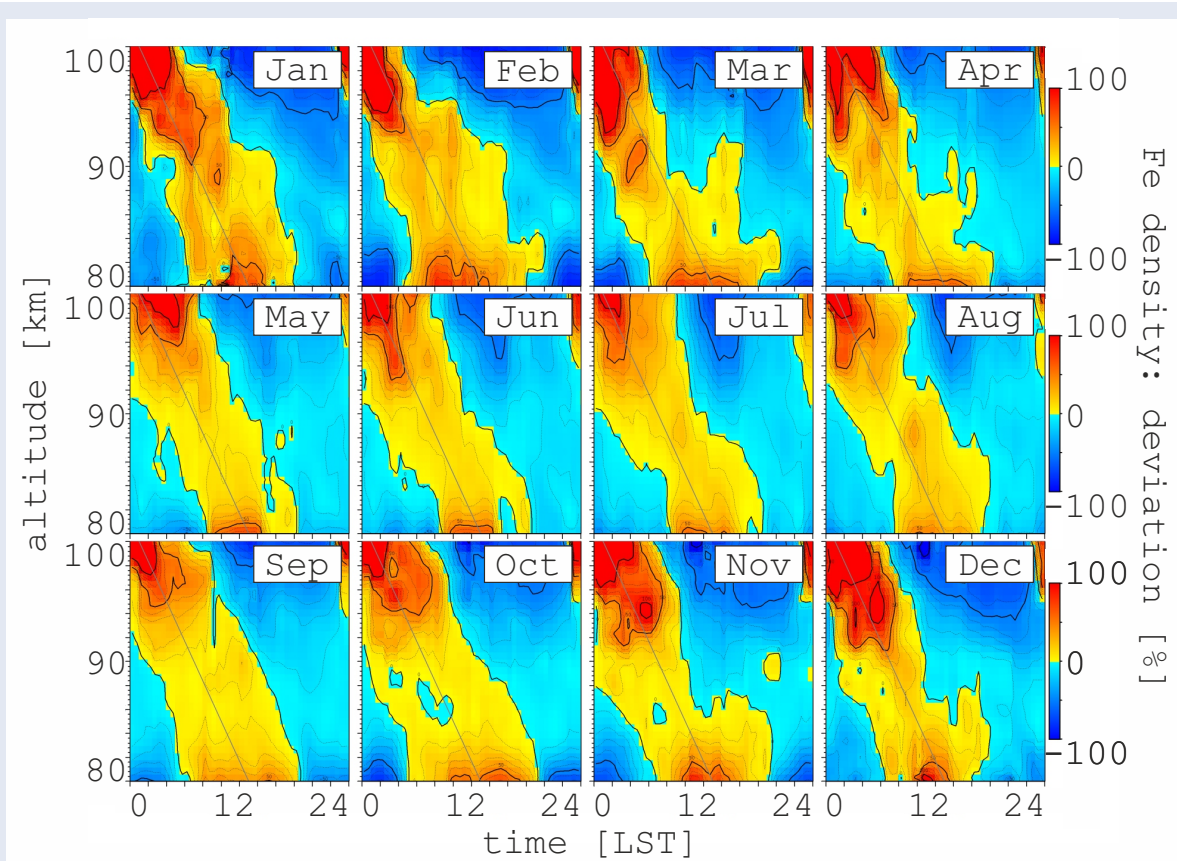


Figure 37: Diurnal deviation from mean Fe density per altitude at Davis, Antarctica (69°S), averaged for all twelve months 12/2010–12/2012. The tidal features in Fe density show the same phase structure throughout the year, despite the pronounced seasonal variability of solar irradiance at polar latitudes. *Preliminary results. Contact author before usage of data. CC BY 4.0*

20 Constant Fe tides in the polar MLT

Fe density measurements at Davis, Antarctica (69°S) have revealed a surprisingly regular tidal structure. All months show the same phase progression, regardless of changes in solar irradiance throughout the year. WACCM-Fe model calculations are currently being analysed to explain these observations.

Observations with the mobile IAP Fe lidar by [Lübken et al. \[2011\]](#) have revealed strong thermal tides at Davis, Antarctica (69°S). The observed tides had a similar phase progression in temperatures and Fe densities (see Section 12). New analysis shown in Figure 37 surprisingly reveal a very constant tidal signature in Fe densities throughout all months of the year, which has neither been observed before nor predicted by model calculations.

Part of the explanation is presumably the very regular occurrence of sporadic Fe layers (Fe_S) at Davis, which is a further unexpected and new observa-

tion: Fe_S were observed to predominantly occur between 18 UT and 22 UT (23 LST and 3 LST). Fe_S are usually first seen at altitudes of around 105 km to 125 km shortly before 18 UT (23 LST), on rare occasions even higher. As are descending in time, they were observed to usually reach an altitude of 100 km at around 19 ± 1 UT (between 23 LST and 1 LST). This probably explains the high densities at the top end of Figure 37.

Furthermore, the strong photolysis of FeOH causes a regular creation of neutral Fe atoms on the bottomside of the Fe layer, centered around local noon (see Section 5). This effect can explain higher densities at altitudes around 80 km at around 12 LT in Figure 37. However, the sun does not set at Davis during the summer months, so this effect alone cannot explain the behaviour. Moreover, the temperature dependence of the neutral Fe layer is strongly reduced during the polar summer months as FeOH is fully depleted (see Section 7). Temperature tides as reported by [Lübken et al. \[2011\]](#) (see Section 12)

are hence presumably not the cause for an enhancement of Fe. The most likely explanation of the constant phase structure in Figure 37 is therefore a tidally driven downward movement of Fe atoms created through the recombination of FeO^+ in regularly occurring Fe_s.

The analyses presented in Section 13 are currently being extended to model runs of WACCM-Fe, including new reaction rates as determined by Viehl *et al.* [2016a] (see Section 6). The new analyses will also allow to directly compare the temperature influence on the chemistry.

21 The mesospheric Fe layer in Antarctica and the Arctic

Observations of the mesospheric Fe layer in Antarctica and the Arctic show several common characteristics but also differences. These differences allow to further investigate the physics and chemistry of the MLT region.

Observations with the mobile IAP Fe lidar at Davis (69°S, 78°E) in Antarctica and ALOMAR (69°N, 16°E) in the Arctic allow comparing differences and similarities in Fe density. Figure 38 shows the mesospheric Fe layer at Davis (top) and ALOMAR (bottom), centred around the respective summer solstice. All available observations (listed in Figure 42 in Appendix C) contribute to these plots. Generally, both stations experience higher densities, a larger RMS layer width, and a lower centroid altitude during winter than during summer. However, average densities at Davis are significantly larger during the winter months than at ALOMAR. Furthermore, although densities in the middle of summer are very low at ALOMAR, the extremely low densities observed at Davis have not yet been observed in the NH. Both polar regions show an uplift of the Fe layer towards to and during the summer months. However, the upper edge of the layer is only clearly elevated at Davis. At ALOMAR, a dip at the top edge of the layer is observed.

As mentioned in Section 4, Davis and ALOMAR have been specifically chosen for the observations with the mobile IAP Fe lidar not only because of the good infrastructure and co-located instruments, but also because they are at nearly exactly opposite latitudes of the globe. This allows for particularly valuable interhemispheric comparisons. The

distance of both observational sites from the respective Geographic Poles (Davis: 2 381 km, ALOMAR: 2 303 km) differs somewhat less than the different geomagnetic latitudes. Davis is currently located at a distance of about 2 505 km from the South Magnetic Pole, while ALOMAR is slightly further away at around 2 702 km from the North Magnetic Pole. This difference may seem small, but a change of around 200 km means that Davis is located in the active region of the auroral oval more often than ALOMAR. Note that the geomagnetic distances were calculated for 2015 and the North Magnetic Pole currently moves north-east, increasing the distance to ALOMAR by about 1 km to 5 km per year.

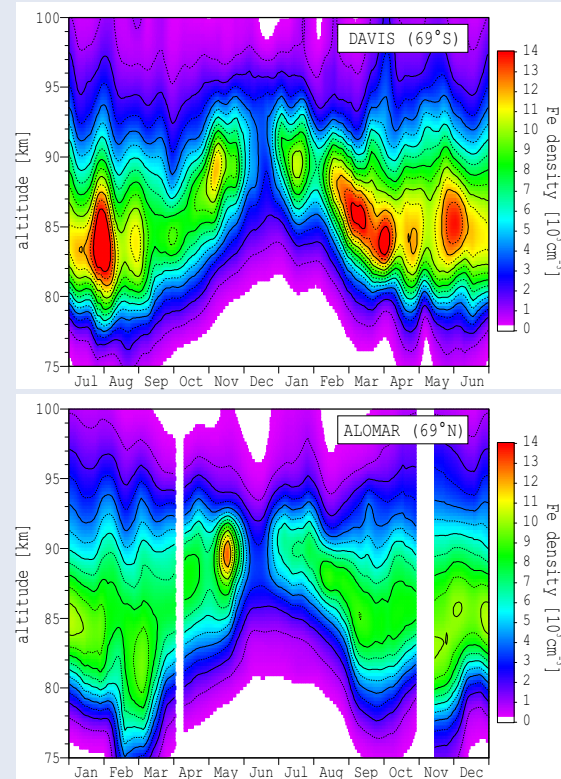


Figure 38: Seasonal variation of the Fe layer at Davis (69°S) and ALOMAR (69°N), centred around the respective summer solstice. Measurements in both hemispheres show an uplift of the layer during the summer months when densities are generally lower than during winter. CC BY 4.0

The geomagnetic differences may explain why lower absolute densities are generally observed at ALOMAR compared to Davis, transporting more FeO^+ and other ionised species to the site. Furthermore, the recombination process $\text{FeO}^+ + e^- \rightarrow \text{Fe} + \text{O}$ may be more efficient during more regular (electron) Auroras at Davis.

The meteoric input is roughly anti-symmetric for Davis and ALOMAR, leading to a similar cosmic dust input during the respective seasons [Fentzke and Janches, 2008]. However, they also experience differences in the meteoric input function to the respective seasons due to the Earth's orbital position throughout the year and the orbit inclination.

Additionally, the both polar hemispheres experience a different activity (and spectrum) of gravity and planetary waves in the MLT. Further differences of the hemispheres include the occurrence of mesospheric ice particles (PMC/NLC, PMSE), and different pressure altitudes due to a stronger contraction of the atmosphere in the colder middle atmosphere of the Southern Hemisphere. A detailed comparison of the data of the two polar locations in combination with comprehensive 3D atmospheric modelling will allow investigating the physics, chemistry, and meteoric input in more detail. The measurements in the Arctic are currently ongoing, filling the data gaps and increasing the measurement statistics at ALOMAR.

22 Intraday variability of the Fe layer and short term influence of ice particles

Previous studies have focused on longer-term investigations of the mesospheric metal layers. Short-term analyses of metal layer variations on time scales of minutes to days allow investigating metal atom transport, interaction with mesospheric ice particles, gravity wave activity, and mixing processes in more detail.

Analyses by Viehl et al. [2015] have shown that a possible uptake of Fe atoms on ice particles (PMC) has no dominating effect on the seasonal variation of the Fe layer (Section 10). However, Viehl et al. [2015] note that a very localised uptake during the day as reported by Plane et al. [2004] might have a measurable short-term effect in addition to vertical and mean meridional transport processes, as well as all chemical factors, involved [Viehl et al., 2016b]. Although this uptake effect is not large enough to dominate the overall mean density of the layer, a quantification seems necessary to fully understand the variability of the Fe layer, for example to allow for gravity waves analyses.

Figure 39 shows an example of the intra-day variability of the Fe layer (blue) and ice particles observed as PMSE (red) during a measurement at Davis (69°S) shortly before the SH summer solstice. Fe densities below $\sim 2\,000\text{ cm}^{-3}$ are observed before 22 UT. After 22 UT, high Fe densities up to $16\,000\text{ cm}^{-3}$ are observed in an altitude range between 86 km and 96 km. The area of high Fe density within the Fe layer generally decreases in altitude with time. No NLC were recorded throughout the duration of this measurement. Several interesting points can be drawn from a preliminary of this plot.

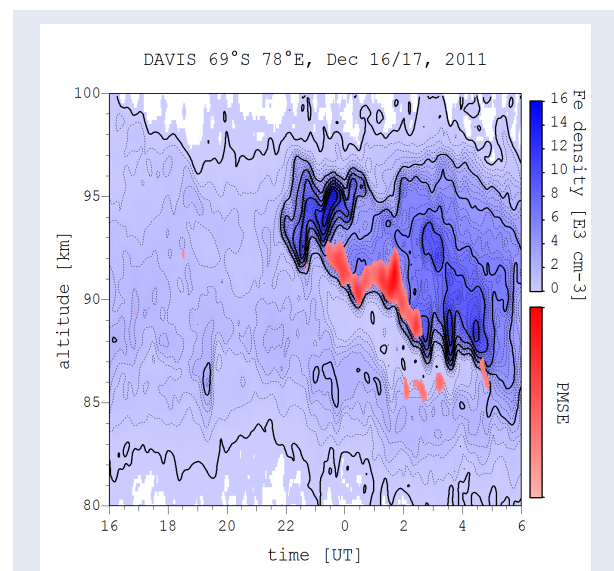


Figure 39: Close-up of the Fe layer (blue) and PMSE (red). The Fe layer shows considerable variation throughout the day with very low densities before 22 UT and high densities thereafter. PMSE occur when high densities are observed and tend to be located at the lower edge of areas with high Fe density. The anti-correlation of low column densities and ice particle occurrence has been analysed by Viehl et al. [2015, 2016b] on seasonal scales. An analysis of the intra-day variability could help to further understand the interaction of ice particles and metal atoms in the MLT region and quantify heterogeneous uptake. *Preliminary results. Contact author before usage of data. CC BY 4.0*

First, no mesospheric ice particles (neither NLC nor PMSE) were observed during the first part of the measurement. In line with the seasonal observations by Viehl et al. [2015, 2016b], column densities (not shown) in this example are low although no ice particles are observed. On the other hand, column densities are high throughout the second part of the observation when mesospheric ice particles were detected through PMSE observations.

Second, PMSE were observed between around 87 km and 93 km at the lower edge of the area of high Fe density, and both Fe density and PMSE show considerable variability. This variability could be caused by gravity waves. The main PMSE layer additionally shows a general downward trend. A second layer of weaker PMSE is further observed at around 86 km altitude below the main PMSE layer.

Third, the altitudes above 94 km show a pronounced variability which can most likely only be explained by strong horizontal transport or the recombination of FeO^+ to Fe in sporadic Fe layers (Fe_S). However, it is noteworthy that at altitudes above 94 km PMSE may not be observed due to the increased kinematic viscosity, as the energy dissipation rate required to achieve a certain radar volume reflectivity increases strongly above 90 km altitude [Lübken, 2013]. Ice particles could still be present but not cause PMSE. However, the presence of ice is not very likely, as the temperature at this altitude also increases significantly. In fact, the measurements show temperatures above 94 km were generally above the freezing point on this day, see left panel of Figure 36.

In many available observations, PMSE track the lower edge of Fe layer where a high gradient of Fe is observed. However, Fe densities are in general not lower after the local occurrence of PMSE in line with the results by Viehl *et al.* [2015]. In fact, the highest densities of the measurement in Figure 39 were observed when PMSE are present. Studies have focussed on the aspect of ice particles necessary for PMSE observation. It might be possible that the combination of metal layer and PMSE observations could also give an insight into the occurrence of turbulence and wave breaking in the MLT. Detailed intra-day analyses of Fe density and PMSE observations will help to understand all short-term variations of the metal density as well as their relation and importance to the occurrence of PMC.

An important point to note is that although lidar and radar measurements have a high vertical and temporal resolution, they only provide a one-dimensional measurement in time. Full 4D modelling of the dependent metal chemistry and transport, as well as aerosol movement, are needed to investigate a potential uptake along the track of PMC particles. Additional 4D observations of the mesospheric Fe layer with tilted lidars could provide a much deeper insight into these processes and other phenomena.

23 Lidar observations of meteor smoke particles

The polymerisation of metallic compounds in the MLT produces meteoric smoke particles (MSP). MSP are important for the nucleation of ice particles in the MLT region and may affect the global climate through interactions in the stratosphere and deposition in the oceans. Observations with the mobile IAP Fe lidar may for the first time have directly measured MSP in the middle atmosphere.

Metallic compounds in the MLT region are presumed to polymerise to meteoric smoke particles (MSP) [Hunten *et al.*, 1980; Kalashnikova *et al.*, 2000]. On the one hand, MSP act as a sink for all mesospheric metals, balancing the input of the meteoric source [Plane *et al.*, 2015]. Their formation is hence important to understand the morphology of the metal layers (e.g., see Section 2.3). On the other hand, MSP are thought to have important impacts not only on the MLT region but also on the atmosphere below and potentially even for the global climate system. It is widely assumed that MSP are the embryonic particles for heterogeneous nucleation of polar mesospheric clouds [e.g., Gumbel and Megner, 2009]. Their abundance or absence can hence influence the nucleation rate of ice particles (PMSE and NLC/PMC) in the MLT region. Furthermore, MSP are thought to interact with sulphuric and nitric acid in the stratosphere [Saunders *et al.*, 2012; Frankland *et al.*, 2015] and might hence also influence catalytic ozone depletion on polar stratospheric clouds. As mentioned in Section 7, MSP may even fertilise phytoplankton and hence have an impact on the biological activity and thus the CO_2 absorbing potential of the oceans [Johnson, 2001; Dhomse *et al.*, 2013].

To date, no direct observations of MSP with lidars were successful, as the particles are presumably smaller than 5 nm and their Mie signal is hence very weak and difficult to distinguish from the background radiation with ground-based or satellite-borne instruments. A method to detect the Mie signal of very small particles in the stratosphere and mesosphere was introduced by Viehl [2010] in a Diplomarbeit (German equivalent of a Master's thesis). Narrowband high power laser sources as operated in the mobile IAP Fe lidar can be used to scan the Mie profile of the MSP. A high resolute con-

focal Fabry-Perot interferometer (CFPI) with high finesse and a FWHM on the order of the expected Mie spectrum (~ 5 Mhz, i.e. 0.01 pm at 772 nm) can then be used to deconvolve the spectral components of the Mie scattering as well as the laser and the optical filter components from the retrieved signal. However, even small mechanical vibrations inherent to common lidar instruments or caused by sound waves or wind disturbances will derivate the CFPI's spectrum and require very fast active stabilisation. The necessary fast stabilisation was successfully demonstrated by Viehl [2010] using a distributed feedback (DFB) laser stabilised to a compact Rubidium saturation spectroscopy and the Pound-Drever-Hall technique [Drever et al., 1983]. The key for atmospheric MSP detection is to eliminate disturbances on the final detector, which can be achieved by employing a slanting passage through the CFPI and using a pickup mirror for the stabilising DFB laser, hence achieving a sufficient signal-to-noise ratio for the atmospheric signal [Viehl, 2010].

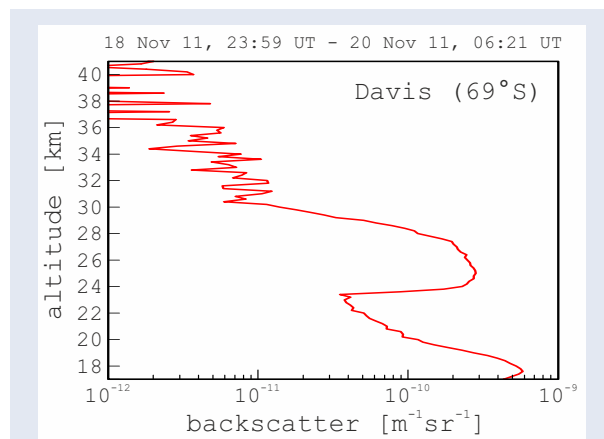


Figure 40: Aerosol measurements with the CFPI of the mobile IAP Fe lidar at Davis, Antarctica. Meteor smoke particles are thought to have been observed at an altitude of 24–30 km above the stratospheric Junge layer. Preliminary results. Contact author before usage of data. CC BY 4.0

An aerosol detection branch with a CFPI as described by Viehl [2010] was implemented in the detection bench of the mobile IAP Fe lidar in 2010. It has been in parallel operation during most measurements since that time, albeit mostly with reduced capability due to the optimisation of the laser cycle for MLT temperature measurements. Nevertheless, preliminary analysis of mesospheric and upper stratospheric aerosol data obtained with the system at Davis, Antarctica (69°S) indicate faint

but lasting aerosols originating at MLT altitudes.

The observed aerosols seem to be primarily created during autumn and descend towards summer. Figure 40 shows an example of measurements with the presumed MSP at altitudes between 24 km and 30 km. A particularity of the measurements of the example shown is that the continuous stratospheric Junge layer had dropped to below 24 km during the days around the observation, enabling to see the presumed MSP very clearly. These results are currently being confirmed and compared to 3D WACCM calculations of MSP creation and transport in cooperation with the School of Chemistry of the University of Leeds.

24 Comparison of Fe lidar and OH spectrometer temperature observations

Temperature measurements of the mobile IAP Fe lidar at Davis, Antarctica are compared to co-located OH(6-2) Czerny-Turner spectrometer measurements. The temporal evolution of the two temperature datasets is strikingly similar but shows a persistent temperature bias. The joint measurements with high precision open up the possibility to investigate the fundamental temperature retrieval of OH* temperature measurements.

Airglow emissions by excited hydroxyl (OH) atoms in the OH layer at around 86 km altitude can be used to observe MLT temperatures remotely. Ground-based spectrometers provide no altitude resolution but can determine temperatures during night-time or deep twilight conditions. These spectrometer measurements can be conducted continuously and have been performed for more than two decades, allowing trend analyses with high precision.

Measurements with the Davis Czerny-Turner spectrometer at the OH(6-2) band near 840 nm have been employed by French and Klekociuk [2011] to determine MLT temperature trends at Davis, Antarctica (69°S) between 1995 and 2011. That study found a solar cycle dependence of 4.8 ± 1.0 K/100 SFU and a long-term cooling trend of 1.2 ± 0.9 K/decade ($R^2=0.70$). Absolute OH temperature measurements require several assumptions about the emission altitude and the transition probabilities of the excited hydroxyl states. The observations at Davis

have been validated by comparison to satellite measurements [French and Mulligan \[2010\]](#) using transition probabilities by [Langhoff et al. \[1986\]](#). During the 2011 winter, both the Davis OH(6-2) Czerny-Turner spectrometer and the mobile IAP Fe lidar have obtained full seasonal coverage of MLT observations at the same location. The different operational principles cause a slightly different temporal coverage of the instruments: due to the warm-up process of up to 1 h and general instrument deterioration considerations, the mobile IAP Fe lidar is only ever switched on for measurement windows which are expected to last several hours. The passive OH spectrometer, however, also observes temperatures through thin cloud cover or during short periods of clear sky in otherwise cloudy tropospheric weather conditions. The mobile Fe lidar, on the other hand, can measure during full daylight. The OH spectrometer only measures during periods of darkness or deep twilight. These instrument differences cause a further and even larger deviation in observational hours in early and late winter, when the sun is not entirely below the horizon.

Figure 41 shows temperature observations by the Davis OH(6-2) Czerny-Turner spectrometer (orange) and the mobile IAP Fe lidar during the joint measurements in 2011. Lidar temperatures are calculated as a weighted composite at the altitudes of the OH layer. The mean vertical weighting profile (VERm) was taken from TIMED/SABER observations [\[French and Mulligan, 2010\]](#) and calculated for two cases, assuming a peak emission altitude at 85.6 km (green) and 84.5 km (blue), respectively. As can be expected from the winter state of the MLT, lidar temperatures are generally higher at lower altitudes. All temperatures shown are smoothed with a 14-day Hann window.

Two important features emerge from the instrument comparison in Figure 41. First, absolute temperature measurements show an average offset of around 9.2 K and 7.8 K when assuming peak emission altitudes at 85.6 km and 84.5 km, respectively. This bias is significant (error bars not shown). Second, temperature measurements from both instruments show a strikingly similar temporal evolution. When artificially shifting one of the temperature sets by 8 K (grey), similarities and differences can be investigated more easily. Deviations are largest at the beginning and end of winter when the periods of observation differ the most.

The strong similarity of the temporal evolution confirms the observations of the co-located instruments. The significant absolute bias, however, can only be explained by a systematic error in the temperature retrieval of at least one of the instruments.

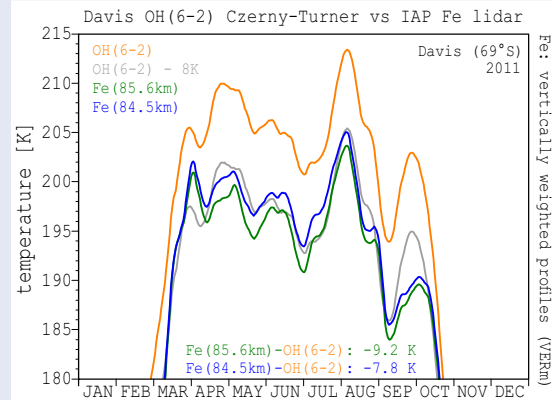


Figure 41: Temperature measurements by the Davis OH(6-2) Czerny-Turner spectrometer (orange) and the mobile IAP Fe lidar at Davis, Antarctica (69°S) during the 2011 winter. OH layer emissions are assumed to peak at around 86 km altitude. Lidar temperatures are calculated for mean OH layer altitude distributions taken from SABER observations (VERm) at around 85.6 km (green) and 84.5 km (blue). The offset between the datasets is significant (error bars not shown). The temperatures agree within the error bars when a bias of 8 K is subtracted (grey). OH(6-2) data courtesy of Dr W. John R. French, AAD. Preliminary results. Contact author before usage of data. CC BY 4.0

As described in Section 3, the mobile IAP lidar's temperature retrieval has been validated against other resonance lidars, as well as falling spheres, and can spectrally determine deviations from the LTE or other inconsistencies in the form of the resonance spectrum. Furthermore, if temperatures by the mobile IAP Fe lidar were to be offset by around -8 K to -10 K, temperatures during summer would no longer be in agreement with the observations of mesospheric ice particles. Indeed, PMSE have been observed exactly during the periods and at altitudes of the super-saturated regions shown in the left panel of Figure 36.

The temperature retrieval of the Davis OH(6-2) Czerny-Turner spectrometer has been compared to satellite observations by Aura(EOS)/MLS and TIMED/SABER. [French and Mulligan \[2010\]](#) find a systematic trend when comparing against SABER v1.07 data, and a warm bias of around 10 K of OH

temperatures compared to MLS v2.2. However, a comparison of Davis OH(6-2) temperatures with more recent SABER v2.0 and MLS v3.3 datasets shows further improved agreements: the previously reported temperature trend of SABER v1.07 is no longer observable in SABER v2.0, and absolute OH(6-2) temperatures now only have a positive bias of around 2 K compared to MLT v3.3 (*W. John R. French, AAD, personal communication*).

Both instruments, therefore, appear not only to be precise, but accurate in their temperature retrieval. However, as Section 19 briefly mentioned, both TIMED/SABER and Aura(EOS)/MLS temperature climatologies have been successfully used for a range of purposes, but also have limitations in their application due to the low vertical and temporal resolution. A warm temperature bias of OH(6-2) temperature therefore currently seems more likely than a negative temperature bias of the mobile IAP Fe lidar.

Indeed, results by *Noll et al.* [2015, 2016] suggest that OH(6-2) could show a positive temperature bias of more than 5 K due to incorrect Einstein coefficients employed by *Langhoff et al.* [1986] and others. Temperatures determined by the Davis OH(6-2) Czerny-Turner spectrometer could, therefore, be significantly lower when being recalculated using revised transition probabilities. The common volume measurements at Davis could be an experimental confirmation of a revised OH temperature retrieval, achieved by comparing a ground-based OH(6-2) spectrometer, not to a satellite, but a high-resolution resonance lidar.

Theoretical considerations by *Grygalashvily et al.* [2014] and recent observational results by *Teiser and von Savigny* [2016] for the Northern Hemisphere additionally suggest that the altitude of the OH layer may have previously been determined to high at polar latitudes. These results make a peak OH emission altitude of around 84.5 km or even lower likely during the polar winter.

These results and hypotheses need to be tested further. However, a detailed comparison of lidar and spectrometer data places important constraints to the uncertainties of the existing studies. The further analysis of Fe lidar and OH spectrometer data could, therefore, have a very significant influence on the calculation of all temperatures derived from OH* emissions and the trends derived from their analyses.

25 Outlook

Measurements with the mobile IAP Fe lidar continue in the Arctic at ALOMAR (69°N). Further analyses of the obtained datasets with co-located instruments may allow insights into ion-molecule chemistry and sporadic (Fe_S and E_S) layers, the magnetosphere, gravity wave activity, and the mixing of trace species. Attempts are being undertaken to detect additional metallic species such as nickel (Ni) or aluminium(II) oxide (AlO), as well as helium (He) in the upper atmosphere. Ongoing technical developments aim to simplify measurement operations further and enable nearly fully automated remote measurements. A newly developed technique will in the near future allow improved lidar wind observations.

The dataset obtained by the mobile IAP lidar is not yet fully analysed, and the publication of results is still ongoing. Several preliminary results of analyses have been briefly described in Sections 19 to 24. Moreover, the datasets of temperatures, Fe densities, and aerosols in the middle atmosphere are still growing as the measurements of the mobile IAP Fe lidar are continuing at ALOMAR (69°N). As section 4 noted, a host of instruments probing various aspects of the MLT region are operated at Davis and ALOMAR. The analyses of the joint datasets will be subject to future studies.

Comparisons with ionosonde, magnetometer, and riometer data

The observations at Davis have shown a very regular occurrence of sporadic Fe layers (Fe_S) at specific local solar times around 2 LST to 3 LST. Fe_S are thought to be composed of ionic species (Fe^+ , Mg^+) and known to be correlated to sporadic E layers (E_S) *MacDougall et al.* [2000]; *Delgado et al.* [2012, e.g.,]. These observations underline the high importance of ion-molecule chemistry for the metal layers. Atmospheric tides further cause a strong vertical coupling of the neutral atmosphere and the ionosphere [*England et al., 2006*]. Lidar observations of mesospheric metals can, therefore, provide insights into the physics and chemistry of E_S .

Measurements of E_S as well as electron densities by an ionosonde are available at Davis. A detailed comparison with Fe lidar data might provide fur-

ther insight into the dynamics of the sporadic layers. Additionally, co-located measurements with a magnetometer and a riometer (SHIRE) at Davis allow the analysis of the geomagnetic influence on the metal layers. Such studies may provide further insights into the ion-molecule chemistry and transport processes, particularly in the polar regions.

Measurement of further species

During the past decades, only a handful of metals and other trace species in the MLT have been successfully probed by lidars on a continuous basis (Fe, Na, K, and Ca/Ca⁺). As briefly described in Section 2.4, this is mainly due to a lack of suitable transitions. However, it may be possible to probe some additional species. *Collins et al. [2015]* recently reported first measurements of the mesospheric Ni layer. However, these measurements have not yet been extended to seasonal scales or reproduced by other groups. Additionally, aluminium(II) oxide (AlO) and helium (He) should also have sufficiently large backscatter coefficients at reasonably high number densities. It might be possible to probe the species by ground-based lidars in the near future.

The resonance lines of AlO and Ni are outside the spectral range of the mobile IAP Fe lidar's alexandrite laser but can be probed with dye lasers. Such observations are interesting for several reasons. First, such analyses allow studying the chemistry of these species. Second, as the knowledge about further metal layers places additional constraints on 3D atmospheric chemistry models, it can improve the overall representation of the MLT. Third, additional metals observations can improve the analysis of the meteoric ablation processes and cosmic dust evolution. Observations of AlO would additionally allow very good estimates of atomic O, which is crucial to the chemistry of the MLT.

Furthermore, the observation of He could allow probing temperatures up to very high altitudes in the thermosphere. Continuous improvements of mobile alexandrite lidars will soon allow the simultaneous measurement of 2–3 species (Fe, K or/and He) as well as an improved detectability of aerosol particles in the mesosphere and stratosphere.

Technical improvements

Continuous technical developments aim at further simplifying the operation of the mobile IAP Fe lidar.

With an increasingly higher degree of automation, more measurement hours can be obtained. Additional improvements are performed to increase the reliability of all components, including the infrastructure components, to ensure little downtime and prolonged maintenance intervals. These advantages are particularly important when operating at remote locations.

The recent development of a new diode-pumped alexandrite laser will allow very small, autonomously operating lidar systems capable of probing the MLT region in four dimensions. Such instruments not only allow improved resolution and coverage of the metal layers but also allow to discern chemical and transport processes and directly probe the diffusion of ablating meteors.

Two important aspects of the successful operation of the mobile IAP Fe lidar are the real-time assessment of the laser spectrum and the ultra-fast data compression of the retrieved signal, allowing an instant feedback of the atmospheric signal to the laser. Both techniques have been described in a patent by *Höffner [2015]*.

A novel method to determine wind speeds in the middle atmosphere with lidars has recently been submitted as a patent by *Höffner et al. [2016]*, currently pending in Germany and to be submitted in Europe and the USA. The method will allow significantly improved lidar measurement of winds from the troposphere to the mesosphere due to a drastically increased SNR compared to other techniques. These examples show the technical spin-off capability of basic atmospheric research.

Ongoing measurements

Measurements with the mobile IAP Fe lidar are currently continuing at ALOMAR (69°N). The temperature climatology will complement previous results by *Lübken [1999]* obtained at the same location. Additionally, the co-located instruments at ALOMAR, as well as the sounding rocket facilities at the ASC, will allow an even more detailed analysis of various atmospheric properties. The upcoming measurement campaigns and analyses may well provide further unique insights into the physics and chemistry of the MLT and its role in the global atmosphere.



Appendices

Appendix A: Abbreviations	57
Appendix B: Rate coefficients	59
Appendix C: Measurement statistics	60
Appendix D: Copyright licenses	61

Appendix A: Abbreviations

AAD	Australian Antarctic Division
AIM	Aeronomy of Ice in the Mesosphere
ALOMAR	Arctic Lidar Observatory for Middle Atmosphere Research
ANARE	Australian National Antarctic Research Expeditions
APD	Avalanche Photodiode
ASC	Andøya Space Center
B3LYP	Becke Three-Parameter Lee-Yang-Parr
BMBF	Bundesministerium für Bildung und Forschung
BOM	Bureau of Meteorology (Australia)
CAM	Coulomb-Attenuated Method
CFPI	Confocal Fabry-Perot Interferometer
CIRA	COSPAR International Reference Atmosphere
CODITA	Cosmic Dust in the Terrestrial Atmosphere
COSPAR	Committee on Space Research
DFB	Distributed Feedback
DFG	Deutsche Forschungsgemeinschaft
DFT	Density Functional Theory
ECMWF	European Centre for Medium-Range Weather Forecasts
EOS	Earth Observing System
ERC	European Research Council
ESM	Elevated Summer Mesopause
FOV	Field of View
FWHM	Full Width at Half Maximum
GOMOS	Global Ozone Monitoring by Occultation of Stars
GPS	Global Positioning System
GSWM	Global Scale Wave Model
GWPED	Gravity Wave Potential Energy Density
HF	Hartree-Fock
HF	High Frequency
IAP	Leibniz-Institute of Atmospheric Physics at the University of Rostock
IR	Infrared
KMCM	Kühlungsborn Mechanistic General Circulation Model
LBO	Lithium Triborate
LIDAR	Light Detection and Ranging
LIMA	Leibniz-Institute Middle Atmosphere Model
LST	Local Solar Time
LT	Local Time
LTE	Local Thermodynamic Equilibrium
MAARSY	Middle Atmosphere ALOMAR Radar System
MaTMeLT	Mixing and Transport in the Mesosphere/Lower Thermosphere
MERRA	Modern-Era Retrospective Analysis for Research and Application
MF	Medium Frequency
MLS	Microwave Limb Sounder
MLT	Mesosphere-Lower Thermosphere
MST	Mesosphere, Stratosphere, Troposphere
MSP	Meteor Smoke Particles
NASA	National Aeronautics and Space Administration (US)
NCAS	National Centre for Atmospheric Science (UK)
NCEP	National Center for Environmental Prediction (US)

NH	Northern Hemisphere
NLC	Noctilucent Cloud
NOAA	National Oceanic and Atmospheric Administration (US)
NRL	Naval Research Laboratory (US)
NRLMSISE	NRL Mass Spectrometer and Incoherent Scatter Radar Extended
OSIRIS	Optical Spectrograph and Infrared Imager System
PACOG	Processes and Climatology of Gravity Waves
PMC	Polar Mesospheric Cloud
PMSE	Polar Mesospheric Summer Echoes
PMT	Photomultiplier Tube
RMR	Rayleigh-Mie-Raman
RMS	Root Mean Square
RSV	Research and Supply Vessel
ROMIC	Role of the Middle Atmosphere in Climate
SABER	Sounding of the Atmosphere Using Broadband Emission Radiometry
SCIAMACHY	Scanning Imaging Absorption Spectrometer for Atmospheric Chartography
SFU	Solar Flux Unit
SH	Southern Hemisphere
SHG	Second Harmonic Generation
SHIRE	Southern Hemisphere Imaging Radiometer Experiment
SNR	Signal-to-Noise Ratio
SOFIE	Solar Occultation for Ice Experiment
SPVBD	Stratospheric Polar Vortex Breakdown
TIMA	Trends in the Middle Atmosphere
TIMED	Thermosphere Ionosphere Mesosphere Energetics and Dynamics
UT	Universal Time
UV	Ultra-Violet
TD	Time Dependent
VHF	Very High Frequency
WACCM	Whole Atmosphere Community Climate Model

Appendix B: Rate coefficients

reaction	rate coefficient ^a	source	
<i>Neutral Chemistry</i>			
R1	$\text{Fe} + \text{O}_3 \longrightarrow \text{FeO} + \text{O}_2$	$2.9 \times 10^{-10} \exp(-174/T)$	Helmer et al. [1998]
R2	$\text{FeO} + \text{O} \longrightarrow \text{Fe} + \text{O}_2$	$4.6 \times 10^{-10} \exp(-350/T)$	Self and Plane [2003]
R3	$\text{FeO} + \text{O}_3 \longrightarrow \text{FeO}_2 + \text{O}_2$	$3.0 \times 10^{-10} \exp(-177/T)$	Rollason and Plane [2000]
R4	$\text{FeO} + \text{O}_2 + \text{M} \longrightarrow \text{FeO}_3 + \text{M}$	$4.4 \times 10^{-30} \exp(T/200)^{0.606}$	Rollason and Plane [2000]
R5	$\text{FeO}_2 + \text{O} \longrightarrow \text{FeO} + \text{O}_2$	$1.4 \times 10^{-10} \exp(-580/T)$	Self and Plane [2003]
R6	$\text{FeO}_2 + \text{O}_3 \longrightarrow \text{FeO}_3 + \text{O}_2$	$4.4 \times 10^{-10} \exp(-170/T)$	Self and Plane [2003]
R7	$\text{FeO}_3 + \text{O} \longrightarrow \text{FeO}_2 + \text{O}_2$	$2.3 \times 10^{-10} \exp(-2310/T)$	Self and Plane [2003]
R8	$\text{FeO}_3 + \text{H}_2\text{O} \longrightarrow \text{Fe}(\text{OH})_2 + \text{O}_2$	5×10^{-12}	Self and Plane [2003]
R9	$\text{FeO} + \text{H}_2\text{O} + \text{M} \longrightarrow \text{Fe}(\text{OH})_2 + \text{M}$	$5 \times 10^{-28} \exp(200/T)^{1.13}$	Rollason and Plane [2000]
R10	$\text{Fe}(\text{OH})_2 + \text{H} \longrightarrow \text{FeOH} + \text{O}_2$	$3.3 \times 10^{-10} \exp(-302/T)$	Jensen and Jones [1974]
R11	$\text{FeO}_3 + \text{H} \longrightarrow \text{FeOH} + \text{O}_2$	$3 \times 10^{-10} \exp(-796/T)$	Plane et al. [1999]
R12a	$\text{FeOH} + \text{H} \longrightarrow \text{Fe} + \text{H}_2\text{O}$	$2 \times 10^{-12} \exp(-600/T)$	Viehl et al. [2016a]
R12b	$\text{FeOH} + \text{H} \longrightarrow \text{FeO} + \text{H}_2$	$6 \times 10^{-11} \exp(-1200/T)$	Viehl et al. [2016a]
R13	$\text{FeOH} + \text{FeOH} \longrightarrow (\text{FeOH})_2$	9.0×10^{-10}	Feng et al. [2013]
R14	$\text{Fe} \longrightarrow \text{FePMC}$	$4.9 \times T^{0.5} \times \text{VSA}_{\text{PMC}}^b$	Feng et al. [2013]
R15	$\text{FeOH} \longrightarrow \text{FePMC}$	$4.3 \times T^{0.5} \times \text{VSA}_{\text{PMC}}$	Feng et al. [2013]
R16	$\text{Fe}(\text{OH})_2 \longrightarrow \text{FePMC}$	$3.8 \times T^{0.5} \times \text{VSA}_{\text{PMC}}$	Feng et al. [2013]
R17	$\text{FeO}_3 \longrightarrow \text{FePMC}$	$3.6 \times T^{0.5} \times \text{VSA}_{\text{PMC}}$	Feng et al. [2013]
<i>Ion-Molecule Chemistry</i>			
R18	$\text{Fe} + \text{NO}^+ \longrightarrow \text{Fe}^+ + \text{NO}$	9.2×10^{-10}	Rutherford and Vroom [1972]
R19	$\text{Fe} + \text{O}_2^+ \longrightarrow \text{Fe}^+ + \text{O}_2$	1.1×10^{-9}	Rutherford and Vroom [1972]
R20	$\text{Fe}^+ \longrightarrow \text{FePMC}$	$4.9 \times T^{0.5} \times \text{VSA}_{\text{PMC}}$	Feng et al. [2013]
R21	$\text{Fe}^+ + \text{O}_3 \longrightarrow \text{FeO}^+ + \text{O}_2$	$7.6 \times 10^{-10} \exp(-241/T)$	Rollason and Plane [2000]
R22	$\text{FeO}^+ + \text{O} \longrightarrow \text{Fe}^+ + \text{O}_2$	3.0×10^{-11}	Woodcock et al. [2006]
R23	$\text{Fe}^+ + \text{N}_2 + \text{M} \longrightarrow \text{Fe}^+ \cdot \text{N}_2$	$4.1 \times 10^{-30} \exp(T/300)^{-1.52}$	Vondrak et al. [2006]
R24	$\text{Fe}^+ \cdot \text{N}_2 + \text{O} \longrightarrow \text{FeO}^+ + \text{N}_2$	5×10^{-11}	Rollason and Plane [1998]
R25	$\text{FeO}_2^+ + \text{O} \longrightarrow \text{FeO}^+ + \text{O}_2$	5×10^{-11}	Rollason and Plane [1998]
R26	$\text{Fe}^+ + \text{O}_2 + \text{M} \longrightarrow \text{FeO}_2^+ + \text{M}$	$8.3 \times 10^{-30} \exp(T/300)^{-1.86}$	Vondrak et al. [2006]
R29	$\text{FeO}^+ + \text{e}^- \longrightarrow \text{Fe} + \text{O}$	5.5×10^{-7}	Bones et al. [2015]
R30	$\text{FeO}_2^+ + \text{e}^- \longrightarrow \text{Fe} + \text{O}_2$	$3 \times 10^{-7} \exp(T/200)^{0.5}$	Plane et al. [1999]
R31	$\text{Fe}^+ + \text{e}^- \longrightarrow \text{Fe} + h\nu$	$6.5 \times 10^{-12} \exp(T/300)^{0.51}$	Nahar et al. [1997]
<i>Photochemical Reactions</i>			
R32	$\text{FeOH} + h\nu \longrightarrow \text{Fe} + \text{OH}$	6×10^{-3}	Viehl et al. [2016a]
R33	$\text{Fe} + h\nu \longrightarrow \text{Fe}^+ + \text{e}^-$	5×10^{-7}	Bautista et al. [1998]

Table 1: Important reaction rate and photochemical coefficients of Fe containing species in the MLT region following Plane et al. [2015]. ^aUnits: unimolecular [s^{-1}], bimolecular [$\text{cm}^3 \text{ molecule}^{-1} \text{ s}^{-1}$], termolecular [$\text{cm}^6 \text{ molecule}^{-2} \text{ s}^{-1}$]. ^bVolumetric Surface Area of the Polar Mesospheric Cloud.

Appendix C: Measurement statistics

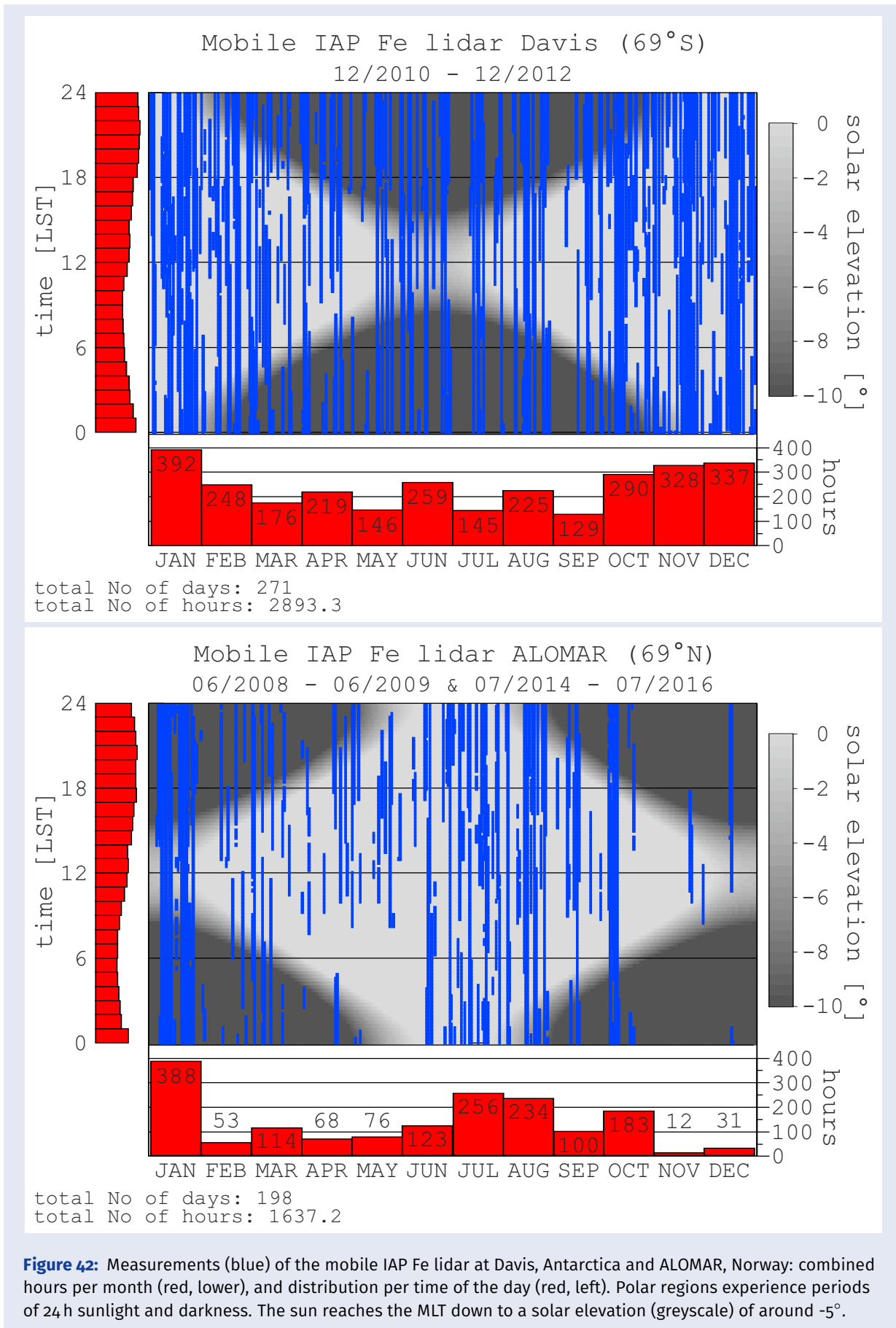


Figure 42: Measurements (blue) of the mobile IAP Fe lidar at Davis, Antarctica and ALOMAR, Norway: combined hours per month (red, lower), and distribution per time of the day (red, left). Polar regions experience periods of 24h sunlight and darkness. The sun reaches the MLT down to a solar elevation (greyscale) of around -5° .

Appendix D: Copyright licenses

This thesis contains copyrighted material which is reprinted with permission under the licences in the following lists in Tables 2 and 3. All rights reserved by the respective licenced content publishers or authors. Commercial redistribution of the entire thesis or the copyrighted material not permitted. Please refer to the original copyright holder for personal copies of the published manuscripts or reuse of the figures.

The non-commercial publication of this thesis (print and electronic) is permitted for fair-use under the licences in Tables 2 and 3 via the institutional repositories, archives, and websites of the University of Rostock, Germany, the Leibniz-Institute of Atmospheric Physics at the University of Rostock in Kühlungsborn, Germany, and associated organisations. In accordance with §5 of the “*Ordnung über die Bereitstellung von Pflichtexemplaren im Rahmen von Promotions- und Habilitationsverfahren an der Universität Rostock (Pflichtexemplarordnung)*” in the version of 18 February 2008 and as detailed in the “*Guidelines for the implementation of a doctoral degree procedure at the Faculty of Mathematics and Natural Sciences*” at the University of Rostock, Germany, this specifically includes the University Library of Rostock as well as the German National Library in Frankfurt am Main, Germany, and Leipzig, Germany.

Figure	Licensed content publisher and/or author(s)	Licence, year	Licence No/link
Fig. 1, Fig. 5, Fig. 8, Fig. 2	Timo P. Viehl American Chemical Society, Plane et al. [2015]	CC BY 4.0, 2016 ACS AuthorChoice, 2015	
Fig. 3, Fig. 7 Fig. 4	Timo P. Viehl Copernicus Publications, Vondrak et al. [2008]	CC BY-NC 4.0, 2012 CC BY 3.0, 2008	
Fig. 6	John Wiley & Sons Inc., Feng et al. [2013]	CC BY 3.0, 2013	
Fig. 9 (left), Fig. 12	Dr Josef Höffner	©print & electronic, 2016	
Fig. 9 (right), Fig. 10 Fig. 11	Timo P. Viehl Commonwealth of Australia, Australian Antarctic Data Centre	CC BY 4.0, 2016 CC BY 3.0, 2009	
Fig. 13, Fig. 14, Fig. 15, Fig. 16 Fig. 17	Raimund Wörl John Wiley & Sons, Inc. Viehl et al. [2016a]	©print & electronic, 2015 ©print & electronic, 2016	3811810557417
Fig. 18 Fig. 19, Fig. 20, Fig. 21 Fig. 22	Timo P. Viehl Elsevier Ltd., Viehl et al. [2015] Elsevier Ltd., Viehl et al. [2016b]	CC BY 4.0, 2016 ©print & electronic, 2015 ©print & electronic, 2016	 3811811217212 3811811335652
Fig. 23, Fig. 24, Fig. 25	John Wiley & Sons, Inc. Lübken et al. [2011]	©print & electronic, 2011	3811810418613
Fig. 26, Fig. 27	John Wiley & Sons, Inc. Feng et al. [2015]	CC BY 4.0, 2013	
Fig. 28, Fig. 29, Fig. 30	John Wiley & Sons, Inc. Kaifler et al. [2015]	©print & electronic, 2015	3811810781035
Fig. 31, Fig. 32 Fig. 33, Fig. 34, Fig. 35, Fig. 36 (right)	Elsevier Ltd., Morris et al. [2012] John Wiley & Sons, Inc. Lübken et al. [2015]	©print & electronic, 2012 ©print & electronic, 2015	3811820000346 3811800959462
Fig. 36 (left)	John Wiley & Sons, Inc. Lübken et al. [2014]	©print & electronic, 2014	3811811028998
Fig. 37, Fig. 38, Fig. 39, Fig. 40, Fig. 41, Fig. 42	Timo P. Viehl	CC BY 4.0, 2016	

Table 2: Copyright licences and licence numbers for the reproduction of the figures in this thesis.

Manuscript	Licensed content publisher	License, year	License No/link
Viehl et al. [2016a]	<i>John Wiley & Sons, Inc.</i>	©print & electronic, 2016	3811800826840
Viehl et al. [2015]	<i>Elsevier Ltd.</i>	©print & electronic, 2015	3811801433629
Viehl et al. [2016b]	<i>Elsevier Ltd.</i>	©print & electronic, 2016	3812390399412
Lübken et al. [2011]	<i>John Wiley & Sons, Inc.</i>	©print & electronic, 2011	3811810278605
Feng et al. [2015]	<i>John Wiley & Sons, Inc.</i>	CC BY 4.0, 2015	
Morris et al. [2012]	<i>Elsevier Ltd.</i>	©print & electronic, 2012	3811801347630
Lübken et al. [2014]	<i>John Wiley & Sons, Inc.</i>	©print & electronic, 2014	3811800467340
Kaifler et al. [2015]	<i>John Wiley & Sons, Inc.</i>	©print & electronic, 2015	3811801162545
Lübken et al. [2015]	<i>John Wiley & Sons, Inc.</i>	©print & electronic, 2015	3811800959462

Table 3: Copyright licences and licence numbers for the reproduction of the full manuscripts of the articles reprinted on pages 65 to 141 in this thesis.



Manuscripts

Viehl et al. [2016a] <i>Geophys. Res. Lett.</i> , 43, 1373–1381	65
Viehl et al. [2015] <i>J. Atmos. Solar-Terr. Phys.</i> , 127, 97–102	75
Viehl et al. [2016b] <i>J. Atmos. Solar-Terr. Phys.</i> , 142, 150–151	81
Lübken et al. [2011] <i>Geophys. Res. Lett.</i> , 38, L24806	83
Feng et al. [2015] <i>Geophys. Res. Lett.</i> , 42, 3619–3626	87
Kaifler et al. [2015] <i>J. Geophys. Res.</i> , 120, 4506–4521	95
Morris et al. [2012] <i>J. Atmos. Solar-Terr. Phys.</i> , 89, 54–61	111
Lübken et al. [2014] <i>Geophys. Res. Lett.</i> , 41, 5233–5238	119
Lübken et al. [2015] <i>J. Geophys. Res.</i> , 120, 12,394–12,409	125

RESEARCH LETTER

10.1002/2015GL067241

Key Points:

- Diurnal variation of the Fe layer bottomsides now explained
- Combination of approaches to determine an important photolysis rate for the first time
- Implications for the Fe speciation in meteoric smoke particles

Correspondence to:

T. P. Viehl,
viehl@iap-kborn.de

Citation:

Viehl, T. P., J. M. C. Plane, W. Feng, and J. Höffner (2016), The photolysis of FeOH and its effect on the bottomsides of the mesospheric Fe layer, *Geophys. Res. Lett.*, *43*, 1373–1381, doi:10.1002/2015GL067241.

Received 14 DEC 2015

Accepted 21 JAN 2016

Accepted article online 28 JAN 2016

Published online 11 FEB 2016

©2016. American Geophysical Union.
All Rights Reserved.

The photolysis of FeOH and its effect on the bottomsides of the mesospheric Fe layer

T. P. Viehl¹, J. M. C. Plane², W. Feng^{2,3}, and J. Höffner¹

¹Leibniz-Institute of Atmospheric Physics, University of Rostock, Kühlungsborn, Germany, ²School of Chemistry, University of Leeds, Leeds, UK, ³National Centre for Atmospheric Science, School of Earth and Environment, University of Leeds, Leeds, UK

Abstract Metal layers in the upper mesosphere and lower thermosphere are created through meteoric ablation. They are important for understanding the temperature structure, dynamics, and chemistry of this atmospheric region. Recent lidar observations have shown a regular downward extension of the Fe layer bottomsides which correlates with solar radiation. In this study we combine lidar observations, quantum chemical calculations, and model simulations to show that this bottomsides extension is primarily caused by photolysis of FeOH. We determine the photolysis rate to be $J(\text{FeOH}) = (6 \pm 3) \times 10^{-3} \text{ s}^{-1}$. We also show that the reaction $\text{FeOH} + \text{H} \rightarrow \text{FeO} + \text{H}_2$ is slower at mesospheric temperatures than previous estimates. With these updated rate coefficients, we are able to significantly improve the modeling of the Fe layer bottomsides. The calculations further show the nearly complete depletion of FeOH during sunlit periods. This may have implications for cloud nuclei in the middle atmosphere.

1. Introduction

Layers of metal atoms are created in the region of the upper mesosphere and lower thermosphere (MLT, ~70–110 km) through meteoric ablation. These layers are important for understanding the temperature structure dynamics and chemistry of this atmospheric region [e.g., Lübken *et al.*, 2015; Feng *et al.*, 2015; Yu *et al.*, 2012], the influx of cosmic material [e.g., Plane, 2012; Gardner *et al.*, 2014; Huang *et al.*, 2015], and the occurrence of thermospheric and sporadic metal layers and their relation to sporadic *E* layers which can influence radio wave propagation [e.g., Chu *et al.*, 2011; Delgado *et al.*, 2012]. Furthermore, meteoric metals are the source of meteoric smoke particles (MSPs) which most likely act as nuclei for ice particles in the mesosphere [e.g., Gumbel and Megner, 2009; Megner and Gumbel, 2009] and may also interact with sulphuric and nitric acid in the stratosphere [Saunders *et al.*, 2012; Frankland *et al.*, 2015]. A recent review on the chemistry of metals in the MLT region summarizes the current understanding and highlights open questions [Plane *et al.*, 2015]. It shows the importance of understanding all chemical reactions, the metals and their molecular species undergo, so that atmospheric chemistry models can correctly describe the dynamical behavior of the metal layers to give insights into some of the topics mentioned above. Laboratory studies have provided a broad insight into many of the important reactions dominating the MLT metal layers. However, some important chemical reactions with metal-containing species do not have a suitable electronic transition for probing by laser-induced fluorescence and could so far not be investigated directly.

The atomic Fe layer at polar latitudes has a mean centroid altitude of around 88 km. Recent lidar observations at polar latitudes show a downward extension of the layer below 80 km during sunlit periods [Yu *et al.*, 2012]. Self and Plane [2003] and Plane [2003] have shown that FeOH should be the dominant reservoir for atomic Fe below 95 km. As Plane *et al.* [1999] have illustrated, one way to dissociate FeOH at sunrise is via reaction with atomic H which is produced by photolysis of H₂O in sunlit periods. However, during nighttime the concentration of this radical decreases rapidly below ~82 km, so that FeOH becomes a stable reservoir for Fe. Within the current understanding, atmospheric chemistry models such as Whole Atmosphere Chemistry Climate Model (WACCM)-Fe [Feng *et al.*, 2013] have so far been unable to correctly reproduce the bottomsides extension of the Fe layer. Here we present a study combining atmospheric lidar observations, quantum chemical calculations, and atmospheric modeling to derive the photolysis rate of FeOH, $J(\text{FeOH})$, which so far has not been measured. We show that only the direct photolysis of FeOH can be fast enough to explain the bottomsides

extension of the mesospheric Fe layer at sunrise. The combination of methods described here also allows us to place upper limits to the rate coefficients under mesospheric conditions for the reactions



2. Atmospheric Observations

2.1. Instrument and Data Set

The Leibniz-Institute of Atmospheric Physics operates a mobile Fe lidar based on a frequency-doubled alexandrite laser scanning the Doppler broadened Fe resonance line at 386 nm [von Zahn and Höffner, 1996; Höffner and Lautenbach, 2009]. The system is capable of nearly background free single photon detection and can determine mesospheric Fe densities in full daylight. Typical measurement uncertainties are on the order of 2–5% at 1 km resolution and 15 min integration.

The Fe lidar was set up at Davis, Antarctica (68°34'S, 77°58'E), in 2010 and was in operation from 15 December 2010 until 31 December 2012 [e.g., Lübken et al., 2011; Viehl et al., 2015; Lübken et al., 2015]. The data set obtained in Antarctica includes 2900 h of Fe density measurements. In the years 2008–2009 and since July 2014, the system has been in operation at the Arctic Lidar Observatory for Middle Atmosphere Research (ALOMAR) on the Norwegian Island of Andøya (69°16'N, 16°00'E). The observations in the Arctic have so far produced more than 1200 h of Fe density measurements.

2.2. Observation and Analysis of the Fe Layer Bottomside

Figure 1 shows two examples of mesospheric Fe layer observations in the summer of the Southern Hemisphere and the winter of the Northern Hemisphere. The pronounced change in the Fe layer below 80–85 km is regularly observed in both hemispheres and all seasons whenever the solar elevation passes a critical level around -5° ; i.e., the MLT experiences sunrise or sunset. Yu et al. [2012] investigated the diurnal behavior of the mesospheric Fe layer at McMurdo, Antarctica (78°), and defined the “bottomside” as the lower 300 cm^{-3} contour. That study analyzed the time-dependent altitude change $\frac{\Delta z}{\Delta t}$ of the defined contour and found a dependence on the time of the season, caused by the change of solar elevation.

In this study, we analyze the rate of change of Fe density, $\frac{\Delta[\text{Fe}]}{\Delta t}$, over an altitude interval of 1 km, thereby quantifying the rate of increase of Fe at each altitude's time of apparent sunrise. The rate of increase is described by direct photolysis ($\text{FeOH} + h\nu$) and chemical reactions (1a) and (1b) producing Fe. We note that although reaction channel (1b) produces FeO, this will mostly be reduced to Fe by subsequent reaction of FeO with atomic O in the sunlit MLT. Further reactions cannot contribute significantly, as other reservoirs are less abundant by 2–4 orders of magnitude [Feng et al., 2013] and additional reaction pathways from FeOH to Fe are not known. As a first approximation, the time-dependent Fe concentration $[\text{Fe}]_t$ produced by photolysis of FeOH is given by

$$[\text{Fe}]_t = [\text{FeOH}]_0 (1 - \exp(-Jt)) \quad (2)$$

where $J = J(\text{FeOH})$ is the photolysis rate of FeOH and $[\text{FeOH}]_0$ is the concentration just before sunrise. Since the resulting Fe will be oxidized via a sequence of reactions involving O_3 , O_2 , and H_2O to reform FeOH [Plane et al., 2015], the observed rate of increase of Fe at sunrise provides a lower limit to $J(\text{FeOH})$.

Figure 2 shows an example of a single day where we have analyzed the rate of increase at sunrise. Figure 2a shows the bottomside extension between 5 and 9 local solar time (LST). The main Fe layer with densities higher than 6000 cm^{-3} is observed above about 82 km. The bottomside extension of the Fe layer builds up below 80 km from 7 LST, extending down to 70 km by 8 LST. The cutoff for Fe densities in Figure 2a is 100 cm^{-3} . Figure 2b shows the analysis of a single altitude. Densities at 76 km are below the cutoff during the night and quickly increase at sunrise. The time to reach $[\text{Fe}]_{t1/2} = 0.5 \times [\text{Fe}]_{t\text{max}}$ can be used to determine a lower limit for $J(\text{FeOH})$ when setting $[\text{FeOH}]_0 = [\text{Fe}]_{t\text{max}}$ in equation (2), assuming a full conversion of FeOH to Fe.

We have analyzed all available cases of the bottomside extension at various altitudes for both hemispheres (Davis, 69°S and ALOMAR, 69°N). We averaged the photolysis coefficients determined using equation (2) for

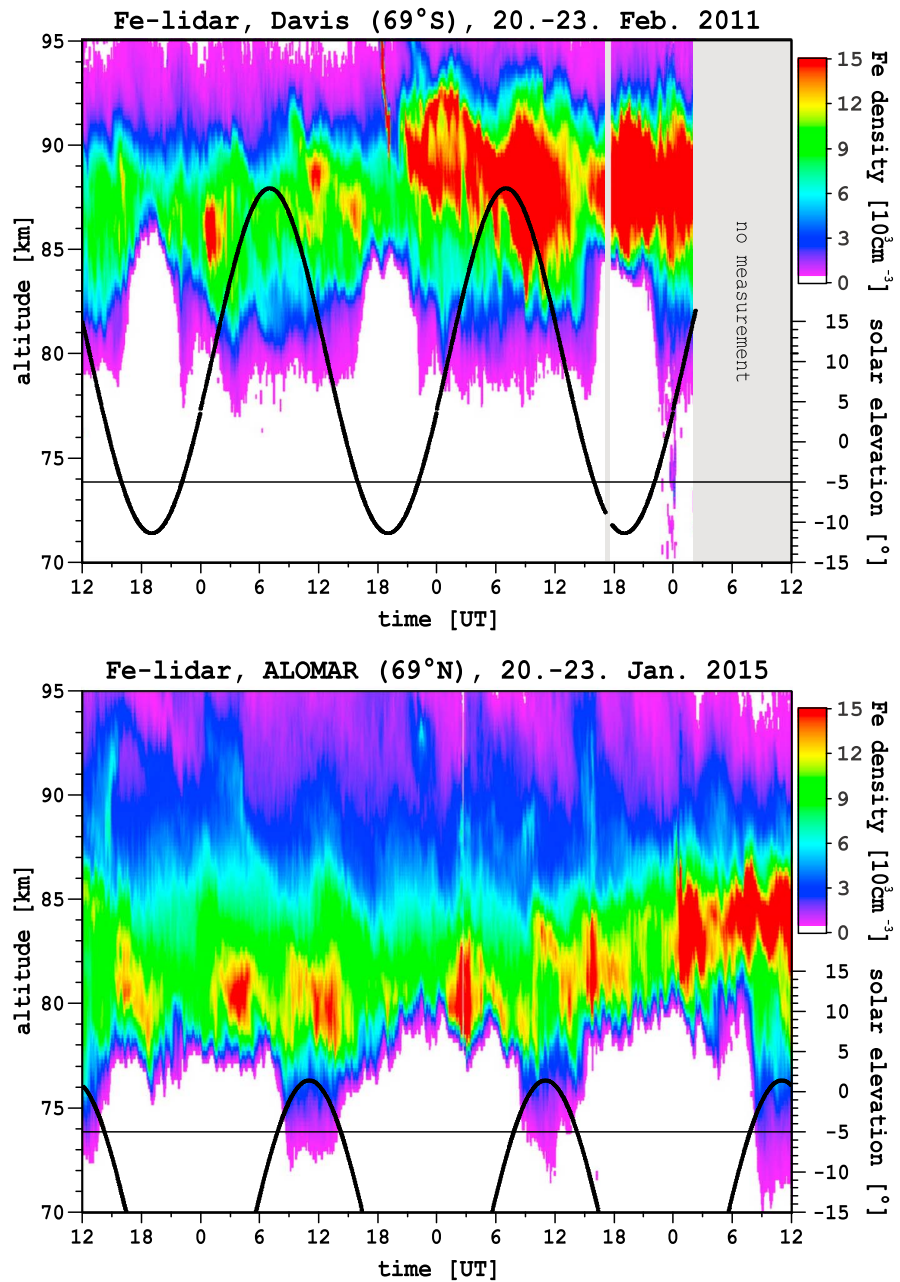


Figure 1. The mesospheric Fe layer at (top) Davis, Antarctica (69°S), and (bottom) ALOMAR, Norway (69°N) during three consecutive cycles of sunset and sunrise. An extension of the metal layer's bottomside is observed whenever sunlight reaches the MLT region.

all days and altitudes to remove the distortions caused by gravity waves (which are observable in Figure 1). The difference between the hemispheres is much smaller than the variability given as the standard deviation. The combined average first-order coefficient observed by lidar is $(1.2 \pm 0.4) \times 10^{-3} \text{ s}^{-1}$. We will show that this corresponds to a photolysis coefficient, setting a lower limit to $J(\text{FeOH})$.

3. Theoretical Considerations

To separate the influence of the photolysis and the reactions of FeOH with H and to compare with the observed rate of increase, we have performed quantum chemical calculations and revisited previous laboratory studies.

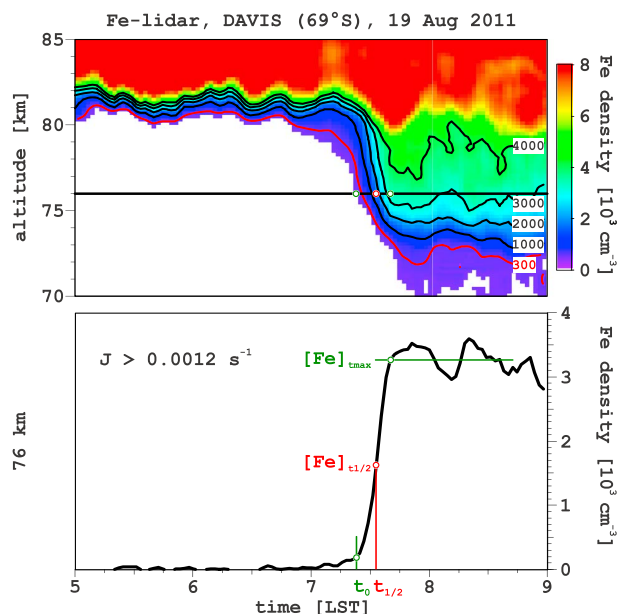


Figure 2. The rate of increase of Fe at sunrise is analyzed at different altitudes for all available days of lidar observations in the Arctic and Antarctica. Analysis of all available days yields a mean rate of $(1.2 \pm 0.4) \times 10^{-3} \text{ s}^{-1}$, which is a lower limit to $J(\text{FeOH})$ because of recycling of Fe to FeOH (see text). Of the available reactions, only the direct photolysis of FeOH can be fast enough to explain such a rapid increase.

3.1. Photolysis of FeOH

To calculate the absorption cross section of FeOH, the molecular geometry was first optimized using the range-separated CAM-B3LYP functional [Yanai *et al.*, 2004] and the 6-311+g(2d,p) basis set in the Gaussian 09 suite of programs [Frisch *et al.*, 2009]. The equilibrium structure of the ground state (X^6A') is bent with $r_e(\text{Fe-O}) = 1.793 \text{ \AA}$, $r_e(\text{O-H}) = 0.957 \text{ \AA}$, and $\angle_e(\text{Fe-O-H}) = 142.0^\circ$. The energies and transition oscillator strengths for vertical transitions to the first 30 excited states were then computed using the time-dependent (TD) density functional method [Scalmani *et al.*, 2006]. The long-range correction in the TD/CAM-B3LYP functional makes it suitable for modeling electron excitations to high-lying orbitals.

Figure 3 illustrates the calculated photolysis cross section as a function of wavelength ($\sigma(\lambda)$) for FeOH. The bond energy of FeOH at 0 K is $323 \pm 16 \text{ kJ mol}^{-1}$ [Schröder, 2008], which corresponds to a thermodynamic

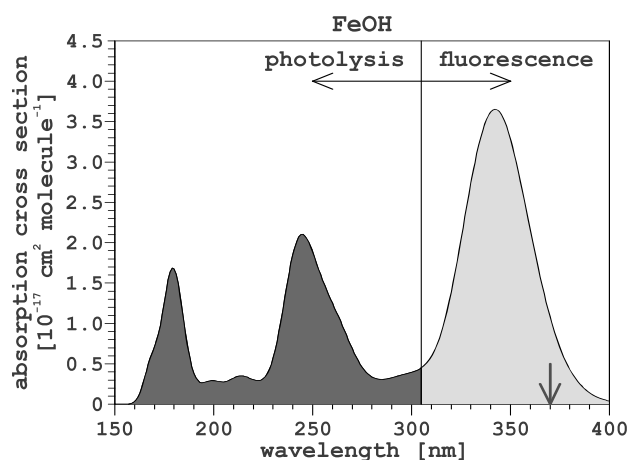


Figure 3. Absorption cross section for FeOH calculated at the TD/CAM-B3LYP/6-311+g(sd,p) level of theory. Wavelengths shorter than $\sim 305 \text{ nm}$ lead to photolysis.

threshold for photolysis of 370 nm (vertical arrow in Figure 3). However, absorption in the large band between 300 and 400 nm does most likely not lead to photolysis. Two pieces of evidence support this.

First, FeOH is electronically analogous to FeCl. Our calculations show that FeCl has a very similar absorption spectrum to FeOH, and absorption between 315 and 370 nm produces fluorescence in FeCl rather than dissociation [Delaval et al., 1980; Lei and Dagdigian, 2000]. Second, inspection of the Mulliken electron populations of the excited states of FeOH shows that these remain ionic like the ground state up to the seventh state. Only the eighth and higher states are covalent and hence more likely to dissociate to Fe + OH. The transition to the eighth state is calculated to occur at 300 nm, so the threshold for photolysis should be slightly red shifted (allowing for internal excitation).

The photolysis coefficient is then computed from the relation

$$J = \int_{\lambda_1}^{\lambda_2} \sigma(\lambda)\Phi(\lambda)d\lambda$$

where $\Phi(\lambda)$ is the solar actinic flux by the semiempirical model SOLAR2000 averaged over a solar cycle [Tobiska et al., 2000]. The integration is performed from 305 to 150 nm, yielding $J(\text{FeOH})=6.2 \times 10^{-3} \text{ s}^{-1}$. The slight uncertainty in the exact transition from fluorescence to photolysis results in an uncertainty of the photolysis rate of about 50%. The order of magnitude of the photolysis, however, is not affected by this. Note that this value of $J(\text{FeOH})$ is about 5 times larger than the lower limit determined from the analysis of lidar observations in section 2.2. As we show in section 4, this value of $J(\text{FeOH})=(3-9) \times 10^{-3} \text{ s}^{-1}$ compares well with the rate required to match the observed increase of Fe below 80 km.

3.2. Reaction of FeOH With H

The reaction between FeOH and H can proceed via the exothermic channels of reactions (1a) and (1b), where $\Delta H^\circ(0\text{K}) = -171 \pm 16$ and $-92 \pm 21 \text{ kJ mol}^{-1}$, respectively [Schröder, 2008]. Note that H can also react with FeOH to form HFeOH, but this is not important under mesospheric conditions [Self and Plane, 2003]. The rate constants for reactions (1a) and (1b) have been determined in studies of Fe-seeded flames at temperatures in excess of 2000 K, indicating that reaction (1b) is the dominant channel even though it is less exothermic [Jensen and Jones, 1974; Rumminger et al., 1999]. However, in a subsequent experimental and theoretical study of the FeOH + H reaction, Self and Plane [2003] showed that there are significant uncertainties regarding both the relative and absolute rate coefficients for these reactions when extrapolated to around 300 K. Theory indicated that reaction (1a) might be the dominant channel, and so Feng et al. [2013] adopted a value of $k_{1a} = 3 \times 10^{-10} \exp(-1264/T) \text{ cm}^3 \text{ molecule}^{-1} \text{ s}^{-1}$ and ignored (1b) for atmospheric modeling purposes. We now reexamine this assumption.

When modeling the underside of the mesospheric Fe layer, a further test of this chemistry is the observed disappearance of Fe between 70 and 80 km at night. Although the atomic H concentration at 70–80 km decreases substantially at night [Plane et al., 2015], sufficient H remains to place upper limits on reactions (1a) and (1b). The rate constant for reaction (1a) from the flame work $k_{1a} = 2 \times 10^{-12} \exp(-600/T) \text{ cm}^3 \text{ molecule}^{-1} \text{ s}^{-1}$ is slow enough at mesospheric temperatures. However, $k_{1b} = 5 \times 10^{-11} \exp(-800/T) \text{ cm}^3 \text{ molecule}^{-1} \text{ s}^{-1}$ [Jensen and Jones, 1974] is too fast by around a factor of 5 when extrapolated to 200 K, where k_{1b} needs to be less than $2 \times 10^{-13} \text{ cm}^3 \text{ molecule}^{-1} \text{ s}^{-1}$. In order to reproduce the nighttime disappearance of Fe below 80 km in the model, the activation energy and preexponential factor can be increased slightly to $k_{1b} = 6 \times 10^{-11} \exp(-1200/T) \text{ cm}^3 \text{ molecule}^{-1} \text{ s}^{-1}$, which still gives the rate constant at 2400 K required for flame modeling. These changes are modest bearing in mind the enormous temperature range being extrapolated over.

At typical MLT temperatures of less than 230 K and $[\text{H}] \sim 1 \times 10^8 \text{ cm}^{-3}$, the rates of reactions (1a) and (1b) are on the order of $k_{1a}[\text{H}] \sim 1.5 \times 10^{-5} \text{ s}^{-1}$ and $k_{1b}[\text{H}] \sim 3 \times 10^{-5} \text{ s}^{-1}$, respectively. Comparison with the value of $J(\text{FeOH})$ determined in section 2.2 shows that these pathways cannot compete with the direct photolysis of FeOH to explain the rate of increase at sunrise. However, at night reactions (1a) and (1b) are probably of similar significance in defining the Fe layer bottomside.

4. Atmospheric Modeling

A series of models for MLT metal chemistry has recently been developed on the basis of the Whole Atmosphere Community Climate Model (WACCM) [Marsh et al., 2013a, 2013b; Feng et al., 2013; Plane et al., 2014;

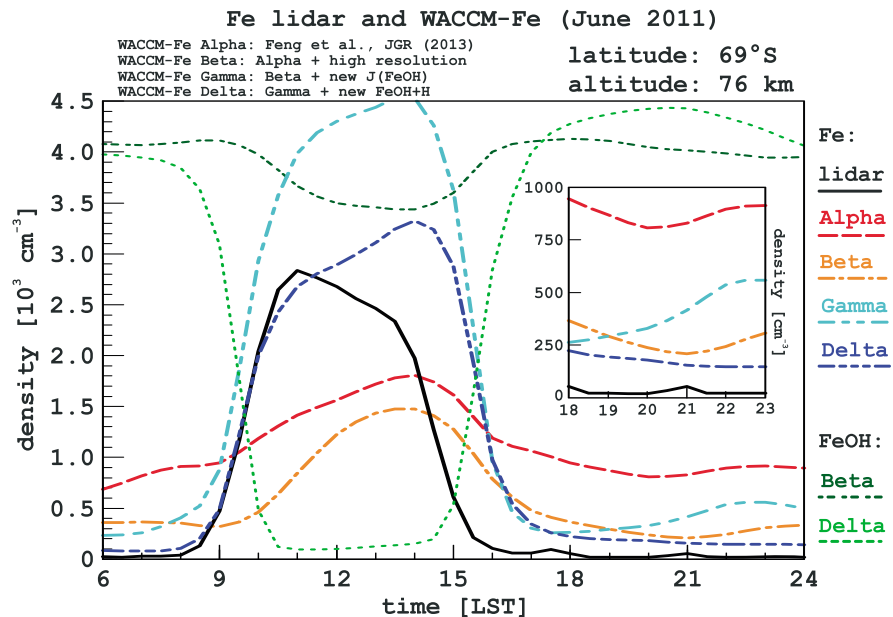


Figure 4. Comparison of the bottomsides extension of the Fe layer at Davis, Antarctica, measured by resonance lidar and simulated with WACCM-Fe. Included are four model runs for Fe and two runs for FeOH. The previously existing model run (Alpha) underestimated the increase of Fe observed by lidar at sunrise but overestimated densities during dark periods. New model simulations with higher resolution as well as new rate coefficients for the photolysis of FeOH and the reactions of FeOH capture the observed behavior, in particular the crucial rate of increase at sunrise and low nighttime densities (Beta to Delta). The latest model runs show a strong depletion of FeOH. See text for more details.

Langowski et al., 2015]. WACCM is a comprehensive “high top” chemistry climate model extending from the surface to 5.96×10^{-6} hPa (~ 140 km). The background chemistry scheme is based on that of Kinnison et al. [2007], which contains 59 species and 217 gas phase chemical reactions. Over 120 gas phase reactions of metallic species are then added [Plane et al., 2015]. The model also includes the meteoric input function which is calculated by combining a cosmic dust astronomical model with a chemical ablation model [e.g., Fentzke and Janches, 2008; Vondrak et al., 2008].

For this study, we compare four runs of WACCM-Fe, the Fe variant of the model [Feng et al., 2013]. In contrast to the existing calculations (run Alpha), the vertical resolution in the MLT region for the new runs (Beta to Delta) was increased from around 3.5 km to less than 500 m by increasing the hybrid σ pressure vertical coordinate from 88 to 144 levels, using the same method as Merkel et al. [2009]. This allows for a better resolution of the highly altitude-dependent distributions of atomic H and O, which are critical for the reactions at the bottomsides of the Fe layer. Run Beta uses same rate coefficients as run Alpha but the higher vertical resolution. Run Gamma increases the photolysis rate to $J(\text{FeOH}) = 6 \times 10^{-3} \text{ s}^{-1}$ as determined in section 3.1. Run Delta additionally changes the rate coefficients for the reaction channels of $\text{FeOH} + \text{H}$ as described in section 3.2.

Figure 4 compares the results of the different model runs with lidar observations. We use a 24 h composite of all observations and simulations at Davis, Antarctica (69°S), for 1 month, thereby averaging out the influence of gravity waves which is apparent in Figure 1. Both WACCM-Fe and lidar data are calculated for a resolution of 30 min and integrated to 1 km. The data are smoothed with a Hann filter of 1 h and 2 km. WACCM-Fe generally simulates the high-latitude Fe layer better during winter than summer, when the model predicts an “hour glass” shape, whereas lidar observations show an uplift of the layer [Feng et al., 2013; Viehl et al., 2015]. Moreover, during winter the impact of ice particles potentially influencing the bottomsides of the layer can be ruled out. June 2011 is the winter month with most lidar measurement (260 h).

The lidar observations in Figure 4 (solid black) show a pronounced increase of the Fe bottomsides density at sunrise. During the sunlit period, densities at 76 km altitude reach around 2500 cm^{-3} and show a slight decline during the day. Densities rapidly fall after sunset and stay below 200 cm^{-3} during the dark period. Run Alpha of WACCM-Fe (dashed red) shows an increase in Fe densities during daytime, peaking toward sunset at

around 1750 cm^{-3} which significantly underestimates the observed Fe density. Also, considerable amounts of Fe persist during the dark period, which are not observed. Using the higher resolution, run Beta (dash-dotted orange) shows a more pronounced relative daytime enhancement and lower absolute densities. With the new estimate of $J(\text{FeOH})$, run Gamma (dash-double-dotted cyan) shows a stronger increase at sunrise. However, absolute densities are overestimated. Closer inspection of the nighttime densities shows that run Gamma predicts considerable amounts of Fe during the night, contrary to the lidar observations (see inlay in Figure 4). Run Delta (dash-triple-dotted blue) additionally uses the revised rate coefficients for reactions (1a) and (1b), which then reproduces satisfactorily the low nighttime densities. The absolute densities in run Delta peak around sunset yet are of comparable abundance to the lidar observations. Most strikingly, the timing and rate of increase at sunrise $\frac{\Delta[\text{Fe}]}{\Delta t}$ in run Delta match the observed behavior very well.

A further result of this comparison is the nearly complete photolysis of FeOH during sunlit periods. Whereas run Beta shows FeOH densities of more than 3500 cm^{-3} at this altitude during all hours of the day (dark green), run Gamma calculates FeOH levels below $\sim 300 \text{ cm}^{-3}$ for most of the sunlit period (light green). We note that the sum of [Fe] and [FeOH] is not constant in time as Fe is further oxidized to other species.

5. Discussion and Summary

Analysis of the solar elevation dependence by *Yu et al.* [2012] demonstrated that the bottomside extension of the mesospheric Fe layer is a solar phenomenon, and FeOH is the dominant reservoir at this altitude [*Self and Plane*, 2003]. Three reactions govern this transition: the direct photolysis of FeOH and the reactions (1a) and (1b) of FeOH with atomic H. Contrary to the reactions depleting Fe, these reactions producing Fe have only been studied indirectly in the laboratory [*Self and Plane*, 2003]. Previously, the photolysis of FeOH was assumed to be negligible, with $J(\text{FeOH})$ set to a low value of $1 \times 10^{-5} \text{ s}^{-1}$ [*Plane et al.*, 2015]. Furthermore, only reaction (1a) had been considered in model simulations by *Feng et al.* [2013] with a rate coefficient of $k_{1a} = 3 \times 10^{-10} \exp(-1264/T)$ (see section 3.2).

In the present study we have compared a new set of high-resolution WACCM-Fe model runs with different rate coefficients to our lidar observations. The crucial H and O distribution with strong gradients in the lower MLT region is thereby resolved more precisely. However, the current set of reaction rate coefficients does not reproduce the marked Fe increase at sunrise observed by lidar. A substantial increase in $J(\text{FeOH})$, supported by the quantum chemical calculations and consistent with lidar observations, yields a much improved simulation of the bottomside extension during sunlit hours.

However, with the previously used rate coefficient for (1a), the low nighttime densities observed by lidar in both hemispheres cannot be reproduced in the model. As section 3.2 shows, the activation energy and preexponential factor of reaction (1b) can be altered slightly to reduce the rate coefficient at mesospheric temperatures while being fast enough at high temperatures to account for Fe-catalyzed flame inhibition [*Jensen and Jones*, 1974; *Rumminger et al.*, 1999]. As a result, reaction (1a) is slower than previously assumed and reaction (1b) should not be neglected under MLT conditions. The inclusion of these new rate coefficients results in a good representation of the diurnal behavior of the Fe layer bottomside and the rate of increase at sunrise. Nevertheless, discrepancies of the model representation still persist during the afternoon hours. WACCM-Fe predicts a further increase of Fe density until sunset and a decrease later at night. This may be due to the fact that reactions (1a) and (1b) are still overestimated, although that would be difficult to reconcile with Fe combustion chemistry. Future laboratory studies would help to resolve this. Two other possibilities are that our knowledge of the neutral gas phase chemistry of Fe is incomplete, and that the diurnal variations of O and H in this altitude range are not properly captured in WACCM, which needs to be further investigated. A potential low bias of atomic O and H in WACCM would lead to even stronger constraints on reactions (1a) and (1b). Indeed, the excellent spatial and temporal resolution achievable with a modern Fe lidar provides a stringent test for a 3-D chemistry model.

We conclude that the direct photolysis of FeOH is the primary cause of the bottomside extension of the mesospheric Fe layer during sunlit hours and determine a new photolysis rate $J(\text{FeOH}) = 6 \times 10^{-3} \text{ s}^{-1}$ which is more than 2 orders of magnitude faster than previously assumed. Furthermore, contrary to previous considerations, reaction (1a) is about an order of magnitude slower and both (1a) and (1b) need to be considered under MLT conditions. These changes of rate coefficients have a profound effect on the diurnal behavior of the Fe layer at all altitudes. Tidal signatures in the Fe layer as observed by *Lübken et al.* [2011] should be strongly influenced

by this effect below the relative maximum abundance of the main reservoir FeOH at around 90 km. Improved model analyses with the new rate coefficients determined in this study will allow a deeper understanding of the dynamical and chemical properties of the MLT.

Our simulations show the strong depletion of FeOH at all altitudes whenever sunlight is present due to the increased photolysis rate. Through reaction with O₃, FeOH may be oxidized to FeOOH. Rietmeijer [2001] has shown that α FeOOH (goethite) is a plausible candidate for MSPs. Alternatively, FeOH can dimerize efficiently [Feng et al., 2013]. The nearly complete removal of FeOH as predicted by WACCM-Fe with the revised Fe chemistry therefore may have implications for an important precursor of MSP formation during sunlit periods, i.e., the whole polar summer season. Small amounts of FeOH are still present as Fe is constantly being recycled to FeOH via the reactions with O₃, O₂, H₂O, and H. Whether these amounts are sufficient to contribute to MSP formation needs to be investigated in more detail. Other metal compounds and silica might polymerize first to form embryonic particles; after which iron is added by the uptake of atomic Fe rather than Fe compounds.

We note that it may be misleading to define the bottomside of a metal layer as the 300 cm⁻³ contour [Yu et al., 2012]. An analysis of $\frac{\Delta z}{\Delta t}$ shows a dependence not only on the solar elevation but also on the strongly altitude-dependent abundance of the reservoir FeOH. The slope of the bottomside extension will vary depending on whether the 300 cm⁻³ contour or any other level is defined.

In this study we have used a combination of resonance lidar observations, quantum chemical calculations, and atmospheric model simulations to determine basic physicochemical parameters (photolysis rates and rate constants) which are very challenging to measure directly. The middle atmosphere has therefore in a sense provided a natural laboratory.

Acknowledgments

The theoretical and modeling work was funded by the European Research Council (grant 291332—CODITA). The measurements at Davis were supported by the Australian Antarctic Division under Australian Antarctic science project 2325 led by R.J. Morris. T.P. Viehl and J. Höffner would like to thank their fellow expeditioners of the 64th, 65th, and 66th ANARE at Davis and the AAD staff for their dedicated support throughout the project as well as R.J. Morris and B. Kaifler for assisting with the measurements in Antarctica. We thank R. Wörl and the staff of the Andøya Space Center in Andenes, Norway, for their ongoing support with the measurements in the Arctic.

References

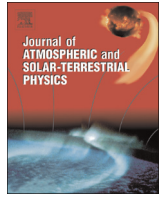
- Chu, X., Z. Yu, C. S. Gardner, C. Chen, and W. Fong (2011), Lidar observations of neutral Fe layers and fast gravity waves in the thermosphere (110–155 km) at McMurdo (77.8°S, 166.7°E), Antarctica, *Geophys. Res. Lett.*, *38*, L23807, doi:10.1002/2011GL050016.
- Delaval, J. M., C. Dufour, and J. Schamps (1980), Rotational analysis of ultraviolet systems of FeCl, *J. Phys. B: At. Mol. Phys.*, *13*, 4757–4769, doi:10.1088/022-3700/13/24/010.
- Delgado, R., J. S. Friedman, J. T. Fentzke, S. Raizada, C. A. Tepley, and Q. Zhou (2012), Sporadic metal atom and ion layers and their connection to chemistry and thermal structure in the mesopause region at Arecibo, *J. Atmos. Sol. Terr. Phys.*, *74*, 11–23, doi:10.1016/j.jastp.2011.09.004.
- Feng, W., D. R. Marsh, M. P. Chipperfield, D. Janches, J. Höffner, F. Yi, and J. M. C. Plane (2013), A global atmospheric model of meteoric iron, *J. Geophys. Res. Atmos.*, *118*, 9456–9474, doi:10.1002/jgrd.50708.
- Feng, W., J. Höffner, D. R. Marsh, M. P. Chipperfield, E. C. M. Dawkins, T. P. Viehl, and J. M. C. Plane (2015), Diurnal variation of the potassium layer in the upper atmosphere, *Geophys. Res. Lett.*, *42*, 3619–3626, doi:10.1002/2015GL063718.
- Fentzke, J. T., and C. Janches (2008), A semi-empirical model of the contribution from sporadic meteoroid sources on the meteor input function in the MLT at Arecibo, *J. Geophys. Res.*, *113*, A03304, doi:10.1029/2007JA012531.
- Frankland, V. L., A. D. James, W. Feng, and J. M. C. Plane (2015), The uptake of HNO₃ on meteoric smoke analogues, *J. Atmos. Sol. Terr. Phys.*, *127*, 150–160, doi:10.1016/j.jastp.2015.01.010.
- Frisch, M. J., et al. (2009), *Gaussian 09, Revision A.1*, Gaussian, Wallingford, Connecticut.
- Gardner, C. S., A. Z. Liu, D. R. Marsh, W. Feng, and J. M. C. Plane (2014), Inferring the global cosmic dust influx to the Earth's atmosphere from lidar observations of the vertical flux of mesospheric Na, *J. Geophys. Res. Space Physics*, *119*, 7870–7879, doi:10.1002/2014JA020383.
- Gumbel, J., and L. Megner (2009), Charged meteoric smoke as ice nuclei in the mesosphere: Part 1—A review of basic concepts, *J. Atmos. Sol. Terr. Phys.*, *71*, 1225–1235, doi:10.1016/j.jastp.2009.04.012.
- Höffner, J., and J. Lautenbach (2009), Daylight measurements of mesopause temperature and vertical wind with the mobile scanning iron lidar, *Opt. Lett.*, *34*, 1351–1353.
- Huang, W., X. Chu, C. S. Gardner, J. D. Carrillo-Sanchez, W. Feng, J. M. C. Plane, and D. Nesvornyy (2015), Measurements of the vertical fluxes of atomic Fe and Na at the mesopause: Implications for the velocity of cosmic dust entering the atmosphere, *Geophys. Res. Lett.*, *42*, 169–175, doi:10.1002/2014GL062390.
- Jensen, D. E., and G. A. Jones (1974), Catalysis of radical recombination in flames by iron, *J. Chem. Phys.*, *60*, 3412–3425, doi:10.1063/1.1681554.
- Kinnison, D. E., et al. (2007), Sensitivity of chemical tracers to meteorological parameters in the MOZART-3 chemical transport model, *J. Geophys. Res.*, *112*, D20302, doi:10.1029/2006JD007879.
- Langowski, M. P., C. von Savigny, J. P. Burrows, W. Feng, J. M. C. Plane, D. R. Marsh, D. Janches, M. Sinnhuber, A. C. Aikin, and P. Liebing (2015), Global investigation of the Mg atom and ion layers using SCIAMACHY/Envisat observations between 70 and 150 km altitude and WACCM-Mg model results, *J. Atmos. Sol. Terr. Phys.*, *127*, 97–102, doi:10.1016/j.jastp.2015.04.013.
- Lei, J., and P. J. Dagdigan (2000), Molecular beam study of the ⁶Π–X⁶Δ electronic transition in FeCl, *J. Chem. Phys.*, *112*, 10,221–10,227, doi:10.1063/1.481664.
- Lübken, F.-J., J. Höffner, T. P. Viehl, B. Kaifler, and R. J. Morris (2011), First measurements of thermal tides in the summer mesopause region at Antarctic latitudes, *Geophys. Res. Lett.*, *38*, L24806, doi:10.1029/2011GL050045.
- Lübken, F.-J., J. Höffner, T. P. Viehl, E. Becker, R. Latteck, B. Kaifler, D. Murphy, and R. J. Morris (2015), Winter/summer transition in the Antarctic mesopause region, *J. Geophys. Res. Atmos.*, *120*, 12,394–12,409, doi:10.1002/2015JD023928.
- Marsh, D. R., M. J. Mills, D. E. Kinnison, J.-F. Lamarque, N. Calvo, and L. M. Polvani (2013a), Climate change from 1850 to 2005 simulated in CESM1(WACCM), *J. Clim.*, *26*, 7372–7391, doi:10.1175/JCLI-D-12-00558.1.
- Marsh, D. R., D. Janches, W. Feng, and J. M. C. Plane (2013b), A global model of meteoric sodium, *J. Geophys. Res. Atmos.*, *118*, 11,442–11,452, doi:10.1002/jgrd.50870.

- Megner, L., and J. Gumbel (2009), Charged meteoric smoke as ice nuclei in the mesosphere: Part 2—A feasibility study, *J. Atmos. Sol. Terr. Phys.*, *71*, 1236–1244, doi:10.1016/j.jastp.2009.05.002.
- Merkel, A. W., D. R. Marsh, A. Gettelman, and E. J. Jensen (2009), On the relationship of polar mesospheric cloud ice water content, particle radius and mesospheric temperature and its use in multi-dimensional models, *Atmos. Chem. Phys.*, *9*, 8889–8901, doi:10.5194/acp-9-8889-2009.
- Plane, J. M. C. (2003), Atmospheric chemistry of meteoric metals, *Chem. Rev.*, *103*(12), 4963–4984, doi:10.1021/cr0205309.
- Plane, J. M. C. (2012), Cosmic dust in the Earth's atmosphere, *Chem. Soc. Rev.*, *41*, 6507–6518, doi:10.1039/c2cs35132c.
- Plane, J. M. C., R. M. Cox, and R. J. Rollason (1999), Metallic metal layers in the mesopause and lower thermosphere region, *Adv. Space Res.*, *24*(11), 1559–1570.
- Plane, J. M. C., W. Feng, E. M. C. Dawkins, M. P. Chipperfield, J. Höffner, D. Janches, and D. R. Marsh (2014), Resolving the strange behavior of extraterrestrial potassium in the upper atmosphere, *Geophys. Res. Lett.*, *41*, 4753–4760, doi:10.1002/2014GL060334.
- Plane, J. M. C., W. Feng, and E. M. C. Dawkins (2015), The mesosphere and metals: Chemistry and changes, *Chem. Rev.*, *115*(10), 4497–4541, doi:10.1021/cr500501m.
- Rietmeijer, F. J. M. (2001), Identification of Fe-rich meteoric dust, *Planet. Space Sci.*, *48*(2001), 71–77.
- Rumminger, M. D., D. Reinelt, V. Babushok, and G. T. Linteris (1999), Numerical study of the inhibition of premixed and diffusion flames by iron pentacarbonyl, *Combust. Flame*, *116*(1–2), 207–219.
- Saunders, R. W., S. Dhomse, W. S. Tian, M. P. Chipperfield, and J. M. C. Plane (2012), Interactions of meteoric smoke particles with sulphuric acid in the Earth's stratosphere, *Atmos. Chem. Phys.*, *12*, 4387–4398, doi:10.5194/acp-12-4378-2012.
- Scalmani, G., M. J. Frisch, B. Menucci, J. Tomasi, R. Cammi, and V. Barone (2006), Geometries and properties of excited states in the gas phase and in solution: Theory and application of a time-dependent density functional theory polarizable continuum model, *J. Chem. Phys.*, *124*(9), 094107.
- Schröder, D. (2008), Gaseous rust: Thermochemistry of neutral and ionic iron oxides and hydroxides in the gas phase, *J. Phys. Chem. A*, *112*, 13215–13224, doi:10.1021/jp8030804.
- Self, D. E., and J. M. C. Plane (2003), A kinetic study of the reactions of iron oxides and hydroxides relevant to the chemistry of iron in the upper mesosphere, *Phys. Chem. Chem. Phys.*, *5*(7), 1407–1418, doi:10.1039/b211900e.
- Tobiska, W. K., T. Woods, F. Eparvier, R. Viereck, L. Floyd, D. Bouwer, G. Rottman, and O. R. White (2000), The SOLAR2000 empirical solar irradiance model and forecast tool, *J. Atmos. Sol. Terr. Phys.*, *62*, 1233–1250.
- Viehl, T. P., J. Höffner, F.-J. Lübken, J. M. C. Plane, B. Kaifler, and R. J. Morris (2015), Summer time Fe depletion in the Antarctic mesopause region, *J. Atmos. Sol. Terr. Phys.*, *127*, 97–102, doi:10.1016/j.jastp.2015.04.013.
- Vondrak, T., J. M. C. Plane, S. Broadley, and D. Janches (2008), A chemical model of meteoric ablation, *Atmos. Chem. Phys.*, *8*, 7015–7031.
- von Zahn, U., and J. Höffner (1996), Mesopause temperature profiling by potassium lidar, *Geophys. Res. Lett.*, *23*, 141–144.
- von Zahn, U., J. Höffner, and W. J. McNeil (2002), Meteor trails as studied by ground-based lidar, in *Meteors in the Earth's Atmosphere*, edited by E. Murad and I. P. Williams, pp. 149–187, Cambridge Univ. Press, Cambridge, U. K.
- Yanai, T., D. Tew, and N. Handy (2004), A new hybrid exchange-correlation functional using the Coulomb-attenuating method (CAM-B3LYP), *Chem. Phys. Lett.*, *292*, 51–57, doi:10.1016/j.cplett.2004.06.011.
- Yu, Z., X. Chu, W. Huang, W. Fong, and B. R. Roberts (2012), Seasonal variations of the Fe layer in the mesosphere and lower thermosphere: Four season variability and solar effects on the layer bottomside at McMurdo (77.8°S, 166.7°E), Antarctica, *J. Geophys. Res.*, *117*, D22302, doi:10.1029/2012JD018079.



Contents lists available at ScienceDirect

Journal of Atmospheric and Solar-Terrestrial Physics

journal homepage: www.elsevier.com/locate/jastp

Summer time Fe depletion in the Antarctic mesopause region

T.P. Viehl^{a,*}, J. Höffner^a, F.-J. Lübken^a, J.M.C. Plane^b, B. Kaifler^{a,c}, R.J. Morris^d^a Leibniz-Institute of Atmospheric Physics (IAP) at the University of Rostock, Schloßstr. 6, 18225 Kühlungsborn, Germany^b School of Chemistry, University of Leeds, Leeds LS2 9JT, United Kingdom^c German Aerospace Centre (DLR), Institute of Physics of the Atmosphere, Münchner Str. 20, 82234 Wessling, Germany^d Australian Antarctic Division (AAD), 203 Channel Hwy, Kingston, Tasmania 7050, Australia

ARTICLE INFO

Article history:

Received 21 August 2014

Received in revised form

4 April 2015

Accepted 27 April 2015

Available online 28 April 2015

Keywords:

Mesospheric iron

Noctilucent clouds

Polar mesospheric clouds

Polar mesosphere summer echoes

Heterogeneous chemistry

ABSTRACT

We report common volume measurements of Fe densities, temperatures and ice particle occurrence in the mesopause region at Davis Station, Antarctica (69°S) in the years 2011–2012. Our observations show a strong correlation of the Fe-layer summer time depletion with temperature, but no clear causal relation with the onset or occurrence of ice particles measured as noctilucent clouds (NLC) or polar mesosphere summer echoes (PMSE). The combination of these measurements indicates that the strong summer depletion can be explained by gas-phase chemistry alone and does not require heterogeneous removal of Fe and its compounds on ice particles.

© 2015 Elsevier Ltd. All rights reserved.

1. Introduction

When meteors enter the Earth's atmosphere they predominantly ablate in an altitude region between 75 and 115 km. Ablated meteoric metal atoms form layers of neutral, ionised and molecular bound species, the latter mainly in the form of oxides and hydroxides (Self and Plane, 2003). The seasonal change in metal abundance is largely determined by the seasonal variation in global circulation and temperature dependent chemistry (Plane et al., 2015). In a recent study Feng et al. (2013) compare the seasonal variation at several sites (including measurements at Davis, Antarctica) with model calculations and list comprehensive references.

Another phenomenon characteristic to the MLT altitude range is the summer time occurrence of ice particles at polar latitudes. These ice particles can be detected by satellites, lidar instruments or the human eye when they have reached sufficient size (with radii typically larger than 20 nm) through condensation growth. In the case of satellite observations the ice particles are known as polar mesospheric clouds (PMC), in the case of ground based observations as noctilucent clouds (NLC), e.g. Baumgarten et al. (2012), DeLand et al. (2006), Russell et al. (2009), and Lübken et al. (2009). Visibly observable ice particles as well as smaller, sub-visible ice particles can lead to polar mesosphere summer echoes

(PMSE), which are strong radar echoes caused by small scale structures in electron densities (Rapp and Lübken, 2004; Lübken, 2013). These structures on the order of the radar Bragg wavelength rely on the combined effect of neutral air turbulence and charged ice particles. It is important to note that PMC and NLC require 'large' ice particles whereas PMSE can also be caused by smaller ice particles ($r \leq 20$ nm). Consequently, PMC/NLC appear at the lower edge of the super-saturated region (approximately 82–84 km) whereas PMSE extend to higher altitudes (up to 94 km).

Observations by Plane et al. (2004) and Lübken and Höffner (2004) and subsequent studies investigated the uptake of metal atoms, in particular of Fe (iron) and K (potassium), on ice particles. These authors report singular events of metal atom depletions with simultaneous occurrence of PMSE as well as NLC in the case of K, and NLC in the case of Fe. She et al. (2006) and Thayer and Pan (2006) found similar anti-correlations for Na (sodium). These studies suggest that the depletion is largely caused by an uptake of metal atoms on the ice particle surface. For K, this was reproduced in a model by Raizada et al. (2007). Northern hemispheric K densities were shown to fall nearly instantaneously at the beginning of the PMSE and NLC season. K densities remained low and steady for the period of ice particle occurrence. Similar to the beginning of the season, densities increased markedly at the end of the PMSE season, i.e. when no further ice particles were observed.

The hypothesis of metal atom adsorption on ice particles was developed further to explain the summer time behaviour of the

* Corresponding author.

E-mail address: viehl@iap-kborn.de (T.P. Viehl).

seasonal Fe cycle in the MLT region of the Southern Hemisphere. Gardner et al. (2011) compared observations performed at Rothera, Antarctica (Chu et al., 2006) and the South Pole (Gardner et al., 2005). Both Rothera and the South Pole show significant Fe depletion at around 80–92 km during the summer months and in particular during a period of about ± 40 days around summer solstice when NLC are observed. Differences in metal layer abundance, height and width between these two stations were attributed to differences in NLC altitude, brightness and occurrence frequency. Spatial and temporal mismatches between the presence of NLC particles and Fe depletion were noted, observable mostly above 87 km altitude and in the month prior to the first NLC detection. Common volume comparisons of Fe densities with PMSE were so far not available. In analogy to results from other metals in the Northern Hemisphere and due to promising modelling efforts, these gaps were attributed to smaller, sub-visible particles.

Gardner et al. (2011) found a high positive correlation of Fe densities with temperature as expected from calculations by Plane (2003) and others and discuss various influences on the seasonal variation of the metal layer. The authors concluded that the peak of the Fe layer was pushed to well above 90 km because persistent ice clouds at lower altitudes removed the Fe atoms in vicinity.

Hence, according to all those studies cited above it seems that the summer time Fe depletion in the Antarctic mesopause region is largely influenced by the uptake of metal atoms on ice particles. We present observations which challenge this hypothesis.

2. Instrumentation

The mobile Fe-Lidar operated by the Leibniz-Institute of Atmospheric Physics (IAP) was commissioned at Davis, Antarctica (68.6°S, 78.0°E) in the early summer season 2010–2011 (Lübken et al., 2011; Morris et al., 2012). It was in operation for more than two consecutive years until the end of the summer season 2012–2013 in early January 2013. The lidar is a two-wavelength system based on a frequency-doubled alexandrite laser (von Zahn and Höffner, 1996; Höffner and Lautenbach, 2009). It is capable of determining mesospheric temperatures and Fe densities in full daylight by scanning the Doppler broadened Fe resonance line at 386 nm. High solar background as well as low Fe densities are the conditions giving the largest possible measurement uncertainty. Typical uncertainties for temperatures are 5 K for 1 h integration and 1 km altitude range in summer time during noon conditions and annual low Fe density. Uncertainties for daily means are on the order of 1 K and less than 1% for temperature and Fe density, respectively. Variations in uncertainties depend on tropospheric weather, absolute Fe densities and observation period. NLC are simultaneously detected by an independent analysis of the retrieved residual infrared laser wavelength at 772 nm. As the system is capable of nearly background free single photon detection during full daylight, NLC are detectable within an integration time as short as 2 min. The complete dataset obtained by the mobile Fe-Lidar at Davis includes 2900 h of lidar measurements nearly equally distributed throughout the year and all hours of the day. During the austral summer months September 2011 to March 2012 a total of 1151 h of temperature and density measurements with at least 1 h duration were obtained on 94 days. The average length of the measurements considered is 12 h 14 min per day.

Another instrument operated at Davis is the 55 MHz Mesosphere–Stratosphere–Troposphere (MST) radar of the Australian Antarctic Division (AAD) which was put into operation in the summer season of 2002–2003 (Morris et al., 2004). This system has been detecting PMSE on a regular basis since the summer season 2003–2004. The AAD MST radar was in operation during all

times when the IAP Fe-Lidar was in operation. As both instruments are located at Davis, common volume measurements of Fe densities, temperatures and ice particles (detected as NLC and PMSE) are available and allow a unique combined analysis of these atmospheric features.

3. Observations of Fe density, temperature and ice particles

3.1. Fe density and temperature in the 2011/2012 summer

Fig. 1 shows Fe densities and temperatures in the mesopause region from spring to autumn. Fe densities are cut off at 100 cm^{-3} . In general, densities and temperatures during the summer months are at their annual low with daily mean temperatures between 87 and 95 km lower than 145 K and densities lower than $10,000 \text{ cm}^{-3}$ except for higher densities in the peak layer from mid-February onwards.

Contrary to model results (Feng et al., 2013) and previous observations (Gardner et al., 2011) for this Antarctic latitude, the upper boundary of the Fe layer at Davis as shown in Fig. 1 is generally higher during the summer months than during spring and autumn. (See, e.g., the $2,000 \text{ cm}^{-3}$ contour line.) High densities at high altitudes in late March are caused by sporadic layers. The centroid altitude rises towards summer solstice and falls thereafter, as the whole Fe layer is shifted upwards. The whole layer thins out throughout all altitudes towards solstice. The figure also shows a very strong short term depletion in Fe densities of about 2 weeks duration around solstice between 87 and 95 km altitude. Simultaneously, record low daily average temperatures below 135 K are shown in the exact same altitude and time region. Some of these temperatures as well as singular short term profiles

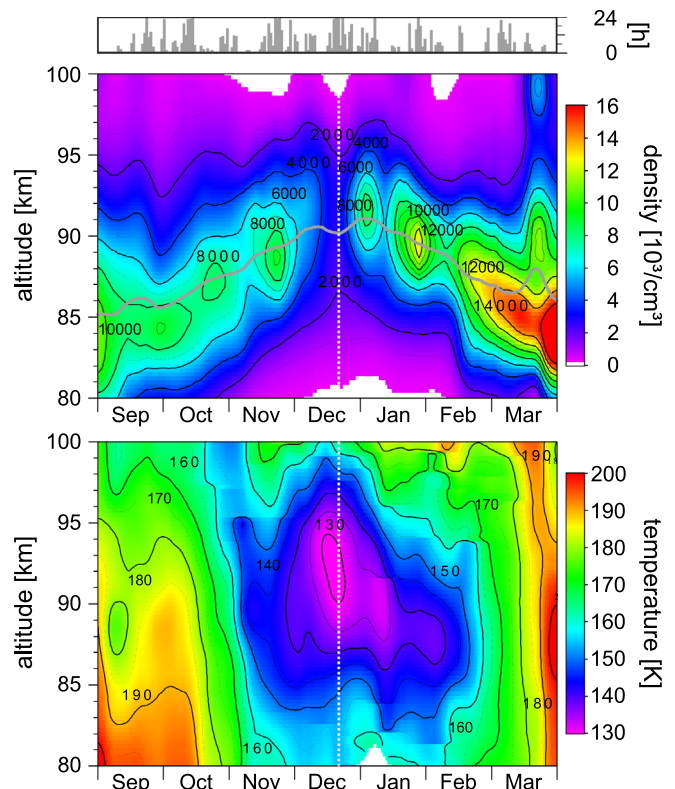


Fig. 1. Fe densities (upper panel) and temperatures (lower panel) September 2011 to March 2012. Lidar measurement periods are displayed as histogram for 0–24 h per day on the very top. The Fe layer's upper boundary and centroid altitude (grey line) are elevated around summer solstice (white dotted line). Very low densities around solstice coincide with very low temperatures.

have recently been published by Lübken et al. (2014). Fig. 1 therein shows temperatures as low as 100 K on 17/18 December 2011.

3.2. Fe density and ice particles

It is well known that low temperatures lead to ice nucleation and successively to the creation of PMSE (Rapp et al., 2002). Simultaneously, it has been shown that low temperatures alter the chemical reactions in the MLT region such that the amount of free, neutral Fe atoms is reduced (Feng et al., 2013). When investigating the causal relationship of ice particle occurrence and the summer time Fe depletion in the Antarctic mesopause region, an obvious problem is therefore to separate those effects. Are low temperatures causing ice particles and are those ice particles then significantly reducing available Fe atoms? Or are low temperatures on their own altering the chemical equilibrium so profoundly that Fe atoms are efficiently converted to reservoir species and disappear—even without adsorption on ice particles in the vicinity? Do we observe a combination of both effects?

To answer these questions we have analysed the annual cycle of the Fe column densities rather than studied a time–altitude plot as in Fig. 1. We see justification for the investigation of column densities in the fact that these should generally decrease in the presence of ice particles at any altitude within the metal layer provided that the seasonal variations of other effects such as the meteor input function (Feng et al., 2013) are comparatively small in that period. As was shown in the case of K in model calculations by Raizada et al. (2007), a potential localised removal of metal atoms at any given altitude will affect the whole layer due to vertical eddy diffusion. Setting aside all other effects such as transport and meteoric input, column densities should be generally lower whenever ice particles are present and remove metal atoms significantly. Furthermore, if ice particles have a significant effect on the seasonal metal layer, then column densities should be expected to show a non-steady behaviour with the onset and suspension of ice particle occurrence.

Fig. 2 shows Fe column densities between July 2011 and May 2012. Column densities are calculated as the integrated densities of the whole MLT neutral Fe layer from the lower edge at about 75 km altitude to 120 km. In general, more than 99% of the Fe atoms are confined to the layer between its lower edge and about

105 km. Only minor amounts of metal atoms are found above this altitude in the daily and annual mean. Model studies have investigated the general behaviour of the Fe-layer at polar latitudes (e.g., Feng et al., 2013). In accordance with these results, winter column densities at Davis are typically larger than $10 \times 10^9 \text{ cm}^{-2}$. Our measurements show a steady decline in column densities from early August to late November.

The summer state of the atmosphere at Davis from mid-November to early February is characterised by relatively low MLT Fe column densities of about $6\text{--}8 \times 10^9 \text{ cm}^{-2}$. For a short period around solstice, column densities drop below $5 \times 10^9 \text{ cm}^{-2}$. The average peak density at summer solstice observed during a measurement period lasting 15.9 h on 20/21 December 2011 is only 1000 cm^{-3} between 90 and 93 km. This feature lasts for only a few days and is thus partly smoothed out by the 2-week Hanning window applied to the Fe density dataset used in Fig. 2. The autumn increase in densities begins towards the end of December, with a particularly interesting local maximum in Fe densities with over $8 \times 10^9 \text{ cm}^{-2}$ in late January.

Also shown in Fig. 2 is the occurrence of larger ice particles (NLC) from mid-December to mid-January. The red shaded area marks the period between 27 December 2011 and 12 January 2012 when nearly all of the NLC were observed. During this main NLC period 94 h of lidar observations were obtained on 9 days. NLC occurred over 42.5% of the time. The red dashed line marks a very weak and short singular NLC event on 17 December 2011 prior to the main NLC period, which is only visible after unusually long integration of more than 20 min. No NLC were observed at any other time during the observations. In particular, no NLC were observed when Fe column densities were at a seasonal low, namely between 17 December and 26 December—even though 130 h of observation were obtained during these 9 days. Additionally, PMSE are shown in Fig. 2. While average temperatures are still decreasing around mid-November, the onset of the first sporadically developing PMSE is dominated by cold phases of waves (predominantly gravity waves) which are capable of enhancing or destroying ice particles (Rapp et al., 2002). PMSE occurrence is therefore low in the period 17–24 November 2011, with PMSE only observable 6.2% of the time (see histogram in Fig. 2). When average temperatures have dropped to the annual summer low in mid-December, PMSE appear every day. Average occurrence per day is 77.2% in the week around solstice with a maximum of 94.1%.

3.3. Temperature dependence

Fig. 1 displays a striking overlap of very low temperatures and low Fe densities in mid-December. We use this prominent time and altitude frame to investigate the relationship between temperatures and Fe densities in more detail. Fig. 3 illustrates the relationship between the Fe density and average temperature between 87 and 92 km, over a ± 40 day window around solstice in the summer months 2011–2012. Included in these calculations are 39 daily mean temperatures and Fe densities from all measurements with more than 6 h duration, totalling 591 h of measurements. The data is plotted in the Arrhenius form, yielding an activation energy of $11.2 \pm 1.5 \text{ kJ mol}^{-1}$.

Table 1 lists the important reactions which convert iron between atomic Fe and its main reservoir, FeOH (Plane et al., 2015). Formation of FeOH starts with R1 which produces FeO. There is then competition between R2 and R3, with the latter further oxidising FeO to FeO₂ (R4 is pressure-dependent and too slow above 82 km to compete with R3). FeO₂ is then oxidised by O₃ to make FeO₃, which is eventually converted to the reservoir FeOH either directly via R11 or indirectly via R8 followed by R10. Inspection of the rate coefficients shows that once Fe has been

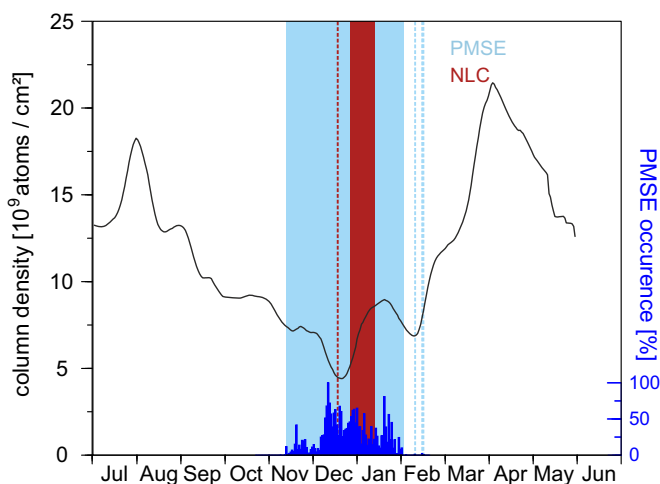


Fig. 2. Annual cycle of column densities of Fe from July 2011 to May 2012. Ice particle measurements are highlighted in blue and red (PMSE and NLC, respectively). The blue histogram shows the occurrence statistics for PMSE. Dashed lines indicate singular, weak PMSE and NLC events outside the main occurrence periods. Note the decline in Fe densities before the onset of ice particle occurrence and the increase during the main NLC period. (For interpretation of the references to colour in this figure caption, the reader is referred to the web version of this paper.)

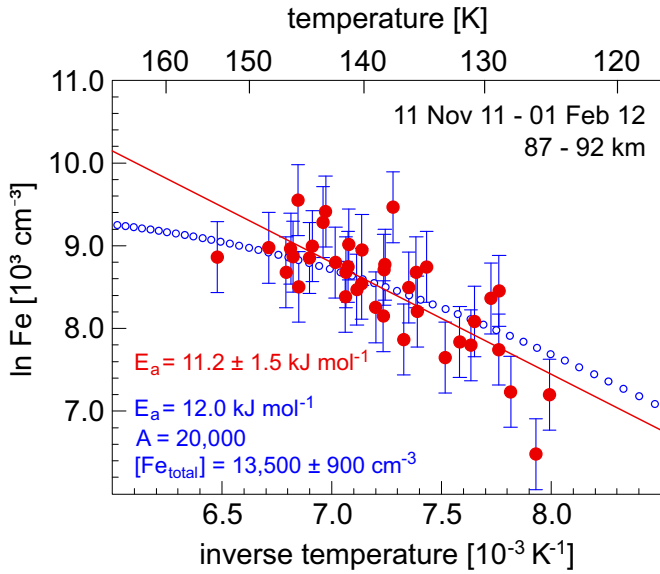


Fig. 3. Arrhenius plot for the potential chemical reactions dominating the strong depletion of atomic Fe between 87 and 92 km, between 11.11.2011 and 01.02.2012. The activation energy calculated from the slope of a linear regression is $11.2 \pm 1.5 \text{ kJ mol}^{-1}$. A good fit to the data is achieved for $E_a = 12.0 \text{ kJ mol}^{-1}$, $A = 2 \times 10^4$ and a total Fe abundance of $[\text{Fe}_{\text{total}}] \approx [\text{Fe}] + [\text{FeOH}] = 13,500 \text{ cm}^{-3}$. See text for details. (For interpretation of the references to colour in this figure caption, the reader is referred to the web version of this paper.)

Table 1

Reactions of neutral Fe-containing species in the MLT. R1 to R12 taken from Plane et al. (2015), M in R4 and R9: N_2 and O_2 . Units of rate coefficients: k_i bimolecular, $\text{cm}^3 \text{ molecule}^{-1} \text{ s}^{-1}$; k_t termolecular, $\text{cm}^6 \text{ molecule}^{-2} \text{ s}^{-1}$; J_i : s^{-1} .

Number	Reaction	Rate coefficient
R1	$\text{Fe} + \text{O}_3 \rightarrow \text{FeO} + \text{O}_2$	$2.9 \times 10^{-10} \exp(-174/T)$
R2	$\text{FeO} + \text{O} \rightarrow \text{Fe} + \text{O}_2$	$4.6 \times 10^{-10} \exp(-350/T)$
R3	$\text{FeO} + \text{O}_3 \rightarrow \text{FeO}_2 + \text{O}_2$	$3.0 \times 10^{-10} (-177/T)$
R4	$\text{FeO} + \text{O}_2 (+ \text{M}) \rightarrow \text{FeO}_3$	$4.4 \times 10^{-30} \exp(T/200)^{0.606}$
R5	$\text{FeO}_2 + \text{O} \rightarrow \text{FeO} + \text{O}_2$	$1.4 \times 10^{-10} \exp(-580/T)$
R6	$\text{FeO}_2 + \text{O}_3 \rightarrow \text{FeO}_3 + \text{O}_2$	$4.4 \times 10^{-10} \exp(-170/T)$
R7	$\text{FeO}_3 + \text{O} \rightarrow \text{FeO}_2 + \text{O}_2$	$2.3 \times 10^{-10} \exp(-2310/T)$
R8	$\text{FeO}_3 + \text{H}_2\text{O} \rightarrow \text{Fe}(\text{OH})_2 + \text{O}_2$	5×10^{-12}
R9	$\text{FeO} + \text{H}_2\text{O} (+ \text{M}) \rightarrow \text{Fe}(\text{OH})_2$	$5.1 \times 10^{-28} \exp(-200/T)^{1.13}$
R10	$\text{Fe}(\text{OH})_2 + \text{H} \rightarrow \text{FeOH} + \text{H}_2\text{O}$	$3.3 \times 10^{-10} \exp(-302/T)$
R11	$\text{FeO}_3 + \text{H} \rightarrow \text{FeOH} + \text{O}_2$	$3.0 \times 10^{-10} \exp(-796/T)$
R12	$\text{FeOH} + \text{H} \rightarrow \text{Fe} + \text{H}_2\text{O}$	$3.1 \times 10^{-10} \exp(-1264/T)$
R13	$\text{FeOH} + h\nu \rightarrow \text{Fe} + \text{OH}$	2×10^{-3}

oxidised to FeO_2 , conversion to FeOH is much more likely than reduction by atomic O, since the activation energies of R5 and R7 are comparatively large.

Yu et al. (2012) have presented an analysis of the solar influence on the altitude of the Fe layer bottomside. This effect is caused by the photolysis R13: $\text{FeOH} + h\nu \rightarrow \text{Fe} + \text{OH}$ and regularly observed at Davis whenever the solar elevation passes -5° , i.e. the altitude of the mesopause changes from being either sunlit or not. The rapid appearance of Fe below 80 km at sunrise is consistent with the photolysis rate of FeOH being much faster than the rate adopted in Feng et al. (2013). Recent analysis of data from Davis indicates that $J_{13}(\text{FeOH})$ is around $2 \times 10^{-3} \text{ s}^{-1}$ (Viehl, Feng and Plane (2015), *personal communication*). Taking all this into account, the rate of change of the Fe concentration, $d[\text{Fe}]/dt$, may be written as the sum of loss and production terms, which is approximately equal to zero at steady state:

$$\frac{d[\text{Fe}]}{dt} = -k_1[\text{Fe}][\text{O}_3] \left(\frac{k_3[\text{O}_3]}{k_2[\text{O}] + k_3[\text{O}_3]} \right) + (k_{12}[\text{H}] + J_{13})[\text{FeOH}] \approx 0$$

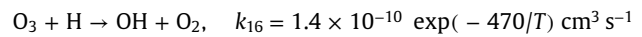
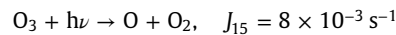
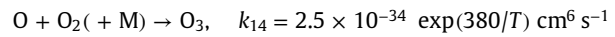
Since $k_2[\text{O}] \gg k_3[\text{O}_3]$ and also $J_{13} \gg k_{12}[\text{H}]$,

$$-k_1[\text{Fe}][\text{O}_3] \frac{k_3[\text{O}_3]}{k_2[\text{O}]} + J_{13}[\text{FeOH}] \approx 0$$

The partitioning of iron between Fe and FeOH is therefore given by the ratio χ :

$$\chi = \frac{[\text{Fe}]}{[\text{FeOH}]} = \frac{J_{13}k_2[\text{O}]}{k_1k_3[\text{O}_3]^2}$$

The O_3 concentration in the MLT is approximately in steady state between formation and loss by photolysis and the reaction with H:



so $[\text{O}_3] = k_{14}[\text{O}][\text{O}_2][\text{M}]/(J_{15} + k_{16}[\text{H}])$. As the solar elevation at Davis is larger than -5° within ± 40 days of the summer solstice, the MLT region is constantly sunlit. Therefore, since $J_{15} > k_{16}[\text{H}]$, $[\text{O}_3] \approx k_{14}[\text{O}][\text{O}_2][\text{M}]/J_{15}$ and χ can be expressed as

$$\chi = \frac{[\text{Fe}]}{[\text{FeOH}]} = \frac{J_{13}k_2[\text{O}]J_{15}^2}{k_1k_3(k_{14}[\text{O}][\text{O}_2][\text{M}])^2}$$

$[\text{O}]$ is not strongly temperature-dependent but largely governed by photochemistry. Since the data is taken over a constant altitude range of less than a scale height, the pressure is nearly constant. $[\text{O}]$, $[\text{O}_2]$ and $[\text{M}]$ will therefore vary as T^{-1} around the geometric mean temperature in this altitude and time range, $T_{\text{eff}} = 136 \text{ K}$. Hence, expressing χ in the Arrhenius form $\chi = A \exp(-E/T)$, the activation energy E is given by

$$E = -E_1 - E_3 + E_2 - 2 \times E_{14} + 5 \times T_{\text{eff}}$$

where E_i corresponds to the activation energy of reaction i divided by $R = 8.314 \text{ J K}^{-1} \text{ mol}^{-1}$ as taken from Plane et al. (2015). E is thus $(-174 - 177 + 350 + 2 \times 380 + 5 \times 136) = 1439 \text{ K}$, or about 12.0 kJ mol^{-1} .

The total amount of Fe, $[\text{Fe}_{\text{total}}] \approx [\text{Fe}] + [\text{FeOH}]$, should be approximately constant during this mid-summer period, since $[\text{Fe}_{\text{total}}]$ is a function of the meteoric injection rate and transport. Thus,

$$[\text{Fe}] = \frac{\chi}{1 + \chi} [\text{Fe}_{\text{total}}]$$

The data (red daily means) in Fig. 3 can then be fitted with three parameters, E_a , A and $[\text{Fe}_{\text{total}}]$. The pre-exponential factor A is given by

$$A = \frac{J_{13}A_2[\text{O}]J_{15}^2}{A_1A_3(A_{14}[\text{O}][\text{O}_2][\text{M}])^2}$$

where A_i refers to the pre-exponential factor of reaction i in Table 1. Taking $[\text{O}] = 6 \times 10^{11} \text{ cm}^{-3}$, $[\text{O}_2] = 1.3 \times 10^{13} \text{ cm}^{-3}$, and $[\text{M}] = 6.4 \times 10^{13} \text{ cm}^{-3}$ at 90 km and $T = 135 \text{ K}$ (Plane et al., 2015), A can be estimated as 2×10^4 . A very satisfactory fit (blue circles in Fig. 3) is achieved with $E_a = 12.0 \text{ kJ mol}^{-1}$, $A = 2 \times 10^4$ and $[\text{Fe}_{\text{total}}] = 13,500 \pm 900 \text{ cm}^{-3}$. The blue errorbars are calculated as RMS of the daily means to the fit.

Since not all activation energies listed in Table 1 are well known and several simplifying assumptions have been made in the above calculation, an additional role played by the uptake of Fe and FeOH on ice particles at low temperatures cannot be ruled out. However, this exercise demonstrates that the decrease of Fe

between 87 and 92 km which is observed in mid-summer can be explained by gas-phase chemistry alone.

4. Discussion

Due to the unique combination of radar and lidar instruments at Davis, we are able to directly investigate the correlation between large and small ice particles (NLC and PMSE) and Fe densities. A striking feature of Fig. 2 is the onset of the Fe depletion before the first occurrence of NLC and PMSE. Furthermore, not only are column densities dropping before a maximum in NLC brightness and occurrence frequency is observed in early January, they even increase significantly during the main NLC period. Indeed, a local column density maximum of $\sim 8 \times 10^9 \text{ cm}^{-2}$ occurs in mid-January when NLC and PMSE occurrence is high. Densities in this period are nearly as high as in mid-September, i.e. well before the summer transition of the MLT. Moreover, no sharp drop in column density, layer shape or other parameters are observed with the beginning and end of both the PMSE and NLC season, in contrast to K observations in the Northern Hemisphere. This is strong evidence that an uptake of Fe on ice particles cannot be the major driving factor in the change of the annual cycle of Fe densities leading to the strong summer time depletion. The density drop is taking place considerably earlier than ice particles occur and shows an unexpected anti-correlated behaviour in January.

These observations question explanations of differences in the midsummer Fe layer behaviour between two Antarctic stations published previously (Gardner et al., 2011). That study attributed the annual change—and especially the summer time Fe depletion below 95 km altitude—to the uptake of Fe on NLC particles. A one-to-one comparison between that work and the current study is not straightforward, as the dataset presented in the earlier study is not only at a different longitude, but includes considerably fewer hours and days of measurement. This was perhaps one reason that those authors applied an harmonic fit to the data. A detailed comparison of the harmonically fitted data with the higher resolution dataset (smoothed with a 14 day Hanning window) presented here may yield misleading results based on the different mathematical treatment of the data, and not on geophysics. For example, the raw data in Fig. 1 in Gardner et al. (2011) shows an indication of low densities for two weeks in mid-December and higher densities in January at Rothera. This feature however disappears after applying the harmonic fit, as a comparison with Fig. 2 therein shows. We conclude from the available datasets that Fe depletion and NLC occurrence are both caused by low temperatures, and not necessarily one by the other.

However, we note that this does not contradict a localised metal uptake by NLC particles as presented by Plane et al. (2004). Those authors observed almost complete removal of Fe within very strong NLCs with high volumetric surface areas. Such localised “bite-outs” (in a vertical sense) are not explicable by gas-phase chemistry, and occur because heterogeneous removal is fast enough to compete with vertical mixing and fresh meteoric ablation. However, heterogeneous removal within weaker NLCs will be difficult to discern from gas-phase removal. As ice particles in the MLT have a relatively short life time compared to the seasonal change, a local uptake might be not large enough or last long enough to significantly impact the entire Fe layer on a seasonal scale.

Murray and Plane (2005) investigated the uptake coefficients for various metals. That study found uptake coefficients for K and Na on cubic ice close to unity. For Fe, an uptake coefficient close to unity was found for higher temperatures above 140 K as well, but this decreased rapidly for temperatures lower than 135 K to

$\gamma_{\text{Fe}} = 3 \times 10^{-3}$ at 80 K. A lower relative importance of metal uptake on ice particles for Fe at Antarctic sites compared to neutral gas chemistry might therefore be caused by the very low mesopause temperatures of down to 100 K in waves and less than 135 K in the daily mean around summer solstice.

We conclude that ice particles in general (NLC and PMSE) and low Fe densities at Antarctic sites largely occur simultaneously during the summer period since they are both consequences of low temperatures. An uptake of Fe atoms on ice particle surfaces cannot be excluded, but is not the driving factor in the annual change of Fe density.

This interpretation is supported by WACCM-Fe calculations which show a strong positive correlation between Fe density and temperature and a decrease in column abundance as observed at Davis, Rothera and the South Pole. Although Fe density is further reduced if an uptake on ice particles is considered, the model captures the seasonal variation of Fe even without PMC scheme (W. Feng (2015), *personal communication*). The model simulations yield realistic results but are limited by the underlying temperature field and circulation used in WACCM. In particular, the high summer mesopause altitude and extremely low mesopause temperatures reported by Morris et al. (2012) and Lübken et al. (2014) have not yet been reproduced. Additionally, absolute density calculations crucially rely on a realistic representation of the meteoric influx as well as careful balancing of reaction rate coefficients. The magnitude of the meteoric influx is a matter of ongoing discussion (Plane, 2012) and not all reaction rates are so far well known from laboratory experiments. Further WACCM-Fe results with improved rate coefficients and better temperature representation might give even better insights in the behaviour of the metal layer.

We want to further point to the uplift of the Fe layer's centroid altitude in the upper panel of Fig. 1. We emphasise that the whole layer including the upper boundary is shifted upwards and that the lower boundary is nearly linearly shifted upwards from September onwards, clearly before the onset of ice particles. This is not simply a relative shift due to a depletion in the lower parts of the MLT Fe layer. We interpret the summer time uplift of the centroid altitude, previously also reported by Gardner et al. (2005, 2011) and others, to be caused by the summer time dynamic uplift at polar latitudes. Other possible causes could be the changed chemical equilibrium between Fe and its reservoir species due to drastically changed temperatures and solar irradiance. However, it should be noted that increased conversion of Fe to Fe^+ on the topside of the layer—caused by charge transfer with NO^+ and O_2^+ ions and photo-ionisation—should depress the topside of the Fe layer. This makes the uplift all the more striking.

The calculations presented in Section 3.3 confirm that temperature dependent chemical reactions play a significant role in the annual cycle of Fe. They alter the equilibrium between atomic Fe and its molecular bound species in such a way that low temperatures favour the latter over the former and remove Fe. These considerations on their own do not completely rule out an additional metal uptake on ice particles. However, the calculations show that under reasonable assumptions neutral gas chemistry alone can explain the strong summer time Fe depletion in the Antarctic mesopause region. Further comprehensive 3D model calculations as performed by WACCM-Fe, laboratory studies of metal containing species and analyses of atmospheric measurements are necessary to improve our knowledge about important reaction rate coefficients. This will help to determine the exact contribution of all chemical reactions, transport and a potential additional effect of ice particle adsorption on the mesospheric Fe layer.

At this point, we cannot provide measurements of winds to

analyse the role of latitudinal transport. Future simulations such as performed by Feng et al. (2013) might help to understand the relative importance of horizontal or vertical transport in relation to the chemical analysis performed here. The role of wintertime convergence and summertime divergence over the South Pole was first proposed by Gardner et al. (2005) to explain the very large seasonal variation of Na and Fe observed. However, the importance of horizontal transport depends on the residence time of Fe and its reservoirs above 80 km, and hence to the rate of vertical transport. More understanding of these processes is required.

Note that optical measurements at polar latitudes pose a significant technological challenge around summer solstice. The mid-December features presented here require regular measurements in a period of a few weeks. In particular the brief low temperatures coinciding with low absolute Fe densities might be easily missed by instruments with low SNR.

5. Conclusion

Our calculations show that neutral gas-phase chemistry alone can explain most of the strong summer time Fe depletion in the Antarctic mesopause region. The measurements presented here show that ice particle occurrence does not appear to be the dominant driving factor in the summer time depletion of the annual cycle of the Fe layer in the mesopause region at Davis, Antarctica. Although conclusive evidence for the uptake of various metals on ice particles has been reported for singular measurements by several authors, the effect alone cannot explain the seasonal Fe layer cycle presented in this study.

Our measurements show a general uplift of the Fe layer during the summer months including the upper boundary. An increase of the layer's centroid altitude due to heterogeneous removal of Fe and FeOH on the underside of the layer alone is therefore not sufficient to account for this.

A detailed analysis of the intraday variability in Fe density, the correlation with temperature and the occurrence of ice particles such as NLC and PMSE on short time scales will be the subject of further studies. This will help to quantify the uptake rates of Fe atoms on ice particles and thus help to understand how large or small an additional uptake effect is on short time scales and at various temperature regimes. A further combination of chemical modelling with the input of our observational data will help to gain a better understanding of the chemical processes involved.

Acknowledgements

This project was funded by the Australian Antarctic Division under AAP 2325 and the Leibniz-Institute of Atmospheric Physics. J.M.C. Plane's work is supported by the European Research Council (Project no. 291332-CODITA). We thank W. Feng, G. Sonnemann and J.C. Gómez Martín for fruitful discussions about Fe chemistry as well as A.D. James for helpful comments on the paper. We thank R. Latteck for his help in preparing PMSE data.

We would like to express our special gratitude to all expeditioners of the 64th, 65th and 66th ANARE at Davis Station for their dedicated support throughout the project.

References

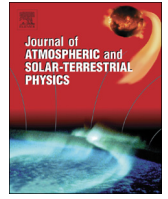
Baumgarten, G., Chandran, A., Fiedler, J., Hoffman, P., Kaifler, N., Lumpe, J., Merkel, A.,

- Randall, C.E., Rusch, D., Thomas, G., 2012. On the horizontal and temporal structure of noctilucent clouds as observed by satellite and lidar at ALOMAR (69N). *Geophys. Res. Lett.* 39, L01803. <http://dx.doi.org/10.1029/2011GL049935>.
- Chu, X., Espy, P.J., Nott, G.J., Dietrich, J.C., Gardner, C.S., 2006. Polar mesospheric clouds observed by an iron Boltzmann lidar at Rothera (67.5°S, 68.0°W), Antarctica, from 2002 to 2005: properties and implications. *J. Geophys. Res.* 108. <http://dx.doi.org/10.1029/2002JD002524>.
- DeLand, M.T., Shettle, E.P., Thomas, G.E., Olivero, J.J., 2006. A quarter-century of satellite polar mesospheric cloud observations. *J. Atmos. Solar-Terr. Phys.* 68, 9–29. <http://dx.doi.org/10.1016/j.jastp.2005.08.003>.
- Feng, W., Marsh, D.R., Chipperfield, M.P., Janches, D., Höffner, J., Yi, F., Plane, J.M.C., 2013. A global atmospheric model of meteoric iron. *J. Geophys. Res.* 118. <http://dx.doi.org/10.1002/jgrd.50708>.
- Gardner, C.S., Plane, J.M.C., Pan, W., Vondrak, T., Murray, B.J., Chu, X., 2005. Seasonal variations of the Na and Fe layers at the South Pole and their implications for the chemistry and general circulation of the polar mesosphere. *J. Geophys. Res.* 110 (D10), D10302. <http://dx.doi.org/10.1029/2004JD005670>.
- Gardner, C.S., Chu, X., Espy, P.J., Plane, J.M.C., Marsh, D.R., Janches, D., 2011. Seasonal variations of the mesospheric Fe layer at Rothera, Antarctica (67.5°S, 68.0°W). *J. Geophys. Res.* 116, D02304. <http://dx.doi.org/10.1029/2010JD014655>.
- Höffner, J., Lautenbach, J., 2009. Daylight measurements of mesopause temperature and vertical wind with the mobile scanning iron Lidar. *Opt. Lett.* 34, 1351–1353.
- Lübken, F.-J., Höffner, J., 2004. Experimental evidence for ice particle interaction with metal atoms at the high latitude summer mesopause region. *Geophys. Res. Lett.* 31. <http://dx.doi.org/10.1029/2004GL019586>.
- Lübken, F.-J., Berger, U., Baumgarten, G., 2009. Stratospheric and solar cycle effects on long-term variability of mesospheric ice clouds. *J. Geophys. Res.* 114, D00106. <http://dx.doi.org/10.1029/2009JD012377>.
- Lübken, F.-J., Höffner, J., Viehl, T.P., Kaifler, B., Morris, R.J., 2011. First measurements of thermal tides in the summer mesopause region at Antarctic latitudes. *Geophys. Res. Lett.* 38. <http://dx.doi.org/10.1029/2011GL050045>.
- Lübken, F.-J., 2013. Turbulent scattering for radars: a summary. *J. Atmos. Solar-Terr. Phys.* 107, 1–7. <http://dx.doi.org/10.1016/j.jastp.2013.10.015>.
- Lübken, F.-J., Höffner, J., Viehl, T.P., Kaifler, B., Morris, R.J., 2014. Winter/summer mesopause temperature transition in 2011/2012 at Davis (68°S). *Geophys. Res. Lett.* 41. <http://dx.doi.org/10.1002/2014GL060677>.
- Morris, R.J., Murphy, D.J., Reid, I.M., Holdsworth, D.A., Vincent, R.A., 2004. First polar mesosphere summer echoes observed at Davis, Antarctica (68°S). *Geophys. Res. Lett.* 31 (16), L16111. <http://dx.doi.org/10.1029/2004GL020352>.
- Morris, R.J., Höffner, J., Lübken, F.-J., Viehl, T.P., Kaifler, B., Klekociuk, A.R., 2012. Experimental evidence of a stratospheric circulation influence on mesospheric temperatures and ice-particles during the 2010–2011 austral summer at 69°S. *J. Atmos. Solar-Terr. Phys.* 89. <http://dx.doi.org/10.1016/j.jastp.2012.08.007>.
- Murray, B.J., Plane, J.M.C., 2005. Uptake of Fe, Na and K atoms on low-temperature ice: implications for metal atom scavenging in the vicinity of polar mesospheric clouds. *Phys. Chem. Chem. Phys.* 7, 3970–3979.
- Plane, J.M.C., 2003. Atmospheric chemistry of meteoric metals. *Chem. Rev.* 103, 4963–4984. <http://dx.doi.org/10.1021/cr0205309>.
- Plane, J.M.C., Murray, B.J., Chu, X., Gardner, C.S., 2004. Removal of meteoric iron on polar mesospheric clouds. *Science* 304 (5669), 426–428. <http://dx.doi.org/10.1126/science.1093236>.
- Plane, J.M.C., 2012. Cosmic dust in the earth's atmosphere. *Chem. Soc. Rev.* 41, 6507–6518.
- Plane, J.M.C., Feng, W., Dawkins, E.M.C., 2015. The mesosphere and metals: chemistry and changes. *Chem. Rev.* <http://dx.doi.org/10.1021/cr500501m>
- Raizada, S., Rapp, M., Lübken, F.-J., Höffner, J., Zeche, M., Plane, J.M.C., 2007. Effect of ice particles on the mesospheric potassium layer at Spitsbergen (78°N). *J. Geophys. Res.* 112, D08307. <http://dx.doi.org/10.1029/2005JD006938>.
- Rapp, M., Lübken, F.-J., Mülleemann, A., Thomas, G., Jensen, E., 2002. Small scale temperature variations in the vicinity of NLC: experimental and model results. *J. Geophys. Res.* 107 (D19), 4392. <http://dx.doi.org/10.1029/2001JD001241>.
- Rapp, M., Lübken, F.-J., 2004. Polar mesosphere summer echoes (PMSE): review of observations and current understanding. *Atmos. Chem. Phys.* 4, 2601–2633.
- Russell III, J.M., Bailey, S.M., Gordley, L.L., Rusch, D.V., Horanyi, M., Hervig, M.E., Thomas, G.E., Randall, C.E., Siskind, D.E., Stevens, M.H., Summers, M.E., Taylor, M.J., Englert, C.R., Espy, P.J., McClintock, W.E., Merkel, A.W., 2009. The Aeronomy of Ice in the Mesosphere (AIM) mission: overview and early science results. *J. Atmos. Solar-Terr. Phys.* 71, 289–299. <http://dx.doi.org/10.1016/j.jastp.2008.08.011>.
- Self, D.E., Plane, J.M.C., 2003. A kinetic study of the reactions of iron oxides and hydroxides relevant to the chemistry of iron in the upper mesosphere. *Phys. Chem. Chem. Phys.* 5. <http://dx.doi.org/10.1039/b211900e>.
- She, C.Y., Williams, B.P., Hoffmann, P., Latteck, R., Baumgarten, G., Vance, J.D., Fiedler, J., Acott, P., Fritts, D.C., Lübken, F.-J., 2006. Simultaneous observation of sodium atoms, NLC and PMSE in the summer mesopause region above ALOMAR, Norway (69°N, 12°E). *J. Atmos. Solar-Terr. Phys.* 68, 93–101. <http://dx.doi.org/10.1016/j.jastp.2005.08.014>.
- Thayer, J.P., Pan, W., 2006. Lidar observations of sodium density depletions in the presence of polar mesospheric clouds. *J. Atmos. Solar-Terr. Phys.* 68, 85–92. <http://dx.doi.org/10.1016/j.jastp.2005.08.012>.
- von Zahn, U., Höffner, J., 1996. Mesopause temperature profiling by potassium lidar. *Geophys. Res. Lett.* 23, 141–144.
- Yu, Zh., Chu, X., Huang, W., Fong, W., Roberts, B.R., 2012. Seasonal variations of the Fe layer in the mesosphere and lower thermosphere: four season variability and solar effects on the layer bottomside at McMurdo (77.8°S, 166.7°E). *J. Geophys. Res.* 117, D22302. <http://dx.doi.org/10.1029/2012JD18079>.



Journal of Atmospheric and Solar-Terrestrial Physics

journal homepage: www.elsevier.com/locate/jastp



Corrigendum

Corrigendum to “Summer time Fe depletion in the Antarctic mesopause region” [J. Atmos. Sol.–Terr. Phys. 127(2015)97–102]



T.P. Viehl^{a,*}, J. Höffner^a, F.-J. Lübken^a, J.M.C. Plane^b, B. Kaifler^{a,c}, R.J. Morris^d

^a Leibniz-Institute of Atmospheric Physics (IAP) at the University of Rostock, Schloßstr. 6, 18225 Kühlungsborn, Germany

^b School of Chemistry, University of Leeds, Leeds LS2 9JT, United Kingdom

^c Now at German Aerospace Centre (DLR), Institute of Physics of the Atmosphere, Münchner Str. 20, 82234 Wessling, Germany

^d Formerly at Australian Antarctic Division (AAD), 203 Channel Hwy, Kingston, Tasmania 7050, Australia

It has been brought to our attention that there is an error in the expression for *A* on p. 100 of Viehl et al. (2015). The quotient of concentrations in the equation for *A* was expressed as

$$\frac{[\text{O}]}{([\text{O}][\text{O}_2][\text{M}])^2} = \frac{[\text{O}]_{\text{eff}}}{([\text{O}]_{\text{eff}}[\text{O}_2]_{\text{eff}}[\text{M}]_{\text{eff}})^2} \left(\frac{T}{T_{\text{eff}}}\right)^5$$

$$\approx \frac{[\text{O}]_{\text{eff}}}{([\text{O}]_{\text{eff}}[\text{O}_2]_{\text{eff}}[\text{M}]_{\text{eff}})^2} e^5 \exp(-5T_{\text{eff}}/T)$$

where the *eff* subscript indicates values at the reference temperature of $T_{\text{eff}} = 136 \text{ K}$.

The factor of e^5 was mistakenly omitted from the equation for *A*. Since $e^5 = 148$, *A* is 3×10^6 , rather than 2×10^4 as stated in the paper. This means that the fit through the lidar observations of [Fe] versus *T* in Fig. 3 (the blue curve) cannot be explained solely by temperature-dependent gas phase chemistry under the assumptions and simplifications made.

In fact, since this paper was published the photolysis rate of FeOH, *J*(FeOH), has been shown by some of the authors to be around $6 \times 10^{-3} \text{ s}^{-1}$, which is even larger than the value listed (for R13) in Table 1 (Viehl et al., 2016). This further increases *A* and questions the simplifications.

Moreover, Viehl et al. (2016) concluded that the much larger photolysis rate leads to a nearly complete depletion of FeOH during sunlit periods. FeOH can therefore not be a significant reservoir for Fe around summer solstice. Hence, the fundamental assumption of a temperature dependent partitioning between FeOH and Fe made by Viehl et al. (2015) is not justified in the polar summer mesosphere.

Nevertheless, the major conclusion of the paper stands:

That the summertime depletion of the Fe layer is not caused primarily by the heterogeneous removal of Fe (and its compounds) on polar mesospheric ice cloud (PMC/NLC) particles. The clear observational evidence for this is described in Section 3.2 of the

paper. Further evidence is provided from 3D model simulations of the Fe layer in the Whole Atmosphere Community Climate Model (WACCM-Fe) (Feng et al., 2013). Simulations were performed for the location of Davis (69°S), both with PMC formation and the uptake of Fe species as described by Feng et al. (2013), and also without PMC uptake. Fig. 1 shows the Fe density at 86 km, recorded every 30 min for the months of December and January. The simulation with PMC uptake is shown in black, and without uptake in red. The temperature-dependence of the Fe density is essentially identical for both scenarios, demonstrating that PMC uptake plays a limited role. Furthermore, the fraction of iron that is in the form of atomic Fe remains roughly constant (~60%) over the 125–180 K temperature range (not shown). Thus, the 7-fold increase in Fe density with temperature may be explained due to a

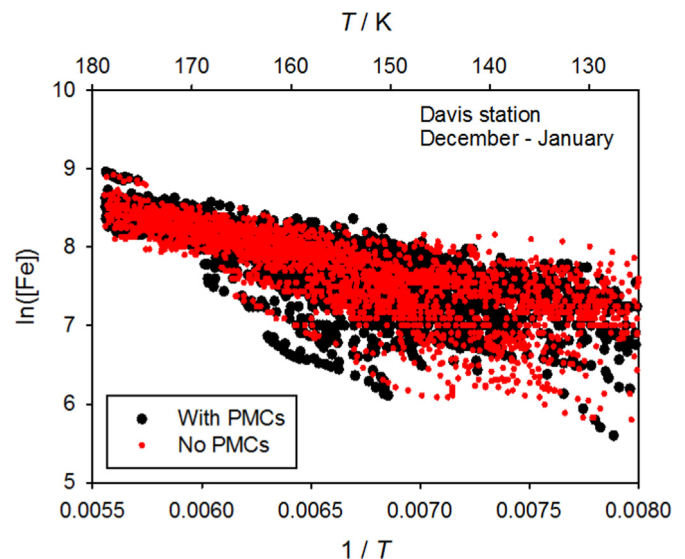


Fig. 1. Fe density at 86 km as a function of temperature, from WACCM-Fe simulations with PMC formation and uptake of Fe species (black points), and in the absence of PMC uptake (red points).

DOI of original article: <http://dx.doi.org/10.1016/j.jastp.2015.04.013>

* Corresponding author.

E-mail address: viehl@iap-kborn.de (T.P. Viehl).

change in the *total* iron density.

This indicates that dynamics plays an important role:

When upwelling is strongest, the divergence of Fe-poor air from the middle mesosphere produces low Fe densities and simultaneously the coldest temperatures. Hence, Fe density and temperature are positively correlated. This interpretation is supported by the reported uplift of the Fe layer at Davis (Viehl et al., 2015). However, Fe atoms do not constitute a passive tracer and the complex temperature dependent interaction with the background atmosphere needs to be considered when quantitatively investigating the upwelling. Further modelling work, high resolution vertical and horizontal wind observations as well as laboratory studies of important chemical reaction rates are required to determine the contributions by upwelling and temperature dependent chemistry.

Finally, there are two typographical errors in Table 1 of the paper. The rate coefficient for R3 should be $3 \times 10^{-10} \exp(-177/T)$, and R4 should be $4.4 \times 10^{-30} (T/200)^{0.606}$.

The authors would like to apologise for any inconvenience caused.

Acknowledgements

We would like to thank Prof. C.S. Gardner for pointing out the mathematical error in the paper, and Dr. W. Feng for providing the WACCM simulations.

References

- Feng, W., Marsh, D.R., Chipperfield, M.P., Janches, D., Hoeffner, J., Yi, F., Plane, J.M.C., 2013. A global atmospheric model of meteoric iron. *J. Geophys. Res.* **118** (16), 9456–9474.
- Viehl, T.P., Höffner, J., Lübken, F.-J., Plane, J.M.C., Kaifler, B., Morris, R.J., 2015. Summer time Fe depletion in the Antarctic mesopause region. *J. Atmos. Sol.-Terr. Phys.* **127**, 97–102.
- Viehl, T.P., Plane, J.M.C., Feng, W., Höffner, J., 2016. The photolysis of FeOH and its effect on the bottomside of the mesospheric Fe-layer. *Geophys. Res. Lett.* accepted for publication, <http://dx.doi.org/10.1002/2015GL067241>.

First measurements of thermal tides in the summer mesopause region at Antarctic latitudes

F.-J. Lübken,¹ J. Höffner,¹ T. P. Viehl,¹ B. Kaifler,¹ and R. J. Morris²

Received 17 October 2011; revised 14 November 2011; accepted 15 November 2011; published 28 December 2011.

[1] We present the first detection of thermal tides in the middle atmosphere at polar latitudes in summer. The IAP iron lidar is in operation in Davis (69°S, 78°E), Antarctica, since December 2011 and measures temperatures in the height range 84–96 km with an accuracy of 1–3 K (after 1 hour integration) with an effective altitude resolution of 1 km. Iron densities are observed from ~75–140 km. We analyze 171 hours of observations in the period 11–28 January, 2011, and find strong tidal modulations in Fe density and temperatures. Typical amplitudes of thermal tides are 2–4 K for both the diurnal and semidiurnal component. The diurnal tide is larger (smaller) than the semidiurnal component below (above) ~90 km. The phase of the diurnal tide decreases with altitude by ~1.3 h/km which corresponds to a vertical wavelength of ~30 km. A similar phase progression is observed in Fe densities extending below and above the height range of temperature measurements. The overlay of diurnal and semidiurnal components leads to tidal modulations of up to ±6 K for temperatures, and up to ±4000/ccm (=±40%) for Fe number densities. These modulations are much larger compared to most simulations and point to some missing processes in tidal modeling. **Citation:** Lübken, F.-J., J. Höffner, T. P. Viehl, B. Kaifler, and R. J. Morris (2011), First measurements of thermal tides in the summer mesopause region at Antarctic latitudes, *Geophys. Res. Lett.*, 38, L24806, doi:10.1029/2011GL050045.

1. Introduction

[2] It is generally recognized that tides can play an important role for the thermal and dynamical structure of the mesosphere/lower thermosphere. Tides can significantly modify gravity wave propagation and change composition due to transport. In general, tides interact with gravity waves and larger scale wave motions (see *McLandress* [2002] and *Mayr et al.* [2005] for some recent results). Tidal amplitudes are largest at equatorial latitudes and are believed to be small at polar latitudes during summer and winter since solar excitation varies only little during 24 hours (permanent sunlight or darkness). Unfortunately, very little is known about thermal tides at polar latitudes during summer, mainly because observations are difficult to perform here. More information on thermal tides is needed, for example, to estimate a potential bias of trends in polar mesospheric clouds (PMC) observed by satellite instruments which cover certain local times only (varying from year to year) [*DeLand et al.*,

2007]. Tidal effects in general may influence the analysis of trends in the middle atmosphere [*Beig et al.*, 2003].

[3] In the summer polar mesosphere most information on tides comes from wind measurements with radars or from satellites [see, e.g., *Portnyagin et al.*, 2004; *Oberheide et al.*, 2006; *Hoffmann et al.*, 2010]. Satellite borne temperature measurements have also been used to deduce thermal tides, but mainly at low latitudes or at lower heights, or during darkness only (for some recent examples see *Forbes and Wu* [2006]). Furthermore, satellite observations of tides are often hampered by the slow orbit precession which requires several weeks for a total coverage of all local times. Resonance and Rayleigh lidars provide quasi-continuous coverage of temperatures in the MLT region and have been used to study thermal tides, but only at mid latitudes mainly because it is difficult to measure temperatures during daylight [*She et al.*, 2002; *Shepherd and Fricke-Begemann*, 2004]. Daylight also prevents ground based airglow measurements of tides to be applied in polar summer. The combination of ground based and satellite borne techniques can circumvent some of the uncertainties described above [*Ward et al.*, 2010].

[4] In this paper we present first observations of tidal signatures in the height range of approximately 80 to 130 km (smaller height range for temperatures) during summer, derived from resonance lidar observations at Davis (69°S, 78°E). We note that from a 24 h/12 h oscillation observed at only one station the cause of this variation (migrating tide, non-migrating tide, gravity waves) cannot be unambiguously identified. As will be discussed later, there are strong indications that the modulations presented in this paper are indeed caused by tides (and not by gravity waves). We will compare our results with the latest version of the Global Scale Wave Model (GSWM09) and also with the tidal variations in the empirical MSIS-00 model (Mass Spectrometer Incoherent Scatter model) [*Zhang et al.*, 2010; *Picone et al.*, 2002].

2. Instrumentation, Observations, and Data Analysis

[5] The mobile scanning iron lidar is a two-wavelength system (772 nm/386 nm). It determines mesospheric temperatures by probing the Doppler broadened iron resonance line at 386 nm with a frequency-doubled alexandrite laser [*Höffner and Lautenbach*, 2009]. The system allows to measure temperatures during full daylight with a typical uncertainty of 1–3 Kelvin after 1 hour integration. These values refer to typical summer conditions with lowest metal densities and the Sun being at the highest elevation. Here we report about observations performed during 12 days at Davis from 11–28 January 2011.

¹Leibniz Institute of Atmospheric Physics, Kühlungsborn, Germany.

²Australian Antarctic Division, Kingston, Tasmania, Australia.

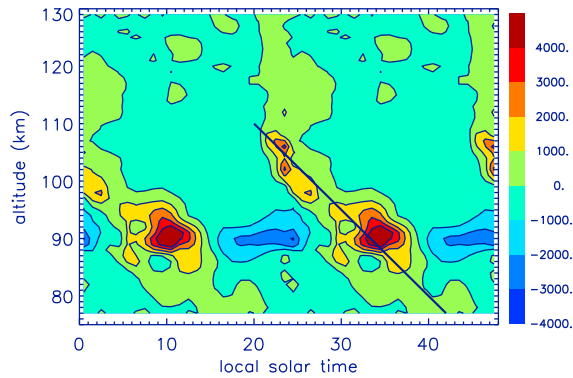


Figure 1. Iron number density deviations from the seasonal mean in $1/\text{cm}^3$. The straight line presents a phase progression corresponding to a vertical wavelength of -36 km. To highlight the phase progression with altitude, the deviations are shown for a period of two days.

[6] We consider only measurement periods which are typically longer than 12 hours. Within a period of 17 days this gave 12 days with observations with an average of 14.3 hours per day (42% of the total time). In total, 171 hours of observations are used for this study. From the raw data we first subtract the seasonal variation consisting of a yearly and half-yearly component. Then all measurements within a given hour-of-day and altitude bin of 1 km are averaged considering instrumental uncertainties (1–3 K, see above) and natural variability. The latter is determined as the root mean square of the deviations of all data from the mean. It amounts to approximately ± 10 K (nearly independent of altitude) and dominates the total uncertainty. Finally, tidal amplitudes and phases are determined from a non-linear fit of the following equation taking these uncertainties into account:

$$T(z) = A_0(z) + \sum_i A_i(z) \cdot \cos\left(\frac{2\pi \cdot (t - \phi_i(z))}{P_i}\right) \quad (1)$$

where $A_i(z)$ are the amplitudes, and $\phi_i(z)$ are the phases (=time of maximum) of the diurnal ($P_1 = 24$ h) and semidiurnal ($P_2 = 12$ h) tide. Times are given in local solar time (LST), i.e., where the Sun has its largest elevation at 12:00 noon (LST = UT + 5 h 12 min; UT = universal time). In order to judge the goodness of the fit we determine the reduced χ^2_ν values. We have considered the uncertainties of the data point, combining instrumental errors and natural variability (see above). In most altitudes we find χ^2_ν values of 0.9–1.2. The fact that χ^2_ν is close to unity indicates that the data are well described by the fit.

3. Results

[7] In Figure 1 we show a contour plot of iron density variations which clearly demonstrates daily variations. We show deviations from a seasonal mean smoothed by a 3 point running mean. The time of local maximum decreases with altitude from 75 km to ~ 108 km. Note that Fe densities rely on the raw signal only (i.e., on signal strength) and do not require any spectral decomposition. Therefore, the tidal analysis is less sensitive to total Fe density and covers an extended height range from 75 to 140 km (shown up to

130 km in Figure 1). Around 90 km the modulation is largest (up to approximately $\pm 4000/\text{ccm}$) which is as much as $\pm 40\%$ compared to typical densities at these altitudes. Above ~ 110 km the tidal modulation is rather small in absolute number densities, but still large considering relative variations.

[8] A summary of temperature deviations is shown in Figure 2. Below approximately 90 km the diurnal component is dominant and leads to generally higher temperatures in the morning hours (~ 6 –12 LST) and lower 12 hours later. The magnitude of the modulation is approximately ± 4 –7 K. Above ~ 92 km a semi-diurnal variation is clearly visible.

[9] In Figure 3 we show the altitude variation of amplitudes and phases (12 h and 24 h). Typical amplitudes are 2–4 K. The diurnal tide is larger compared to the semi-diurnal component for $z < 90$ km. The phase of the diurnal tide decreases with height up to 96 km, except for a ‘jump’ at 93–94 km. This phase jump might be caused by data coverage which is somewhat poor at altitudes above 92 km. As can be seen from Figure 3 the error bars at these altitudes are indeed larger, but only moderately since the total uncertainty is determined by natural variability (and less by instrumental uncertainties) which is nearly constant with altitude. The general phase decrease with altitude of the diurnal tide is approximately -1.26 km/h which corresponds to a vertical wavelength of ~ 30 km. The phases of both tidal components are rather similar (~ 5 –10 LST) at most altitudes which leads to constructive interference and substantial temperature deviations. The observed amplitudes are much larger compared to GSWM09, both for the diurnal and semi-diurnal component. The diurnal tide from observations is out of phase with GSWM09, whereas the semi-diurnal phases are similar at higher altitudes. We have also compared with MSIS-00 and find poor agreement, in particular for the diurnal amplitude below 90 km which is only 0.5–1.0 K in MSIS-00, i.e., much smaller compared to our lidar results. These discrepancies are perhaps not surprising since MSIS-00 is based on very limited observations in the high latitude summer MLT region.

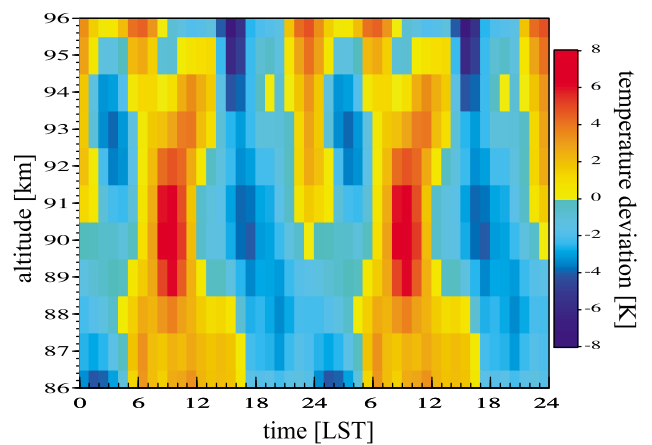


Figure 2. Temperature deviations from the seasonal mean in Kelvin. A total of 171 hours of observations within 12 days in January 2011 contribute to this plot. To highlight the phase progression with altitude, the deviations are shown for a period of two days.

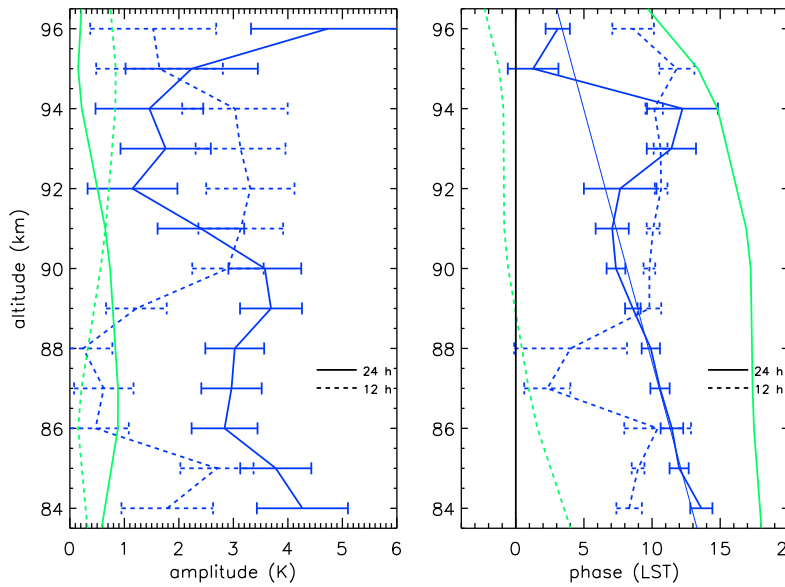


Figure 3. (left) Amplitudes and (right) phases of diurnal (solid lines) and semi-diurnal (dotted lines) tides. Blue: from observations; green: from GSWM09 [after Zhang *et al.*, 2010]. The blue straight line in the right panel presents a phase progression corresponding to a vertical wavelength of -30 km.

[10] Using the fit coefficients shown in Figure 3 we determined the superposition of diurnal and semidiurnal temperature fluctuations at all heights (Figure 4). Temperatures are systematically lower (higher) compared to the mean by as much as approximately ± 6 K. This is significantly larger compared to GSWM09 which shows maximum deviations of only ± 1 K in the entire height range. The overlay of 24 h and 12 h tides leads to a systematic variation of temperature minima with altitude where the minimum appears shortly after midnight at 84–85 km and significantly later (16–18 LST) at ~ 90 –96 km. The temperature deviations shown in Figure 4 resemble the original deviations as shown in Figure 2. We have studied the differences between the original temperatures and the reconstructions and did not find any systematic variations. This implies that tides cover a substantial part of the systematic temperature variations.

4. Discussion

[11] What distinguishes our tides from gravity waves? Since gravity waves are generated with random phase they average out if several days are overlayed. Furthermore, modulation at several altitudes with time would hardly show a variation compatible with diurnal and semidiurnal tides. The goodness of fit test suggests that indeed a major part of the systematic temperature variability is expressed in terms of tides. From the density variations shown in Figure 1 we see that the tidal phase structure extends way below and above the height region where temperatures are derived. A typical vertical wavelength in the lower part of Figure 1 is $\lambda_z \approx -36$ km which is consistent with the phase progression of the temperature variations shown in Figure 2. Since Fe densities and ambient temperatures are derived independently from each other, this supports our conclusion that the modulations observed are indeed caused by tides. The fact that the tidal component is persistent when averaging over

several days indicates that the processes leading to tidal modulation are not random.

[12] Murphy *et al.* [2006] have summarized tidal analysis from radar wind measurements performed at several stations in Antarctica. The amplitude and phase variations with height are rather complex and vary substantially with season. In January, diurnal and semidiurnal tide are of similar magnitude. The phase of the semidiurnal tide varies by several hours throughout the month, whereas the variation is smaller but still significant for the diurnal component. If such phase variations should also exist for temperatures during the 12 days of our observations, this could reduce the amplitude derived from our data, and also modify the phase. The tidal signal in temperatures is not strong enough to examine such a phase shift.

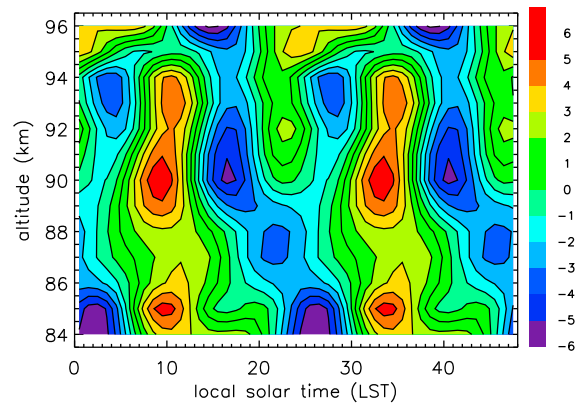


Figure 4. Temperature deviations in Kelvin due to a combination of 24 h and 12 h tides. To highlight the phase progression with altitude, the deviations are shown for a period of 2 days.

[13] We note that there are several similarities in the tidal variations of Fe densities and temperatures, as can be seen by comparing Figures 1 and 2. For example, temperature and iron density deviations are both positive and large around 90 km between 6 and 12 LST. This indicates that temperature dependent chemistry may contribute to Fe density variation. We realize that other factors may influence diurnal variations of Fe densities, such as variable sources (meteors), vertical/horizontal transport, varying solar inclination, etc. A full chemistry/transport model is required to disentangle the physical/chemical processes involved.

[14] In general, theoretical studies predict rather small amplitudes for thermal tides at polar latitudes during summer [e.g., Achatz et al., 2008]. Most model studies do not even present results on thermal tides under these conditions. The observed amplitudes presented in this paper are generally larger compared to these models. This is true also for GSWM09 which includes consideration of non-migrating tides. We note that radar wind observations at high latitudes in summer also show tidal amplitudes significantly larger compared to GSWM09 [Murphy et al., 2006]. Mayr et al. [2005] have studied the excitation of non-migrating tides by the interaction of planetary waves, gravity waves, and migrating tides. In the southern hemisphere summer at high latitudes they find amplitudes of several Kelvin for the semi-diurnal component (at 100 km) which is consistent with our observations (see Figure 3). This suggests that non-linear interactions of waves may play a key role in explaining the thermal tides observed by our lidar.

[15] In summary, we present the first detection of thermal tides at polar latitudes in summer. We find surprisingly large tidal modulations of temperatures up to ± 6 K and even larger (up to $\pm 40\%$) in Fe number densities. Since the observed thermal tides are significantly larger compared to most models this asks for a comprehensive investigation of the potential mechanisms leading to tides at high latitudes, namely excitation, propagation, and interaction with waves at various spatial and temporal scales. The Fe lidar will continue to be in operation for at least another austral summer season which will hopefully indicate intra-seasonal variability of tides. We will expand our tidal analysis to winter but expect larger interference from gravity waves. Furthermore, we will compare with tidal observations from radars, and stimulate model studies to better understand the cause for the tidal variation by (non-)migrating tides, or perhaps by propagation from lower latitudes.

[16] **Acknowledgments.** We thank Torsten Köpnick for his continuing contribution in developing the Fe lidar. FJL thanks the AAD for the cooperation with IAP on the experimental investigations in Davis. We thank the Australian Antarctic Advisory Committee for support with Project 2325, and the Davis expeditioners with installation and maintenance of the Fe lidar facility at Davis.

[17] The Editor thanks the two anonymous reviewers for their assistance in evaluating this paper.

References

- Achatz, U., N. Grieger, and H. Schmidt (2008), Mechanisms controlling the diurnal solar tide: Analysis using a GCM and a linear model, *J. Geophys. Res.*, *113*, A08303, doi:10.1029/2007JA012967.
- Beig, G., et al. (2003), Review of mesospheric temperature trends, *Rev. Geophys.*, *41*(4), 1015, doi:10.1029/2002RG000121.
- DeLand, M. T., E. P. Shettle, G. E. Thomas, and J. J. Olivero (2007), Latitude-dependent long-term variations in polar mesospheric clouds from SBUV version 3 PMC data, *J. Geophys. Res.*, *112*, D10315, doi:10.1029/2006JD007857.
- Forbes, J. M., and D. Wu (2006), Solar tides as revealed by measurements of mesosphere temperature by the MLS experiment on UARS, *J. Atmos. Sci.*, *63*, 1776–1797.
- Hoffmann, P., E. Becker, W. Singer, and M. Placke (2010), Seasonal variation of mesospheric waves at northern middle and high latitudes, *J. Atmos. Sol. Terr. Phys.*, *72*, 1068–1079, doi:10.1016/j.jastp.2010.07.002.
- Höfner, J., and J. Lautenbach (2009), Daylight measurements of mesopause temperature and vertical wind with the mobile scanning iron lidar, *Opt. Lett.*, *34*, 1351–1353.
- Mayr, H., J. Mengel, E. Talaat, H. Porter, and K. L. Chan (2005), Mesospheric non-migrating tides generated with planetary waves: I. characteristics, *J. Atmos. Sol. Terr. Phys.*, *67*, 959–980.
- McLandress, C. (2002), The seasonal variation of the propagating diurnal tide in the mesosphere and lower thermosphere. Part I: The role of gravity waves and planetary waves, *J. Atmos. Sci.*, *59*, 893–906.
- Murphy, D. J., et al. (2006), A climatology of tides in the Antarctic mesosphere and lower thermosphere, *J. Geophys. Res.*, *111*, D23104, doi:10.1029/2005JD006803.
- Oberheide, J., Q. Wu, T. L. Killeen, M. E. Hagan, and R. G. Roble (2006), Diurnal nonmigrating tides from TIMED Doppler Interferometer wind data: Monthly climatologies and seasonal variations, *J. Geophys. Res.*, *111*, A10S03, doi:10.1029/2005JA011491.
- Picone, J. M., A. E. Hedin, D. P. Drob, and A. C. Aikin (2002), NRLMSISE-00 empirical model of the atmosphere: Statistical comparisons and scientific issues, *J. Geophys. Res.*, *107*(A12), 1468, doi:10.1029/2002JA009430.
- Portnyagin, Y. I., et al. (2004), Monthly mean climatology of the prevailing winds and tides in the Arctic mesosphere/lower thermosphere, *Ann. Geophys.*, *22*, 3395–3410.
- She, C. Y., S. Chen, B. P. Williams, Z. Hu, D. A. Krueger, and M. E. Hagan (2002), Tides in the mesopause region over Fort Collins, Colorado (41°N, 105°W) based on lidar temperature observations covering full diurnal cycles, *J. Geophys. Res.*, *107*(D18), 4350, doi:10.1029/2001JD001189.
- Shepherd, M. G., and C. Fricke-Begemann (2004), Study of the tidal variations in mesospheric temperature at low and mid latitudes from WINDII and potassium Lidar observations, *Ann. Geophys.*, *22*, 1513–1528.
- Ward, W. E., et al. (2010), On the consistency of model, ground-based, and satellite observations of tidal signatures: Initial results from the CAWSES tidal campaigns, *J. Geophys. Res.*, *115*, D07107, doi:10.1029/2009JD012593.
- Zhang, X., J. M. Forbes, and M. E. Hagan (2010), Longitudinal variation of tides in the MLT region: 2. Relative effects of solar radiative and latent heating, *J. Geophys. Res.*, *115*, A06317, doi:10.1029/2009JA014898.

J. Höfner, B. Kaifler, F.-J. Lübken, and T. P. Viehl, Leibniz Institute of Atmospheric Physics, Schloss-Str. 6, D-18225 Kühlungsborn, Germany. (luebken@iap-kborn.de)

R. J. Morris, Australian Antarctic Division, Channel Highway, Kingston, Tas 7050, Australia. (ray.morris@aad.gov.au)



RESEARCH LETTER

10.1002/2015GL063718

Key Points:

- Pronounced local time dependency in the K number density
- WACCM-K simulates the diurnal variation of K in good agreement with observation
- Photochemistry plays an important role in the diurnal variation of K

Correspondence to:

J. M. C. Plane,
j.m.c.plane@leeds.ac.uk

Citation:

Feng, W., J. Höffner, D. R. Marsh, M. P. Chipperfield, E. C. M. Dawkins, T. P. Viehl, and J. M. C. Plane (2015), Diurnal variation of the potassium layer in the upper atmosphere, *Geophys. Res. Lett.*, 42, doi:10.1002/2015GL063718.

Received 16 MAR 2015

Accepted 9 APR 2015

Accepted article online 14 APR 2015

Diurnal variation of the potassium layer in the upper atmosphere

W. Feng^{1,2}, J. Höffner³, D. R. Marsh⁴, M. P. Chipperfield², E. C. M. Dawkins², T. P. Viehl³, and J. M. C. Plane¹

¹School of Chemistry, University of Leeds, Leeds, UK, ²NCAS, School of Earth and Environment, University of Leeds, Leeds, UK, ³Leibniz-Institute of Atmospheric Physics, University of Rostock, Kühlungsborn, Germany, ⁴National Center for Atmospheric Research, Boulder, Colorado, USA

Abstract Measurements of the diurnal cycle of potassium (K) atoms between 80 and 110 km have been made during October (for the years 2004–2011) using a Doppler lidar at Kühlungsborn, Germany (54.1°N, 11.7°E). A pronounced diurnal variation is observed in the K number density, which is explored by using a detailed description of the neutral and ionized chemistry of K in a three-dimensional chemistry climate model. The model captures both the amplitude and phase of the diurnal and semidiurnal variability of the layer, although the peak diurnal amplitude around 90 km is overestimated. The model shows that the total potassium density ($\approx K + K^+ + KHCO_3$) exhibits little diurnal variation at each altitude, and the diurnal variations are largely driven by photochemical conversion between these reservoir species. In contrast, tidally driven vertical transport has a small effect at this midlatitude location, and diurnal fluctuations in temperature are of little significance because they are small and the chemistry of K is relatively temperature independent.

1. Introduction

Layers of metal atoms in the upper mesosphere and lower thermosphere (MLT) region have been observed by twilight photometry and lidar since the mid-1960s [Plane, 1991]. The metals are produced by meteoric ablation. Observations of the layers, combined with laboratory studies of reaction rate coefficients and modeling, have contributed significantly to our understanding of chemical and dynamical processes in the MLT [Plane, 2003; Plane et al., 2015]. The metal layers are affected by transport processes ranging from the hemispheric-scale meridional circulation to small-scale perturbations from gravity waves and tides [Eiska and Höffner, 1998; Feng et al., 2013; Lübken et al., 2011; Marsh et al., 2013]. A recent development has been the inclusion of the chemistry of Na [Marsh et al., 2013], Fe [Feng et al., 2013], K [Plane et al., 2014], and Mg [Langowski et al., 2015] in a three-dimensional (3-D) whole atmosphere model.

Atmospheric tides have an important impact in the upper atmosphere. Much work has been conducted on investigating the MLT tidal signature using satellite, ground-based measurements and models, with a primary focus on the temperature and wind components [e.g., see Ward et al., 2010] as well as atmospheric constituents [e.g., Marsh and Roble, 2002; Smith et al., 2010]. The first study of potential tidal impacts on the Na layer density was conducted by Clemesha et al. [1982], who found that there was no significant diurnal variation in the Na density, which suggested that the tide had little impact on the Na layer at 23°S. In contrast, Zhou et al. [2008], Yu et al. [2012], and Lübken et al. [2011] have all reported significant diurnal variations of the Fe layer, which indicate a combination of tidal and photochemical influences. The response of K is of particular interest, as the K layer exhibits a completely different seasonal behavior to the other observable metals; a semiannual seasonality (summer and winter maxima) versus the annual variation (winter maximum and summer minimum) seen in other metals like Na and Fe [Plane et al., 2014]. As yet, there have been no direct comparisons of the observed and modeled response of the metals layers to the atmospheric solar tide and photochemistry in the MLT.

In this paper, we use a combination of lidar measurements and modeling to investigate the impact of chemistry and dynamics on the diurnal behavior of the K layer. The paper is organized as follows: Section 2 describes the measurements and model used in the study. Section 3 compares the model results with lidar observations by examining important parameters of the K layer as well as diagnosing the diurnal and semidiurnal amplitude and phase of the K density variation. The model results are then used to

©2015. The Authors.

This is an open access article under the terms of the Creative Commons Attribution License, which permits use, distribution and reproduction in any medium, provided the original work is properly cited.

compare the role of photochemistry with tidally driven transport and temperature fluctuations. Section 4 summarizes the conclusions.

2. Potassium Doppler Lidar Measurements and the WACCM-K Model

Measurements of the K(D₁) resonance wavelength at 770 nm [see von Zahn and Höffner, 1996; Höffner and Lübken, 2007] have been made at Kühlungsborn (54.1°N, 11.7°E) across the period 2002 to 2012. Here we use measurements in October averaged from 2004 to 2011, because this provides the longest available monthly observational record of K with a total of 363 h on 18 days of measurement, a sufficiently long data set to investigate the diurnal variation of K. The large number of available days from different years allows the averaged diurnal variability, rather than a snapshot from a few consecutive days, to be determined. After stacking all data into a single day with 1 h resolution, gravity waves and other disturbances are mostly averaged out by the large number of long measurements. Whereas K densities can be measured over a 24 h diurnal cycle, this is often not possible for temperatures because the temperature analysis requires a much better signal to noise. Temperatures are derived from the Doppler broadening of the K line, which is a relatively small effect. The large solar background during daytime, when exacerbated by the haze which often occurs over Kühlungsborn at noon, does not allow the accurate determination of temperatures. As a result, only a few temperatures with relatively large uncertainties are available around midday. It is possible to determinate temperature tides if shorter measurements are considered. For measurements longer than 6 h a tidal analysis has been performed by Kopp et al. [2014] for a different data set. A tidal analysis of temperature variations would therefore contain data from a small subset of the days that have been used for the K density analysis, and so this is not included in the present study. We also note that Lübken et al. [2011] have reported a comparison of the temperature and Fe density tidal variations using a mobile Fe lidar, but this was possible because of the nearly solar background free measurements under all conditions which cannot be achieved with a K or Na Doppler lidar.

A global model of meteoric K (WACCM-K) has been developed recently [Plane et al., 2014]. WACCM-K combines three components: the Whole Atmosphere Community Climate Model (WACCM) which includes the important MLT chemistry and dynamical features [Marsh et al., 2013]; a description of the neutral and ion-molecule chemistry of K in the MLT; and the injection rate profile of K atoms which is calculated by combining a meteoric ablation model with an astronomical model of near-Earth cosmic dust. The ablation flux of K during October at the latitude of Kühlungsborn is $150 \text{ atom cm}^{-2} \text{ s}^{-1}$. WACCM-K successfully reproduces the observed semiannual variation in the K layer [Plane et al., 2014]. WACCM also reproduces diurnal and semidiurnal tide in the MLT [Chang et al., 2012]. Here we have used the same specified dynamics version nudged with the Goddard Earth Observing System 5 (GEOS-5) meteorological data set [Feng et al., 2013; Langowski et al., 2015; Plane et al., 2014], with a horizontal resolution of $1.9^\circ \times 2.5^\circ$ and $\sim 3.5 \text{ km}$ vertical resolution in the MLT. The Prandtl number is set to 4. We sampled the model output every 30 min for Kühlungsborn from January 2004 until the end of December 2011.

A linear least squares fit method is also used to diagnose the diurnal/semidiurnal amplitude and phase of K layer, and the modeled temperature (T) and vertical wind velocity (w):

$$f(t) = f_0 + \sum_n A_n \cos(2n\pi t/24 + \phi_n) \quad (1)$$

where $f(t)$ is the time series of K, T , or w . The local time is t , f_0 is diurnal mean value, n is wave number where $n = 1$ describes the diurnal variation while $n = 2$ describes the semidiurnal variation. A_n is amplitude and ϕ_n is phase.

The K chemical lifetime (τ) with respect to conversion to the reservoirs KHCO_3 and K^+ can be derived from the chemical reaction set listed in Table 1:

$$\tau^{-1} = \left[k_1[\text{O}_3] + k_3[\text{O}_2][\text{M}] \left(\frac{k_4[\text{O}]}{k_4[\text{O}] + J_{11}} \right) \right] \left[\frac{k_5[\text{H}_2\text{O}] + k_6[\text{H}_2]}{k_2[\text{O}] + k_5[\text{H}_2\text{O}] + k_6[\text{H}_2]} \right] \left[\frac{k_8[\text{CO}_2][\text{M}]}{k_8[\text{CO}_2][\text{M}] + k_7[\text{H}] + J_{12}} \right] + k_9[\text{NO}^+] + k_{10}[\text{O}_2^+] + J_{13} \quad (2)$$

Table 1. Neutral and Ionic Gas-Phase Reactions Required to Estimate the Lifetime of K With Respect to Conversion to the Reservoir Species KHCO_3 and K^+

Number	Reaction	Rate Coefficient ^a
<i>Neutral Chemistry</i>		
R1	$\text{K} + \text{O}_3 \rightarrow \text{KO} + \text{O}_2$	$1.15 \times 10^{-9} \exp(-120/T)$
R2	$\text{KO} + \text{O} \rightarrow \text{K} + \text{O}_2$	$2 \times 10^{-10} \exp(-120/T)$
R3	$\text{K} + \text{O}_2 (+\text{M}) \rightarrow \text{KO}_2$	$1.3 \times 10^{-29} (T/200)^{-1.23}$
R4	$\text{KO}_2 + \text{O} \rightarrow \text{KO} + \text{O}_2$	$2 \times 10^{-10} \exp(-120/T)$
R5	$\text{KO} + \text{H}_2\text{O} \rightarrow \text{KOH} + \text{OH}$	$2 \times 10^{-10} \exp(-120/T)$
R6	$\text{KO} + \text{H}_2 \rightarrow \text{KOH} + \text{H}$	$2 \times 10^{-10} \exp(-120/T)$
R7	$\text{KOH} + \text{H} \rightarrow \text{K} + \text{H}_2\text{O}$	$2 \times 10^{-10} \exp(-120/T)$
R8	$\text{KOH} + \text{CO}_2 (+\text{M}) \rightarrow \text{KHCO}_3$	$7.1 \times 10^{-28} (T/200)^{-4.2}$
<i>Ion-Molecule Chemistry</i>		
R9	$\text{K} + \text{NO}^+ \rightarrow \text{K}^+ + \text{NO}$	9.4×10^{-10}
R10	$\text{K} + \text{O}_2^+ \rightarrow \text{K}^+ + \text{O}_2$	3.2×10^{-9}
<i>Photochemical Reactions</i>		
R11	$\text{KO}_2 + h\nu \rightarrow \text{K} + \text{O}_2$	2.2×10^{-3}
R12	$\text{KOH} + h\nu \rightarrow \text{K} + \text{OH}$	2.7×10^{-2}
R13	$\text{K} + h\nu \rightarrow \text{K}^+ + e^-$	4×10^{-5}

^aRate coefficients from *Plane et al. [2014]*. Units: unimolecular, s^{-1} ; bimolecular, $\text{cm}^3 \text{molecule}^{-1} \text{s}^{-1}$; termolecular, $\text{cm}^6 \text{molecule}^{-2} \text{s}^{-1}$.

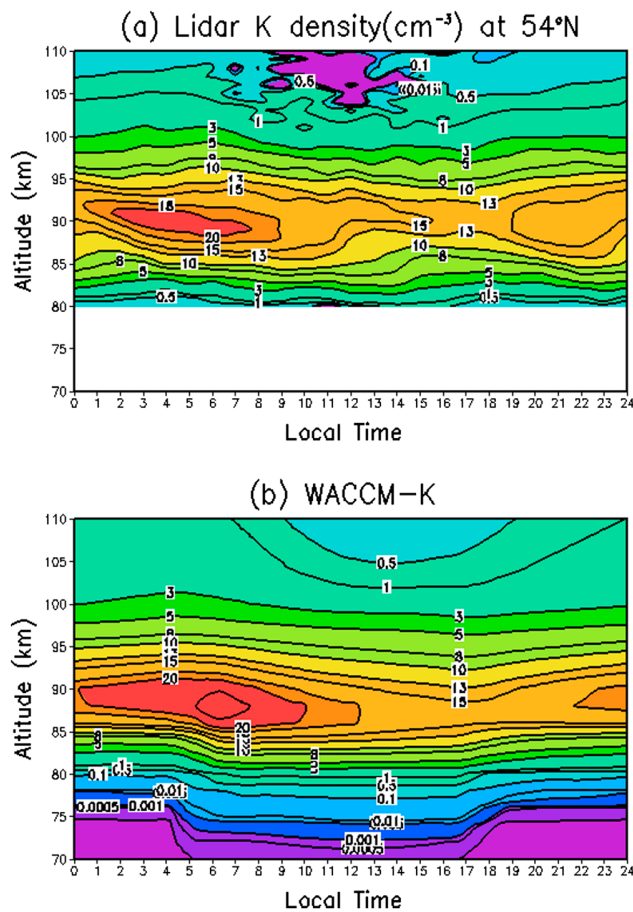


Figure 1. Diurnal variation of the K layer for October at Kühlungsborn, Germany (54°N, 12°E), averaged from 2004 to 2011. (a) K density (atom cm^{-3}) as a function of altitude and local time, measured by lidar. (b) K density as a function of altitude and time from WACCM-K.

The first term on the right-hand side describes the rate of conversion of K to KHCO_3 , with the short-lived intermediates KO, KO_2 , and KOH assumed to be in chemical steady state; the final three terms define the rate of conversion to K^+ via charge transfer and photoionization.

3. Results and Discussion

Figure 1 shows the observed and modeled diurnal variation of the K layer. The measurements show that the K layer peaks around 90 km with a maximum density of $\sim 20 \text{ cm}^{-3}$ between 0300 and 0900 LT, which then decreases to $\sim 13 \text{ cm}^{-3}$ around 2100 LT (Figure 1a). Overall, WACCM-K simulates the observed K layer quite well and also captures the large differences between dawn (around 0600 LT) and dusk (around 1800 LT) at 90 km (Figure 1b). The layer bottomsides production and loss of K is similar to Fe [Feng et al., 2013; Yu et al., 2012]. There is a large decrease of observed neutral K around 105–110 km which is due to the conversion of K to K^+ ions, through charge transfer with NO^+ and O_2^+ and photoionization. This observed decrease in neutral K is also

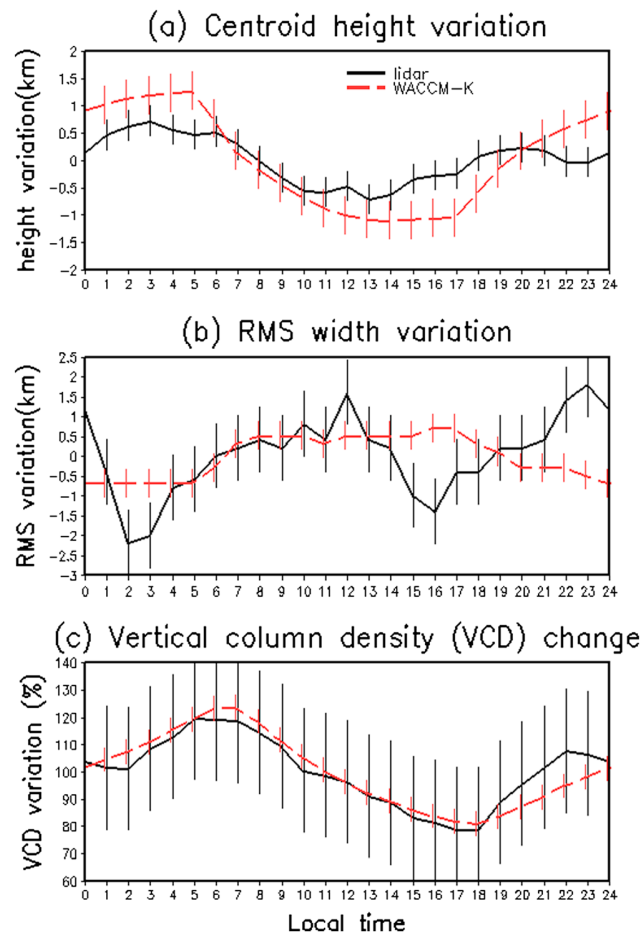


Figure 2. Diurnal variation of (a) the K centroid height (km), (b) RMS width (km) which are subtracted from the 24 h averaged value, and (c) the vertical column density (VCD) changes (average = 100%) over 24 h. The error bars are calculated from standard deviation of the October mean K density.

$1.99 \times 10^7 \text{ cm}^{-2}$ and the modeled column density is $2.04 \times 10^7 \text{ cm}^{-2}$. Both lidar and model show that the centroid height of K layer occurs at nighttime then decreases during the day. The width of the K layer from lidar varies from a minimum at 0200–0300 LT to a maximum at midnight, whereas the model somewhat overestimates and then underestimates it, though the mean K RMS width is very similar to that measured. Both model and observation show that the K column abundance increases from 1800 LT to a maximum around 0700 LT and then decreases throughout the daytime. Clearly, WACCM-K reproduces the observed K column abundance variation quite well though the model slightly overestimates the total column abundance value.

Figures 3a and 3b show height profiles of the amplitude and phase (diurnal and semidiurnal) for the measured and modeled K density. The observed maximum diurnal amplitude is 1.1 cm^{-3} around 90 km, while the maximum semidiurnal amplitude is 1.0 cm^{-3} around 87 km. Although the maximum diurnal and semidiurnal K amplitude from the model is at a similar altitude to that observed, the model largely overestimates the observed K diurnal amplitude maximum. Above 105 km, there is significant sharp decrease in the observed K diurnal amplitudes, whereas the model still exhibits large diurnal modeled K amplitude. This is due to the overestimation of the K density above 105 km by the model compared with lidar observation (Figure 1). The K diurnal and semidiurnal phase is shown in Figure 3b, which is defined with respect to the time of maximum K in the oscillation. At the layer peak altitude, the diurnal and semidiurnal variations peak near sunrise in both observations and the model. The observed diurnal K phase indicates the time of maximum K perturbation is ~ 14 h at 80 km down to 2 h around 110 km, which is well captured by the model. The model also correctly predicts a later semidiurnal phase than diurnal phase.

well captured by the model, although WACCM-K overestimates the daytime atomic K density around 105–110 km by a factor of 5. As we have discussed in Feng et al. [2013], this likely arises because there is an accumulation in the lower thermosphere of K^+ ions (and hence K, with which K^+ is in quasi steady state) since WACCM does not include the Lorentz force which distributes long-lived metal ions over greater heights in the thermosphere.

In order to explore the characteristics of the K layer in greater detail, we have calculated the centroid height and RMS (root-mean-square) width, which is a measure of the layer thickness, as well as the K column abundance. Figure 2 shows the diurnal variation of the K centroid height, RMS width minus its 24 h averaged value as well as K vertical column density (VCD) percentage change over 24 h (the average column density is 100%) calculated from the K density in Figure 1. This highlights any changes caused by tides which move the layer up/down within 24 h. WACCM-K captures the mean K characteristics quite well. The mean K centroid height is 90.9 km from lidar while it is 90.2 km from WACCM-K. The observed K RMS width is 4.7 km and the modeled width is 4.4 km, the observed K VCD (integrated from 80 to 110 km) is

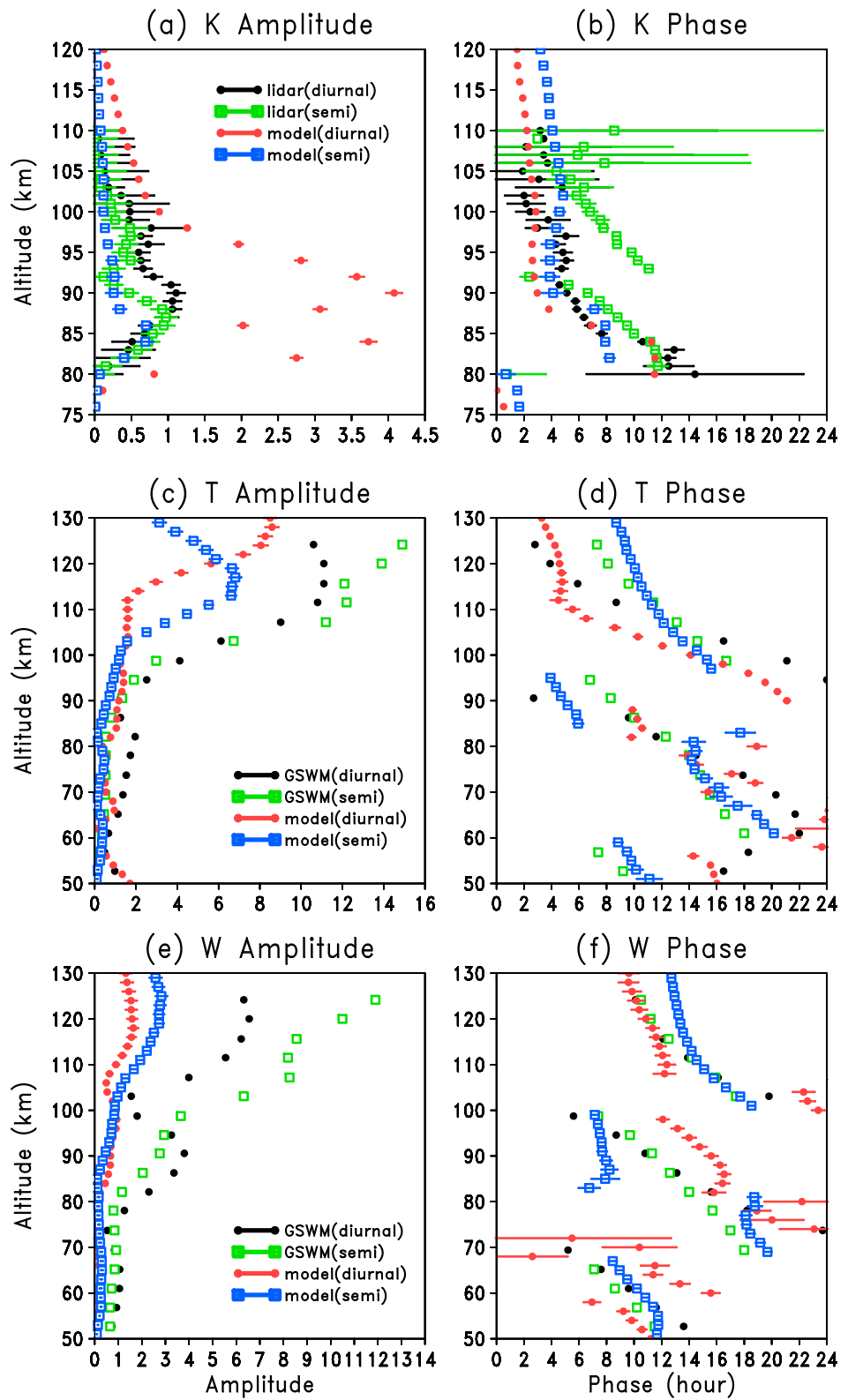


Figure 3. The diagnosed amplitude and phase (h) of the diurnal and semidiurnal variations in: (a and b) K (cm^{-3}) from lidar and WACCM-K model, (c and d) temperature, and (e and f) vertical wind (cm/s) as a function of altitude from GSWM and WACCM-K model simulations. The error bars represent 1 sigma uncertainty from the regression calculation.

The potassium lidar temperature data are insufficient for detailed diurnal analysis. We have therefore compared the tidal components of the temperature T (Figures 3c and 3d) and vertical velocity w (Figures 3e and 3f) in WACCM-K with those from the global scale wave model (GSWM) [Hagan et al., 1995], which has been widely used to investigate tides in MLT. GSWM predicts that the tidal amplitude of T for October around Kühlungsborn (Figure 3c) increases with altitude, and the semidiurnal amplitude (with a maximum value of 14–16 K around 125 km) is larger than the diurnal temperature amplitude above 100 km, whereas WACCM underestimates both the diurnal and semidiurnal T amplitudes. However, below 100 km the models are in good agreement (less than 5 K difference). Generally, both the diurnal and semidiurnal phases for T from GSWM and WACCM (Figure 3d) exhibit downward progression between 60 and 90 km and above 95 km. There is upward progression for the diurnal T between 94 and 98 km and semidiurnal T between 90 and 95 km. Kopp et al. [2014] reported temperature phases and amplitudes for October using a Rayleigh-Mie-Raman (RMR) lidar. Even though this data set differs from the data set herein, it gives an indication of the observed temperature tide during the period discussed here. We note that WACCM and GSWM have lower diurnal and semidiurnal amplitudes (less than 3 K) between 85 and 95 km compared with Kopp et al. [2014] (1–8 K).

The amplitudes of the diurnal and semidiurnal tidal components of w from both GSWM and WACCM (Figure 3e) also increase with altitude in the MLT region. The semidiurnal variation in w dominates above 100 km. WACCM appears to capture the main features of the diurnal and semidiurnal tide both in amplitude and phase, though it has smaller amplitude compared with GSWM at this midlatitude location.

In order to investigate the possible effect of the tide on the diurnal cycle of the K layer, we start by considering how the total density of K-bearing chemical species (which is essentially the sum of K, K^+ , and $KHCO_3$ in WACCM-K) varies as a function of height and local time. Figure 4a shows that the total K density peaks around 90 km ($\sim 65 \text{ cm}^{-3}$), which is slightly higher than the peak altitude of neutral K atom density (Figure 1b). Significantly, the total K is almost constant at each height over a diurnal cycle, which suggests that vertical transport plays a minor role. Figures 4b–4d show the vertical profiles as a function of time of the three main species K^+ , K, and $KHCO_3$ expressed as a percentage fraction of total K. K^+ ions dominate on the topside of the K layer, accounting for more than 60% of total K above 90 km and more than 90% above 100 km. Neutral K atoms comprise 20–40% of the total density around the layer peak, with very small insignificant contributions below 80 km and above 100 km. $KHCO_3$ is the dominant reservoir species on the bottomside of the K layer, contributing more than 90% below 79 km. Other K-containing species make very small contributions [Plane et al., 2014].

Above 87 km, K and K^+ simply interconvert over a diurnal cycle: K is converted into K^+ during daytime through photoionization and charge exchange reactions, and K^+ is neutralized through cluster formation and dissociative recombination with electrons [Plane et al., 2014]. Photochemistry also explains the buildup of neutral K atoms below 87 km after sunrise via the photolysis of the reservoir species $KHCO_3$. The marked increase in K between 83 and 87 km after ~ 0600 LT disappears again by 1200 LT, due to conversion of atomic K into K^+ . On the underside of the layer below 85 km, there is a complete removal of K during nighttime (1800–0500 LT), as K is converted into the dominant reservoir $KHCO_3$. After dawn this reservoir is converted back to K by photolysis. Furthermore, the conversion of K back to $KHCO_3$ involves three steps: the reaction of K with O_3 to form KO; reaction of KO with H_2O/H_2 to yield KOH; and recombination of KOH with CO_2 [Plane et al., 2014]. The rates of these three steps in the mechanism slow down after sunrise. This is because during daytime at 74 km more than 70% of the O_3 is photolyzed, and the daytime O and H concentrations are ~ 50 and 10 times higher than during the night, respectively (these variations are illustrated in Figure 4 of Plane et al. [2015]). Thus, during the day K is oxidized more slowly by O_3 , and the increased O and H radical concentrations convert KO and KOH, respectively, more rapidly back to K.

The diurnal variation in temperature predicted by WACCM is small over Kühlungsborn: less than 4 K at each height between 80 and 100 km, compared with RMR measurements between 85 and 95 km [Kopp et al., 2014]. Since the temperature dependencies of the relevant reactions in the K chemistry scheme are comparatively small (and the reaction of $KHCO_3 + H$ has too large an activation energy to be important)

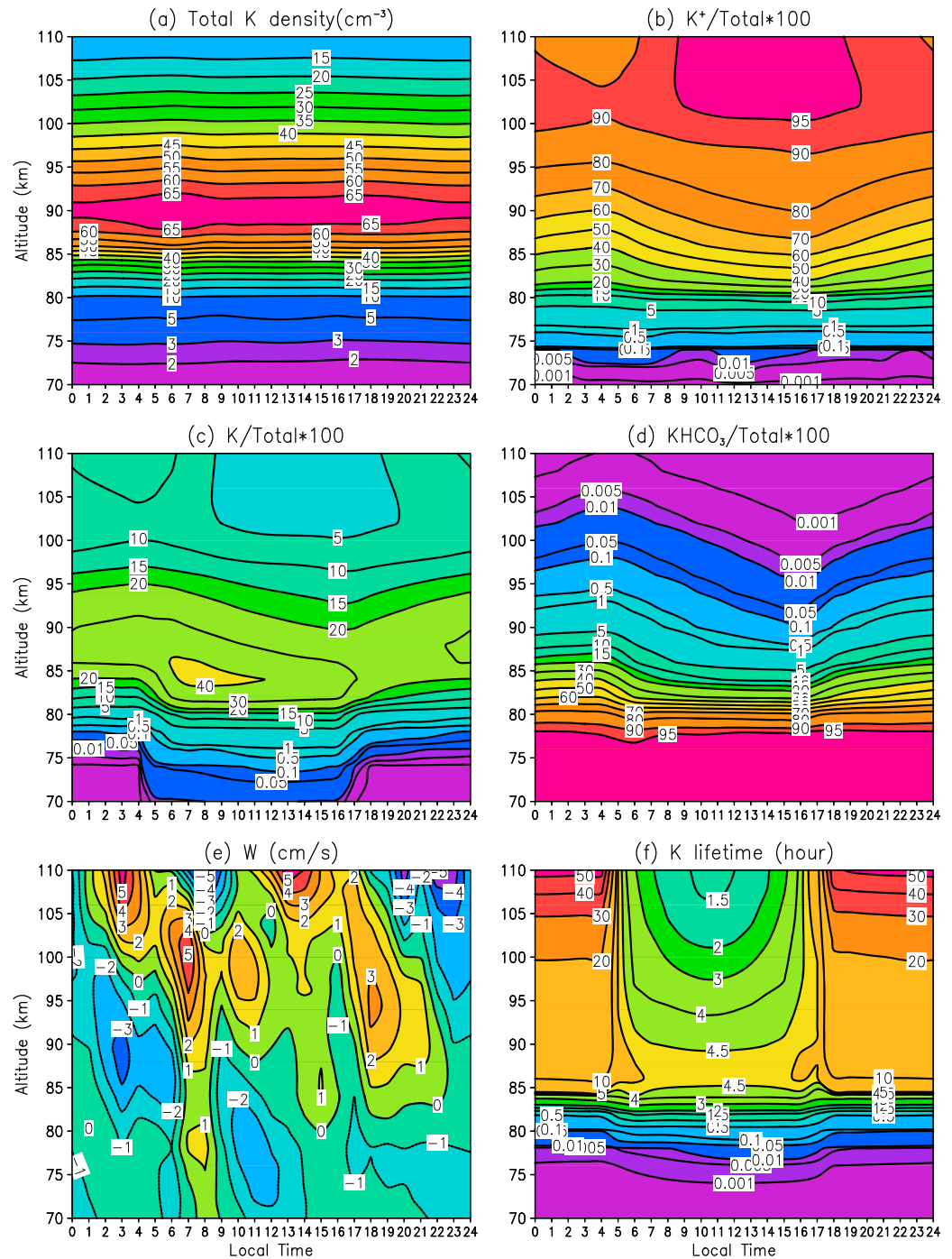


Figure 4. Diurnal variation of simulation of (a) the total K layer, (b) the percentage of ionic K, (c) neutral K atoms and (d) reservoir species KHCO_3 with respect to (e) the total K density and diagnosed vertical velocity and (f) chemical K lifetime for October at Kühlungsborn, Germany (54°N , 12°E), averaged from 2004 to 2011.

[Plane *et al.*, 2014], diurnal variations in temperature do not play a significant role in the diurnal variation of the K layer. Figure 4e shows that the modeled vertical wind w at 54°N during October is small ($\leq 5 \text{ cm s}^{-1}$) in the MLT, corresponding to tidally driven vertical displacements of less than 1 km. This lack of vertical transport explains the near-constant total K density at each height (Figure 4a).

Finally, Figure 4f shows the K lifetime τ calculated using equation (2). Below 80 km, τ is short (<10 min), although it effectively doubles at each height during the day because of the increased concentrations of O and H and decreased O₃ (see above). The longest lifetimes are during the night, less than 1 day below 100 km, and much longer higher in the thermosphere. However, during daytime the lifetime is always less than 4.5 h throughout the MLT. This explains why in situ photochemistry plays a much more important role than vertical transport in controlling the diurnal variation of atomic K.

4. Conclusions

The diurnal variation of the midlatitude K layer has been measured using a lidar located at Kühlungsborn (54.1°N, 11.7°E), Germany. Data obtained between 2004 and 2011 were used to construct a height profile of the K density as a function of local time, for the month of October. Even though this is a single site observation, the data provide a comprehensive test for the interplay between dynamics and chemistry in a 3-D model of the K layer. Overall, WACCM-K reproduces the observed diurnal and semidiurnal variations in the K layer satisfactorily. It is shown that most of the variability is accounted for by photochemistry, both directly through photolysis of the reservoir species KHCO₃ and photoionization of K and indirectly by changing the concentrations of O₃, O, and H which affect the rates of important reactions. Diurnal variations in temperature, and tidally driven vertical transport, appear to play a minor role in the upper atmospheric potassium layer at this midlatitude location.

Acknowledgments

This work was supported by the UK Natural Environment Research Council (NERC grant NE/G019487/1) and by the European Research Council (project 291332—CODITA). The National Center for Atmospheric Research is sponsored by the National Science Foundation. The lidar data set is available upon request to J.H. and WACCM-K data set is available upon request to W.F. and J.M.C.P.

The Editor thanks two anonymous reviewers for their assistance in evaluating this paper.

References

- Chang, L. C., et al. (2012), Comparison of diurnal tide in models and ground-based observations during the 2005 equinox CAWSES tidal campaign, *J. Atmos. Sol. Terr. Phys.*, 78–79, 19–30, doi:10.1016/j.jastp.2010.12.010.
- Clemesha, B. R., D. M. Simonich, P. P. Batista, and V. W. J. H. Kirchhoff (1982), The diurnal variation of atmospheric sodium, *J. Geophys. Res.*, 87(A1), 181–186, doi:10.1029/JA087iA01p00181.
- Eska, V., and J. Höffner (1998), Observed linear and nonlinear K layer response, *Geophys. Res. Lett.*, 25(15), 2933–2936, doi:10.1029/98GL02110.
- Feng, W., D. R. Marsh, M. P. Chipperfield, D. Janches, J. Höffner, F. Yi, and J. M. C. Plane (2013), A global atmospheric model of meteoric iron, *J. Geophys. Res. Atmos.*, 118, 9456–9474, doi:10.1002/jgrd.50708.
- Hagan, M. E., J. M. Forbes, and F. Vial (1995), On modeling migrating solar tides, *Geophys. Res. Lett.*, 22(8), 893–896, doi:10.1029/95GL00783.
- Höffner, J., and F. J. Lübken (2007), Potassium lidar temperatures and densities in the mesopause region at Spitsbergen (78°N), *J. Geophys. Res.*, 112, D20114, doi:10.1029/2007JD008612.
- Kopp, M., M. Gerding, J. Höffner, and F. J. Lübken (2014), Tidal signatures in temperatures derived from daylight lidar soundings above Kühlungsborn (54°N, 12°E), *J. Atmos. Sol. Terr. Phys.*, doi:10.1016/j.jastp.2014.09.002.
- Langowski, M., C. von Savigny, J. P. Burrows, W. Feng, J. M. C. Plane, D. R. Marsh, D. Janches, M. Sinnhuber, A. C. Aikin, and P. Liebing (2015), Global investigation of the Mg atom and ion layers using SCIAMACHY/Envisat observations between 70 km and 150 km altitude and WACCM-Mg model results, *Atmos. Chem. Phys.*, 15, 273–295, doi:10.5194/acp-15-273-2015.
- Lübken, F. J., J. Höffner, T. P. Viehl, B. Kaifler, and R. J. Morris (2011), First measurements of thermal tides in the summer mesopause region at Antarctic latitudes, *Geophys. Res. Lett.*, 38, L24806, doi:10.1029/2011GL050045.
- Marsh, D., and R. Roble (2002), TIME-GCM simulations of lower-thermospheric nitric oxide seen by the halogen occultation experiment, *J. Atmos. Sol. Terr. Phys.*, 64(8–11), 889–895, doi:10.1016/S1364-6826(02)00044-5.
- Marsh, D., D. Janches, W. Feng, and J. M. C. Plane (2013), A global model of meteoric sodium, *J. Geophys. Res. Atmos.*, 118, 11,442–11,452, doi:10.1002/jgrd.50870.
- Plane, J. M. C. (1991), The chemistry of meteoric metals in the Earth's upper atmosphere, *Int. Rev. Phys. Chem.*, 10(1), 55–106, doi:10.1080/01442359109353254.
- Plane, J. M. C. (2003), Atmospheric chemistry of meteoric metals, *Chem. Rev.*, 103(12), 4963–4984, doi:10.1021/cr0205309.
- Plane, J. M. C., W. Feng, E. Dawkins, M. P. Chipperfield, J. Höffner, D. Janches, and D. R. Marsh (2014), Resolving the strange behavior of extraterrestrial potassium in the upper atmosphere, *Geophys. Res. Lett.*, 41, 4753–4760, doi:10.1002/2014GL060334.
- Plane, J. M. C., W. Feng, and E. C. M. Dawkins (2015), The mesosphere and metals: Chemistry and changes, *Chem. Rev.*, doi:10.1021/cr500501m.
- Smith, A. K., D. R. Marsh, M. G. Mlynczak, and J. C. Mast (2010), Temporal variations of atomic oxygen in the upper mesosphere from SABER, *J. Geophys. Res.*, 115, D18309, doi:10.1029/2009JD013434.
- von Zahn, U., and J. Höffner (1996), Mesopause temperature profiling by potassium lidar, *Geophys. Res. Lett.*, 23(2), 141–144, doi:10.1029/95GL03688.
- Ward, W. E., et al. (2010), On the consistency of model, ground-based, and satellite observations of tidal signatures: Initial results from the CAWSES tidal campaigns, *J. Geophys. Res.*, 115, D07107, doi:10.1029/2009JD012593.
- Yu, Z., X. Chu, W. Huang, W. Fong, and B. R. Roberts (2012), Diurnal variations of the Fe layer in the mesosphere and lower thermosphere: Four season variability and solar effects on the layer bottomside at McMurdo (77.8°S, 166.7°E), Antarctica, *J. Geophys. Res.*, 117, D22303, doi:10.1029/2012JD018079.
- Zhou, Q., S. Raizada, C. A. Tepley, and J. M. C. Plane (2008), Seasonal and diurnal variation of electron and iron concentrations at the meteor heights above Arecibo, *J. Atmos. Sol. Terr. Phys.*, 70(1), 49–60, doi:10.1016/j.jastp.2007.09.012.

RESEARCH ARTICLE

10.1002/2014JD022879

Key Points:

- Gravity wave signatures are extracted from lidar data
- Gravity wave activity in the Antarctic middle atmosphere is characterized
- Critical-level filtering of gravity waves is investigated

Correspondence to:

B. Kaifler,
bernd.kaifler@dlr.de

Citation:

Kaifler, B., F.-J. Lübken, J. Höffner, R. J. Morris, and T. P. Viehl (2015), Lidar observations of gravity wave activity in the middle atmosphere over Davis (69°S, 78°E), Antarctica, *J. Geophys. Res. Atmos.*, 120, doi:10.1002/2014JD022879.

Received 19 NOV 2014

Accepted 10 APR 2015

Accepted article online 20 APR 2015

Lidar observations of gravity wave activity in the middle atmosphere over Davis (69°S, 78°E), Antarctica

B. Kaifler^{1,2}, F.-J. Lübken², J. Höffner², R. J. Morris³, and T. P. Viehl²¹Institute of Atmospheric Physics, German Aerospace Center, Oberpfaffenhofen, Germany, ²Leibniz Institute of Atmospheric Physics, Rostock University, Kühlungsborn, Germany, ³Australian Antarctic Division, Kingston, Tasmania, Australia

Abstract A 16 month series of lidar measurements in the stratosphere and mesosphere-lower thermosphere (MLT) region over Davis Station (69°S, 78°E) in Antarctica is used to study gravity waves. The unprecedentedly large number of observations totaling 2310 h allows us to investigate seasonal variations in gravity wave activity in great detail. In the stratosphere the gravity wave potential energy density (GWPED) is shown to have a large seasonal variation with a double peak in winter and minimum in summer. We find conservative wave propagation to occur between 29 and 41 km altitude in winter as well as in summer, whereas smaller energy growth rates were observed in spring and autumn. These results are consistent with selective critical-level filtering of gravity waves in the lower stratosphere. In the MLT region the GWPED is found to have a semiannual oscillation with maxima in winter and summer. The structure of the winter peak is identical to that in the stratosphere, suggesting that the gravity wave flux reaching the MLT region is controlled by the wind field near the tropopause level.

1. Introduction

Atmospheric gravity waves are important for vertical coupling in the atmosphere. They transport energy and momentum vertically and horizontally over large distances. At high latitudes, dissipation of these waves in the mesosphere-lower thermosphere region (hereafter MLT region) transfers momentum into the background flow, driving a global meridional circulation from the summer pole to the winter pole [Lindzen, 1981; Holton, 1983]. Associated with this circulation is the upwelling of air at the summer pole causing the strong adiabatic cooling of the summer MLT region [Andrews *et al.*, 1987; Becker, 2012]. This gravity wave-induced cooling gives rise to observed temperatures as low as 130 K which are far from radiative equilibrium [Lübken, 1999; Lübken *et al.*, 2014]. For this reason, phenomena like noctilucent clouds and polar mesospheric summer echoes are limited to the summer polar region [Olivero and Thomas, 1986]. Without gravity wave-induced cooling, temperatures in the summer MLT remain above the frost point [Rapp and Thomas, 2006]. The occurrence of noctilucent clouds is thus a result of gravity waves propagating from the troposphere/lower stratosphere into the MLT region.

Gravity waves have been extensively studied in models [e.g., Zhang, 2004] as well as through employing observational techniques such as lidars [e.g., Rauthe *et al.*, 2008; Yamashita *et al.*, 2009], radars [e.g., Nicolls *et al.*, 2010; Lue *et al.*, 2013], radiosondes [e.g., Allen and Vincent, 1995; Moffat-Griffin *et al.*, 2011], satellite-based radiometers [e.g., Alexander *et al.*, 2008; Wright and Gille, 2013], and Global Positioning System radio occultation [e.g., Wang and Alexander, 2010]. Among all observational techniques, lidars provide the highest temporal and vertical resolutions over a wide altitude range and observation periods up to several days.

Lidar observations in the Antarctic region are rare due to the difficulties involved in setting up and operating complex optical instruments in such a harsh environment. First, lidar-based measurements of gravity waves on the Antarctic continent were reported by Nomura *et al.* [1989]. Nomura *et al.* [1989] used a sodium lidar located at Syowa Station (69°S, 40°E) in 1985 to derive gravity wave parameters from density perturbations in the sodium layer (approximately 80–105 km). Collins and Gardner [1995] studied gravity waves observed in 1990 at the South Pole in the sodium layer and in stratospheric clouds between 15 and 30 km. An iron Boltzmann/Rayleigh lidar was used to investigate gravity waves in 30–45 km altitude at the South Pole and at Rothera between 2000 and 2005 [Yamashita *et al.*, 2009]. This instrument was later moved to McMurdo (78°N, 167°E) [Chen *et al.*, 2013]. A Rayleigh lidar providing temperature profiles for gravity wave studies between 30 and 70 km has been operational at Davis (69°S, 78°E) since 2001 [Klekociuk *et al.*, 2003; Alexander *et al.*, 2011].

Table 1. Statistics of the Lidar Observations

	Year	Jan	Feb	Mar	Apr	May	Jun	Jul	Aug	Sep	Oct	Nov	Dec	Total
Observations	2011	11	4	5	7	4	8	4	7	4	6	5	9	
Observation hours		185.8	128.8	71.8	121.8	97.0	260.3	124.8	213.0	108.5	183.3	189.0	215.3	
Observations	2012	8	3	5	5									95
Observation hours		166.8	108.3	64.8	71.5									2310.3

Finally, in December 2010 the Leibniz Institute of Atmospheric Physics (IAP) iron Doppler lidar was installed at Davis Station and took data until December 2012 [Lübken *et al.*, 2014]. This lidar was capable of measuring gravity waves in the iron layer (approximately 80–100 km) and between 30 and 50 km. As distinguished from all previous lidars in Antarctica, the IAP lidar was operated during a full annual cycle achieving on average 158 observation hours per month. The resulting data set is the largest high-resolution temperature data set to date. In this work we report on gravity analysis using this data set.

2. Lidar System, Observations, and Analysis

The IAP mobile iron lidar is a mesospheric lidar system designed to probe the Doppler-broadened resonance line of iron at 386 nm wavelength to measure atmospheric temperature profiles in the MLT region [Lautenbach and Höffner, 2004]. It uses a frequency-doubled Alexandrite ring laser as light source operating at 33 Hz pulse repetition rate. Emitted pulse energies are 30 mJ in the UV (386 nm) and 100 mJ in the IR (772 nm). The receiver comprises a telescope with 80 cm aperture and a narrow field of view of 66 μ rad, a double-etalon narrow-band filter for each of the two wavelengths, and photon detectors operated in single photon counting mode. Photon count profiles with 25 m vertical resolution are stored for each individual laser pulse. The lidar system is capable of measuring atmospheric temperatures in full daylight with a typical uncertainty of 1–5 K in the MLT region (approximately 80–100 km altitude) after 1 h integration and binning to 2 km vertical resolution. Stratospheric temperatures with 1 km vertical resolution and 1 h integration time are retrieved between 25 and 60 km altitude with typical uncertainties ranging from approximately 7 K at 55 km altitude to less than 2 K below 40 km altitude. Higher vertical and temporal resolutions are possible for lidar measurements acquired in darkness.

The lidar system was operated at the Australian Antarctic station Davis (68.58°S, 77.97°E) between December 2010 and December 2012 for more than 2600 h. Thus, the lidar measurements form the most extensive high-resolution middle atmosphere temperature data set available to date. This data set covers a full annual cycle with approximately equal sampling and is therefore well suited for studying seasonal variations of, e.g., temperature and gravity wave activity. Because no lidar observations were acquired in austral winter 2012, we limited our gravity wave study presented here to the period January 2011 to April 2012. Also, we discarded all lidar observations shorter than 6 h in order to guarantee sampling of at least one half-period of long-period inertia gravity waves (the Coriolis parameter for the location of Davis Station is approximately 12.7 h). Monthly statistics of the resulting subset of lidar observations (2310 h in total) are listed in Table 1. With more than 260 h, the largest number of observation hours per month was achieved in June 2011. This number corresponds to an average of 8.7 h of lidar observations per day or 37% of the total time. Considering the 16 month period selected for this study, the average observation period per day is 4.8 h or about 20% of the total time.

In this work we characterize gravity waves by wave-induced temperature perturbations $T'(z, t)$ and gravity wave potential energy densities (from now on referred to as GWPED), E_p , defined as

$$E_p(z) = \frac{1}{2} \frac{g^2}{N^2(z, t)} \overline{\left(\frac{T'(z, t)}{T_0(z, t)} \right)^2}, \quad (1)$$

where g is the gravitational acceleration, equal to approximately 9.7 m s^{-2} ; T_0 is the undisturbed background temperature; and z and t denote altitude and time, respectively. The squared buoyancy frequency N^2 is calculated from temperature profiles using the relation

$$N^2(z, t) = \frac{g}{T_0(z, t)} \left(\frac{\partial T_0(z, t)}{\partial z} + \frac{g}{c_p} \right), \quad (2)$$

where c_p is the specific heat at constant pressure, equal to $1004 \text{ J K}^{-1} \text{ kg}^{-1}$. Overbars in equation (1) denote temporal averages with regard to the duration of the lidar observation of typically 19 h.

Several methods for deriving wave-induced perturbations $T'(z, t)$ from the original lidar measurements $T(z, t)$ have been devised and used in the past. *Gerrard et al.* [2004] computed background density profiles based on a third-order polynomial fit to measured atmospheric density profiles. The fit was then subtracted from the measured profile, and the residuals were low-pass filtered. Finally, the resulting filtered residuals were added to the fit to form the undisturbed background profile. *Yamashita et al.* [2009] took a similar approach except that they used a fifth-order polynomial, while *Rauthe et al.* [2008] extracted wave-induced temperature perturbations in the time domain by subtracting the nightly mean from measured profiles. *Duck et al.* [2001] and more recently *Alexander et al.* [2011] determined the background profile from a series of fits with a third-order polynomial. In contrast to techniques mentioned above, *Duck et al.* [2001] limited fits to a certain height window which is shifted vertically in each cycle. The background profile is then obtained by computing the weighted average of all fits. We consider this method as most reliable for extracting gravity waves given that the alternatives are generally most sensitive to waves with periods comparable to the averaging period. For example, subtraction of the nightly mean [e.g., *Rauthe et al.*, 2008] favors waves with periods in the order of the length of the observations, which range from 3 to 12 h. While in the former case (3 h) extracted gravity wave perturbations are biased toward short-period waves, disturbances from, e.g., tides and planetary waves may be falsely identified as gravity waves in the latter case (12 h). The polynomial fit method described in *Duck et al.* [2001] does not suffer from this problem because the response function in the range of relevant gravity wave periods is mostly flat.

Following the approach used by *Alexander et al.* [2011], we resampled the measured stratospheric temperature profiles with 2 km vertical resolution. Mean statistical uncertainties of the $1 \text{ h} \times 2 \text{ km}$ profiles $T(z, t)$ are 2.8 K at 50 km and 0.5 K at 30 km altitudes. We note that biases in the temperature retrieval resulting from, e.g., aerosol scattering in the lower stratosphere and inaccuracies in the treatment of the narrowband optical filters may be larger. These biases are, however, approximately constant over the duration of typical lidar observations and can therefore be regarded as modification of the background temperature profile. For this reason, wave-induced temperature perturbation profiles $T'(z, t)$ calculated as

$$T'(z, t) = T(z, t) - T_0(z, t) \quad (3)$$

are not sensitive to biases, and statistical uncertainties (photon noise) are the main error source in the gravity wave analysis.

To extract the background temperature $T_0(z, t)$ from the observed temperature $T(z, t)$, we employ the method which is described in detail by *Alexander et al.* [2011] and *Duck et al.* [2001]. The following is a short summary: The observed profile $T(z, t)$ is split into overlapping segments of 20 km vertical extent, where the lower end of each segment is shifted by 2 km in altitude relative to the previous segment. Next, a third-order polynomial is fitted to each segment, and $T_0(z, t)$ is calculated as weighted average of all fits. The weights are distributed as follows: The central four bins of the fitted polynomial are weighted fully, while the contribution of the lower and upper three bins is smoothly reduced to zero toward the ends of each segment by decreasing the weights exponentially with an e -folding length of 3 km. This weighting scheme reduces the discontinuities which may arise from the fits wagging at the endpoints. The resulting profile is smoothed by applying a 6 km averaging filter. We call the result the background profile $T_0(z, t)$. Finally, the wave-induced perturbations $T'(z, t)$ are derived by subtracting the background profile from the measured profile (equation (3)).

Although the sensitivity of the wave extraction procedure described above drops significantly for waves with vertical wavelengths λ_z larger than 20 km (a careful analysis is presented in *Duck et al.* [2001]), $T'(z, t)$ may still contain remains from planetary waves or tides (typical $\lambda_z > 30 \text{ km}$). In order to isolate the gravity wave-induced perturbations, we filter $T'(z, t)$ in the vertical domain with a high-pass filter. By choosing a cutoff wavelength of 20 km, most gravity wave signatures present in $T'(z, t)$ are retained while background effects such as tides are sufficiently suppressed. Changes in $T'(z, t)$ caused by filtering are typically in the order of 10% or less. Note that perturbations are not bandlimited in the time domain. The vertical filtered $T'(z, t)$ were then used to compute GWPED profiles according to equation (1). The overbar in equation (1) denotes the temporal average over the duration of the lidar observation (typically 19 h). We call this average the "observational mean" in analogy to the "nightly mean" which is often used in studies based on lidar data

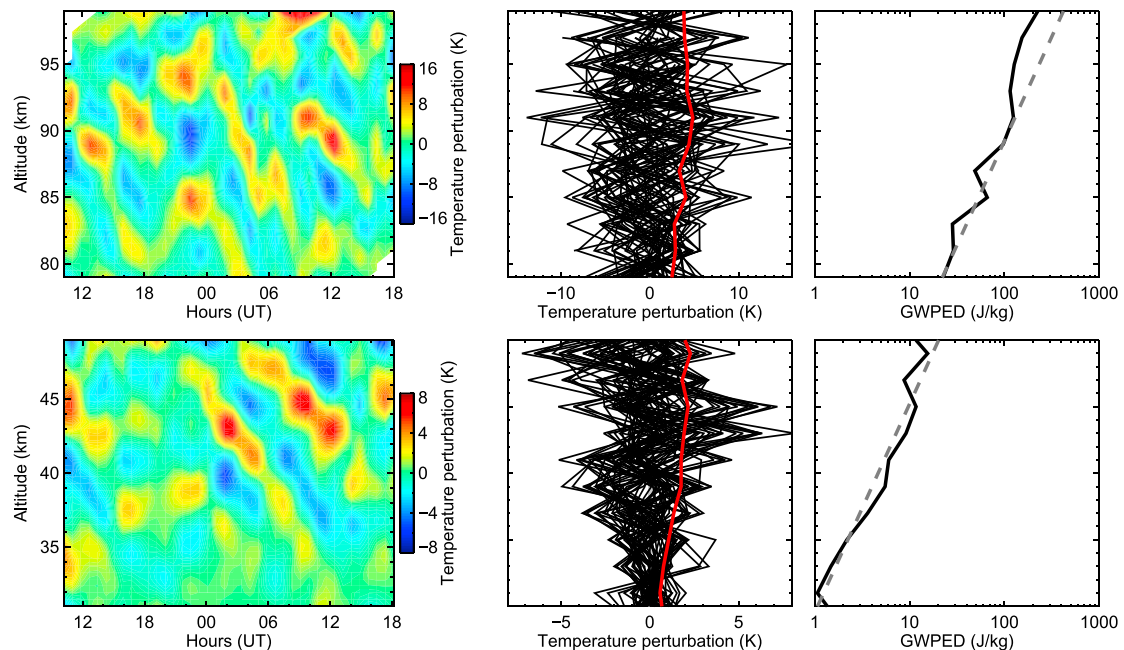


Figure 1. Illustration of data processing for gravity waves on 15/16 August 2011. (left column) Temperature perturbations in time. (middle column) Hourly perturbation profiles (black) and mean perturbation profile (red). (right column) Mean gravity wave potential energy density GWPED profile (solid line) and conservative growth rate (dashed line).

acquired with lidar instruments which are not capable of observing in daylight conditions. In this study we divided the gravity wave analysis in two sections: First, we analyzed Rayleigh temperature profiles which are typically retrieved between 25 and 60 km altitude. In a second step we analyzed iron Doppler temperature measurements between approximately 80 and 100 km. Extraction of GWPED profiles from our mesospheric temperature data is, however, complicated by the fact that the iron layer shows strong seasonal variations in layer width and metal density [Gardner *et al.*, 2011]. As the iron lidar can measure iron temperature only in altitude regions where the iron density is sufficiently high, the upper and lower ends of the temperature profiles are affected by variations of the iron layer. Especially in summer when the iron density reaches the annual minimum, the length of the retrieved temperature profile often falls below the minimum of 20 km required by the gravity wave extraction procedure, and no GWPED profiles can be obtained. For this reason, in our data set mean GWPED in the summer mesosphere is less reliable than in winter, contrary to statistics of observation hours (Table 1).

Figure 1 shows gravity wave signatures extracted from 32 h of lidar observations on 15/16 August 2011. In the stratosphere, large wave amplitudes occurred during the first 4 h followed by a relatively quiet period from about 1400 UT to midnight. Then gravity wave amplitudes increased again and remained at this level for the remainder of the observation period. In contrast, no such distinct temporal variation in amplitude is visible at mesospheric altitudes. The mean vertical wavelength is approximately 9 km in both cases, and observed wave periods range from 4 to 10 h. Phase progression was predominantly downward, implying upward transport of energy. As evident from Figure 1 (middle column), hourly perturbation amplitudes range from approximately 0.5 K in amplitude at 30 km altitude to the maximum of 15 K in 89–94 km altitude (note the different color scale). Mean perturbation amplitudes are generally about 50% smaller. Typical values are 0.3–2 K in the stratosphere and 3–5 K in the mesosphere.

Figure 1 (right column) shows mean GWPED profiles computed according to equation (1). Note the different growth rates of T' and GWPED. As the energy density is proportional to the square of the perturbation amplitudes, the GWPED increases with height more quickly than T' . On 15/16 August 2011, the GWPED increased proportional to $\exp(z/H)$ up to approximately 45 km, where H is the density scale height of the atmosphere. For reference, the growth rate of the exponential $\exp(z/6.8\text{km})$ is also shown, with $H = 6.8$ km being a typical value for the density scale height in the stratosphere. The steady increase in GWPED is indicative of freely propagating gravity waves, while the reduced growth rate observed above 45 km may be associated with wave

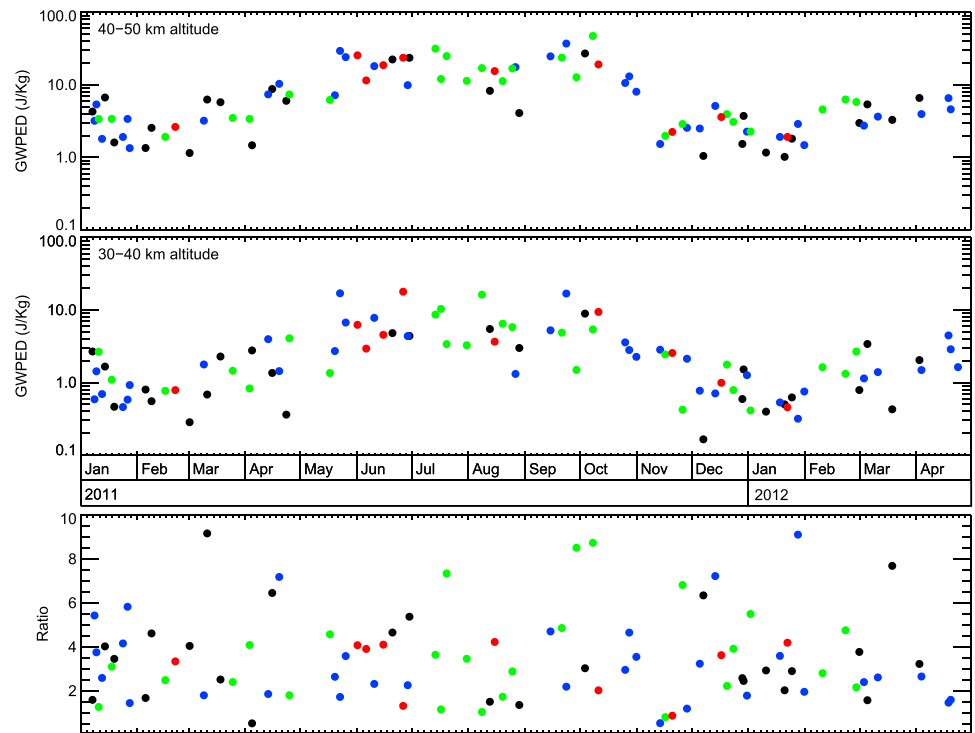


Figure 2. GWPED at (top) 40–50 km altitude and (middle) 30–40 km altitude; (bottom) GWPED ratio. Color indicates the length of the lidar observation: black: 6–12 h, blue: 12–24 h, green: 24–48 h, and red: >48 h.

breaking. Given the large variability of temperature perturbations, we note that based on the single observation shown in Figure 1, the observed decrease in GWPED above 45 km may not be significant. However, we will present seasonal averages which clearly show a significant decrease in section 3.2.

Similar behavior is observed in the mesosphere: The GWPED increases exponentially between 79 and 91 km altitude, implying conservative wave propagation in this region. Above, the growth rate is distinctly smaller but still positive. At first glance this seems to be contradictory to the mean temperature perturbation profile which shows a clear decline above 91 km. However, we need to keep in mind the influence of the background atmosphere in order to understand propagation of gravity waves. On 15/16 August 2011, the atmosphere was nearly isothermal between 79 and 91 km, implying a constant buoyancy frequency in this region, while at higher altitudes the temperature decreased rapidly toward the mesopause at approximately 100 km. The negative temperature gradient reduces the buoyancy frequency according to equation (2), and this in turn leads to an increase in GWPED despite decreasing temperature perturbation amplitudes. In the following sections we use GWPED to analyze and interpret the gravity wave activity over Davis Station.

3. Gravity Wave Activity in the Stratosphere

3.1. Short-Term and Seasonal Variation

Measurements of gravity waves in the stratosphere are typically available between 28 and 50 km. To study vertical propagation, we divided the altitude range into two altitude regions 30–40 km and 40–50 km. For each of the two regions we calculated the observational mean assuming a lognormal distribution of GWPED values.

Figure 2 shows the GWPED for the two altitude regions, each of the dots representing a single lidar observation. It is evident from this figure that there is significant short-term variability, i.e., from one lidar observation to the next few days later. On this time scale, GWPED values can vary by as much as half an order of magnitude, whereas the typical variation is in the order of 100%. It is important to note that this variability is of geophysical origin and not related to problems with the lidar instrument, as photon noise and other instrumental effects amount to typical uncertainties in GWPED of less than 10%. Though sampling of single large-amplitude gravity wave may contribute to the variability, we believe that sampling effects are sufficiently reduced as a result

Table 2. Relative Mean Variability of GWPED, \overline{q}_x , for Two Altitude Regions^a

x (days)	4	6	8	10	20	40
\overline{q}_x 40–50 km (%)	41	38	38	37	39	47
\overline{q}_x 30–40 km (%)	58	56	53	53	57	64

^aThe index x specifies the analyzing period in days. See text for details.

of the long observation periods. Even for long-period inertia gravity waves, it is reasonable to expect a minimum of two to three wave maxima and minima within the mean observation period of 24.3 h. This guarantees realistic estimates of mean T' . In contrast, short observations of, e.g., less than 6 h may sample only one half or one third of a wave period leading to underestimates in mean T' (GWPED).

To quantify the variability on short time scales, we introduce a quantity termed “mean relative variability” \overline{q}_x , where the index x specifies the analyzing period. The \overline{q}_x values are computed as follows: A time interval of x days is formed for each lidar observation centered at the observation time. Next, the mean \overline{E}_p and the standard deviation σ_{E_p} of all observational means within the time interval is computed. Finally, \overline{q}_x is found by averaging all ratios $\sigma_{E_p}/\overline{E}_p$. Results for analyzing periods between 4 and 40 days are listed in Table 2. The most striking feature is a significant difference in short-term variability in the two altitude regions. For all analyzing periods up to 40 days, the variability at lower altitudes is larger, e.g., 35% in 40–50 km versus 53% in 30–40 km altitude. The absolute difference is approximately constant (8 days: 15% and 20 days: 18%), and there is no significant correlation with the length of the analyzing period.

Comparing q_x values at fixed altitudes reveals another interesting characteristic of the short-term variability: Starting with short analyzing periods, the relative variability decreases with increasing averaging intervals and reaches a minimum at 8–10 days. For longer periods the variability increases again. Latter increase is mainly attributed to large-amplitude seasonal variations becoming increasingly dominant over short-term variations, while the initial decrease is likely a statistical effect. The mean number of observations per 4 day period is 2.2; i.e., there are only two observations for the majority of the intervals. Such small sample populations introduce a significant bias in estimates of q_x . Hence, we conclude that q_x values in the range of 8–10 days represent the most reliable estimate for characterization of the short-term variability of gravity waves. We tested against possible influences of the observation length on GWPED estimates by computing correlations. We first remove seasonal variations by subtracting the time series smoothed with a 30 day Hann filter from the original time series. The correlation coefficient obtained from correlating the reduced time series with the length of individual observations is found to be 0.005 at 40–50 km and 0.004 at 30–40 km. We conclude that the length of the observation has negligible influence.

In addition to variations on time scales of few days, the GWPED observations in Figure 2 show also a clear annual oscillation with low gravity wave activity in austral summer and large GWPED values in austral winter. To study this oscillation in more detail, we computed monthly means for both altitude regions assuming a lognormal distribution. Figure 3 shows the monthly means as well as the standard deviation of the means. In the lower altitude band (30–40 km altitude) small GWPED values occur in December and January with 1.0 J/kg and 0.8 J/kg, respectively. The wave activity increases through austral autumn and reaches a first maximum in months May–July, followed by a small dip in August. A second maximum of equal height occurs in September/October before the wave activity falls off again in late austral spring. Maximum GWPED values were observed in July (5.9 J/kg) and October (5.4 J/kg). By comparison, the local minimum (3.9 J/kg) which occurs in August is rather distinct though still within standard deviation of the means of the surrounding months. The seasonal oscillation of the GWPED in the higher-altitude band (40–50 km altitude) is quite similar to the lower altitude band. Notable differences include a faster decrease in GWPED at the end of austral autumn (October and November) and a larger oscillation amplitude. Monthly GWPED values in 40–50 km altitude vary by a factor of 7.6 (peak to valley), while in the lower altitude band with a value of 6.6 the variation is slightly smaller.

3.2. Seasonal Profiles

In the absence of dissipation, the GWPED grows with height proportional to $\exp(z/H)$. Measured GWPED profiles matching this conservative growth rate are therefore indicative of freely propagating (conservative) waves. The reverse is, however, not necessarily true, namely, that a nonconservative growth rate implies

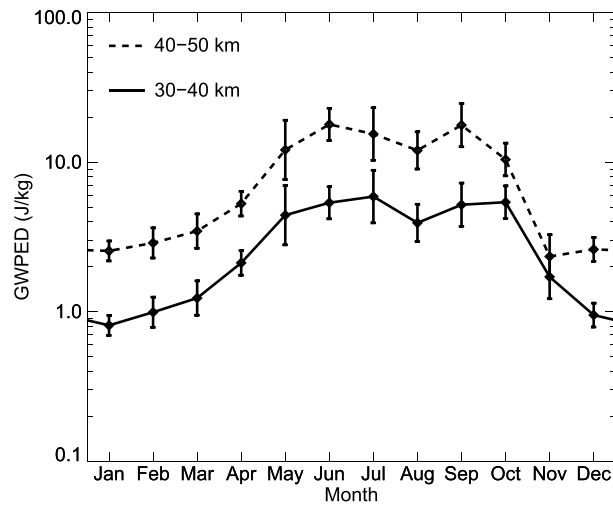


Figure 3. Seasonal variation of GWPED at 30–40 km (solid line) and 40–50 km (dashed line). Vertical bars mark the standard deviation of the mean.

energy dissipation. Under certain atmospheric conditions gravity waves can be refracted in “atmospheric waveguides” [Fritts and Yuan, 1989]. While gravity waves may propagate freely inside these waveguides, the GWPED profile decreases directly above the waveguide.

In order to study the vertical propagation of gravity waves as well as seasonal variations, we split our data set into four parts: summer (months January and February, 26 observations), autumn (months March and April, 22 observations), winter (months May–August, 23 observations), and remaining months (September–December) designated “transition period.” The breakdown of the Antarctic vortex falls in the latter period. Because gravity wave propagation is strongly influenced by the breakdown of the vortex, we discuss the transition period in detail in the section 5.

For the remaining three seasons we computed seasonal averages and estimates of the variability defined as the standard deviation of the mean. Figure 4 shows the resulting profiles. The summer profile clearly indicates conservative wave propagation up to approximately 43 km altitude. This suggests that nearly all wave energy is carried up to this level with no or very little dissipation between 29 and 43 km. Above, the GWPED profile deviates slightly from the conservative growth rate, resulting in approximately 10% loss in GWPED at 51 km altitude. The winter profile shows characteristics similar to the summer profile. Conservative wave propagation is observed between 29 and 41 km, followed by rapidly decreasing growth rates above. At 49 km altitude, gravity waves have lost more than half of their potential energy density. Note that the seasonal variation in atmospheric temperature causes modulation of the density scale height. In winter, the temperature in the region of interest is on average 29 K lower than in summer.

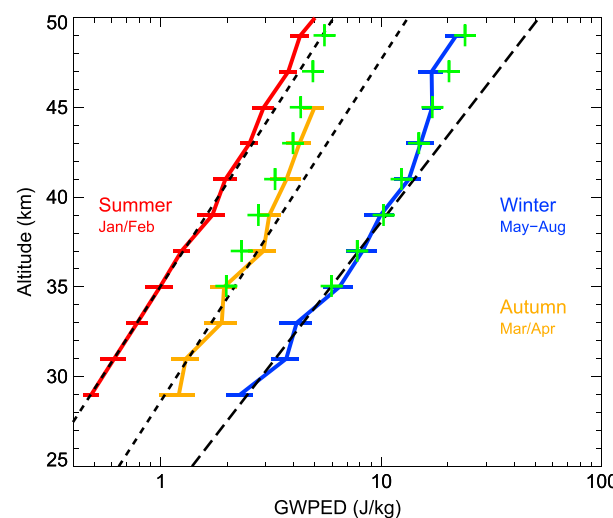


Figure 4. Vertical GWPED profiles for summer (red), autumn (orange), and winter (blue). Horizontal lines mark the standard deviation of the mean. For comparison conservative growth rates are also shown (dashed lines). Profiles marked by green crosses are taken from Alexander et al. [2011].

This temperature difference translates into a 13% decrease in scale height and hence larger conservative growth rates. The autumn GWPED profile may be considered as mixed state in between the summer profile and the winter profile. The bottom part of the profile follows approximately the conservative growth rate, while above 37 km altitude the profile converges toward the summer profile. Values above 45 km altitude are not shown because of large statistical uncertainties caused by low lidar return signal in March/April 2012.

4. Gravity Wave Activity in the Mesosphere

Figure 5 shows monthly and seasonal mean GWPED profiles extracted from mesospheric temperature measurements. The vertical extent of the profiles follows closely the seasonal variation of the iron density, the largest extent of the iron layer occurring in winter. In addition to seasonal

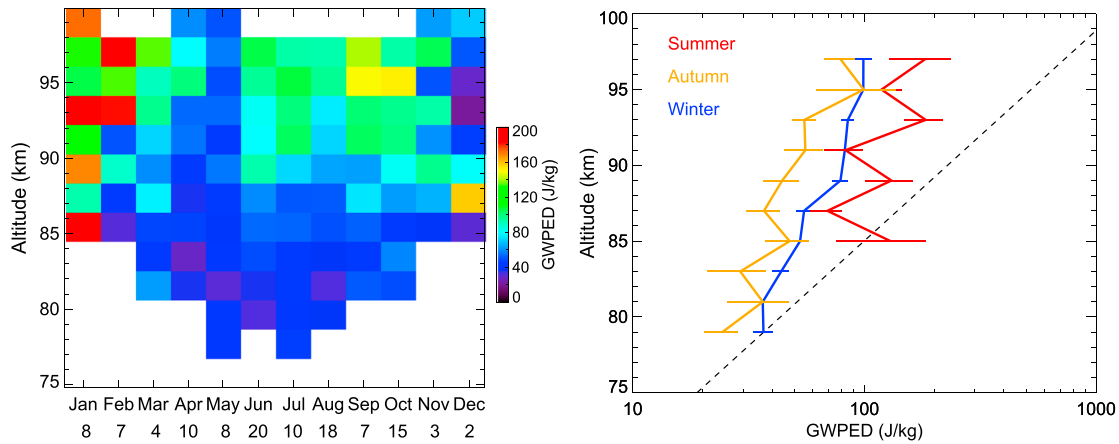


Figure 5. (left) Monthly GWPED profiles observed by the iron lidar at Davis. The number of observation per month is written below the figure. (right) Seasonal profiles with standard errors (horizontal bars). The dashed line shows the expected growth rate for conservative waves in winter scaled to the observed value at 79 km altitude.

variations, there is a substantial day-to-day variability in iron density which defines the altitude range of retrieved temperature profiles. Other prominent sources of variability include, e.g., tides and the solar effect on the layer bottom side [Yu *et al.*, 2012]. The variability described above results in retrieved temperature/GWPED profiles which vary in vertical extent from one profile to the next. Therefore, when calculating monthly mean profiles, the number of GWPED values per altitude bin may vary substantially. In order to make sure that calculated means are representative, we disregarded all data (altitude bins) where the number of observational means for a given month and altitude is less than half the maximum number for this month.

Vertical GWPED profiles in the MLT region remain well below the growth rate of conservatively propagating waves. The slopes of all three seasonal profiles in Figure 5 are roughly identical and indicate energy loss rates in the order of 80% per 10 km. We note that due to reasons given in section 2, the summer profile shows greater fluctuations, and we therefore refrain from quantitative analysis. Largest GWPED values occur in the summer months (January and February), whereas minimum values are observed in autumn (March and April). Values for December are unusual because the GWPED shows a local maximum at about 87 km altitude followed by a minimum at 94 km before the GWPED increases again further up. This profile may suggest very localized wave breaking confined to the mesopause region (about 90 km). However, there is no statistical evidence for such a conclusion, given the fact that the December profile comprises two observational means only.

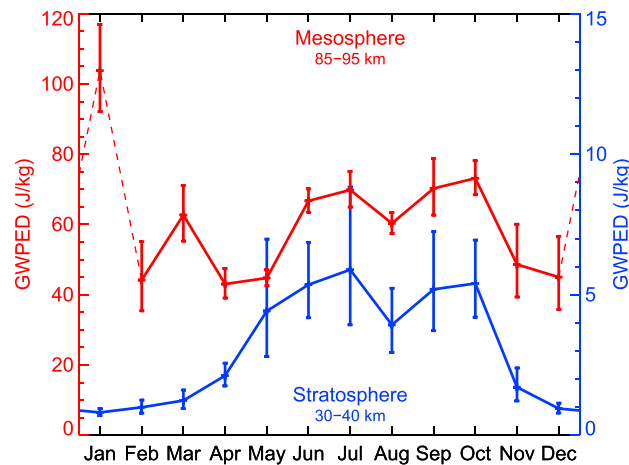


Figure 6. Seasonal variation of GWPED in the stratosphere and mesosphere. Vertical bars mark the standard deviation of the mean. Note that in winter (months May–October) values are strongly correlated.

Figure 6 shows the vertical average of monthly means. For comparison, we added the stratospheric GWPED retrieved in section 3.1. Interestingly, there appears to be a strong correlation between GWPED in the stratosphere and mesosphere as the GWPED averaged in 85–95 km shows the same double-humped structure in winter. Unlike the stratosphere, however, there is a narrower but larger secondary maximum in

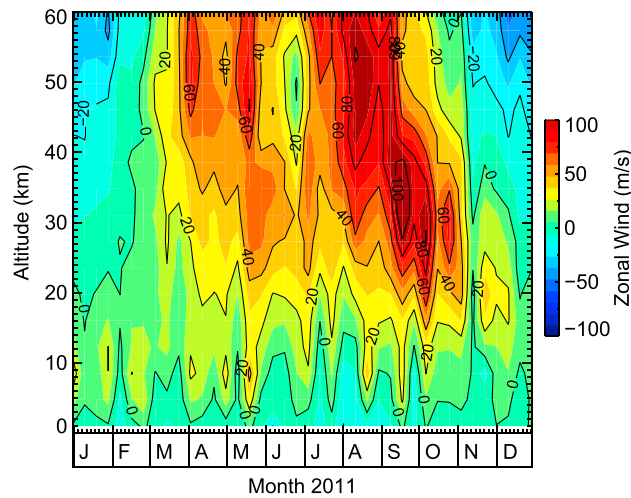


Figure 7. Zonal wind structure above Davis Station in 2011. Data are taken from the ECMWF operational analysis.

summer. The peak in January with 104 J/kg is about 50% larger than average GWPED values in winter (68 J/kg). A third maximum in March (62 J/kg) is statistically not significant.

5. Gravity Wave Filtering

At high polar latitudes the probability of gravity waves penetrating into the winter stratosphere is significantly enhanced due to the strong polar night jet which facilitates westward propagating gravity waves. Figure 7 shows the vertical structure of the zonal wind for the location of Davis Station data taken from European Centre for Medium-Range Weather Forecasts (ECMWF) operational analysis. A westerly circulation develops in the stratosphere in autumn and strengthens over the winter months, reaching wind speeds of more than 80 m/s in the upper stratosphere. This jet blocks all eastward propagating waves with the exception of waves with very large phase speeds, while westward propagating waves can reach the stratopause without hindrance. With the breakdown of the polar vortex at the end of winter, the zonal wind speed reverses. Now the path is open for eastward propagating waves while westward propagating waves are blocked. This selective filtering of gravity waves is symmetric to the winter case with regard to the direction of propagation. However, in the lower stratosphere the wind speed remains slightly positive throughout the summer months. As a consequence, waves with lower phase speeds are blocked in the summer stratosphere regardless of the direction of propagation. Because most gravity waves excited in the troposphere are expected to have small phase speeds, stratospheric GWPED in summer is also expected to be much smaller than in winter although conservative propagation of waves in the upper stratosphere may be observed in both cases. This interpretation is supported by measured GWPED profiles discussed in the previous section.

We want to study the relation between zonal wind speed and gravity wave propagation in more detail. First, we identified regions where filtering of waves with small phase speeds is expected, i.e., regions with small zonal wind speeds. For this purpose we computed daily mean profiles from ECMWF model data and selected all altitude ranges with $|u| < 2$ m/s. These ranges are marked in blue color in Figure 8. It is evident from this figure that the region where the wind reverses is progressing downward, starting at 60 km in late October and reaching approximately 25 km in December. In contrast, the second reversal in February occurs nearly instantaneously at all altitudes. Next, we computed 14 day mean GWPED profiles also shown in Figure 8. We note that due to the short averaging period, GWPED profiles are more noisy in comparison to seasonal profiles (Figure 4). However, general characteristics can still be identified. Approximately conservative wave propagation is evident in the two profiles in October up to shortly below the region of wind reversal. In November, the region moves into the altitude range where the lidar can measure GWPED, and loss of GWPED becomes more apparent. The “bulge” visible in the second November profile coincides with the location of the wind reversal. Wind filtering is even more clear in the first profile in December. The GWPED decreases strongly up to the blue shaded region, and free propagation of waves which pass through the reversal zone is observed above. In January, the region drops below the observing range of the lidar; i.e., only remaining waves with high phase speeds are visible. Because low-speed waves are filtered at the lowest altitude with low wind speed,

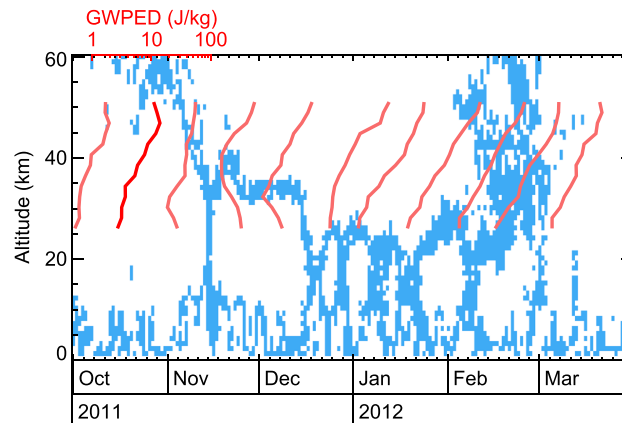


Figure 8. Interaction of gravity waves with the background wind. Blue shaded areas mark altitude ranges with $|u| < 2$ m/s (ECMWF data). Red lines show 14 day mean GWPED profiles measured by lidar. Note the strong reduction in GWPED just below the blue shaded areas in November and December.

free propagation of waves is observed throughout February even though the wind reversal zone extends over the whole observing range.

We developed a simplistic gravity wave propagation model to obtain quantitative estimates for wind filtering of gravity waves over Davis Station. In this model, waves with a given GWPED distribution in phase speed space are launched at the 12 km level and propagate upward. It is important to note that the total GWPED per unit phase speed is the primary quantity here, and we do not make any assumptions of how this energy is distributed over multiple waves with equal phase speed. In fact, we chose the energy associated with waves with a certain phase speed to be carried by a single “model wave.” On first sight this seems to be a rather crude oversimplification because it is well known that the more waves are present, the more energy can be carried. However, as we are only interested in the total GWPED as function of altitude, it makes no difference whether the GWPED is distributed between few high-energy waves or many low-energy waves. To model the phase speed spectrum of gravity waves, we used a Gaussian $\propto \exp(-c^2/\sigma^2)$, where c is the phase speed and $\sigma = 8$ m/s. For reasons of simplicity, we assume a constant launch spectrum which does not vary over time. The spectrum in the range of -40 m/s to 40 m/s is partitioned into 100 bins approximately 0.8 m/s wide, and the fractional GWPED in each bin is represented by a single model wave. These 100 waves then propagate upward in vertical steps of 1 km. Wind filtering of waves is modeled by comparing in each step the phase speed of the waves with the zonal wind speed u extracted from ECMWF data. Waves are assumed to propagate freely if $|c - u| \geq 5$ m/s. In this case, the fractional GWPED is multiplied according to the conservative growth rate proportional $\exp(z/H)$, which evaluates to 1.145 for a 1 km interval. Conversely, waves are assumed to be close to a critical level if $|c - u| < 5$ m/s. Dissipation of energy is modeled by reducing the multiplication factor in three steps as listed in Table 3. We determined these factors empirically with the goal to achieving a best fit to our measurement data. By not eliminating the wave entirely, e.g., setting the multiplication factor to zero, we allow for a nonzero probability that some waves can penetrate through the critical level. These waves may in the real atmosphere originate from secondary gravity waves, come from outside the model domain, or simply represent limitations of the model, e.g., not taking into account wave-wave interactions. In a last step we integrated the modeled GWPED spectrum over phase speed at each altitude to produce a GWPED profile similar to lidar measurements. The resulting integrated profile must be scaled properly in order to convert arbitrary energy units used in model calculations to the GWPED unit J/kg. The scaling factor

Table 3. Multiplication Factors Used in the Simplistic Gravity Wave Propagation Model

Condition	Multiplication Factor
$ c - u \geq 5$ m/s	1.156
2 m/s $\leq c - u < 5$ m/s	1.000
1 m/s $\leq c - u < 2$ m/s	0.500
$ c - u < 1$ m/s	0.100

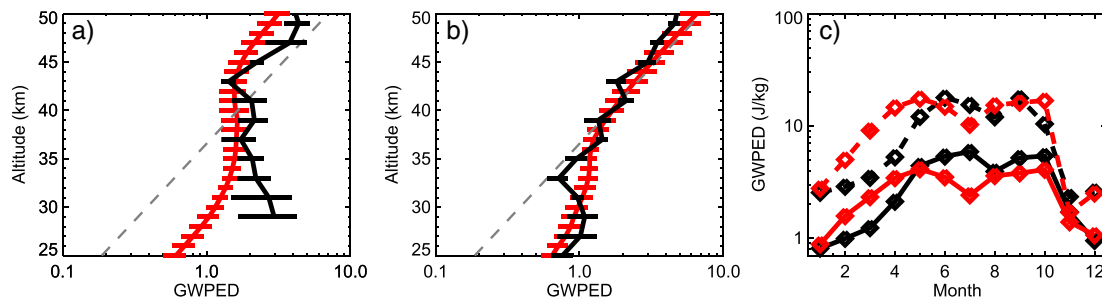


Figure 9. (a) Observed (black) and modeled monthly mean GWPED profile (red) for November 2011. Horizontal bars mark the standard deviation of the mean. The dashed line shows the conservative growth rate. (b) Same as Figure 9a but for December 2011. (c) Annual oscillation of the GWPED in 30–40 km (solid lines) and 40–50 km altitude (dashed lines).

is found by comparing the annual oscillation in GWPED observed by lidar with model results. Note that the very same scaling factor is applied to all model data.

Figure 9 shows model results as well as corresponding lidar observations. It is evident from this figure that the model reproduces the approximate altitude regions where filtering of waves takes place, i.e., altitudes where GWPED profiles deviate from the conservative growth rate. Also, total dissipation in the model matches the observations in December (Figure 9b) quite well, and energy densities at 25 km altitude and above 37 km altitude agree within one standard deviation. In November (Figure 9a) the total dissipation is underestimated by approximately 50%. However, large uncertainty estimates of measured GWPED below 32 km make dissipation estimates unreliable. A good agreement between observations and model is found for altitudes above 34 km. Figure 9c shows observed and modeled annual oscillations in GWPED. Significant seasonal variations are captured by the model. In particular, the double-humped structure of the winter maximum is reproduced for both altitude ranges, although in model data the local minimum in July precedes the observations by 1 month. We note that in late summer/autumn (months February–April) the GWPED in our model increases much faster compared to observations. On the other hand, the sharp decrease in GWPED caused by the breakdown of the polar vortex is well reproduced.

6. Discussion

The gravity wave measurements in the stratosphere obtained by the IAP iron lidar can be compared with results from other instruments on the Antarctic continent. GWPED measurements in the Antarctic region have been published in several recent studies. The study by *Alexander et al.* [2011] is based on 839 h of Rayleigh lidar measurements at Davis Station acquired during the winters of March–October 2007 and March–September 2008. The instrument was colocated with our lidar, and the results are thus predestined for comparisons. *Yamashita et al.* [2009] discuss GWPED measured by an iron Boltzmann lidar at Rothera (67.5°S, 68.0°W) and at the South Pole. This is so far the only previous lidar-based study which covers all 12 months throughout a year. Because of 24 h of daylight, lidar observations in polar summer are, in general, difficult and require special narrowband optical filter. From December 2002 to March 2005 the Boltzmann lidar was located at Rothera and operated for 507 h [*Yamashita et al.*, 2009]. The second group of GWPED measurements are based on radiosonde soundings. *Moffat-Griffin et al.* [2011] analyzed an 8 year series of 965 soundings over Rothera and published a gravity wave climatology. *Yoshiki et al.* [2004] show GWPED results from twice daily soundings over Syowa Station (69.0°S, 39.6°E) for the time frame February 1997 to January 1999.

Vertical GWPED profiles published by *Alexander et al.* [2011] are shown in Figure 4. Given that the lidar observations were carried out before the IAP iron lidar was installed at Davis and therefore do not overlap in time with our measurements, differences between the two winter profiles are surprisingly small. In fact, variations between our results and the GWPED profile published by *Alexander et al.* [2011] amount to less than 5% for altitudes below 47 km. Differences in the autumn profiles are slightly larger (approximately 20%). The largest part of these differences can be attributed to a horizontal shift of the two profiles. Because there are relatively few measurement hours in March, our autumn GWPED profile is likely biased toward the winter state, i.e., the profile is shifted toward larger values. Taking this bias into account, again there is a surprisingly good agreement between our results and the lidar measurements collected 4 years earlier.

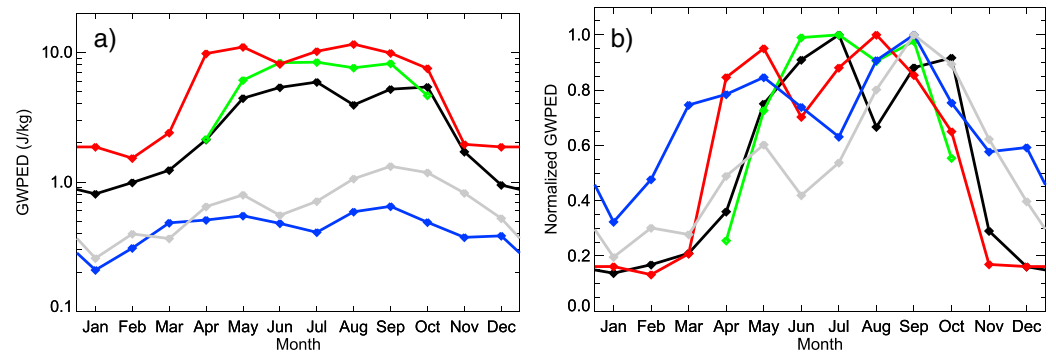


Figure 10. (a) Seasonal variations of monthly mean GWPED at Davis: black: 30–40 km (this work) and green: 37 km [from Alexander *et al.*, 2011]. Rothera: red: 30–45 km [from Yamashita *et al.*, 2009] and blue: 15–22 km [from Moffat-Griffin *et al.*, 2011]. Syowa: gray: 20–22 km [from Yoshiki *et al.*, 2004]. (b) Same as Figure 10a with maxima of traces scaled to unity. See text for details.

In order to compare seasonal variations in GWPED with our results, we digitized and processed data published in previous studies. The processing was done as follows: First, we computed monthly means from daily [Alexander *et al.*, 2011] and weekly averages [Yamashita *et al.*, 2009]. In the case of Yoshiki *et al.* [2004] we computed monthly means from the digitized time series. Figure 10a shows the resulting climatologies. While lidars generally observe stratospheric gravity waves in the range 30–50 km, radiosonde soundings are limited to much lower altitudes. To compare the different observations in terms of seasonal variations, in a second step we removed the altitude dependence of the GWPED (the GWPED grows approximately exponentially with altitude) by scaling each trace such that the maximum equals unity. The normalized traces (Figure 10b) show several interesting features: (1) The annual oscillations of the GWPED in the upper stratosphere at Davis and Rothera (black and red line) are almost identical with same values in summer and similar peak values in winter. (2) All observations show a double-humped structure with a dip around midwinter. At Rothera and Syowa the dip occurs earlier (June/July) than at Davis (August). (3) In the lower stratosphere the first winter maximum is smaller than the second maximum (gray and blue lines), while maxima of equal height are observed in the upper stratosphere (black and red lines). Also, the summer/winter and winter/summer transitions are more gradual in the lower stratosphere.

Quantitative comparisons are often hindered by research groups using different analysis and gravity wave extraction techniques or simply by publishing results which are averaged over different altitude ranges. Nonetheless, our GWPED measurements are comparable in magnitude and show generally the same seasonal variations. Minimum gravity wave activity occurs in January which is in agreement with the Syowa and Rothera radiosonde measurements. Only the Rothera lidar-based data set shows a minimum in February, 1 month later than the other data sets. The good agreement between the data sets is even more surprising given that data were recorded in different years. This suggests very stable atmospheric conditions in summer with little year-to-year variation and similar gravity wave transmission characteristics across the Antarctic continent. Davis (78°E) and Rothera (68°W) are nearly opposite to each other with respect to the South Pole. Moreover, all data sets show a rapid decrease in GWPED correlated with the breakdown of the polar vortex in months October and November. In accordance with the reversal of the zonal wind progressing downward during these months, the decrease in GWPED happens faster for lidar-based measurements in the upper stratosphere. Radiosonde-based observations show a more gradual decrease because radiosondes are limited to the lower stratosphere and are thus farther away from the wind speed maximum of the polar jet.

The relative constancy of the circulation in the Antarctic and the small interannual variability in GWPED found in this study are characteristics of the Southern Hemisphere. By contrast, the circulation in the Arctic is much more variable. In winter, the abrupt deceleration of the zonal wind associated with sudden stratospheric warmings can even cause reversal of the mean flow [Matsuno, 1971]. Such drastic changes to the wind field and thermal structure affect the generation and propagation of gravity waves. As a result, at northern middle to high latitudes gravity wave activity shows a significant interannual variability. For example, Thurairajah *et al.* [2010] report for three consecutive winter seasons (Chatanika; 65°N, 147°W) average stratospheric GWPED values 2.1 J/kg, 1.1 J/kg, and 5.7 J/kg. Interannual variability of approximately half an order of magnitude is also evident in long-term lidar observations at Esrange (68°N, 21°E) [Ehard *et al.*, 2014]. Differences in gravity

wave activity between the Northern and Southern Hemispheres are also likely candidates to explain observed interhemispheric differences in polar mesospheric summer echoes and noctilucent clouds [Morris *et al.*, 2009; Kaifler *et al.*, 2013].

We studied the influence of the polar jet on gravity wave propagation based on a very simplistic model in section 5. Despite all the obvious shortcomings and oversimplifications, the GWPED climatology produced by the model agrees surprisingly well with our lidar observations. This leads us to the conclusion that major seasonal variations in gravity wave activity are caused by filtering of waves in the lower stratosphere. More specifically, we postulate that the gravity wave flux observed in the middle atmosphere is largely independent of variations in the tropospheric source region or modulations of the strength and characteristics of the sources. Tropospheric sources may emit waves with different spectral characteristics. However, most of this variability is lost once waves pass through the lower stratosphere which acts as a selective filter. The spectral shape of the sources is thus less significant as long as the sources are on average spectrally broad enough to cover the passband of the stratospheric filter. This insensitivity to spectral characteristics is the main reason the simplistic model works so well in reproducing the observed seasonal oscillation in GWPED.

Modulation of gravity wave activity by winds has been investigated in previous studies [Wilson *et al.*, 1991; Thurairajah *et al.*, 2010]. Wilson *et al.* [1991] noted the correlation between gravity wave energies and wind speed. They concluded that the atmosphere could act as a selective filter for gravity waves and the filtering process could induce a seasonal variability in gravity wave activity in the middle atmosphere. The work by Wilson *et al.* [1991] is based on lidar observations at a midlatitude site. For Davis, the selective filtering of waves plays an even more important role because Davis is at high latitudes and thus closer to the wind speed maximum of the polar jet. The upper stratosphere over Davis in winter as well as in summer is characterized by zonal wind speeds increasing with altitude (see Figure 7). Gravity waves with small phase speeds are thus far from encountering critical levels in this region. Filtering of waves takes place predominantly in the tropopause region where wind speeds are lowest. Consequently, low-speed waves which penetrate into the upper stratosphere in winter or summer are likely to propagate freely until the wave spectrum becomes saturated and wave breaking sets in. Alexander *et al.* [2011] published evidence for conservative wave propagation over Davis in winter between 35 and 39 km altitude. Our measurements confirm GWPED growth rates which are compatible with free wave propagation between 29 and 40 km (Figure 4). Moreover, excellent agreement is found between the two data sets in the overlapping region (39–49 km), and both data sets show first signs of wave breaking around 42 km. This suggests very little year-to-year variation in gravity wave activity in the winter upper stratosphere, given that measurements were carried out in different years. Consequently, we conclude that either variability of gravity wave sources is also small in winter or this variability is effectively removed by selective filtering of gravity waves in the lower stratosphere/upper troposphere.

Since our lidar data cover two summer seasons, we can use the large number of observations (590 observation hours in total) to estimate the precision of our summer GWPED profile. Assuming conservative wave propagation between 29 and 43 km, GWPED grows proportional to $\exp(z/h)$. Fitting this exponential to our data yields a goodness of fit χ^2 value which summarizes the discrepancy between our data and the model (exponential growth). Using the standard deviation of the mean as uncertainty estimate yields $\chi^2 = 0.24$. This suggests that the standard deviation of the mean overestimates the true uncertainty of the mean. One likely explanation is non-Gaussian distributed natural variability in gravity wave activity. Only if we reduced the uncertainty estimates by a factor 4.3 we were able to achieve a χ^2 value of close to unity. This translates to a true relative uncertainty in our summer GWPED profile of less than 2.7%. In other words, our measurements are compatible with a constant GWPED growth rate indicative of conservative wave propagation if we assume measurement uncertainties as small as 2.7%. Note that this value applies only to the summer mean profile. Uncertainties of individual observational means are generally larger.

Even though waves start to break near the stratopause, temperature perturbation amplitudes generally increase with height throughout the upper stratosphere and mesosphere. This assumption appears to be valid also for individual waves in a partitioned phase speed spectrum. In section 5 we discussed the influence of the zonal wind on filtering selectively gravity waves with certain phase speeds. As we cannot measure the phase speed of waves directly, we rely on the GWPED as diagnostic tool. We showed in Figure 8 that the GWPED is strongly reduced in regions of heights where the zonal wind speed is close to zero. The correlation suggests filtering of waves with small phase speeds in these regions because waves removed from the phase speed spectrum do not contribute to the GWPED anymore. This has important consequences for the gravity wave

flux in the stratosphere as well as in the mesosphere. In the absence of additional wave sources and nonlinear wave-wave interactions, gaps once created in the phase speed spectrum persist all the way up through the atmosphere. As a result, selective filtering of gravity waves in the lower stratosphere reduces the wave flux (GWPED) not only in the upper stratosphere but also in the mesosphere. The vertical coupling is clearly visible in Figure 6. During winter months June–October GWPED values in the stratosphere are strongly correlated with those in the mesosphere. In particular, the dips in August are comparable in magnitude. The dip separating the two winter peaks also appears in our model results (Figure 9) although shifted by 1 month. Inspection of the ECMWF zonal wind data reveals that the reduction in GWPED results from selective filtering of gravity waves near the tropopause level. Most likely, this is also the case for the measurement data showing the dip in August. Thus, the combination of model results and lidar observations demonstrates that the gravity wave flux (GWPED) in the MLT region is effectively controlled by the structure of the zonal wind in the tropopause region and lower stratosphere. In summer the situation is more complicated. Fluctuations in wind speed also likely modulate the wave flux. However, the modulation has little effect on the MLT region because the zonal wind reverses in the stratosphere, thus blocking all gravity waves with small phase speeds. According to this, the GWPED peak in summer must result from waves with larger phase speeds which penetrate through the stratosphere mostly unaffected. The result is a characteristic semiannual oscillation previously reported by Hoffmann *et al.* [2010]. One notable exception is the smaller peak in March. Studying the structure of the zonal wind reveals a short period in the beginning of March which is characterized by low positive wind speeds throughout the stratosphere and lower mesosphere. The contour lines in Figure 7 run almost vertically during this period. Consequently, gravity waves with small phase speeds are able to propagate deeply into the mesosphere, while before and after this period these waves are filtered. The increased wave flux reaching the MLT region causes the GWPED enhancement in March which is not seen in the stratosphere. Dowdy *et al.* [2007] published a gravity wave climatology for the Davis MLT region based on multiyear MF radar observations. Because the climatology does not show any enhancement in the relevant period, we conclude that the GWPED peak in March is most likely the result of sporadic events which do not occur every year.

7. Summary and Conclusion

In this work, we analyze lidar observations made at the Antarctic research station Davis for gravity waves. We use the gravity wave potential energy density (GWPED) as proxy for wave activity and study vertical propagation of waves as well as selective filtering of waves due to critical levels caused by the structure of the zonal wind.

We find a clear annual oscillation in gravity wave activity showing a broad double maximum in winter. The seasonal variation is similar in both the midstratosphere (30–40 km) and the upper mesosphere (85–95 km). Variations in gravity wave activity in the stratosphere are correlated with zonal wind and can be modeled as variations due to critical layer filtering by the wind. The seasonal behavior in gravity wave activity is remarkably similar across the Antarctic continent. Interannual variations are smaller than in the Northern Hemisphere.

The correlation between gravity wave activity in the stratosphere and upper mesosphere suggest that the wavefield in the mesosphere is dominated by waves propagating from below. In comparing model results with observations we find that most of the wave filtering takes place in the lower stratosphere; i.e., the wind field in the lower stratosphere essentially controls the gravity wave flux in the upper mesosphere.

The extensive lidar data set will enable more detailed investigations of gravity wave parameters in the stratosphere as well as the mesosphere. Such studies will be important for understanding deep gravity wave propagation and effects resulting from the coupling between the troposphere, stratosphere, mesosphere, and lower thermosphere. The studies may also contribute to the understanding of gravity wave-related phenomenon such as structures in polar mesospheric clouds and the occurrence of polar mesospheric summer echoes.

References

- Alexander, M. J., et al. (2008), Global estimates of gravity wave momentum flux from High Resolution Dynamics Limb Sounder observations, *J. Geophys. Res.*, *113*, D15518, doi:10.1029/2007JD008807.
- Alexander, S. P., A. R. Klekociuk, and D. J. Murphy (2011), Rayleigh lidar observations of gravity wave activity in the winter upper stratosphere and lower mesosphere above Davis, Antarctica (69°S, 78°E), *J. Geophys. Res.*, *116*, D13109, doi:10.1029/2010JD015164.
- Allen, S. J., and R. A. Vincent (1995), Gravity wave activity in the lower atmosphere: Seasonal and latitudinal variations, *J. Geophys. Res.*, *100*(D1), 1327–1350, doi:10.1029/94JD02688.

Acknowledgments

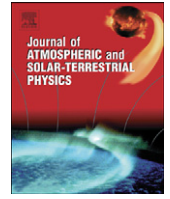
We would like to thank the Australian Antarctic Division for logistics and support in carrying out lidar measurements at Davis Station. ECMWF data used in this study have been obtained from the ECMWF data server. Lidar data are archived by the Leibniz Institute of Atmospheric Physics and are available on request from www.iap-kborn.de. Analysis methods used to extract gravity wave parameters are described in the text.

- Andrews, D., J. Holton, and C. Leovy (1987), *Middle Atmosphere Dynamics*, Academic Press, Orlando, Fla.
- Becker, E. (2012), Dynamical control of the middle atmosphere, *Space Sci. Rev.*, *168*, 283–314, doi:10.1007/s11214-011-9841-5.
- Chen, C., X. Chu, A. J. McDonald, S. L. Vadas, Z. Yu, W. Fong, and X. Lu (2013), Inertia-gravity waves in Antarctica: A case study using simultaneous lidar and radar measurements at McMurdo/Scott Base (77.8°S, 166.7°E), *J. Geophys. Res. Atmos.*, *118*, 2794–2808, doi:10.1002/jgrd.50318.
- Collins, R., and C. Gardner (1995), Gravity wave activity in the stratosphere and mesosphere at the South Pole, *Adv. Space Res.*, *16*(5), 81–90, doi:10.1016/0273-1177(95)00175-E.
- Dowdy, A. J., R. A. Vincent, M. Tsutsumi, K. Igarashi, Y. Murayama, W. Singer, and D. J. Murphy (2007), Polar mesosphere and lower thermosphere dynamics: 1. Mean wind and gravity wave climatologies, *J. Geophys. Res.*, *112*, D17104, doi:10.1029/2006JD008126.
- Duck, T. J., J. A. Whiteway, and A. I. Carswell (2001), The gravity wave-Arctic stratospheric vortex interaction, *J. Atmos. Sci.*, *58*, 3581–3596, doi:10.1175/1520-0469(2001)058<3581:TGWASV>2.0.CO;2.
- Ehard, B., P. Achtert, and J. Gumbel (2014), Long-term lidar observations of wintertime gravity wave activity over northern Sweden, *Ann. Geophys.*, *32*(11), 1395–1405, doi:10.5194/angeo-32-1395-2014.
- Fritts, D. C., and L. Yuan (1989), An analysis of gravity wave ducting in the atmosphere: Eckart's resonances in thermal and Doppler ducts, *J. Geophys. Res.*, *94*(D15), 18,455–18,466, doi:10.1029/JD094iD15p18455.
- Gardner, C. S., X. Chu, P. J. Espy, J. M. C. Plane, D. R. Marsh, and D. Janches (2011), Seasonal variations of the mesospheric Fe layer at Rothera, Antarctica (67.5°S, 68.0°W), *J. Geophys. Res.*, *116*, D02304, doi:10.1029/2010JD014655.
- Gerrard, A. J., T. J. Kane, J. P. Thayer, and S. D. Eckermann (2004), Concerning the upper stratospheric gravity wave and mesospheric cloud relationship over Søndrestrom, Greenland, *J. Atmos. Sol. Terr. Phys.*, *66*(3–4), 229–240, doi:10.1016/j.jastp.2003.12.005.
- Hoffmann, P., E. Becker, W. Singer, and M. Placke (2010), Seasonal variation of mesospheric waves at northern middle and high latitudes, *J. Atmos. Sol. Terr. Phys.*, *72*(14–15), 1068–1079, doi:10.1016/j.jastp.2010.07.002.
- Holton, J. R. (1983), The influence of gravity wave breaking on the general circulation of the middle atmosphere, *J. Atmos. Sci.*, *40*(10), 2497–2507, doi:10.1175/1520-0469(1983)040<2497:TIOGWB>2.0.CO;2.
- Kaifler, N., G. Baumgarten, A. Klekociuk, S. Alexander, J. Fiedler, and F.-J. Lübken (2013), Small scale structures of NLC observed by lidar at 69°N/69°S and their possible relation to gravity waves, *J. Atmos. Sol. Terr. Phys.*, *104*, 244–252, doi:10.1016/j.jastp.2013.01.004.
- Klekociuk, A., M. Lambert, R. Vincent, and A. Dowdy (2003), First year of Rayleigh lidar measurements of middle atmosphere temperatures above Davis, Antarctica, *Adv. Space Res.*, *32*(5), 771–776, doi:10.1016/S0273-1177(03)00421-6.
- Lautenbach, J., and J. Höffner (2004), Scanning iron temperature lidar for mesopause temperature observation, *Appl. Opt.*, *43*(23), 4559–4563, doi:10.1364/AO.43.004559.
- Lindzen, R. S. (1981), Turbulence and stress owing to gravity wave and tidal breakdown, *J. Geophys. Res.*, *86*(C10), 9707–9714, doi:10.1029/JC086iC10p09707.
- Lübken, F.-J. (1999), Thermal structure of the Arctic summer mesosphere, *J. Geophys. Res.*, *104*(D8), 9135–9149, doi:10.1029/1999JD900076.
- Lübken, F.-J., J. Höffner, T. P. Viehl, B. Kaifler, and R. J. Morris (2014), Winter/summer mesopause temperature transition at Davis (69°S) in 2011/2012, *Geophys. Res. Lett.*, *41*, 5233–5238, doi:10.1002/2014GL060777.
- Lue, H. Y., F. S. Kuo, S. Fukao, and T. Nakamura (2013), Studies of gravity wave propagation in the mesosphere observed by MU radar, *Ann. Geophys.*, *31*(5), 845–858, doi:10.5194/angeo-31-845-2013.
- Matsuno, T. (1971), A dynamical model of the stratospheric sudden warming, *J. Atmos. Sci.*, *28*(8), 1479–1494, doi:10.1175/1520-0469(1971)028<1479:ADMOTS>2.0.CO;2.
- Moffat-Griffin, T., R. E. Hibbins, M. J. Jarvis, and S. R. Colwell (2011), Seasonal variations of gravity wave activity in the lower stratosphere over an Antarctic Peninsula station, *J. Geophys. Res.*, *116*, D14111, doi:10.1029/2010JD015349.
- Morris, R. J., A. R. Klekociuk, R. Latteck, W. Singer, D. A. Holdsworth, and D. J. Murphy (2009), Inter-hemispheric asymmetry in polar mesosphere summer echoes and temperature at 69° latitude, *J. Atmos. Sol. Terr. Phys.*, *71*(3–4), 464–469, doi:10.1016/j.jastp.2008.09.042.
- Nicolls, M. J., R. H. Varney, S. L. Vadas, P. A. Stamus, C. J. Heinselman, R. B. Cosgrove, and M. C. Kelley (2010), Influence of an inertia-gravity wave on mesospheric dynamics: A case study with the Poker Flat Incoherent Scatter Radar, *J. Geophys. Res.*, *115*, D00N02, doi:10.1029/2010JD014042.
- Nomura, A., Y. Iwasaka, and T. Kano (1989), Gravity wave activities over Syowa Station, Antarctica, in *Proceedings of the NIPR Symposium on Polar Meteorology and Glaciology*, vol. 2, edited by T. Hoshiai, pp. 1–7, Nat'l. Inst. of Polar Res., Tokyo.
- Olivero, J. J., and G. E. Thomas (1986), Climatology of polar mesospheric clouds, *J. Atmos. Sci.*, *43*(12), 1263–1274, doi:10.1175/1520-0469(1986)043<1263:COPMC>2.0.CO;2.
- Rapp, M., and G. E. Thomas (2006), Modeling the microphysics of mesospheric ice particles: Assessment of current capabilities and basic sensitivities, *J. Atmos. Sol. Terr. Phys.*, *68*(7), 715–744, doi:10.1016/j.jastp.2005.10.015.
- Rauthe, M., M. Gerding, and F.-J. Lübken (2008), Seasonal changes in gravity wave activity measured by lidars at mid-latitudes, *Atmos. Chem. Phys.*, *8*(22), 6775–6787, doi:10.5194/acp-8-6775-2008.
- Thurairajah, B., R. L. Collins, V. L. Harvey, R. S. Lieberman, and K. Mizutani (2010), Rayleigh lidar observations of reduced gravity wave activity during the formation of an elevated stratopause in 2004 at Chatanika, Alaska (65°N, 147°W), *J. Geophys. Res.*, *115*, D13109, doi:10.1029/2009JD013036.
- Wang, L., and M. J. Alexander (2010), Global estimates of gravity wave parameters from GPS radio occultation temperature data, *J. Geophys. Res.*, *115*, D21122, doi:10.1029/2010JD013860.
- Wilson, R., M. L. Chanin, and A. Hauchecorne (1991), Gravity waves in the middle atmosphere observed by Rayleigh lidar: 2. Climatology, *J. Geophys. Res.*, *96*(D3), 5169–5183, doi:10.1029/90JD02610.
- Wright, C. J., and J. C. Gille (2013), Detecting overlapping gravity waves using the S-Transform, *Geophys. Res. Lett.*, *40*, 1850–1855, doi:10.1002/grl.50378.
- Yamashita, C., X. Chu, H.-L. Liu, P. J. Espy, G. J. Nott, and W. Huang (2009), Stratospheric gravity wave characteristics and seasonal variations observed by lidar at the South Pole and Rothera, Antarctica, *J. Geophys. Res.*, *114*, D12101, doi:10.1029/2008JD011472.
- Yoshiki, M., N. Kizu, and K. Sato (2004), Energy enhancements of gravity waves in the Antarctic lower stratosphere associated with variations in the polar vortex and tropospheric disturbances, *J. Geophys. Res.*, *109*, D23104, doi:10.1029/2004JD004870.

- Yu, Z., X. Chu, W. Huang, W. Fong, and B. R. Roberts (2012), Diurnal variations of the Fe layer in the mesosphere and lower thermosphere: Four season variability and solar effects on the layer bottomside at McMurdo (77.8°S, 166.7°E), Antarctica, *J. Geophys. Res.*, *117*, D22303, doi:10.1029/2012JD018079.
- Zhang, F. (2004), Generation of mesoscale gravity waves in upper-tropospheric jet-front systems, *J. Atmos. Sci.*, *61*(4), 440–457, doi:10.1175/1520-0469(2004)061<0440:GOMGWI>2.0.CO;2.

Contents lists available at [SciVerse ScienceDirect](http://www.sciencedirect.com)

Journal of Atmospheric and Solar-Terrestrial Physics

journal homepage: www.elsevier.com/locate/jastp

Experimental evidence of a stratospheric circulation influence on mesospheric temperatures and ice-particles during the 2010–2011 austral summer at 69°S

Ray J. Morris^{a,*}, Josef Höffner^b, Franz-Josef Lübken^b, Timo P. Viehl^b, Bernd Kaifler^b, Andrew R. Klekociuk^a^a Australian Antarctic Division, Department of Sustainability, Environment, Water, Population and Communities, Kingston 7050, Tasmania, Australia^b Leibniz-Institute of Atmospheric Physics, Kühlungsborn, Germany

ARTICLE INFO

Article history:

Received 30 January 2012

Received in revised form

18 June 2012

Accepted 12 August 2012

Available online 21 August 2012

Keywords:

Mesopause

Temperature

Ice particles

Stratosphere

ABSTRACT

A significant inter-annual decrease in polar mesosphere ice-particles, i.e., PMSE and PMC, during 2010–2011 is compared with earlier austral summers, in particular with 2009–2010. The first IAP iron lidar temperature measurement at Davis (68.6°S), Antarctica from 14 December 2010 are used to assess thermal effects of atmospheric processes on the mesopause region. We report low average temperatures of ~ 125 K measured by Fe-lidar near 90 km when the PMSE season commenced, whereas temperatures were warmer in 2010–2011 compared to 2009–2010 at altitudes where PMSE normally occur (around 86 km). Summer mesopause region temperature anomalies are derived using Aura MLS records. We reveal that the late break-down of the Antarctic stratospheric polar vortex on 5 January 2010, coupled with enhanced early summer mesospheric zonal wind field, provide a barrier to upward propagation of atmospheric gravity waves to be the main mechanism for the observed warm early summer season below the mesopause. The mesopause in 2010–2011 was unusually high and cold. We conclude that the timing of the annual break-down of the southern polar stratospheric vortex as manifest in zonal winds at 30 hPa impacts mesosphere temperature and ice-particle formation early in the austral summer.

Crown Copyright © 2012 Published by Elsevier Ltd. All rights reserved.

1. Introduction

Summer polar mesosphere ice-particles provide important information regarding the thermal, dynamical and chemical state of the environment adjacent the mesopause region (78–94 km). They cause strong radar echoes called ‘polar mesosphere summer echoes’ (PMSE) which are theoretically well understood (see Rapp and Lübken, 2004). Initial investigation focussed extensively on the Northern Hemisphere (NH) observations of PMSE using MST radar, and ‘polar mesospheric clouds’ (PMC) using lidar and space-borne optical instrumentation (although historically called noctilucent clouds (NLC) based on ground visual and photographic observations). Recent observational knowledge of Southern Hemisphere (SH) PMSE (Morris et al., 2007; Kirkwood et al., 2007; Latteck et al., 2007) and PMC (Klekociuk et al., 2008) and temperature (Lübken et al., 2004) canvassed similarities and differences between their northern counterparts.

Latteck et al. (2007) revealed a lower peak volume reflectivity at Davis ($\eta \sim 3.7 \times 10^{-11} \text{ m}^{-1}$) compared with Andenes ($\eta \sim 6.8 \times$

10^{-10} m^{-1}). Whilst Kirkwood et al. (2007) reported similar volume reflectivity at Wasa (73°S) and Kiruna (68°N), where $\eta \sim 6 \times 10^{-14} \text{ m}^{-1}$ for 2007 toward the end of the PMSE season (observations were not available for the start of the SH summer). Morris et al. (2009a) reported that Davis PMSE had lower occurrence rates and strength compared with Andenes, and attributed this to warmer mesopause region temperatures in the SH based on Aura/MLS records. Further these authors concluded that PMSE at the latitude of Davis were more variable and near the margin of existence, being affected by atmospheric perturbations more than their equivalent latitude NH counterpart. Similarly, Bailey et al. (2005) reported an inter-hemispheric difference in PMC characteristics and later provided evidence that SH PMC exhibit larger variability (Bailey et al., 2007). Kirkwood et al. (2008) showed that for some austral summers the centroid altitude of PMSE at two SH locations, Davis and Wasa early in the season were elevated by several kilometres as a consequence of atmospheric dynamics, unlike at two NH locations, Andenes and Kiruna where the PMSE centroid altitude remains relatively constant. Additionally the Leibniz-Institute Middle Atmosphere Ice model (LIMA) showed differences in ice clouds in the NH and SH (Lübken and Berger, 2007, 2011). Hence, in general inter-hemisphere studies reveal SH PMSE and PMC to be more variable in their seasonal occurrence distribution, start date and early season

* Corresponding author. Tel.: +61 3 6232 3315; fax: +61 3 6232 3496.

E-mail address: ray.morris@aad.gov.au (R.J. Morris).

onset altitude, in comparison to more stable and predictable NH equivalent parameters.

Interestingly in the context of our findings, the initial SH observations of PMSE at Machu Picchu (62.1°S) exhibited considerable seasonal variability in occurrence rates: no PMSE during January–February 1994 (Balsley et al., 1993); limited PMSE during January–February 1995 (Woodman et al., 1999); and frequent PMSE during 1997–1998 (and at Artigas ~62°S) during 2000–2001 (Sarango et al., 2003).

In this paper we report a significant reduction in the occurrence of PMSE (and PMC) observed at Davis during the austral summer of 2010–2011 compared to the high occurrence rate for 2009–2010. The Davis observations are consistent with low occurrence rates of PMC detected by the Aeronomy of Ice in the Mesosphere (AIM) satellite for the 2010–2011 austral summer (personnel communications with Gary Thomas) and for 2007–2008 and 2008–2009 (Karlsson et al., 2011), and Odin (Gumbel and Karlsson, 2011). Finally we examine the linkage between PMSE characteristics and the late break-down of the southern polar stratospheric vortex in the context of the Canadian Middle Atmosphere Model (CMAM) account of a similar reduction in PMC observed from satellite (Karlsson et al., 2011).

2. Experiment

We present a comparison of PMSE characteristics in the SH between the austral summers 2009–2010 and 2010–2011 using measurements by calibrated mesosphere–stratosphere–troposphere (MST) radar (Morris et al., 2006) at Davis, Antarctica (68.6°S). The mesosphere zonal wind field was derived using collocated MF radar observations (Morris et al., 2006). Mesopause region temperature anomalies were derived from Aura Microwave Limb Sounder (MLS) version 3.3 data (Schwartz et al., 2008). The Leibniz-Institute of Atmospheric Physics, Germany mobile scanning Fe-lidar was commissioned at Davis in November 2010 to measure mesospheric Doppler temperatures, vertical winds and PMC (Höffner and Lautenbach, 2009).

The Fe-lidar measured mesospheric Doppler temperatures and vertical winds by scanning the iron resonance line at 386 nm during the 2010–2011 austral summer. Daylight measurements utilise a 2 pm double etalon with high transmission and a small field-of-view of 65 μ rad. The unique combination of high iron number density, low backscatter coefficient and narrow atomic line, together with atmospheric properties and specific instrumental capabilities allow daylight measurements with high signal-to-background (Höffner and Lautenbach, 2009). The low background enhances the Fe-lidar sensitivity for detection of PMC. Note that PMC are distinguished from the iron signal by its spectral signature in the backscattered signal. Secondly the fundamental wavelength at 772 nm of the frequency doubled alexandrite ring laser is used as an independent PMC/aerosol lidar. The AAD Rayleigh lidar (Klekociuk et al., 2008) was not operational during the 2010–2011 austral summer.

3. Observations

3.1. Ice particle measurements

A significant reduction in PMSE was observed at Davis during the austral summer of 2010–2011 compared to 2009–2010 as shown in Fig. 1. The PMSE season started on 1 December 2010 some 12 days later than the previous summer on 19 November 2009. Also the PMSE season ended on 17 February 2011 some 6 days earlier than the previous season on 23 February 2010. The

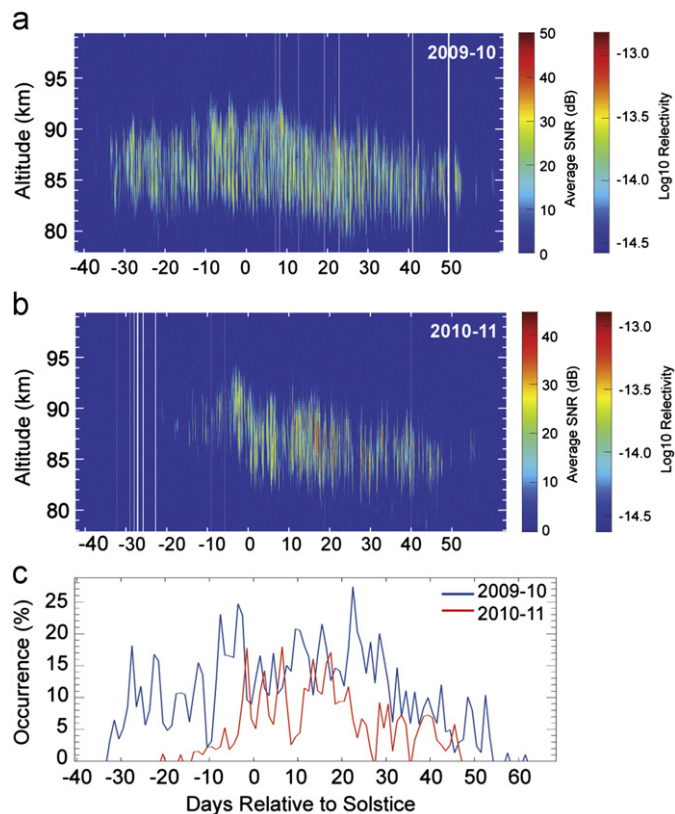


Fig. 1. Season contour images of PMSE intensity (SNR and volume reflectivity) versus altitude for 2009–2010 (a), and 2010–2011 (b). The white lines correspond to data gaps. (c) Seasonal percentage occurrence rates of PMSE versus month for both 2009–2010 (blue) and 2010–2011 (red). We count an event for PMSE occurrence in each 300 m \times 1 h spatiotemporal bin in the altitude range 80–94 km for SNR > 7 dB. (For interpretation of the references to colour in this figure legend, the reader is referred to the web version of this article.)

PMSE image plots of height versus time show the obvious difference in occurrence and intensity (signal-to-noise ratio (SNR) or volume reflectivity) between the two austral summers (Fig. 1a, b). From the PMSE seasonal occurrence histograms for SNR > 7 dB, shown in Fig. 1c, we estimate an overall reduction of 59% in season occurrence (based on hourly–300 m bins in the altitude range 80–94 km) between 2009–2010 (blue) and 2010–2011 (red). Major PMSE occurrence rate reductions were evident at the start and end of the 2010–2011 season, although more comparable if not marginally higher than the 2009–2010 season from the solstice to early January 2011, although several minima in occurrence were evident particularly in January.

The centroid altitude of PMSE onset was also higher than the previous summer and the highest since 2004–2005 when austral summer observations became routine at Davis. There is typically more inter-annual variability with the PMSE during the early part of the season; onset, height of layer, and intensity in the SH compared with stable characteristics in the NH at 69°S (Kirkwood et al., 2008). However, the 2010–2011 PMSE season revealed a late start, higher initial layer at lower intensity, and significantly lower occurrence rates, compared to the previous 6 summers at Davis. Furthermore, a significant reduction in lidar observation mean probability of PMC detection in a season (PMC hours/observation hours or %) also occurred during 2010–2011 (3.5/321.6 or 1.1% between 18 December 2010 and 8 February 2011 on the Fe-lidar) compared with 2009–2010 (51.7/266.2 or 19.4% between 22 November 2009 and 28 February 2010 on the AAD Rayleigh lidar) austral summer.

3.2. Temperature measurements

Previous SH studies revealed that the contour of $T-T_f$ (T_f is the frost point temperature) estimated from Aura MLS measurements (Schwartz et al., 2008) were remarkably similar in structure to the height versus time contour of PMSE (Morris et al., 2007, 2009a). The 2009–2010 and 2010–2011 austral summer Aura MLS mesopause region temperatures (not shown) reveal similar spatial and temporal contours to those of PMSE shown in Fig. 1. To place the 2009–2010 and 2010–2011 temperatures in perspective with recent climatology, we have shown the zonal mean temperature anomaly from Aura MLS (version 3.3 data) for the 5° latitude band centred on Davis (69°S) in Fig. 2. The anomaly temperature is obtained by subtracting the daily mean temperature for the austral summers 2004–2009 from the daily mean temperature of the 2009–2010 (Fig. 2a) and 2010–2011 (Fig. 2b) austral summers. The double hatching shows values at minima and maxima, and single hatching is for values exceeding the 9th decile. We have shown the relevant cold-point mesopause location of the climatology (white line) and the reference seasons (black line). Additionally, in Fig. 2c we provide the absolute MLS temperature time-series averaged for the altitude range 86–90 km for the reference years 2009–2010 (blue) and 2010–2011 (red)

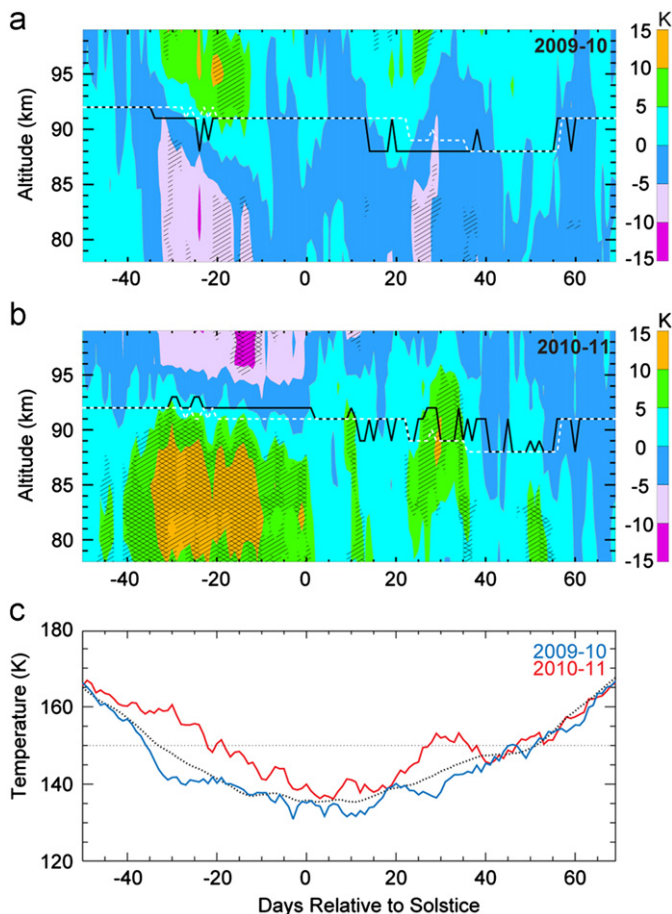


Fig. 2. (a) MLS anomaly plot of mesopause region summer temperatures in a 5° latitude band centred on Davis for the climatology years minus 2009–2010. (b) Same as (a) for the climatology years minus 2010–2011. The MLS temperature climatology is derived for the seasons from 2004–2005 to 2008–2009. The cold point mesopause altitude for the MLS climatology (white dashed lines) and the respective 2009–2010 and 2010–2011 seasons (black lines) are plotted for reference. (c) Time series of absolute MLS temperatures averaged between 86 and 90 km for 2009–2010 (blue) and 2010–2011 (red) and the MLS climatology temperature (black dotted line). (For interpretation of the references to colour in this figure legend, the reader is referred to the web version of this article.)

(red), and for the climatology (dashed line) to facilitate interpretation of the thermal environment for the intervals not covered by the Fe-lidar temperature measurements (i.e., 2009–2010 and November/early December 2010). We note that the altitude resolution of Aura MLS is 8–13 km in the mesopause region and temperature data are only validated to about 90 km (0.001 hPa).

A comparison of the 2009–2010 season PMSE occurrences (Fig. 1a) and MLS anomaly temperature (Fig. 2a) reveals a clear mesopause region thermal control of charged ice particle above the latitude of Davis. In particular the early December PMSE (Fig. 1a) occur for an interval of anomalously colder temperatures below the mesopause (Fig. 2a), and there is a correspondingly cold mesopause region during the mid-January increase in PMSE occurrence and intensity (Fig. 2a). Similarly, it is evident that the significant reduction in PMSE during 2010–2011 (Fig. 1b) is primarily related to the unusually warm temperatures below the mesopause in this latitude zone early in the summer and from mid-January onward (Fig. 2b). However, a higher mesopause will give an anomaly that is cold above the mesopause and warm below the mesopause. Fig. 2b indicates that the mesopause is higher by ~1 km in December 2010 compared with the climatology, although it is hard to be confident given the vertical resolution of the data (which are interpolated to 1 km intervals, but in reality have a resolution of several kilometres). As shown in Fig. 2b, the anomaly in the first half of December 2010 is up to +15 K at 80–85 km, and -5 K to -15 K at 95–99 km (the latter height range is outside the validated range of the MLS data). We note that below the mesopause the lapse rate is about -5 K/km (at 84 km) and above the mesopause it is ~+10 K/km (at 91 km). So with a 1 km altitude shift we can explain about 5 K (about half) of the anomaly below the mesopause and 10 K (about 2/3 or perhaps more) of the anomaly above the mesopause. This figure also shows unusually cold temperatures near the mesopause at ~90 km in early to mid-December 2010. The main point is that the MLS thermal variations are consistent with the general occurrence and intensity of the respective 2009–2010 (Fig. 1a) and 2010–2011 (Fig. 1b) PMSE season observations.

Importantly, the first Fe-lidar observations at Davis during 2010–2011 measured the precise thermal state of the local mesopause region (Höfner and Lautenbach, 2009). In Fig. 3a we show the austral summer temperature measurement at 86 km and 90 km from 10 December 2010 to 31 March 2011. The plot was smoothed using a 14-day Hanning filter applied to the 476 h of temperature measurements obtained from 49 days of Fe-lidar operation. The dashed horizontal lines illustrate the water vapour saturation levels, $S=1$ at 86 km for ~145 K (blue) and at 90 km for ~138 K (red) using H_2O concentrations from von Zahn and Berger (2003). Fe-lidar temperature measurements commenced on 14 December 2010 for ~1 h although with an error bar of ± 5 K (Fig. 3a). The first substantial Fe-lidar temperature measurements (~11 h) on 18 December 2010 revealed extremely cold average temperatures with minima of $T \sim 125$ K at 90 km and $T \sim 135$ K at 86 km. Notice that both heights exhibited a January warming, prior to cooling again, ahead of the summer-to-winter thermal transition of the mesopause region (Fig. 2b) reaching $T \sim 190$ K by mid-March. Mesopause region temperatures from MLS revealed $125 < T < 145$ K early in December when PMSE at Davis were on the margin of existence near 90–92 km with low intensity or were not present at all. The first image contour plot of the Fe-lidar derived temperature above Davis given in Fig. 3b also demonstrates that the decrease in PMSE occurrence during 2010–2011 is a consequence of a warmer mesopause region environment. Fe-lidar temperatures were not available prior to 14 December 2010 and the mesopause can only be tracked to ~91 km in Fig. 3b (as a consequence of the

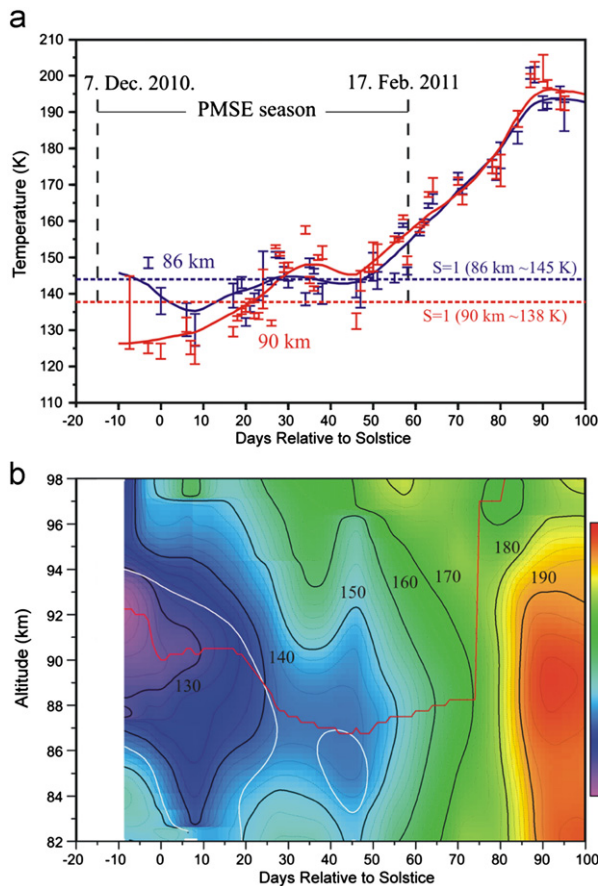


Fig. 3. (a) Fe-lidar mesopause region temperature measurements at 86 km (blue) and 90 km (red) from 14 December 2010 to 31 March 2011, where the dashed horizontal lines depict the respective saturation point temperature ($S=1$). (b) The corresponding image contour plot of Fe-lidar temperature for the altitude interval 82–98 km, which depicts the average seasonal (red) mesopause altitude. The white contour line depicts the saturation point temperature ($S=1$). (For interpretation of the references to colour in this figure legend, the reader is referred to the web version of this article.)

application of the 14-day Hanning smoothing filter ending on 10 December). The red line in Fig. 3b depicts the mesopause altitude and reveals a downward progression of the mesopause altitude throughout the austral summer—unlike the more constant mesopause altitude observed at equivalent NH latitudes (e.g., Lübken, 1999; Kirkwood et al., 2008). This seasonal downward progression in temperature appears to be a feature of the austral mesopause and is consistent with observations from the AIM satellite (Karlsson et al., 2011), and our explanation of the early season (mid-December) high altitude PMSE near 90 km for conditions with extremely cold average mesopause temperatures ~ 125 K. The white line in Fig. 3b depicts the water vapour saturation condition with $S=1$ derived from LIMA for 69°N (Andenes). We note that extremely cold mesopause temperatures with $T_{\text{frost}} \sim 128$ K is required for ice particles to occur near 93–94 km according to saturation theory for the NH (see von Zahn and Berger, 2003).

In Fig. 4a we show an interval of ~ 11 h of semi-continuous PMSE occurrence at relatively high altitudes between 88 and 94 km on 18 December 2010 (day-3 relative to solstice) and importantly prior to the polar stratospheric vortex break-down, when the zonal winds at 60°S (NCEP at 30 hPa) exceeded 10 ms^{-1} . Significantly, in Fig. 4b we show the iron lidar temperatures (red curve) averaged over the same time interval ($\sim 12:19$ – $23:19$ UT) along with the average PMSE SNR (blue curve) versus

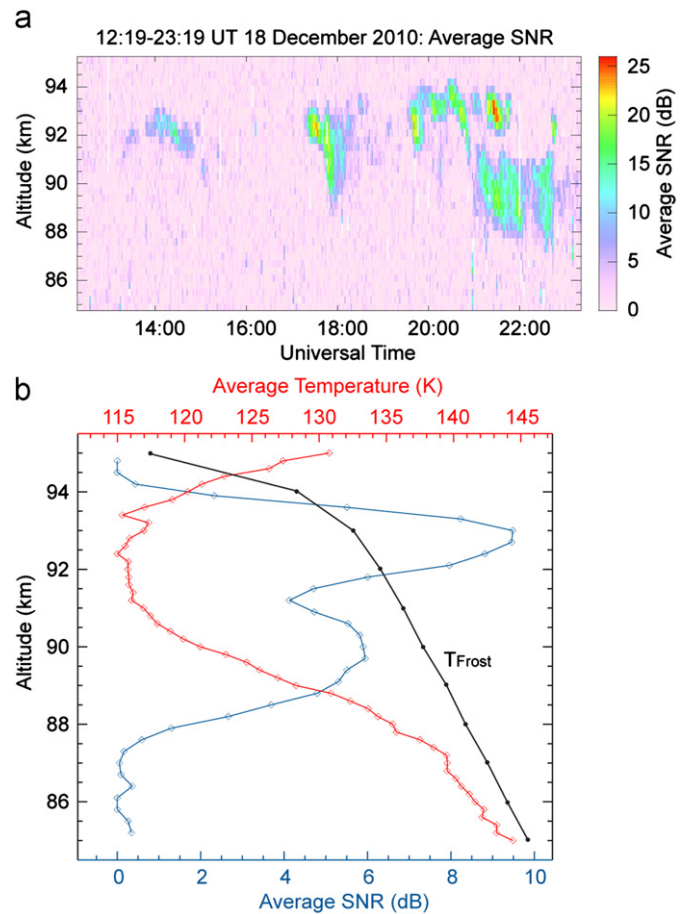


Fig. 4. (a) Altitude versus time image of a PMSE event from 12:19 to 23:19 UT on 18 December 2010 (day-3 relative to solstice). (b) Corresponding composite profile of iron lidar temperature (red curve), PMSE intensity (blue curve), and frost point temperature (black curve). The temperature (K) scale is on the upper axis and the SNR (dB) scale is on the lower axis, both for the altitude range 85–95 km. (For interpretation of the references to colour in this figure legend, the reader is referred to the web version of this article.)

altitude. Where the frost point temperature T_{frost} (black curve) is superimposed – as given in von Zahn and Berger (2003) for Andenes $\sim 69^\circ\text{N}$ – which is at an equivalent latitude to Davis $\sim 69^\circ\text{S}$. Fig. 4b reveals a low mesopause temperature of ~ 116 K with a statistical uncertainty of ~ 1.6 K at an altitude of ~ 92.4 km. We also mention that the first lidar temperature measurement (~ 1 h) obtained on 14 December 2010 (day-7) showed the mesopause temperature with $T \sim 113.8$ K with an uncertainty of ± 5 K at an altitude of ~ 92.4 km. We have shown that high altitude PMSE observed between 90 and 94 km prior to the polar stratospheric vortex break-down interval occurred for conditions of sustained cold temperatures below the frost point in this altitude range – consistent with theory (see Rapp and Lübken, 2004).

Aura MLS temperatures reveal temperatures, $T > T_{\text{frost point}}$ during November 2010 consistent with no PMSE, and intermittent temperatures, $T < T_{\text{frost point}}$ consistent with sporadic PMSE observed from 1 to 17 December 2010, after which PMSE were clearly evident. However, the very low Fe-lidar temperatures at 90–94 km shown in Fig. 3 are not seen in the temperature differences of MLS shown in Fig. 2. This suggests that the temperatures seen by the Fe-lidar are either localised or not resolved by MLS. Alternatively, it is plausible that the low mesopause temperatures above 90 km were also a feature of earlier austral summers. Lidar temperatures are very low around

the mesopause from the first substantial measurement on 18 December 2010, until mid-February. Using water vapour from a model (von Zahn and Berger, 2003) we have calculated the degree of saturation (S) and found regions with supersaturation ($S > 1$) around 90 km (see Fig. 3b). Under these circumstances we would expect the formation of ice particles provided condensation nuclei are available. A note of caution is required when comparing temperatures and PMSE. Apart from (charged) ice particles the formation of PMSE requires free electrons and atmospheric neutral air turbulence (see Rapp and Lübken, 2004). We note that kinematic viscosity increases with altitude and destroys small scale neutral density fluctuations more and more effectively. For altitudes considerably above 90 km it is therefore increasingly difficult for neutral air turbulence in combination with charged aerosols to create plasma fluctuations causing PMSE. This hampers a direct comparison of temperatures and PMSE. In fact, low enough temperatures and high supersaturation but still no PMSE have been observed at high latitudes (78°N) in the NH (see Lübken et al., 2009). Despite all these objections we find general agreement between PMSE and regions of supersaturation, which implies that the other prerequisites for creating PMSE mentioned above play only a minor role in our case. A detailed comparison of temperatures and PMSE is beyond the scope of this paper and will be published in the near future.

3.3. Wind field measurements

An examination of the zonal and meridional wind field derived from the Davis 1.94 MHz Medium Frequency radar (Morris et al., 2006) reveals two interesting characteristics for 2010–2011 in the mesopause region condition relevant to the observed reduction in PMSE and possibly linked to the initial higher than usual ice-particle layer. Firstly, the meridional wind velocity at 86 km where PMSE peaked in average season altitude (Fig. 5a), shows a tendency for episodic intervals of enhanced poleward (warm) wind flow for most of January and early February 2011 (red) in comparison to the same time during 2010 (blue). Secondly, the magnitude of the zonal wind field is significantly greater early in the December–January interval for 2010 (red) than the corresponding period for 2009 (blue) between 84 and 94 km (Fig. 5b). Of particular interest for the early part of the PMSE season is the greater magnitude of the zonal wind and its penetration to higher altitudes, which appears to be linked with the high PMSE layer for 2010–2011. In Fig. 5c we plot the centroid altitude of PMSE for 2009–2010 (blue) and 2010–2011 (red). It is clearly obvious that the PMSE centroid altitude is significantly higher at times when the zonal winds are larger (i.e., more negative) which is the case during the early part of 2010–2011. Note that the NH tends to have less inter-annual variability in early season PMSE altitude as discussed by Kirkwood et al. (2008).

4. Discussion

Observations from MST radar reveal a significant 59% reduction in PMSE occurrence at Davis (69°S) between the austral summers of 2009–2010 and 2010–2011. Three previous PMSE seasons at Davis (i.e., 2006–2007; 2007–2008 and 2008–2009) also exhibited noticeable inter-annual variability in their properties, including; onset date, altitude of layer, intensity and occurrence rate, albeit not as pronounced as in 2010–2011. Indeed early SH ground observations hint at previous inter-annual variability (Woodman et al., 1999; Balsley et al., 1995) although complete seasons were not available, and observations during January and February were possibly affected by 2-day planetary waves heating the mesopause region thus reducing the PMSE

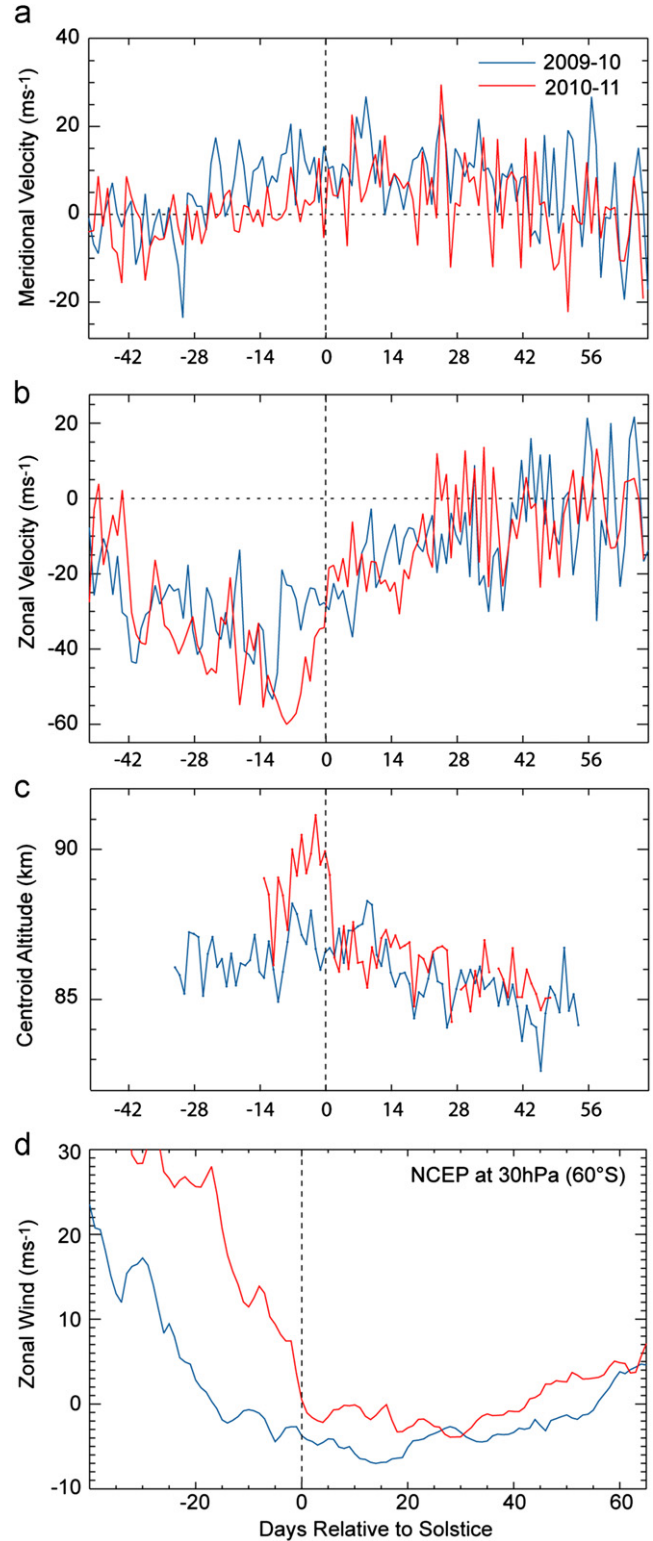


Fig. 5. (a) Meridional wind velocity where poleward flow corresponds to negative values. (b) Zonal wind velocity where westward flow corresponds to negative values, derived at 86 km from the Davis 2 MHz MF radar. (c) Centroid altitude of the PMSE layer (km). (d) Corresponding stratospheric zonal wind flow at 30 hPa for 60°S estimated using NCEP data. (For all plots 2009–2010 (blue) and 2010–2011 (red) and the vertical dashed line marks the summer solstices.) (For interpretation of the references to colour in this figure legend, the reader is referred to the web version of this article.)

intensity and occurrence rate (see Morris et al., 2009b). Furthermore, SNOE (Bailey et al., 2005, 2007; Wrotny and Russell, 2006) and SCIAMACHY (Robert et al., 2009) satellite observations

showed how SH PMC observations vary seasonally as a function of latitude. Similarly, the LIMA Ice model yields significant year-to-year variation in SH PMC occurrence as a function of latitudinal extent for the model run between 1962 and 2009 (Lübken and Berger, 2007, 2011).

So why did a major reduction PMSE occur above Davis during the summer of 2010–2011? The new observation of higher and enhanced magnitude of the zonal mesospheric winds early in the austral summer of 2010–2011 (similar for the high variability seasons discussed) may provide some insight into the larger than normal variability in PMSE characteristics. In particular, the record latest ever break-down of the SH stratosphere polar vortex on 5 January 2011 is worth consideration in the context of any upward affect on the mesosphere state by the stratospheric zonal wind flow. An examination of the zonal winds versus time at 30 hPa for 60°S from the National Center for Environmental Prediction (NCEP) Reanalysis-1, shown in Fig. 5d, reveals two interesting features. Firstly, the 2009–2010 austral summer (blue) exhibits more normal PMSE centroid altitudes (Fig. 5c) corresponding to more regular lower magnitude stratospheric zonal wind winter-to-summer transition. Secondly, the 2010–2011 austral summer (red) exhibits an early season high PMSE centroid altitude (Fig. 5c) corresponding to an interval with high magnitude stratospheric zonal winds persisting until early January. Whereby the larger magnitude zonal winds ($\sim 27 \text{ ms}^{-1}$) flowing before the 2010–2011 summer solstices provide a barrier to atmospheric gravity wave transport to the SH polar mesopause.

Furthermore, of the 8 austral summer PMSE seasons recorded at Davis, 4 seasons had large inter-annual variability (i.e., 2006–2007; 2007–2008; 2008–2009 and 2010–2011), whilst 4 had little inter-annual variability similar to NH sites (i.e., 2003–2004 part season (not shown); 2004–2005, 2005–2006 and 2009–2010). To place into perspective the 2009–2010 and 2010–2011 austral summer PMSE centroid altitude relationship with the break-down of the SH polar stratosphere vortex, we compare 7 seasons of PMSE centroid altitude (Fig. 6a) with the respective NCEP 30 hPa zonal winds (Fig. 6b). It is evident that early season PMSE centroid altitudes are higher (lower) for late (early) polar vortex break-down seasons, i.e., as shown in Fig. 6 by warm colours (red) and cold colours (blue), respectively. This observation is consistent with the results of Kirkwood et al. (2008) (their figure 2) for the austral summers from 2000–2001 to 2008–2009, and early season high centroid altitude of SH PMSE at Davis and Wasa during 2006–2007. When considered with observations reported here provide evidence of a causal effect on PMSE occurrence height, intensity and onset time with the timing of the SH polar stratospheric vortex break-down. Moreover, our reported downward altitude movement of the austral summer mesopause (Fig. 3b) at the latitude of Davis (68.6°S) interestingly mirrors the seasonal movement of the centroid altitude of the PMSE layer (Figs. 3c and 6a).

We suggest that the reduced PMSE intensity and occurrence rates early in the 2010–2011 season is caused by anomalous temperatures and zonal and meridional winds. The Fe-lidar observations at Davis in mid-December 2010 revealed record low temperatures with $T \sim 116 \text{ K}$ at elevated altitudes near 92 km when PMSE were initially evident, whereas at lower altitudes near 86 km very little PMSE was detected. We suggest that unusually warm temperatures reported below the mesopause were not conducive to the creation of PMSE. Following Karlsson et al. (2011) we may also expect that gravity waves produce turbulence at elevated altitudes which diminishes the creation of PMSE at normal altitudes. Note that the unusually strong zonal winds are consistent with the model calculations from Karlsson et al. (2011). Above 90 km, temperatures were low and ice particles were likely created. However, kinematic viscosity increases exponentially with height and prevents the formation of small scale structures

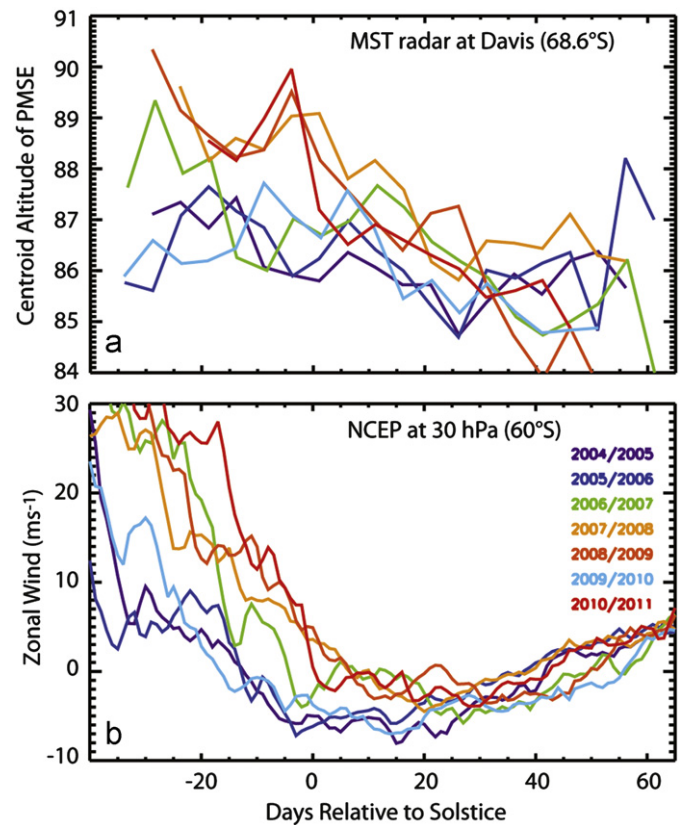


Fig. 6. (a) Centroid altitude of the PMSE layer for 7 austral summers from 2004–2005 until 2010–2011 above Davis, Antarctica (68.6°S). (b) Corresponding southern stratospheric zonal wind flow at 30 hPa for 60°S estimated using NCEP data for the above 7 summers. (For interpretation of the references to colour in this figure legend, the reader is referred to the web version of this article.)

necessary for PMSE (Lübken et al., 2009). In summary, the discernable reduction in PMSE and PMC was a consequence of overall warmer mesosphere temperatures below 86 km.

We also suggest that the diminution in PMSE intensity and occurrence rates during January (Fig. 1c) closely follows the poleward meridional wind flow (Fig. 5a) consistent with a 2-day planetary wave warming effect (Morris et al., 2009b), water vapour saturation for the latitude 69° (Fig. 3b), and larger magnitude tides evident in both the MF radar wind field (Morris et al., 2006), and the Fe-lidar thermal record at Davis (Lübken et al., 2011). Our reported inter-annual variability in ice-particles at 69°S is consistent with the variability of PMSE at Machu Picchu (Woodman et al., 1999), SNOE (Bailey et al., 2005, 2007; Wrotny and Russell, 2006), and SCIAMACHY (Robert et al., 2009) satellite observations of PMC, and LIMA Ice model simulations (Lübken and Berger, 2007, 2011).

Our report of the first ground-based PMSE/PMC observations to be linked to the late break-down of the stratospheric polar vortex is consistent with satellite observations of PMC recently reported by Gumbel and Karlsson (2011) and Karlsson et al. (2011). The CMAM model results of Karlsson et al. (2011) account for our reported elevation of the early season PMSE layer or higher mesopause, the enhanced mesospheric zonal winds (both in height and strength), and the altitude difference (few kilometres) between 'early' and 'late' vortex break-down seasons. However, the CMAM model predicts a warmer mesopause in the latitude band (65–70°S) near Davis which is contrary to the Fe-lidar results presented here of a colder mesopause with temperatures as low as 116 K. Similarly, Aura MLS anomaly analyses provide some evidence for a colder mesopause near $\sim 90 \text{ km}$ in

mid-December 2010 for the late polar vortex break down season, and a warmer mesopause in December 2009 for the more typical early polar vortex break-down season (the limitations of the MLS observations were considered in Section 3.2).

We note that the zonal winds for the 4 seasons with late polar vortex break-down (i.e., 2010–2011; 2008–2009; 2007–2008 and 2006–2007) have stronger wind strength up to day 20. However, low temperatures are observed at solstice onward, when the wind in the stratosphere reduces in strength rapidly towards 'normal' summer conditions so that most of the eastward gravity waves driving the equator-ward flow are let through. However, for 18 December 2010 (day-3) as discussed (see Figs. 3 and 4) the stratosphere winds are greater than 10 ms^{-1} —so a pre-polar vortex break-down condition is clearly evident. At this time high altitude (88–94 km) semi-continuous PMSE occurred (Fig. 4a), when coincident Fe-lidar observations showed the mesopause altitude was high at $\sim 92.4 \text{ km}$ and unusually cold $\sim 116 \text{ K}$ for saturation $S=1$ (Fig. 4b). Although the Fe-lidar data on 14 December 2010 (day-7) is statistically short in duration, this day also revealed some evidence of a cold mesopause $T \sim 113.8 \text{ K}$ at an altitude of $\sim 92 \text{ km}$ during PMSE occurrence at high altitude (not shown). To cover the mesopause region thermal environment pre 14 December 2010 (day-7) and for the 2009–2010 austral summer we utilised MLS temperature data. With consideration of known MLS temperature altitude resolution constraints—the reported thermal variations appear to effect ice particle creation/sustenance similar to the reported PMSE seasonal variability (see Figs. 1 and 2) consistent with theory (see Rapp and Lübken, 2004).

We stated above that the mesopause for 2010–2011 appeared to be $\sim 1 \text{ km}$ higher than the MLS anomaly field climatology (Fig. 2), and this could contribute to the anomalously low temperatures at high altitudes. But we claim that this does not necessarily mean there was no cooling above the mesopause or warming below the mesopause in early December 2010. Indeed we argue that when Fe-lidar observations commenced in mid-December prior to the stratospheric polar vortex break-down—the mesopause was indeed very cold at high altitude and the temperature below the mesopause was warmer than the frost point. We are cognisant that Karlsson et al. (2011) considered data in the window from 'day-40 to day-20'. We also note these authors stated that for the window 'day-20 to day-10' the pre vortex break-down state still prevailed for 2010–2011 (and 2007–2008 and 2008–2009).

Interestingly, an $\sim 11 \text{ h}$ averaged iron lidar mesopause temperature profile for 18 December 2010 (Fig. 4b) is remarkably similar to the CMAM model mesopause temperature profile shown in figure 7 of Karlsson et al. (2011), for the late break-down of the polar stratospheric vortex for the latitude band $70\text{--}85^\circ\text{S}$. We suggest that the latitude of Davis at 68.6°S early to mid-December 2010 was more representative of the CMAM mesopause region temperature profile for the latitude band $70\text{--}85^\circ$ rather than for $65\text{--}70^\circ$ pre the late polar vortex break-down condition (see Karlsson et al., 2011).

5. Conclusions

In conclusion, we report a significant reduction in PMSE (and in PMC) during the austral 2010–2011 summer compared with the previous more stable 2009–2010 season as being related to a confluence of several processes. Significantly, the reported early summer warmer mesosphere temperatures below the mesopause appear to be linked to vertical intra-hemisphere upward coupling processes triggered by the late break-down of the SH stratospheric polar vortex. Thus the enhanced stratospheric zonal

winds created a barrier to the vertical propagation of atmospheric gravity waves (Kirkwood et al., 2008; Karlsson et al., 2011) that under normal conditions cools the summer polar mesopause region. Further an enhanced poleward mesosphere meridional wind and related 2-day planetary wave heating (Morris et al., 2009b), as well as atmospheric tides (Lübken et al., 2011) warms the mid-January mesosphere to reduce PMSE occurrence rates. Whilst temperatures below the mesopause were ostensibly warmer throughout the 2010–2011 austral summer we report extremely low mesopause temperatures of $\sim 116 \text{ K}$ measured by Fe-lidar at elevated altitudes near 92 km when the PMSE season commenced. The major mechanism controlling the start of the mesosphere ice-particle season appears linked to the timing of the break-down of the southern stratospheric vortex. A future study will investigate the thermal environment during PMSE and provide a complete season (2011–2012) comparison with CMAM.

Acknowledgements

We thank A. Christensen and D. Tulloh for technical support with the Davis radars. Aura/MLS data were acquired by NASA's Earth-Sun System Division. NCEP Reanalysis data provided by the NOAA/OAR/ESRL PSD, Boulder, Colorado, USA, from their web site at www.esrl.noaa.gov/psd/. Data was acquired by ASAC Projects: 2325 – MST radar, Fe-lidar and meteor radar; 737 – AAD Rayleigh lidar; and 674 – MF radar thanks to Dr. Robert Vincent. RJM thanks the Leibniz Institute of Atmospheric Physics for positioning their Fe-lidar at Davis. D. Ratcliffe assisted with the figures. We thank the reviewers for their valuable comments.

References

- Bailey, S.M., Merkel, A.W., Thomas, G.E., Carstens, J.N., 2005. Observations of polar mesospheric clouds by the student nitric oxide explorer. *Journal of Geophysical Research* 110, D13203, <http://dx.doi.org/10.1029/2004JD005422>.
- Bailey, S.M., Merkel, A.W., Thomas, G.E., Rusch, D.W., 2007. Hemispheric differences in polar mesospheric cloud morphology observed by the student nitric oxide explorer. *Journal of Atmospheric and Solar-Terrestrial Physics* 69, 1407–1418.
- Balsley, B.B., Woodman, R.F., Sarango, M., Urbina, J., Rodriguez, R., Ragaini, E., Carey, J., 1993. Southern-hemisphere PMSE: where are they? *Geophysical Research Letters* 20, 1983–1985.
- Balsley, B.B., Woodman, R.F., Sarango, M., Rodriguez, R., Urbina, J., Ragaini, E., Carey, J., Huaman, M., Giraldez, A., 1995. On the lack of southern hemisphere polar mesosphere summer echoes. *Journal of Geophysical Research* 100, 11685–11693.
- Gumbel, J., Karlsson, B., 2011. Intra- and inter-hemispheric coupling effects on the polar summer mesosphere. *Geophysical Research Letters* 38, L14804, <http://dx.doi.org/10.1029/2011GL047968>.
- Höffner, J., Lautenbach, J., 2009. Daylight measurements of mesopause temperature and vertical wind with mobile scanning iron Lidar. *Optical Letters* 34, 1351–1353.
- Karlsson, B., Randall, C.E., Shepherd, T.G., Harvey, V.L., Lumpe, J., Nielsen, K., Bailey, S.M., Hervig, M., Russell III, J.M., 2011. On the seasonal onset of polar mesospheric clouds and the breakdown of the stratospheric polar vortex in the Southern Hemisphere. *Journal of Geophysical Research* 116, D18107, <http://dx.doi.org/10.1029/2011JD015989>.
- Kirkwood, S., Wolf, I., Nilsson, H., Dalin, P., Mikhaylova, D., Belova, E., 2007. Polar mesosphere summer echoes at Wasa, Antarctica (73°S): first observations and comparison with 68°N . *Geophysical Research Letters* 34, L15803, <http://dx.doi.org/10.1029/2007GL030516>.
- Kirkwood, S., Nilsson, H., Morris, R.J., Klekociuk, A.R., Holdsworth, D.A., Mitchell, N.J., 2008. A new height for the summer mesopause—Antarctica, December 2007. *Geophysical Research Letters* 35, L23810, <http://dx.doi.org/10.1029/2008GL035915>.
- Klekociuk, A.R., Morris, R.J., Innis, J.L., 2008. First southern hemisphere common-volume measurements of PMC and PMSE. *Geophysical Research Letters* 35, L24804, <http://dx.doi.org/10.1029/2008GL035988>.
- Latteck, R., Singer, W., Morris, R.J., Holdsworth, D.A., Murphy, D.J., 2007. Observations of mesosphere summer echoes with calibrated VHF radars at 69° on northern and southern latitudes. *Geophysical Research Letters* 34, L14805, <http://dx.doi.org/10.1029/2007GL030032>.
- Lübken, F.-J., 1999. Thermal structure of the Arctic summer mesosphere. *Journal of Geophysical Research* 104, 9135–9149.

- Lübken, F.-J., Berger, U., 2007. Interhemispheric comparison of mesospheric ice layers from the LIMA model. *Journal of Atmospheric and Solar-Terrestrial Physics* 69/17–18, 2292–2308, <http://dx.doi.org/10.1016/j.jastp.2007.07.006>.
- Lübken, F.-J., Berger, U., 2011. Latitudinal and interhemispheric variation of stratospheric effects on mesospheric ice layer trends. *Journal of Geophysical Research* 116, D00P03, <http://dx.doi.org/10.1029/2010JD015258>.
- Lübken, F.-J., Höffner, J., Viehl, T.P., Kaifler, B., Morris, R.J., 2011. First measurements of thermal tides in the summer mesopause region at Antarctic latitudes. *Geophysical Research Letters* 38, L24806, <http://dx.doi.org/10.1029/2011GL050045>.
- Lübken, F.-J., Lautenbach, J., Höffner, J., Rapp, M., Zecha, M., 2009. First continuous temperature measurements within polar mesosphere summer echoes. *Journal of Atmospheric and Solar-Terrestrial Physics* 71, 453–463, <http://dx.doi.org/10.1016/j.jastp.2008.06.001>.
- Lübken, F.-J., Müllemann, A., Jarvis, M.J., 2004. Temperature and horizontal winds in the Antarctic summer mesosphere. *Journal of Geophysical Research* 109, D24112, <http://dx.doi.org/10.1029/2004JD005133>.
- Morris, R.J., Murphy, D.J., Vincent, R.A., Holdsworth, D.A., Klekociuk, A.R., Reid, I.M., 2006. Characteristics of the wind, temperature and PMSE field above Davis, Antarctica. *Journal of Atmospheric and Solar-Terrestrial Physics*, 68, <http://dx.doi.org/10.1016/j.jastp.2005.04.011>.
- Morris, R.J., Murphy, D.J., Klekociuk, A.R., Holdsworth, D.A., 2007. First complete season of PMSE observations above Davis, Antarctica, and their relation to winds and temperatures. *Geophysical Research Letters* 34, L05805, <http://dx.doi.org/10.1029/2006GL028641>.
- Morris, R.J., Klekociuk, A.R., Latteck, R., Singer, W., Holdsworth, D.A., Murphy, D.J., 2009a. Inter-hemispheric asymmetry in polar mesosphere summer echoes and temperature at 69° latitude. *Journal of Atmospheric and Solar-Terrestrial Physics* 71, 464–469, <http://dx.doi.org/10.1016/j.jastp.2008.09.042>.
- Morris, R.J., Klekociuk, A.R., Holdsworth, D.A., 2009b. Low latitude 2-day planetary wave impact on austral polar mesopause temperatures: revealed by a January diminution in PMSE above Davis, Antarctica. *Geophysical Research Letters* 36, L11807, <http://dx.doi.org/10.1029/2009GL037817>.
- Rapp, M., Lübken, F.-J., 2004. Polar mesosphere summer echoes (PMSE): review of observations and current understanding. *Atmospheric Chemistry and Physics* 4, 2601–2633.
- Robert, C.A., von Savigny, C., Burrows, J.P., Baumgarten, G., 2009. Climatology of noctilucent cloud radii and occurrence frequency using SCIAMACHY. *Journal of Atmospheric and Solar-Terrestrial Physics* 71, 408–423, <http://dx.doi.org/10.1016/j.jastp.2008.10.015>.
- Sarango, M.F., Woodman, R.F., Flores, L.A., Villegas, S., 2003. Further observations of PMSE in Antarctica. In: *MST10 Radar Workshop Proceedings*. Piura, Peru, [May 13–20](http://dx.doi.org/10.1016/j.jastp.2008.10.015).
- Schwartz, M.J., et al., 2008. Validation of the Aura Microwave Limb Sounder temperature and geopotential height measurements. *Journal of Geophysical Research* 113, D15S11.
- von Zahn, U., Berger, U., 2003. Persistent ice cloud in the midsummer upper mesosphere at high latitudes: three-dimensional modeling and cloud interactions with ambient water vapor. *Journal of Geophysical Research* 108 (D8), 8451, <http://dx.doi.org/10.1029/2002JD002409>.
- Woodman, R.F., Balsley, B.B., Aquino, F., Flores, L., Vazquez, E., Sarango, M., Huaman, M.M., Soldi, H., 1999. First observations of polar mesosphere summer echoes in Antarctica. *Journal of Geophysical Research* 104, 22,577–22,590.
- Wrotny, J.E., Russell III, J.M., 2006. Interhemispheric differences in polar mesospheric clouds observed by the HALOE instrument. *Journal of Atmospheric and Solar-Terrestrial Physics*, 68, <http://dx.doi.org/10.1016/j.jastp.2006.05.014>.

RESEARCH LETTER

10.1002/2014GL060777

Key Points:

- Quasi-continuous temperature measurements at Antarctic mesopause heights
- Winter/summer transition of mesopause is different from Northern Hemisphere
- Mesospheric temperatures are strongly correlated to stratospheric circulation

Correspondence to:

F.-J. Lübken,
luebken@iap-kborn.de

Citation:

Lübken, F.-J., J. Höffner, T. P. Viehl, B. Kaifler, and R. J. Morris (2014), Winter/summer mesopause temperature transition at Davis (69°S) in 2011/2012, *Geophys. Res. Lett.*, 41, doi:10.1002/2014GL060777.

Received 6 JUN 2014

Accepted 4 JUL 2014

Accepted article online 10 JUL 2014

Winter/summer mesopause temperature transition at Davis (69°S) in 2011/2012

F.-J. Lübken¹, J. Höffner¹, T. P. Viehl¹, B. Kaifler², and R. J. Morris³¹Leibniz-Institute of Atmospheric Physics, Kühlungsborn, Germany, ²Institute of Physics of the Atmosphere, Wessling, Germany, ³Australian Antarctic Division, Kingston, Tasmania, Australia

Abstract We present quasi-continuous measurements of temperature profiles in the Southern Hemisphere mesopause region during the transition from winter to summer conditions in 2011/2012. In a period of 120 days around solstice, we have performed iron lidar observations at Davis (69°S), Antarctica, for a total of 736 h. The winter/summer transition is identified by a downward shift of the mesopause which occurs on 8 November 2011. Soon after transition, mesopause heights and temperatures are similar to the Northern Hemisphere (NH) colatitude summer (88 km, 130 K). Around solstice, the mesopause is elevated for several days by 4–5 km and is colder than typical NH temperatures by 10 K. In this period individual profiles show temperatures as low as 100 K. The occurrence of polar mesosphere summer echoes is closely connected to low temperatures. Below 88 to 90 km and in the main summer season of 2011/2012 temperatures at Davis are generally warmer compared to the NH by 5–15 K, whereas temperatures are generally colder above 90 km. The winter/summer transition and the first appearance of polar mesosphere summer echoes are strongly correlated to maximum zonal winds in the stratosphere which constrain gravity waves with eastward momentum reaching the mesosphere. At the breakdown of the stratospheric vortex around solstice, the mesopause is higher and, surprisingly, colder than normal.

1. Introduction

The winter/summer transition in the mesosphere/lower thermosphere (MLT) region is substantially more variable in the Southern Hemisphere (SH) compared to its Northern Hemisphere (NH) counterpart, mainly due to altering stratospheric circulation changes impacting gravity wave forcing of the MLT [Karlsso et al., 2007; Smith et al., 2010]. Ice layers in the summer mesopause region require very low temperatures and have therefore been used as indirect indicators of the thermal conditions in the MLT. They have recently been studied with respect to circulation changes in the stratosphere [Karlsso et al., 2011; Benze et al., 2012]. Under summer conditions temperature measurements with sufficient temporal/spatial sampling and adequate accuracy are limited to few lidar observations and a couple of sounding rocket flights [Pan and Gardner, 2003; Lübken et al., 2004; Chu et al., 2011]. We have transported our mobile iron lidar to Davis, Antarctica, in late 2010 and performed measurements until the end of 2012. First results from the summer season 2010/2011 have been reported elsewhere [Lübken et al., 2011; Morris et al., 2012]. Although temperatures are available throughout the instrument operation period, here we present temperature measurements in the MLT region from spring equinox throughout the summer to examine the winter/summer transition 2011/2012 and to compare with circulation conditions in the stratosphere.

We compare our lidar temperatures with polar mesosphere summer echoes (PMSE) measured by the Australian Antarctic Division (AAD) 50 MHz VHF radar which is also located at Davis [Morris et al., 2006]. PMSE are strong radar echoes in the summer mesopause region which are caused by fluctuations in electron densities at the radar Bragg scale ($\lambda/2 = 3$ m). These fluctuations rely on neutral air turbulence in combination with charged ice particles (see review by Rapp and Lübken [2004], and references therein). PMSE are therefore an indication of the presence of ice particles and low temperatures.

We would like to compare the winter/summer transition in 2011/2012 with the “normal” state of the SH summer mesopause region. Unfortunately, a reliable reference climatology based on observations is not available since measurements are sparse and do not cover the entire season or height. For example, the compilation published in Pan and Gardner [2003] relies on only 26 h of lidar observations in December–February (none in November) and hardly covers the mesopause. We therefore decided to use the NH climatology from Lübken [1999] as a reference which is tempting because the winter/summer transition in NH stratospheric winds is much more regular compared to the SH.

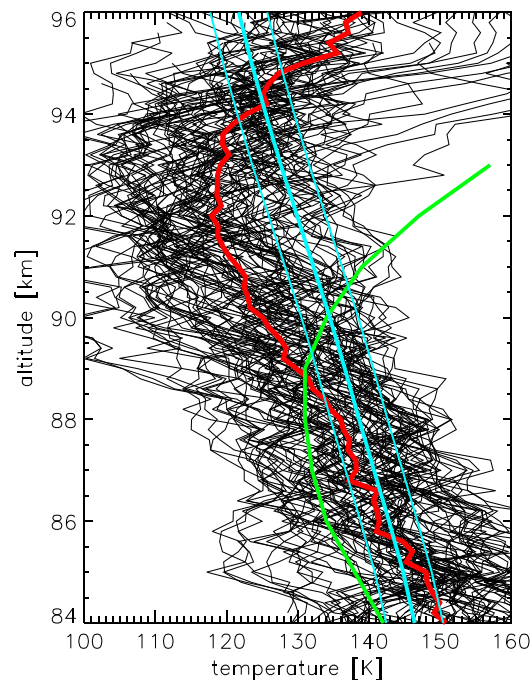


Figure 1. A total of 96 temperature profiles obtained on 17/18 December 2011 ($\text{drs} = -3/-4$). Red line: mean profile; green line: reference profile from the NH for mid-June [from Lübken, 1999]; blue lines: frost-point temperatures and variation by ± 4 K.

limited by low iron number densities. Above approximately 95–96 km, Fe density gets low which implies less reliable temperatures and larger uncertainties. From the mean of individual profiles shown in Figure 1, we determine a mesopause altitude and temperature of approximately 92.5 ± 1.5 km and $T = 119 \pm 1.3$ K, respectively (the temperature uncertainty is given by counting statistics of the lidar). The root-mean-square variation of temperatures at a fixed altitude is on the order of ± 10 K. From the temperature climatology in the Northern Hemisphere at the same latitude (69°N) and in the corresponding time of year (= mid-June), we find a mesopause height and temperature of 88–89 km and 131 K [Lübken, 1999], i.e., the mesopause at Davis at the day shown in Figure 1 is significantly higher (by ~ 4 km) and colder (by ~ 12 K) compared to the NH reference. Furthermore, at altitudes below approximately 89 km, temperatures over Davis on that day are higher by typically 5–8 K compared to the NH reference. The positive temperature gradient above the mesopause is rather similar in both hemispheres.

We also show frost-point temperatures T_f in Figure 1 where we have used water vapor concentrations from an updated version of the model by Sonnemann et al. [2012]. We have added lines by varying T_f by ± 4 K to roughly indicate that the actual H_2O profile on that day may have been different from the model profile (note that in the Southern Hemisphere summer mesopause region, a variation of T_f by 4 K corresponds to a change of H_2O concentration by a factor of 4). As can be seen from Figure 1 temperatures are low enough for ice particles to exist ($T < T_f$) up to ~ 94 –95 km. Indeed, PMSE were observed on that day between 86 and 93 km (not shown). Note that at altitudes significantly above 93 km PMSE cannot be created even if charged ice particles are present because increasing kinematic viscosity prevents the generation of small scale fluctuations by neutral air turbulence [Lübken et al., 2009].

In Figure 2 we show the seasonal variation of temperatures around summer solstice smoothed by a 14 days Hanning filter. A total of 736 h of measurements on 62 days contribute to this plot. The distribution of observations is fairly homogeneous; i.e., there are no large data gaps in this period. In particular, 262 h of measurements have been performed during the period of the high and cold mesopause in December. In Figure 2 the altitude of the mesopause (white line) drops from greater heights to the standard NH summer value of ~ 88 km around $\text{drs} = -43$ (= 8 November), and temperatures drop quickly prior to that day by

2. Lidar Observations at Davis

The mobile scanning iron lidar is a two-wavelength system (772 nm/386 nm). It determines mesospheric temperatures by probing the Doppler broadened iron resonance line at 386 nm with a frequency-doubled alexandrite laser [Höffner and Lautenbach, 2009]. The system allows to measure temperatures during full daylight with a typical uncertainty of less than ± 5 K after 1 h integration. These values refer to summer conditions when metal densities are lowest, and the Sun is at its highest elevation. In this study we use a height resolution of 1 km. The iron lidar of the Institute of Atmospheric Physics (IAP) in Kühlungsborn, Germany, was transported to Davis, Antarctica (68.6°S), in November 2010. It performed first measurements on 15 December 2010 and finished operation on 31 December 2012. In total, 2900 h of temperature profiles are now available. Here we concentrate on 736 h of measurements performed during the full summer season of 2011/2012, more precisely from days relative to solstice ($\text{drs} = -60$ to $\text{drs} = +60$).

In Figure 1 we show 24 h of temperature measurements (96 profiles) on 17/18 December 2011. Occasionally, temperatures are as low as 100 K.

The altitude range of reliable temperatures is lim-

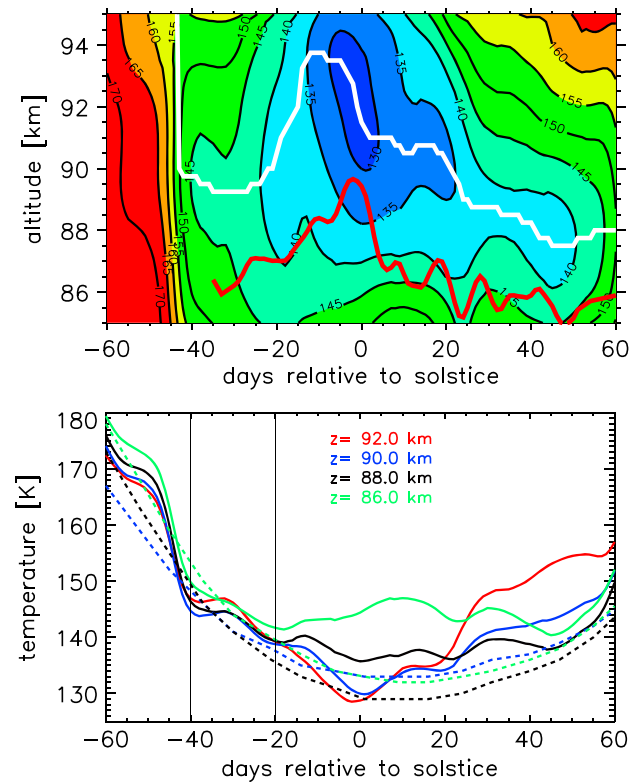


Figure 2. (top) Seasonal variation of smoothed lidar temperatures. White line: mesopause altitude; red line: peak height of the PMSE layer. (bottom) Seasonal variation of temperatures at given altitudes (solid lines; see inlet). Northern Hemisphere reference temperatures are shown as dashed lines [from Lübken, 1999], except for 92 km (see text for more details).

as much as 20 K per week at nearly all altitudes. In the NH reference the winter/summer mesopause drop occurs around $drs = -45$, i.e., at a rather similar day compared to 2011/2012 at Davis. We note that the time scale of our smoothing procedure (14 days) is roughly equivalent to the smoothing applied for the NH climatology (see Lübken [1999] for more details). For reasons explained later we call the period from $drs = -40$ to -20 the “onset period.” During the onset period in 2011/2012, temperatures at Davis are rather similar to the NH reference. Thereafter and below ~ 88 km, they are significantly warmer by ~ 5 K. We hesitate to compare with the NH reference above approximately 90–92 km because the falling sphere technique applied for that climatology is somewhat uncertain at these high altitudes [Lübken, 1999]. Comparing Figures 1 and 2, it is obvious that smoothed temperatures can deviate significantly from daily means. For example, mesopause temperatures at $drs = -4/-3$ (17/18 December) in Figure 2 are ~ 130 K, significantly warmer compared to Figure 1.

In Figure 2 we also show PMSE peak altitudes. PMSE started very sparsely around $drs = -35$ (16 November) with a mean height of 86 km. At that altitude and time

of year, the frost-point temperature is approximately 135 K which is smaller compared to mean temperatures in that period and altitude (~ 145 – 150 K; see Figure 2). Still, ice particles may exist ($T < T_f$) for shorter periods if we consider a temperature variability of roughly ± 10 K d^{-1} and water vapor uncertainties mentioned above. We note that PMSE occur when temperatures drop below the frost point, as expected. For the rest of the season, PMSE nicely follow the general temporal development of the mesopause, i.e., the peak of the PMSE layer is located approximately 3–4 km below the mesopause (see Figure 2). The good agreement between periods when lidar temperatures predict ice particles to exist, i.e., $T < T_f$, and the occurrence of PMSE is an independent confirmation of the reliability of the lidar technique. We note that PMSE and other MLT ice cloud phenomena give only indirect evidence for certain temperatures but cannot provide details about, for example, the height structure around the mesopause. We plan to perform a detailed comparison between temperatures and PMSE in the near future.

In Figure 3 we show mean temperature profiles at three selected times during the season and compare with the NH reference. We picked $drs = -2$ (rather than $drs = 0$) since this is in the center of the cold mesopause period around solstice (see Figure 2). At the beginning of the summer season ($drs = -30$) temperatures at Davis are rather similar compared to the NH (differences are smaller than ± 5 K), whereas close to solstice ($drs = -2$) the mesopause at Davis is much higher and colder compared to the NH reference for several days. This can be seen from the mean temperature profile for the period 17–25 December ($drs = -4$ to $drs = +4$) in Figure 3 where the mesopause height and temperature is 92 km and 124 K, respectively, averaging 130 h of observations corresponding to 67% of the time from first switch-on on 17 December until last switch-off on 25 December. Smoothing the temperature field by a 14 days Hanning filter (see above) gives average mesopause temperatures of ~ 130 K, similar to the NH. Later in the summer season ($drs = +30$), temperatures at Davis are higher by typically 10 K compared to the NH reference.

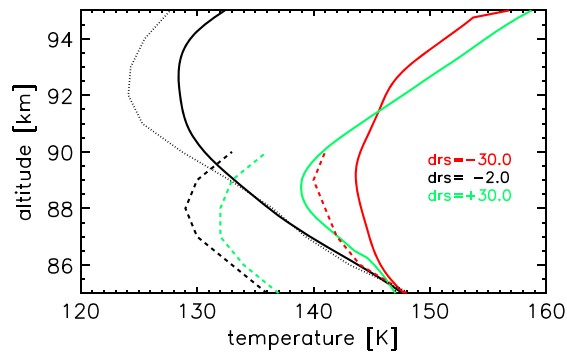


Figure 3. Solid lines: altitude variation of smoothed lidar temperatures at given times (see inlet; drs = days relative to solstice). Dotted line: mean temperature profile from 17 to 25 December 2011 (drs = -4 to +4). Dashed lines: corresponding profiles from the Northern Hemisphere reference [from Lübken, 1999] ignoring the uppermost heights (see text for more details).

vertex being representative of a “winter-like” (summer-like) condition leading to a high and warm (low and cold) mesopause. “Late” (early) means that zonal winds during the onset-period are higher (lower) by $0.5 \cdot \sigma$ compared to the climatological mean (σ = standard deviation of wind anomalies). If zonal winds develop monotonically with time (as in Figure 2 in BK11), this is equivalent to a late or early breakdown which is defined to occur when the zonal wind at 50 hPa and 65°S gets lower than $+10$ m/s.

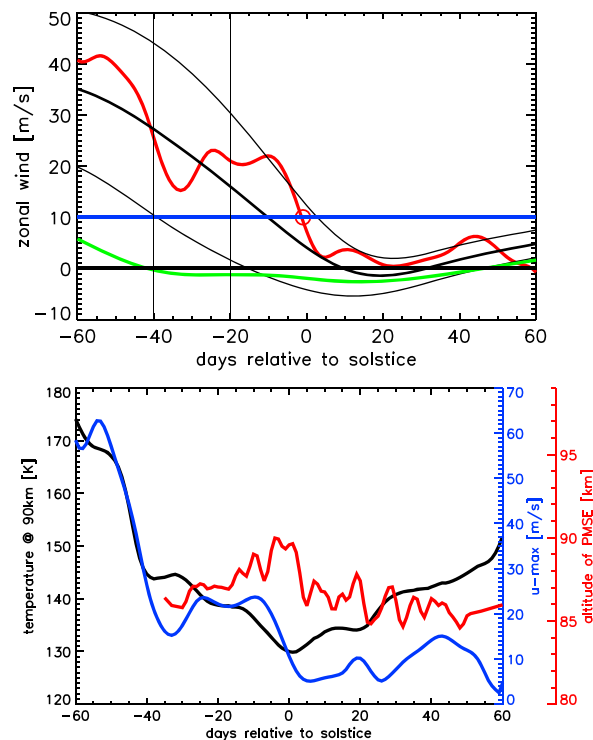


Figure 4. (top) Zonal mean zonal winds at 69°S close to 50 hPa (red line), climatological mean values (thick black line), and standard deviations of wind anomalies (thin black lines). Green line: corresponding mean zonal winds from the NH summer. The horizontal lines mark winds of 0 m/s (for reference) and 10 m/s (the breakdown limit). The two vertical lines mark the onset period (see text). (bottom) Lidar temperatures at 90 km (black) and maximum zonal wind in the stratosphere (blue). Red line: peak height of the PMSE layer.

3. Discussion

We discuss our observations with respect to theoretical expectations presented in Karlsson *et al.* [2011] (hereafter BK11). The main idea is to study stratospheric winds and their impact on mesospheric temperatures [Smith *et al.*, 2010]. Coupling between stratospheric winds and upper mesosphere temperatures comes from gravity waves which are generated in the troposphere and, while propagating upward, are filtered at heights where the phase velocity equals the mean wind velocity. The dissipation of gravity waves deposits momentum, changes vertical winds, and thereby modifies the thermal structure.

BK11 classify stratospheric winds according to a late (early) breakdown of the polar vortex

In Figure 4 we show zonal mean zonal winds at 69°S from the MERRA reanalysis at ~ 50 hPa [Rienecker *et al.*, 2011]. Winds are close to climatology during most of the onset period which would classify this season as being neither late nor early. On the other hand, winds are much larger compared to the climatology from drs ≈ -20 until solstice and the breakdown ($u < +10$ m/s at 50 hPa) occurs at drs = -1. This would classify the season 2011/2012 as an example of a late breakdown. The situation is obviously more complicated than in BK11. We decided to address the wind situation in the stratosphere as being a quasi-late breakdown.

During the beginning of the onset period we observe the mesopause at standard heights (~ 88 km) with rather similar temperatures compared to the NH reference (Figure 2). Later in the season, namely, around drs = -20 to +20, the mesopause is higher than the NH reference (90–92 km). Shortly before solstice, the mesopause is highest (93 km) and coldest (119 K). From the discussion in BK11 including the seasonal variation of polar mesospheric clouds (PMC) characteristics, we had expected a higher but warmer(!) mesopause. Relating PMC occurrence to the thermal structure of the summer mesopause is not trivial for

various reasons. The morphology of PMC discussed in BK11 is a consequence of various factors such as temperatures, water vapor, and circulation. For example, lifting the mesopause altitude from its standard value (88 km) by 5 km (keeping the mesopause temperature and the temperature gradient above and below constant) reduces the amount of water vapor molecules available for ice particle nucleation by roughly a factor of 10 and the visibility of these particles by a factor of 100. The relative importance of water vapor and other factors for the visibility of PMC can only be studied by appropriate models. In this context it is interesting to note that weak and short noctilucent clouds (NLC) were first observed by our lidar on 17 December 2011 ($drs = -4$), i.e., several weeks after the first appearance of PMSE and significantly later than the winter/summer transition. It is obvious that a SH/NH comparison of PMSE, PMC, and NLC should consider the circulation in the stratosphere. We note that the drop of the mesopause in Figure 4 occurs several days before the onset of the PMSE season. This is because during the winter/summer transition at $drs = -43$ temperatures in the mesopause region are not low enough to allow for ice particles to exist. In general, the first appearance of PMSE may not coincide with the time of winter/summer transition. This is even more true for PMC and NLC which require ice particles of a sufficiently large size (typically > 20 nm). Obviously, there may be a significant offset between the winter/summer transition in temperatures, the onset of PMSE, and the first appearance of "visible" ice particles (NLC/PMC), respectively. Studies regarding the onset of PMC and its relation to stratospheric circulation changes may therefore be somewhat biased [Karlsson et al., 2011; Benze et al., 2012].

In Figure 4 (bottom) we show the seasonal development of temperatures at 90 km and the maximum zonal wind in the stratosphere, which appear at approximately 10 hPa at $drs = -60$, declining in altitude to ~ 300 hPa after $drs = 20$. During winter/summer transition in 2011/2012 the maximum wind drops from $\sim +60$ m/s to $\sim +20$ m/s within 10 days around $drs = -45$. As can be seen in Figures 4 and 2, this occurs nearly simultaneously with the steep decline of temperatures at 90 km and the drop of the mesopause. First PMSE appear a few days later. This close correlation between stratospheric winds and MLT temperatures is explained by filtering of gravity waves which are generated in the lower atmosphere [Smith et al., 2010; Karlsson et al., 2011]. Gravity waves with eastward momentum can propagate to the mesosphere only if their phase speed is larger than the maximum zonal wind in the stratosphere. We note that the close correlation between stratospheric winds and temperatures in the mesopause region disappears later in the season, which is presumably due to several factors. For example, the activity of stationary Rossby waves in the winter stratosphere may modify SH mesospheric temperatures, an effect which is known as "interhemispheric coupling" [Karlsson et al., 2009; Körnich and Becker, 2010] (note that stationary Rossby wave activity in the NH fully develops only after solstice, i.e., after the winter/summer transition in the SH). Furthermore, the morphology of gravity waves launched in the lower atmosphere may change with season. Other factors such as radiation, chemistry, and turbulence also contribute to the energy budget of the atmosphere and therefore to the seasonal variation of temperatures. More sophisticated modeling is required to study the impact of gravity wave propagation and stratospheric circulation on MLT temperatures.

4. Summary and Conclusions

We have performed quasi-continuous temperature measurements in the SH mesopause region during the winter/summer transition 2011/2012 with high accuracy and high temporal and spatial coverage. Comparison with simultaneous and colocated PMSE observations provides independent confirmation of the seasonal development of low temperatures. We compare the 2011/2012 transition with a NH reference since (i) a suitable climatology is not available for the SH and (ii) winter/summer transitions in the NH stratosphere and mesosphere vary little from year to year, different from the SH. For the winter/summer transition in 2011/2012 we find not only similarities but also significant differences to the NH transition. During the summer season the mesopause is occasionally observed at normal NH values (88 km, 130 K) but also at much higher altitudes ("elevated mesopause"). In the latter case mean mesopause temperatures are typically colder by up to 10 K for several days around solstice. In contrast to mean values, individual temperatures may be as cold as 100 K. We find a good correlation between (i) the time when mesopause heights/temperatures change from winter to summer conditions and (ii) when maximum zonal winds in the stratosphere drop from large to moderate values. After the transition time, the correlation between mesopause heights/temperatures and maximum stratospheric winds is limited. In the future we intend to perform more sophisticated model simulations to better understand the impact of gravity wave sources and propagation through stratospheric winds on the winter/summer transition in the mesopause region

and their impact on NLC, PMC, and PMSE. Unlike in the NH, the SH exhibits significant variability in this transition period and therefore allows to study the relationship between stratospheric dynamics and mesospheric temperatures.

Acknowledgments

Data used for this paper are available via IAP's ftp server at <ftp://ftp.iap-kborn.de/data-in-publications/LuebkenGRL2014> and (for MERRA) from <http://gmao.gsfc.nasa.gov/merra/>. We thank Erich Becker for fruitful discussions on the impact of dynamics on summer mesopause temperatures and Koki Chau for general comments. Michael Grygalashvyly has kindly provided updated water vapor profiles from his model. We thank Ralph Latteck for reprocessing PMSE data for our application and Jens Fiedler for providing MERRA data. The engagement of TOSCA is appreciated. IAP thanks our colleagues from AAD for their stimulating cooperation and their extraordinary efforts when transporting and operating our Fe lidar.

The Editor thanks two anonymous reviewers for their assistance in evaluating this paper.

References

- Benze, S., C. Randall, B. Karlsson, V. Harvey, M. Deland, G. Thomas, and E. Shettle (2012), On the onset of polar mesospheric cloud seasons as observed by SBUV, *J. Geophys. Res.*, *117*, D07104, doi:10.1029/2011JD017350.
- Chu, X., W. Huang, W. Fong, Z. Yu, Z. Wang, J. A. Smith, and C. S. Gardner (2011), First lidar observations of polar mesospheric clouds and Fe temperatures at McMurdo (77.8° S, 166.7° E) Antarctica, *Geophys. Res. Lett.*, *38*, L16810, doi:10.1029/2011GL048373.
- Höffner, J., and J. Lautenbach (2009), Daylight measurements of mesopause temperature and vertical wind with the mobile scanning iron lidar, *Opt. Lett.*, *34*, 1351–1353.
- Karlsson, B., H. Körmich, and J. Gumbel (2007), Evidence for interhemispheric stratosphere-mesosphere coupling derived from noctilucent cloud properties, *Geophys. Res. Lett.*, *34*, L16806, doi:10.1029/2007GL030282.
- Karlsson, B., C. McLandress, and T. G. Shepherd (2009), Inter-hemispheric mesospheric coupling in a comprehensive middle atmosphere model, *J. Atmos. Sol. Terr. Phys.*, 518–530, doi:10.1016/j.jastp.2008.08.006.
- Karlsson, B., C. E. Randall, T. G. Shepherd, V. L. Harvey, J. Lumpe, K. Nielsen, S. M. Bailey, M. Hervig, and J. M. Russell III (2011), On the seasonal onset of polar mesospheric clouds and the breakdown of the stratospheric polar vortex in the Southern Hemisphere, *J. Geophys. Res.*, *116*, D18107, doi:10.1029/2011JD015989.
- Körnich, H., and E. Becker (2010), A simple model for the interhemispheric coupling of the middle atmosphere circulation, *Adv. Space Res.*, *45*, 661–668, doi:10.1016/j.asr.2009.11.001.
- Lübken, F.-J. (1999), Thermal structure of the Arctic summer mesosphere, *J. Geophys. Res.*, *104*, 9135–9149.
- Lübken, F.-J., A. Müllemann, and M. J. Jarvis (2004), Temperatures and horizontal winds in the Antarctic summer mesosphere, *J. Geophys. Res.*, *109*, D24112, doi:10.1029/2004JD005133.
- Lübken, F.-J., J. Lautenbach, J. Höffner, M. Rapp, and M. Zecha (2009), First continuous temperature measurements within polar mesosphere summer echoes, *J. Atmos. Sol. Terr. Phys.*, 453–463, doi:10.1016/j.jastp.2008.06.001.
- Lübken, F.-J., J. Höffner, T. P. Viehl, B. Kaifler, and R. J. Morris (2011), First measurements of thermal tides in the summer mesopause region at Antarctic latitudes, *Geophys. Res. Lett.*, *38*, L24806, doi:10.1029/2011GL050045.
- Morris, R. J., D. J. Murphy, R. A. Vincent, D. A. Holdsworth, A. R. Klekociuk, and I. M. Reid (2006), Characteristics of the wind, temperature and PMSE field above Davis, Antarctica, *J. Atmos. Sol. Terr. Phys.*, 68(3–5), 418–435, doi:10.1016/j.jastp.2005.04.011.
- Morris, R. J., J. Höffner, F.-J. Lübken, T. Viehl, B. Kaifler, and A. K. Klekociuk (2012), Experimental evidence of a stratospheric circulation influence on mesospheric temperatures and ice-particles during the 2010–11 austral summer at 69° S, *J. Atmos. Sol. Terr. Phys.*, 54–61, doi:10.1016/j.jastp.2012.08.007.
- Pan, W., and C. S. Gardner (2003), Seasonal variations of the atmospheric temperature structure at South Pole, *J. Geophys. Res.*, *108*(D18), 4564, doi:10.1029/2002JD003217.
- Rapp, M., and F.-J. Lübken (2004), Polar mesosphere summer echoes (PMSE): Review of observations and current understanding, *Atmos. Chem. Phys.*, *4*, 2601–2633.
- Rienecker, M. M., et al. (2011), MERRA: NASA's modern-era retrospective analysis for research and applications, *J. Clim.*, *24*, 3624–3648, doi:10.1175/JCLI-D-11-00015.1.
- Smith, A. K., R. R. Garcia, D. R. Marsh, D. E. Kinnison, and J. H. Richter (2010), Simulations of the response of mesospheric circulation and temperature to the Antarctic ozone hole, *Geophys. Res. Lett.*, *37*, L22803, doi:10.1029/2010GL045255.
- Sonnemann, G. R., P. Hartogh, U. Berger, F.-J. Lübken, and M. Grygalashvyly (2012), Anthropogenic effects on the distribution of minor chemical constituents in the mesosphere/lower thermosphere—A model study, *Adv. Space Res.*, *50*, 598–618.

RESEARCH ARTICLE

Winter/summer transition in the Antarctic mesopause region

10.1002/2015JD023928

Key Points:

- New set of temperature data by lidar in the mesopause region at Antarctic latitudes
- Temperatures/winds at winter/summer transition correlated to stratospheric winds
- Unusual high and cold mesopause at summer solstice (elevated summer mesopause)

Correspondence to:

F.-J. Lübken,
luebken@iap-kborn.de

Citation:

Lübken, F.-J., J. Höffner, T. P. Viehl, E. Becker, R. Latteck, B. Kaifler, D. J. Murphy, and R. J. Morris (2015), Winter/summer transition in the Antarctic mesopause region, *J. Geophys. Res.* *Atmos.*, *120*, 12,394–12,409, doi:10.1002/2015JD023928.

Received 13 JUL 2015

Accepted 24 NOV 2015

Accepted article online 27 NOV 2015

Published online 17 DEC 2015

F.-J. Lübken¹, J. Höffner¹, T. P. Viehl¹, E. Becker¹, R. Latteck¹, B. Kaifler², D. J. Murphy³, and R. J. Morris⁴

¹Leibniz-Institute of Atmospheric Physics, Rostock University, Kühlungsborn, Germany, ²Institute of Atmospheric Physics, German Aerospace Center, Oberpfaffenhofen, Germany, ³Australian Antarctic Division, Kingston, Tasmania, Australia, ⁴Formerly at Australian Antarctic Division, Kingston, Tasmania, Australia

Abstract A new set of temperature data with unprecedented resolution and accuracy has been obtained from Fe lidar measurements at Davis, Antarctica (69°S). Here we concentrate on the months of the winter/summer transition (November to February) where we have collected a total of 1305 h of observations in the three seasons 2010/2011, 2011/2012, and 2012/2013. The temporal development of temperatures around the mesopause in 2012/2013 is rather similar to the Northern Hemisphere (NH), whereas the other seasons are significantly different, exhibiting, e.g., an unusual higher and colder mesopause around solstice (elevated summer mesopause). During this exceptional period mean daily mesopause heights and temperatures are approximately 92.0 ± 0.5 km and 125 K, respectively. The seasonal variation of temperatures in the mesopause region is closely related to the circulation in the stratosphere which exhibits an early (late) vortex breakdown in 2012/2013 (2010/2011). The situation is more complicated in 2011/2012. The early (late) transition in the mesopause region is accompanied by an early (late) appearance of polar mesosphere summer echoes. Zonal winds as measured by an MF radar also show systematic differences with westward winds reaching up to very high altitudes (nearly 100 km) for the late transition in 2010/2011 and to more common heights (~90 km) for the early transition in 2012/2013. A mesopause being higher and colder compared to the NH (as occasionally observed at Davis) cannot be achieved by standard models. More sophisticated characterization of gravity wave forcing might be required.

1. Introduction

The transition from winter to summer conditions in the Southern Hemisphere (SH) summer mesopause region has attracted substantial interest in recent years since it was realized that the timing of this transition varies significantly from year to year, as indicated, for example, by the presence of ice clouds or related phenomena [see, e.g., DeLand *et al.*, 2003; Latteck *et al.*, 2008; Kirkwood *et al.*, 2008; Smith *et al.*, 2010; Karlsson *et al.*, 2011; Benze *et al.*, 2012]. The onset of the summer season in the SH is closely related to the breakdown of the polar vortex and the transition of winds in the stratosphere which can extend way into the summer season, whereas this breakdown occurs much earlier and more regularly in the Northern Hemisphere (NH). The coupling between stratospheric circulation and mesospheric temperatures is established by gravity waves which are generated in the troposphere. Some of these waves are filtered by stratospheric winds, whereas those reaching the mesosphere/lower thermosphere (MLT) drive the summer pole to winter pole residual circulation that induces the cold summer mesopause. Significant hemispheric differences are well known for the stratosphere and lower mesosphere [Rosenlof, 1996; Alexander and Rosenlof, 1996; Siskind *et al.*, 2003; Becker *et al.*, 2015]. Comparing measurements in the mesopause region between both hemispheres offers the opportunity to study vertical coupling processes in detail.

In this paper we report on a new and unique data set, namely, on iron resonance lidar temperature measurements at Davis Station, Antarctica (68.58°S, 77.97°E) which provide unprecedented details of the thermal structure in the mesopause region. These observations allow us to study the reaction of MLT temperatures to circulation changes in the stratosphere in detail. We also compare lidar temperatures with other relevant observations at Davis, in particular with polar mesosphere summer echoes (PMSE) observed by a VHF radar, and with winds in the mesopause region obtained by an MF radar. PMSE are strong radar echoes in the summer mesopause region which are caused by fluctuations in electron densities at the radar Bragg scale ($\lambda/2 \sim 3$ m). These fluctuations rely on neutral air turbulence in combination with charged ice particles (see review by Rapp and Lübken [2004, and references therein]). PMSE are therefore an indication of the presence of ice particles and low temperatures, typically less than 150 K.

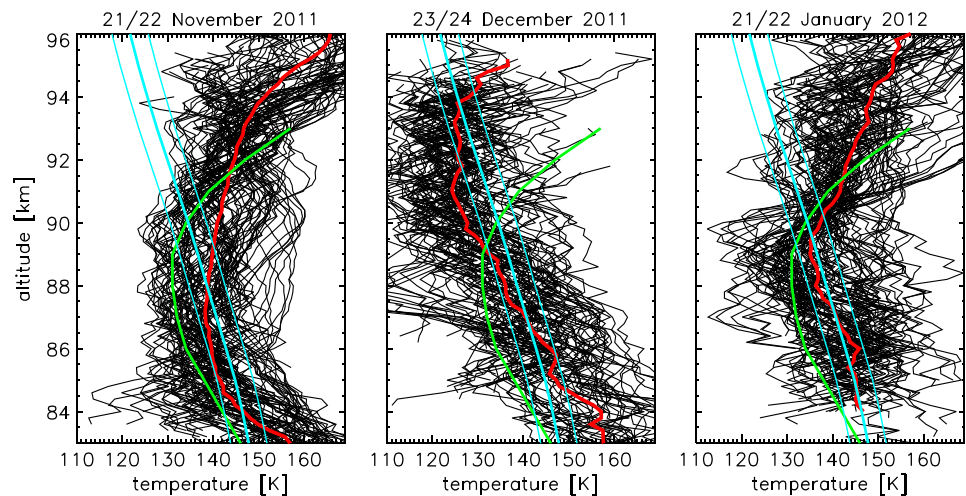


Figure 1. All single profiles available on three different days (more precisely during 24 h from noon to noon), namely, (from left to right) on 21/22 November 2011, 23/24 December 2011, and 21/22 January 2012 (drs = -29 , $+2$, and $+32$), respectively. A total of 92, 89, and 95 profiles are shown (see text for more details). The days were chosen because they are before, during, and after the occurrence of an elevated summer mesopause (ESM), respectively. Red lines: mean profiles; green lines: reference profile from the NH for mid June [from Lübken, 1999]; and blue lines: frost-point temperatures and variation by ± 4 K.

First results from the Fe lidar measurements at Davis and related observations have been published previously [Lübken et al., 2011; Morris et al., 2012; Lübken et al., 2014; Viehl et al., 2015]. In order to explain the seasonal variation of mesopause temperatures and altitudes in the SH and to compare with the NH, we present simulations with the KMCM (Kühlungsborn Mechanistic Circulation Model) (see Becker et al. 2015 for some model results on NH/SH comparison).

2. Techniques and Data Base

2.1. Fe Lidar

The mobile scanning iron lidar is a two-wavelength system (772 nm/386 nm). It determines mesospheric temperatures by probing the Doppler-broadened iron resonance line at 386 nm with a frequency-doubled alexandrite laser [Höffner and Lautenbach, 2009]. The system allows us to measure temperatures during full daylight with a typical uncertainty of less than ± 5 K after 1 h integration. These values refer to summer conditions when metal densities are lowest and the Sun is at its highest elevation, which both decrease the signal-to-noise ratio and increase uncertainties. The high accuracy of the instrument is achieved by spectrally analyzing the retrieved signal and applying narrow-band filters [Lautenbach and Höffner, 2004; Höffner and Fricke-Begemann, 2005]. In this study we use a height resolution of 1 km. The iron lidar of the Leibniz Institute of Atmospheric Physics in Kühlungsborn, Germany, was transported to Davis, Antarctica (69°S) in November 2010. It performed first measurements on 15 December 2010 and finished operation on 31 December 2012. In total, 2900 h of temperature profiles are now available. Temperatures are available throughout the entire instrument operation period (with interruptions), but here we concentrate on the winter/summer transition and the summer season, more precisely on the time from drs = -60 to drs = $+60$, i.e., from 22 October to 19 February (drs = days relative to solstice). In that period we have obtained 324 h on 34 days in the season 2010/2011, 740 h on 68 days in 2011/2012, and 217 h on 25 days in 2012/2013. Note that we have not covered the entire winter/summer transition period in the first and the third seasons, but the main features relevant in this paper are captured. The data coverage is fairly evenly distributed over all local times. It is therefore rather unlikely that our sampling has produced a significant bias caused, for example, by thermal tides.

In Figure 1 we show single temperature profiles measured on three different days (more precisely from noon to noon), namely, on 21/22 November 2011, 23/24 December 2011, and 21/22 January 2012. Raw profiles were averaged in a sliding window of 1 h length, shifted by 15 min. As will be seen later, these days are representative for periods before, during, and after the occurrence of an “elevated summer mesopause” (ESM).

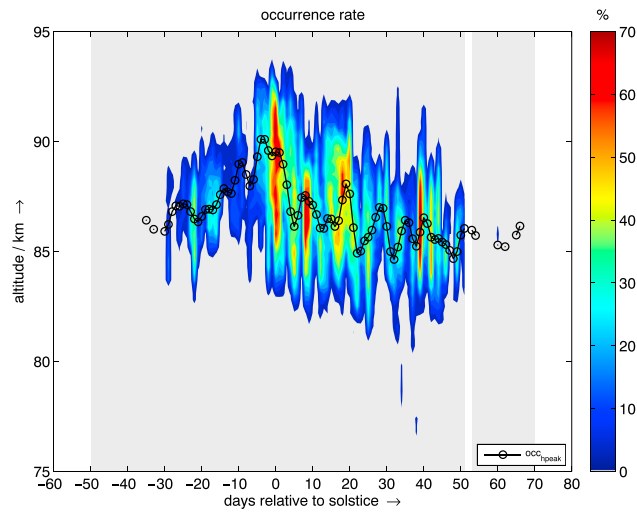


Figure 2. Daily occurrence rates of PMSE for the austral summer season 2011/2012 based on radar volume reflectivities ($\eta \geq 10^{-17} \text{ m}^{-1}$) detected by the Davis VHF radar. The dots indicate the altitudes of maximum occurrence rates smoothed over 5 days.

We also show frost point temperatures (T_{frost}) in that figure. It is obvious from Figure 1 that there is substantial variability within 1 day with peak-to-peak deviations of up to 30 K. This needs to be taken into account when we later compare the occurrence of ice particles, more precisely PMSE, with mean temperatures. In particular, mean temperatures might be larger than the frost point temperature (i.e., too warm for ice particles and PMSE), but individual profiles may well be much colder allowing for ice particles to exist and to grow. For the 3 days shown in Figure 1 there are several profiles (and also part of the mean profile) which indicate conditions of supersaturation, namely, $T < T_{\text{frost}}$. Despite the large fluctuations seen in Figure 1, the mesopause temperatures and altitudes can clearly be identified in all three cases. Certainly, the mesopause is higher and colder on 23/24 December compared to the other 2 days. Another example of all individual profiles measured within 24 h on 17/18 December 2011 is shown in *Lübken et al.* [2014]. These examples highlight the improvement of the data set compared to previous observations and to satellites. In this paper we use temperatures derived from smoothing the original observations by a 14 days Hann filter. This also implies that tides and traveling planetary waves are smoothed out to a large extent.

2.2. VHF and MF Radars: PMSE and Winds

We use observations from two radars of the Australian Antarctic Division also located at Davis, namely, polar mesosphere summer echoes from a 55 MHz VHF radar and winds in the upper mesosphere from an MF radar [*Morris et al.*, 2006]. We will also use PMSE data from a new VHF radar in the NH called Middle Atmosphere Alomar Radar System (MAARSY) and winds from the Saura MF radar, which are both parts of the Arctic Lidar Observatory for Middle Atmospheric Research (ALOMAR) facility in Northern (69°N) [*Singer et al.*, 2008; *Latteck et al.*, 2012].

In Figure 2 we show the occurrence frequency of PMSE at Davis as a function of time in the summer season 2011/2012. In that season PMSE started around $\text{drs} = -30$ (21 November 2011) and terminated around $\text{drs} = +50$ (9 February) with some weak activity thereafter. Note that PMSE appears in the mesopause region, namely, from approximately 83 km to 92 km. As can be seen from Figure 2, peak heights are higher around solstice in 2011, namely, almost 94 km, which is rarely observed at Davis [*Latteck et al.*, 2008]. The mean PMSE altitude is around 87 km at the beginning of the season and generally descends with time. Shortly before solstice the mean PMSE altitude is considerably higher (~ 90 km) than in the periods before or after. In the context of this paper the existence of PMSE is an independent confirmation of low temperatures. A detailed comparison of the occurrence of PMSE with lidar temperatures confirms the reliability of the lidar technique [*Lübken et al.*, 2009]. We note that PMSE and other MLT ice cloud phenomena such as noctilucent clouds (NLC) and polar mesosphere clouds (PMC) give only indirect evidence for low temperatures but cannot provide details about the thermal structure around the mesopause.

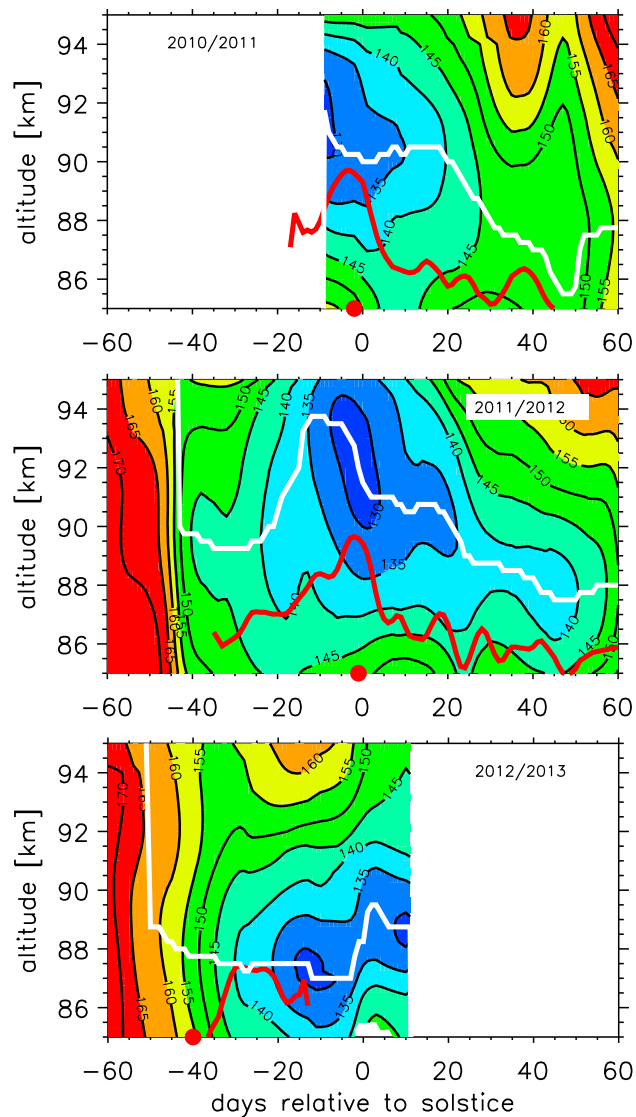


Figure 3. Contour plot of temperatures observed by the Fe lidar at Davis. The altitudes of the mesopause (white lines) and mean PMSE heights (red lines) are also shown. Note that PMSE data are not available after $drs = -8$ in 2012/2013 due to technical reasons. The x axis spans the time period from 22 October ($drs = -60$) to 15 February ($drs = +60$). The red dots mark the days of the vortex breakdown ($drs = -2, -1,$ and -40 , respectively) in the stratosphere, applying the criterion $\bar{u} < 10\text{m/s}$ at 50 hPa (see Figure 9).

2.3. MERRA and KMCM

As will be seen later the temporal development of the thermal and dynamical structure in the upper mesosphere/lower thermosphere is closely related to the circulation in the stratosphere. For the latter we use data from NASA's Modern-Era Retrospective analysis for Research and Applications (MERRA) [Rienecker *et al.*, 2011]. Furthermore, we compare our Fe lidar results with the temperature climatology during summer at 69°N derived from falling sphere flights (hereafter referred to as FJL99) [Lübken, 1999]. It should be noted that the falling sphere technique gets somewhat uncertain above approximately 92 km. Therefore, the FJL99 climatology should be interpreted with care at these altitudes.

We use the Kühlungsborn Mechanistic general Circulation Model (KMCM) in its more recent version as an idealized climate model (see Becker *et al.* [2015, and references therein] for more details). This version extends from the surface to the lower thermosphere (uppermost level around 3×10^{-3} hPa corresponding to about 125 km height) and employs a conventional resolution of a T32 spectral truncation in horizontal direction

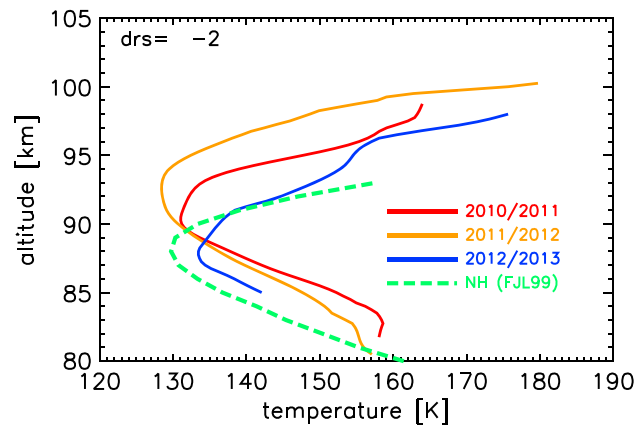


Figure 4. Temperatures derived from Fe lidar observations in the mesosphere smoothed by a 14 days Hann filter and shown here at $drs = -2$ (19 December). The three seasons are indicated by different colors (see inset). For comparison the temperature profile from the FJL99 climatology in the NH closest to $drs = -2$ is also shown (green dashed line).

and 70 full layers in the vertical. It uses explicit computations of radiative transfer and the tropospheric moisture cycle. Land-sea contrasts are taken into account by orography and a slab ocean model, as well as by land-sea masks for surface parameters such as heat capacity, albedo, and relative humidity. Despite some idealizations, the model reproduces a reasonable synoptic and planetary wave activity for the lower and middle atmosphere. The dynamical control of the mesopause region is described by parameterized gravity waves.

3. Experimental Results at Davis

3.1. Fe Lidar Temperatures

In Figure 3 we show smoothed temperature fields derived from the Fe lidar observations for the three available winter/summer transitions, more precisely from $drs = -60$ (22 October) to $drs = +60$ (19 February). Generally speaking, the cold summer mesopause is clearly visible in all three seasons, although the first (last) part of the season 2010/2011 (2012/2013) is not covered by observations. In the first two seasons there is a period around solstice where the mesopause is unusually high (around 92 km) compared to “standard” summer heights of 88 km (see FJL99). We call this feature an elevated summer mesopause (ESM). Mesopause temperatures and altitudes vary substantially throughout the season. After solstice there is a tendency for mesopause heights to descend in time in the first two seasons. The mean PMSE altitudes closely follow the mesopause heights (perhaps with a time lag of a few days) and are in general a few kilometers lower than the mesopause (see Figure 3). This demonstrates the close connection between low temperatures and PMSE which is consistent with the generally accepted idea that ice particles start to nucleate around the mesopause (but are still too small to create PMSE) then descend and grow until they reach a region of higher temperatures and sublimate.

A closer look reveals substantial differences in the mean temperature profiles from year to year and also systematic differences to the NH (Figure 4). In the seasons 2010/2011 and 2011/2012, and in a period around solstice, the mesopause is located substantially higher compared to the season 2012/2013. More precisely, for the day shown in Figure 4 ($drs = -2$) the mesopause heights for the three seasons 2010/2011, 2011/2012, and 2012/2013 are in the range 89.25–92.75 km, 90.0–94.5 km, and 86.75–89.5 km, respectively, where we allow for a deviation of 2 K from the absolute temperature minimum. We note that the mesopause height in 2012/2013 is close to the NH climatology published in FJL99.

Mesopause temperatures in this period are rather similar in all three seasons (~130–135 K) and are similar to the NH. As an indication of the uncertainty of the NH climatology we recall that the variability (RMS) of the original temperature profiles contributing to the mean is 4.8 K, 6.2 K, and 12.4 K at 80 km, 85 km, and 90 km, respectively [see Lübken, 1999, Figure 7]. We emphasize again that our daily-mean lidar temperatures can deviate substantially from the smoothed version shown in Figures 3 and 4. For example, the mean mesopause altitude and temperature on 17/18 December 2011 are 92.5 km and 119 K, respectively, which is higher and colder compared to the NH climatology [see Lübken et al., 2014, Figure 1].

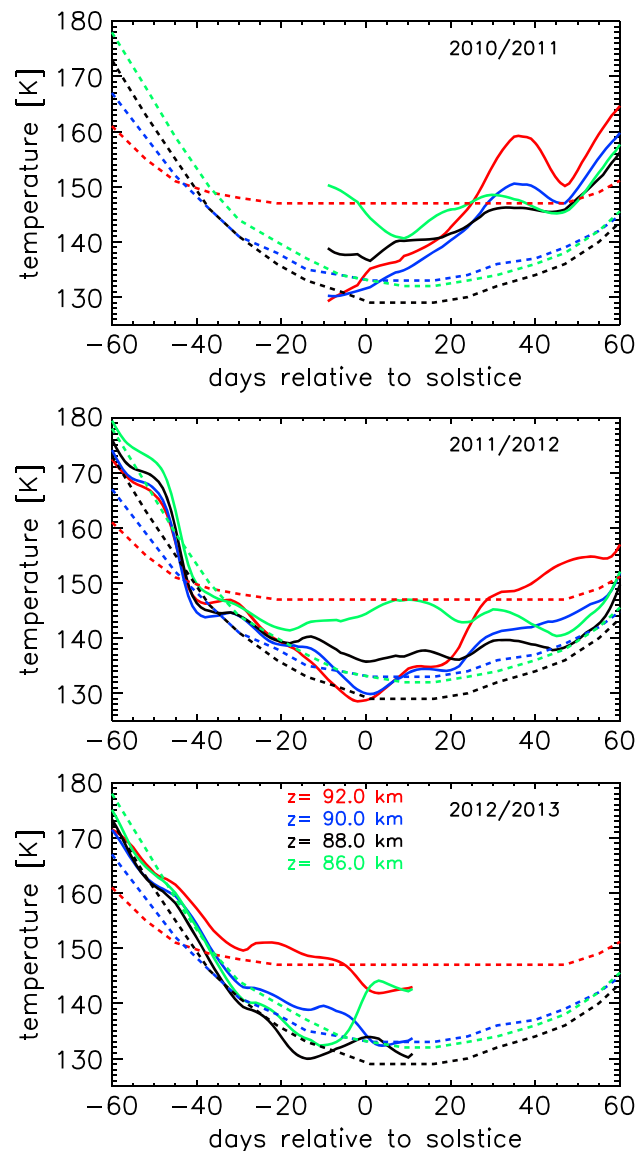


Figure 5. Temperatures as function of season (drs) at certain altitudes (see inset) and comparison with FJL99 from the NH (dashed lines). Note that the variability (RMS) of the original temperature profiles contributing to the mean in FJL99 is approximately 5–10 K at these altitudes.

In Figure 5 we compare in more detail the seasonal variation of temperatures at specific heights for the three seasons and also with the NH. Again, there are systematic differences between the first two seasons and 2012/2013, in particular around solstice. In 2010/2011 and 2011/2012 temperatures at 92 km are significantly lower compared to the NH by up to 15–20 K, whereas they are similar to the NH in 2012/2013. At lower altitudes, temperatures are more similar in both hemispheres except for 86 km where it is warmer in the SH. Outside the solstice period, temperatures in the SH are generally higher compared to the NH, in particular after solstice. The transition from high to low temperatures occurs rather quickly in 2011/2012 (no data in 2010/2011) and comparatively smoothly in 2012/2013. In summary, the development of the temperature field is similar in 2010/2011 and 2011/12 with a high mesopause (relative to the NH) around solstice, whereas the morphology in 2012/2013 is generally different from the first two seasons and is closer to typical NH conditions with a typical summer mesopause altitude around 88 km.

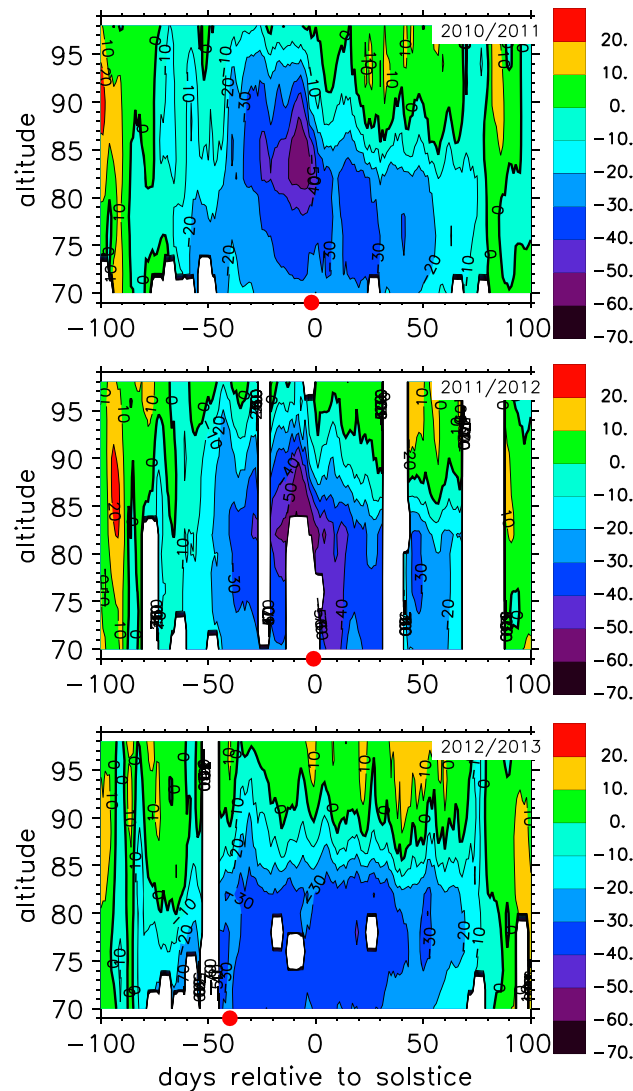


Figure 6. Temporal development of zonal winds in [m/s] as measured by the MF radar at Davis. The red dots mark the days of the vortex breakdown (drs=-2, -1, and -40, respectively) in the stratosphere applying the criterion $\bar{u} < 10$ m/s at 50 hPa (see Figure 9).

3.2. Winds in the MLT

In Figure 6 we show zonal winds for the three lidar seasons as measured by the MF radar at Davis. Daily averaged profiles were further smoothed by a 5 day running mean. Despite some data gaps due to strong absorption in the ionosphere, the difference between the first two seasons (2010/2011 and 2011/2012) and the season 2012/2013 is striking, as is the case for the seasonal variation of temperatures in these years. For example, for several weeks close to and prior to solstice the wind reversal from westward to eastward winds (negative to positive) occurs at 95–100 km in the first 2 years, whereas it takes place at substantially lower heights in the last year. Regarding the variation of winds with season, a strong westward jet lasting several days develops around solstice, coincident with the period of the elevated summer mesopause (see Figure 3). The overall differences in zonal winds and temperatures between the first two seasons and the 2012/2013 season are strongly reminiscent of the systematic hemispheric difference between southern and northern summer as found in the model study of *Becker et al.* [2015] (see, e.g., their Figures 6a and 6b).

For further comparison we show MF zonal winds (5 day means) measured by the ALOMAR Saura MF radar at 69°N in Figure 7. These winds are from the summer season 2010 but are typical for all NH seasons at ALOMAR [see, for example, *Placke et al.*, 2015]. Comparison with Figure 6 demonstrates the similarity between winds

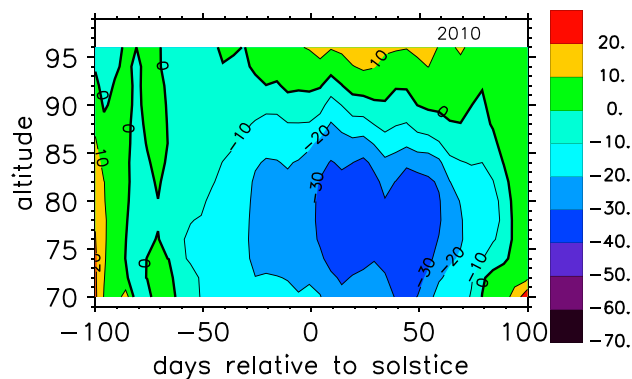


Figure 7. Temporal development of zonal winds in [m/s] as measured by the Saura MF radar at ALOMAR (69°N) in the year 2010.

in the NH and those in the SH season of 2012/2013. For a large part of the summer season the reversal from negative (westward) to positive (eastward) winds occurs at roughly 90 km, descending with time. This altitude is significantly lower compared to the first two seasons at Davis. We also note that MF winds are more variable at Davis compared to ALOMAR although both data sets have been smoothed similarly (see Figures 6 and 7). This difference is not of importance in this paper and will be investigated further in the near future.

4. Comparison With Stratospheric Winds

In Figure 8 we show zonal-mean zonal winds from the troposphere to the lower mesosphere for the three seasons when we performed Fe lidar observations at Davis. It is obvious that winds in the first two seasons are systematically different from the last season: in 2010/2011 and 2011/2012 strong zonal winds of typically +40–50 m/s are present in the lower stratosphere, persisting until solstice. In other words, the breakdown of the polar vortex is late and extends way into the summer season. The final breakdown occurs very late in both seasons, namely, around $drs = 0$. The situation is completely different in 2012/2013: zonal winds are already weak at $drs = -60$ and the breakdown of the vortex occurs several weeks before solstice, i.e., at $drs \sim -40$.

Karlsson *et al.* [2011] (hereafter referred to as BK11) classify stratospheric winds into a late and early breakdown of the polar vortex, being representative of a “winter-like” and “summer-like” condition, respectively. “Late/early” means that zonal winds during the “onset-period” (defined as the period from $drs = -40$ to -20) are more/less eastward by $0.5 \cdot \sigma$ compared to the climatological mean ($\sigma =$ standard deviation of wind anomalies). Late and early conditions lead to a high/warm and low/cold mesopause around solstice, respectively. Note that we have used a more relaxed limit of $0.5 \cdot \sigma$ instead of $1.0 \cdot \sigma$ as in BK11. Normally, when winds are strongly eastward in the onset period, the transition to weaker eastward winds occurs late. When winds are weak in the onset period, the transition occurs early. More precisely, the time of wind transition (t_{rev}) is defined as the day when zonal-mean zonal wind at 50 hPa and 65°S gets lower than +10 m/s. As can be seen from Figure 9 the latter criterion leads to wind transitions at $drs = -2, -1,$ and -40 for the three seasons 2010/2011, 2011/2012, and 2012/2013, respectively. This implies that the first two seasons are to be classified as “late breakdown,” whereas the last season is representative of an early breakdown, presumably one of the earliest breakdowns ever observed. We note that there is a tendency for a weakening of zonal winds in 2011/2012 around $drs = -33$, but winds recover thereafter. After vortex breakdown, zonal winds in the lower stratosphere are still positive but rather small (around 0–10 m/s) for the rest of the summer in all three seasons. In Figure 9 we also show zonal-mean zonal winds in the NH, i.e., at the latitude of ALOMAR (69°N), averaged for the years 1995 to 2013 (green lines). These winds are much smaller in magnitude and point to a very early breakdown at approximately $drs = -80$.

A more detailed plot of the entire zonal wind field at the latitude of ALOMAR is shown in Figure 10. More precisely, zonal-mean zonal winds from MERRA are shown for the year 2010 at the latitude of ALOMAR (69°N). We note that other years look rather similar to this example. Stratospheric winds in the NH are much weaker compared to our first two seasons at Davis and are in fact similar to the last season (2012/2013). In the NH the conditions of an early breakdown occur basically every year.

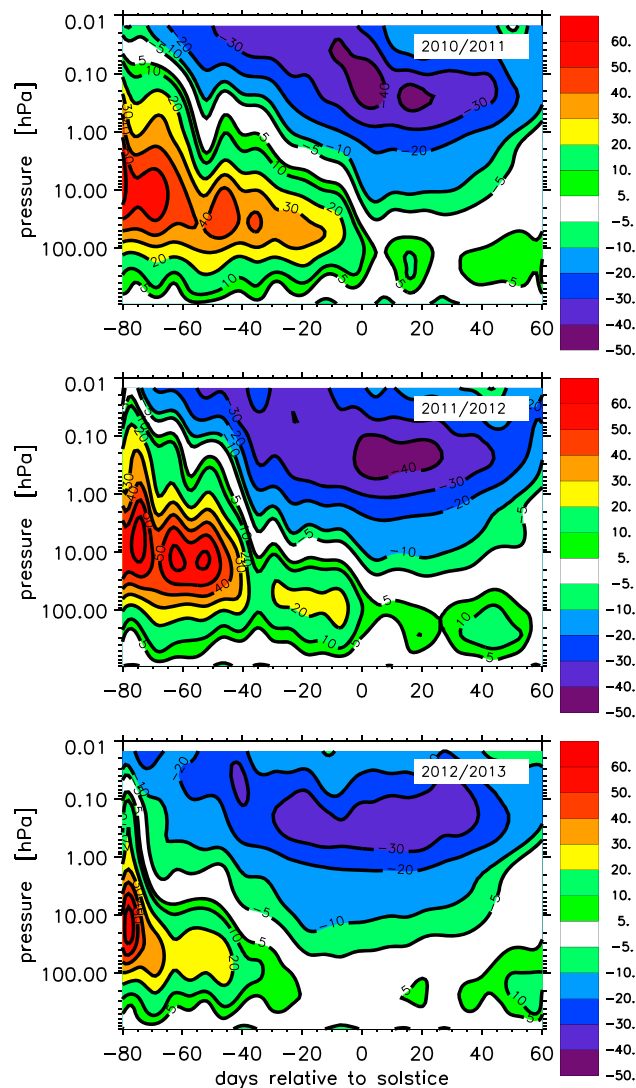


Figure 8. Contour plot of zonal-mean zonal winds in [m/s] from MERRA at the latitude of Davis for three seasons (see inset).

5. Discussion and Summary

We are aware of the fact that we have performed measurements at a single station, whereas general circulation models normally cover the entire globe. Model results of zonal-mean values suggest, however, that temperature observations performed at Davis are representative for conditions within the polar cap and that the temporally averaged zonal wind observations are representative of the zonal-mean zonal wind [see, for example, *Karlsson et al., 2011; Becker et al., 2015*]. In the data analyzing phase we have tentatively used local zonal winds from MERRA at Davis and ALOMAR, respectively, instead of zonally averaged zonal winds as shown in Figures 8, 9, and 10. We did not find any significant difference between both cases. Still, we cannot explicitly exclude that our local measurements deviate from zonal-mean values.

5.1. Comparison With Other Measurements

Pan and Gardner [2003] published a temperature climatology summarizing their measurements with a Boltzmann lidar and balloonsonde data at the South Pole. We have reproduced their summer profiles around the mesopause in Figure 11. It is obvious that the altitudinal and temporal coverage of the summer mesopause region is rather limited. Only 26 h of observations are available in the months November to February. During the crucial transition period and during most of the summer, the mesopause in that study is largely

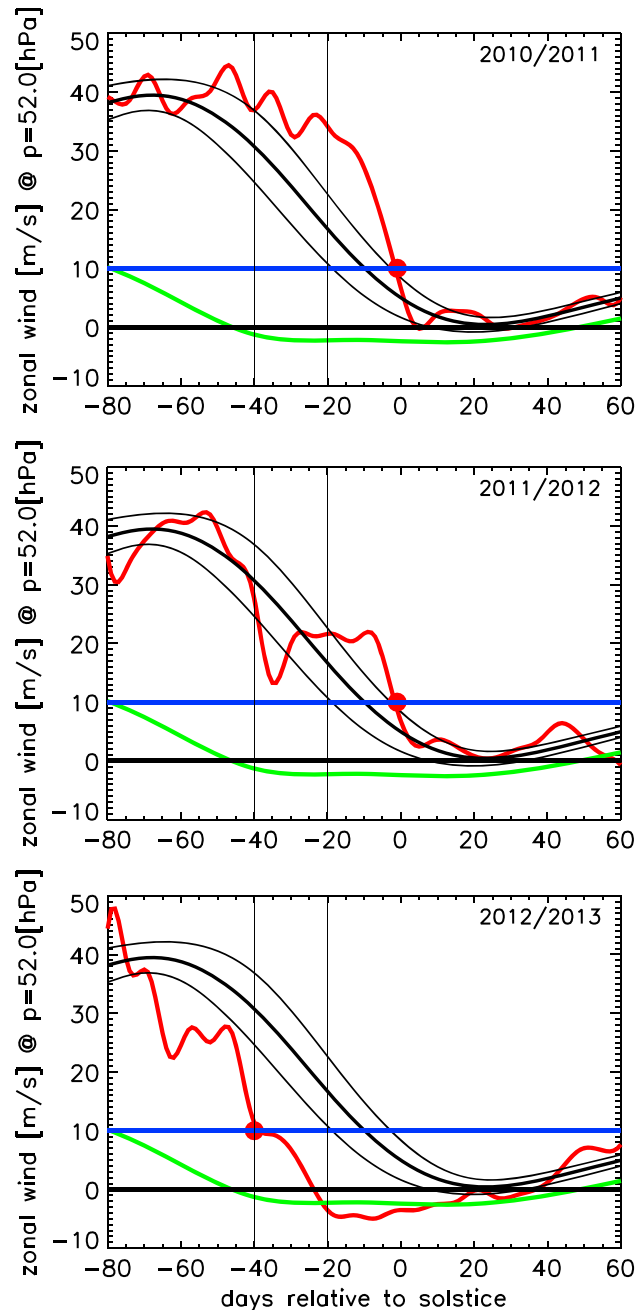


Figure 9. Temporal development of zonal-mean zonal winds at 69°S close to 50 hPa for the three seasons relevant in this paper (red lines). Also shown are zonal-mean zonal winds at the latitude of Davis averaged for the years 1995–2013 (thick black lines) along with 50% of the standard deviations of wind anomalies (thin black lines, see text for more details). Green lines: corresponding zonal-mean zonal winds in the NH summer at the latitude of ALOMAR (69°N) again averaged for the years 1995–2013. The horizontal lines mark winds of 0 m/s (for reference) and 10 m/s (the breakdown limit). The red dots mark the days of the vortex breakdown (drs = -2 , -1 , and -40 , respectively) applying the criterion $\bar{u} < 10$ m/s. The two vertical lines mark the onset period.

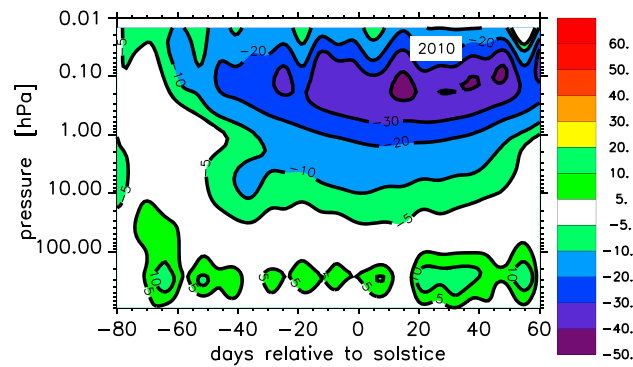


Figure 10. Contour plot of zonal-mean zonal winds from MERRA at the latitude of ALOMAR (69°N) for the summer season 2010.

determined by interpolation. Since then, a few more observations were performed by that lidar but only sporadically and not covering an entire winter/summer transition at mesopause altitudes [see, e.g., *Chu et al.*, 2011]. Nearly all temperature measurements in the MLT region published from that instrument were made in winter time [e.g., *Lu et al.*, 2015] and mostly only for singular days [e.g., *Chen et al.*, 2013]. We note that for the same period in summer (November to February) we have collected a total of 1305 h of temperature observations in the mesopause region.

In Figure 11 we also show another example of a daily-mean profile from our Fe lidar that also exhibits the elevated summer mesopause at 92–93 km on that day, which is not observed in the profiles from *Pan and Gardner* [2003].

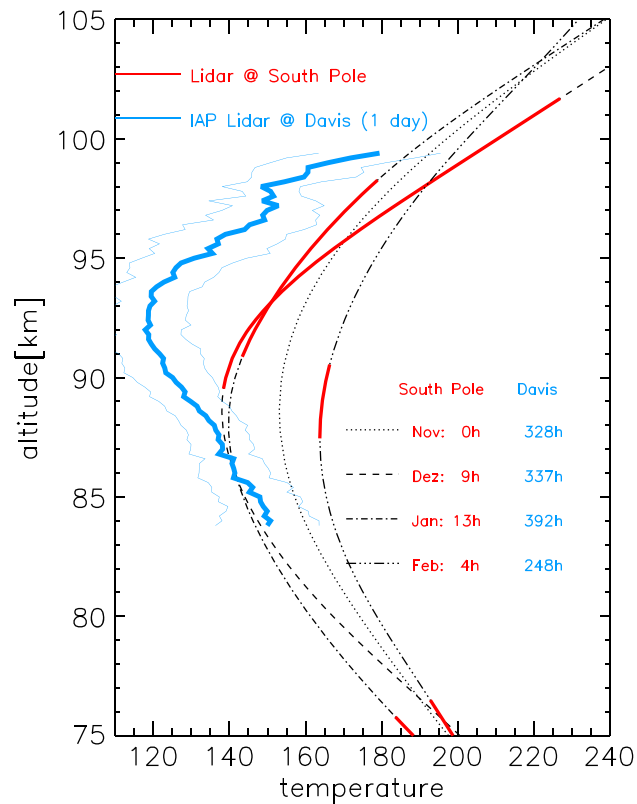


Figure 11. Red: lidar temperature profiles from *Pan and Gardner* [2003] for the months November–February (see inset, including hours of observations). Dashed: interpolations as shown in the Pan and Gardner paper. Blue: our Fe lidar temperatures at Davis for 16 h on 17/18 December 2011: mean and standard deviation. The blue numbers in the inset show the total hours of lidar observations per months obtained with our Fe lidar at Davis.

The first temperature measurements by meteorological rockets in the SH summer mesopause region took place in January/February 1998 from Rothera 68°S [Lübken et al., 1999]. It was concluded that the thermal structure at that latitude is similar to the summer at the NH colatitude. In the light of the results presented in the current paper, this is not surprising since the breakdown in the season 1997/1998 occurred very early. Applying the definition introduced above and using winds from MERRA the breakdown took place on $\text{drs} = -30$ (21 November 1997) which is several weeks before the first rocket was launched on 5 January 1998 ($\text{drs} = +15$). The early breakdown in the season 1997/1998 has therefore led to mesopause temperatures and altitudes at Rothera which were rather similar to the NH in the SH season of 1997/1998.

5.2. Seasonal Variation of Ice Layers

A detailed comparison of PMSE in the SH and NH was performed by Latteck et al. [2008] which showed that the PMSE season at Davis (69°S) is more variable compared to ALOMAR (69°N), both in terms of length of the season and occurrence rates within the season. This is caused by the longer extent and the larger variability of the polar vortex breakdown in the SH compared to the NH. Furthermore, the PMSE heights in the SH are generally ~ 1 km higher compared to the NH. This is consistent with a higher and colder mesopause along with warmer temperatures at lower heights (~ 85 km).

Kirkwood et al. [2008] noticed the unusual high altitudes of PMSE observed at Davis and at the Swedish Antarctic station Wasa (73°S). They also reported the close connection to circulation changes in the stratosphere and the elevated summer mesopause from microwave limb sounder on the Aura satellite. These results are similar to the observations presented in this paper. We note, however, that our Fe lidar provides greater details regarding the temporal and vertical structure of temperatures in the mesopause region. Furthermore, MF radar winds from Davis were not considered by Kirkwood et al. [2008].

The transmissivity of the stratosphere to gravity waves with vertical flux of eastward momentum is limited by the maximum zonal wind encountered by the gravity waves on their way from their generation at lower levels to the mesosphere. We therefore compare the maximum zonal wind in the stratosphere with the occurrence of PMSE in the mesosphere in Figure 12. More precisely, zonal-mean zonal winds for the latitude of Davis have been used, and maximum winds in the stratosphere were selected, which (in the time period considered here) typically occur at pressure levels between 10 and 100 hPa. It is obvious that PMSE occur when the maximum eastward zonal wind in the stratosphere decreases from strong winter values to about 10–20 m/s or less. Comparison with Figure 3 shows that this coincides with a severe temperature drop in the mesosphere. The onset of PMSE is therefore an indication of low temperatures, low enough for the existence of ice particles. It marks the transition from winter to summer conditions which may be used as a criterion to determine the onset of the summer state in the MLT region when direct temperature measurements are not available. However, we need to add a note of caution: the presence of ice particles (PMC, NLC, and PMSE) manifests that temperatures are below the frost point temperature T_{frost} , which is only an indirect estimation of an upper limit of real temperatures assuming some standard water vapor densities. Furthermore, PMSE require turbulence and electrons. Therefore, low enough temperatures are a necessary, but not sufficient condition for PMSE. On the other hand, there is significant evidence that, generally speaking, requirements other than $T < T_{\text{frost}}$ are usually fulfilled. This can be seen from Figure 3 and also from earlier comparisons of PMSE and the thermal structure, e.g., in Lübken et al. [2009]. We have demonstrated the close relationship between low temperatures and PMSE in Figures 3 and 12. Regarding the maximum altitude of PMSE we note that kinematic viscosity is increasing with height, which makes it more and more difficult for small scale structures in the plasma (required for PMSE) to survive [Lübken et al., 2009]. Therefore, PMSE are not a good indicator of low temperatures at altitudes above ~ 94 –95 km.

Benze et al. [2012] have studied in detail the relation between the onset of PMC (t_{PMC}) as observed by SBUV (Solar Backscatter Ultraviolet) satellite instruments and the circulation in the stratosphere. The timing of the wind transition from winter to summer conditions (t_{rev}) was defined as the day of the final decrease of the zonal-mean zonal wind at 50 hPa below 10 m/s, i.e., identical to the definition used by BK11 (see above). They found an almost linear relation $t_{\text{PMC}} \sim t_{\text{rev}}$ with a small delay of 1–2 days, i.e., the PMC onset day is delayed relative to the stratospheric wind transition. They realized that this relation depends on the sensitivity of detecting ice clouds (and on the definition of t_{rev} , of course). The relevance of these considerations is clearly demonstrated in Figure 12: ice clouds, namely, PMSE, are sometimes seen up to 30 days prior to the day of the stratospheric wind transition. In other words, summer conditions (low temperatures) may occur several weeks before vortex breakdown as defined in BK11 and Benze et al. [2012]. This implies that the

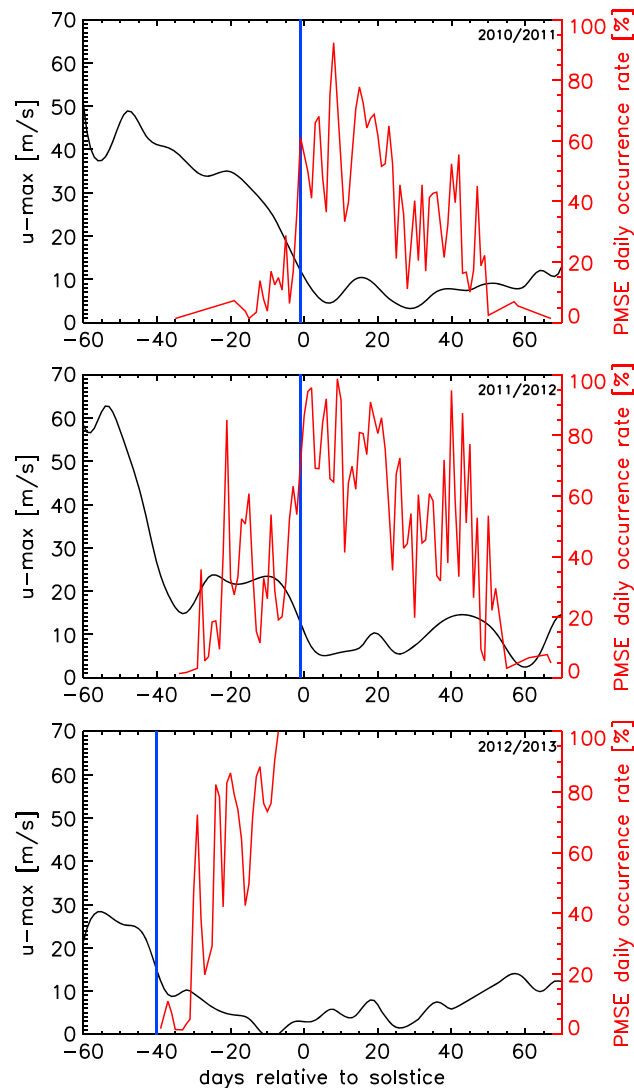


Figure 12. Temporal development of (left scale) the maximum zonal wind in the stratosphere (black lines) and (right scale) the occurrence of PMSE (red lines). See text for more details. For comparison the dates of vortex breakdown as determined in Figure 9 are indicated (blue vertical lines).

stratospheric circulation change leading to low and summer-like temperatures (supporting ice particles) may not be appropriately characterized by the transition criterion described above.

5.3. Comparison With Models

The explanation of the reaction of the MLT to the circulation in the stratosphere is rather complicated and involves the interaction of several processes. For example, intrahemispheric coupling plays an important role prior to and around summer solstice, while interhemispheric becomes important later on [Smith *et al.*, 2010; Karlsson *et al.*, 2011; Becker *et al.*, 2015]. These coupling mechanisms can be applied within the framework of the stationary downward control principle in the extratropical SH in combination with arguments of gravity-wave filtering and breaking. The situation is, however, further complicated by traveling planetary waves [Siskind and McCormack, 2014], the interaction of thermal tides with gravity waves [Senf and Achatz, 2011], and the seasonal evolution determined by radiative transfer. In the following discussion we mainly restrict ourselves to arguments of intrahemispheric coupling. A more detailed discussion is provided in, for example, Karlsson *et al.* [2011] and Becker *et al.* [2015].

To the best of our knowledge there are no model studies available which describe in detail the entire seasonal development of the dynamical and thermal state of the middle atmosphere in the SH for early, late, and

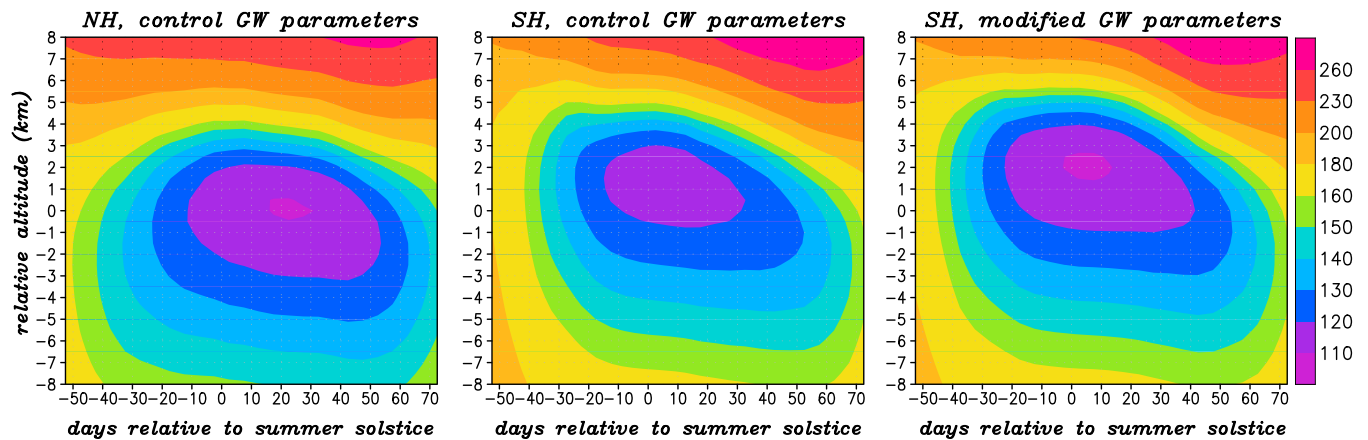


Figure 13. Seasonal evolution of temperatures (in Kelvin) in the summer mesopause region from KMCM model simulations. (left and middle) Results from the control simulation of *Becker et al.* [2015] where the launch level parameters for parameterized nonorographic gravity waves are the same in both hemispheres. (right) The result when the launch level spectrum in the SH is shifted toward higher frequencies and smaller amplitudes (see text for further details). Temperatures were averaged over the polar caps (from 70° to 90°) and over 10 seasons in each case. Then, interpolation from pressure surfaces to geometric height (averaged like the temperatures) was performed. The altitude is relative to that of the mean summer mesopause in the NH which is located in KMCM at 86 km.

mean transitions. BK11 study the conditions in the onset period (drs = -40 to -20) for early and late transitions but cover the development before and after the onset period only to a small extent. *Becker et al.* [2015] compared coupling mechanisms in the NH and SH during the winter/summer transitions in detail, but only for climatological mean conditions.

We start with a comparison of our observations with the model study of BK11, i.e., during the onset period and for the specific cases of early and late breakdown. We have sufficient temperature coverage in the onset period only for the early case (2012/2013). Regarding observations for the late case, we started too late with our measurements in 2010/2011 (a late case), and the season 2011/2012 is not a clear late case but is more complicated. For example, the condition $u < 10$ m/s at 50 hPa occurs in that season at drs = -1 (late) and MF winds are similar to 2010/2011 (a late case). But the early appearance of PMSE indicates an early case. Since the situation is not unambiguous in 2011/2012 we decided to ignore this season in this context. We note that we have nearly full seasonal coverage of winds from the MF radar for all seasons and both cases (late/early).

In our observations the temperature of the mesopause during the onset period in the early case is declining from 155 K to 135 K and is on average somewhat warmer than in BK11 (140 K) and also warmer (but at the same altitude) compared to the standard mesopause in the NH (130 K/88 km). From our MF radar winds we see that maximum zonal winds in the mesopause region during the onset periods are significantly smaller (i.e., less negative) compared to BK11. The difference is larger in the late case (-70 m/s in BK11 versus -30 to -40 m/s observed by MF radar) compared to the early case (-50 m/s versus -30 m/s).

We are not aware of any model which reproduces the “mesopause jump” to higher altitudes/lower temperatures around summer solstice as shown in Figure 3b (and to a certain extent also in Figure 3a) leading to an elevated summer mesopause (ESM). Models suggest that if the mesopause in the summer SH is higher than “normal” (= 88 km), then it is necessarily warmer than normal (see, for example, Figure 6 in BK11). We have reproduced this standard behavior with KMCM, namely, a higher and warmer mesopause in Davis (for mean conditions) compared to ALOMAR (see Figure 13). In this simulation, the model was used with identical parameters of parameterized nonorographic gravity waves in each hemisphere (which was called “control simulation” in *Becker et al.*, 2015). An obvious possibility to reproduce a higher and colder(!) mesopause (as observed) is to modify the gravity wave source spectrum in the SH. The modification is zero north of 20° S and concentrated at 56° S. It sets in at day -110 (relative to summer solstice) and maximizes from day -50 to day 70 on. The most important modifications are such that the maximum vertical wavelength is increased from 11.0 km to 14.6 km, the horizontal wavelength is reduced from 500 km to 415 km, and the total horizontal wind variance is reduced from 0.95 to 0.78 m s^{-1} [see also *Becker and McLandress*, 2009, section 3]. These modifications enhance the high-altitude gravity-wave drag around solstice and lead to the desired effect, namely, a higher and colder mesopause in the SH in early summer, which is in better agreement with our observations.

A possible implication of this finding is that the nonorographic tropospheric gravity sources during late winter and spring in the SH may be significantly different from those in the NH, i.e., with a tendency toward higher frequencies in the SH.

The observed downward propagation of the mesopause after summer solstice has been explained in *Becker et al.* [2015] by the gradual weakening of the wintertime stratospheric vortex and its transition to summer conditions. At the same time, the interhemispheric coupling effect caused by a weak polar night jet in the northern winter hemisphere becomes important and enhances the downward propagation of the summer mesopause in the SH. Here we argue that also the seasonal evolution of the sources of nonorographic gravity waves from higher to lower frequencies may play a role.

Obviously, the reaction of the mesopause thermal structure to the breakdown in the stratosphere depends on the time when this breakdown occurs. This is evident from Figure 3: The breakdowns in the seasons 2010/2011 and 2012/2013 occur at different times in the season ($drs = -2$ and -40 , respectively), and the reaction of the mesopause region is rather different. We suggest that this difference is due to the circulation at higher altitudes, namely, in the mesosphere. It is the circulation in the entire middle atmosphere which finally determines the propagation conditions for gravity waves and their impact on the mesopause region. This is also evident when considering the difference in the stratospheric circulation in the NH and SH. In the NH the stratospheric vortex breakdown occurs much earlier compared to the SH, namely, around $drs = -70$, because of stronger planetary Rossby waves. Nevertheless, the weak zonal wind in the mesosphere from about $drs = -70$ to $drs = -40$ (see Figure 7) causes eastward gravity waves to break in the middle and lower mesosphere and thereby hinders the northern mesopause to turn to summer conditions. On the other hand, the strong upper mesospheric westward wind in the SH mesosphere (Figures 6a and 6b) allows eastward gravity waves to propagate to high altitudes and induces an ESM as soon as the wave filtering in stratosphere permits. This reasoning is consistent with the model study of *Becker et al.* [2015].

5.4. Summary

In this paper we report on a significant part of new temperature observations at Antarctic latitudes by a Fe lidar being located at Davis (69°S). Measurements were performed from 15 December 2010 until 31 December 2012. Here we concentrate on data in the mesopause region relevant for the winter/summer transition. We compare our results with collocated wind observations by an MF radar and PMSE detection by a VHF radar and also with stratospheric winds from MERRA. Generally speaking, mesopause temperatures (and altitudes) are strongly related to the circulation in the stratosphere. In the summer season 2012/2013 the vortex breakdown in the stratosphere occurs very early ($drs = -40$) and the mesopause altitude and temperature is "normal," i.e., similar to the climatological mean in the NH ($\sim 88\text{ km}/130\text{ K}$). In 2010/2011, however, the breakdown occurs much later ($drs = -2$) and the mesopause is higher and colder (note that our operation started only a few days before solstice). The situation in the season 2011/2012 is more complex as some atmospheric parameters indicate a late transition, whereas others point to an early transition. MF radar winds also show a systematic difference between the situation in 2012/2013 and the two earlier summer seasons. In 2010/2011 and 2011/2012 the final vortex breakdown in the stratosphere occurs around solstice. During that period the mesopause "jumps" to unusual high altitudes and low temperatures for a few days (elevated summer mesopause, ESM). Daily mean mesopause temperatures below 120 K at 93 km are observed during this period. During the ESM period, zonal winds from the MF radar are also much more westward than normal and westward winds reach to unusual high altitudes. Regarding ice layers in the mesosphere (here: PMSE) we find that they are not necessarily a good indicator for stratospheric vortex breakdown.

Our results clearly indicate the requirement for a more sophisticated representation of gravity waves in models. For example, simplifications of the seasonal variation of sources may lead to an incorrect thermal structure in the MLT region and to a misinterpretation of related phenomena.

The results presented in this paper and in previous publications on winter/summer transitions in the SH are of potential importance, for example, when comparing interhemispheric differences in the occurrence of ice clouds observed from satellites by, e.g., SBUV instruments [see, for example, *DeLand et al.*, 2007]. Defining a fixed "summer period" is probably inadequate for the SH since the winter/summer transition is rather variable. This may cause biases in the parameters describing the morphology of ice layers such as occurrence rates, brightness, and altitudes.

Acknowledgments

Data used for this paper are available via IAP's ftp server at <ftp://ftp.iap-kborn.de/data-in-publications/LuebkenJGR2015> and (for MERRA) from <http://gmao.gsfc.nasa.gov/merra/>. IAP thanks our colleagues from Australian Antarctic Division (AAD) for their stimulating cooperation and extraordinary efforts when transporting and operating our Fe lidar. We thank Peter Hoffmann for providing the MF radar winds from ALOMAR and Jens Fiedler and Gerd Baumgarten for their support in retrieving MERRA data. This paper is partly supported by the TIMA project of the BMBF research initiative ROMIC and by the PACOG project of DFG. The IAP Fe lidar measurements at Davis and the Davis radars were supported under Australian Antarctic science projects 674, 2325, and 4025.

References

- Alexander, M. J., and K. H. Rosenlof (1996), Nonstationary gravity wave forcing of the stratospheric mean zonal wind, *J. Geophys. Res.*, *101*(D18), 23,465–23,474.
- Becker, E., and C. McLandress (2009), Consistent scale interaction of gravity waves in the Doppler-spread parameterization, *J. Atmos. Sci.*, *66*, 1434–1449, doi:10.1175/2008JAS2810.1.
- Becker, E., R. Knöpfel, and F.-J. Lübken (2015), Dynamically induced hemispheric differences in the seasonal cycle of the summer polar mesopause, *J. Atmos. Sol. Terr. Phys.*, *129*, 128–141, doi:10.1016/j.jastp.2015.04.014.
- Benze, S., C. Randall, B. Karlsson, V. Harvey, M. Deland, G. Thomas, and E. Shettle (2012), On the onset of polar mesospheric cloud seasons as observed by SBUV, *J. Geophys. Res.*, *117*, D07104, doi:10.1029/2011JD017350.
- Chen, C., X. Chu, A. J. McDonald, S. L. Vadas, Z. Yu, W. Fong, and X. Lu (2013), Inertia-gravity waves in Antarctica: A case study using simultaneous lidar and radar measurements at McMurdo/Scott Base (77.8°S, 166.7°E), *J. Geophys. Res. Atmos.*, *118*, 2794–2808, doi:10.1002/jgrd.50318.
- Chu, X., W. Huang, W. Fong, Z. Yu, Z. Wang, J. A. Smith, and C. S. Gardner (2011), First lidar observations of polar mesospheric clouds and Fe temperatures at McMurdo (77.8°S, 166.7°E), Antarctica, *Geophys. Res. Lett.*, *38*, L16810, doi:10.1029/2011GL048373.
- DeLand, M. T., E. P. Shettle, G. E. Thomas, and J. J. Olivero (2003), Solar backscattered ultraviolet (SBUV) observations of polar mesospheric clouds (PMCs) over two solar cycles, *J. Geophys. Res.*, *108*(D8), 8445, doi:10.1029/2002JD002398.
- DeLand, M. T., E. P. Shettle, G. E. Thomas, and J. J. Olivero (2007), Latitude-dependent long-term variations in polar mesospheric clouds from SBUV version 3 PMC data, *J. Geophys. Res.*, *112*, D10315, doi:10.1029/2006JD007857.
- Höffner, J., and C. Fricke-Begemann (2005), Accurate lidar temperatures with narrowband filters, *Opt. Lett.*, *30*(8), 890–892.
- Höffner, J., and J. Lautenbach (2009), Daylight measurements of mesopause temperature and vertical wind with the mobile scanning iron lidar, *Opt. Lett.*, *34*, 1351–1353.
- Karlsson, B., C. E. Randall, T. G. Shepherd, V. L. Harvey, J. Lumpe, K. Nielsen, S. M. Bailey, M. Hervig, and J. M. Russell III (2011), On the seasonal onset of polar mesospheric clouds and the breakdown of the stratospheric polar vortex in the Southern Hemisphere, *J. Geophys. Res.*, *116*, D18107, doi:10.1029/2011JD015989.
- Kirkwood, S., H. Nilsson, R. J. Morris, A. R. Klekociuk, D. A. Holdsworth, and N. J. Mitchell (2008), A new height for the summer mesopause: Antarctica, December 2007, *Geophys. Res. Lett.*, *35*, L23810, doi:10.1029/2008GL035915.
- Latteck, R., W. Singer, R. J. Morris, W. K. Hocking, D. J. Murphy, D. A. Holdsworth, and N. Swarnalingam (2008), Similarities and differences in polar mesosphere summer echoes observed in the Arctic and Antarctica, *Ann. Geophys.*, *26*, 2795–2806.
- Latteck, R., W. Singer, M. Rapp, B. Vandeppeer, T. Renkowitz, M. Zecha, and G. Stober (2012), MAARSY: The new MST radar on Andøya—System description and first results, *Radio Sci.*, *47*, RS10006, doi:10.1029/2011RS004775.
- Lautenbach, J., and J. Höffner (2004), Scanning iron temperature lidar for mesopause temperature observation, *Appl. Opt.*, *43*(23), 4559–4563.
- Lu, X., X. Chu, W. Fong, C. Chen, Z. Yu, B. R. Roberts, and A. J. McDonald (2015), Vertical evolution of potential energy density and vertical wave number spectrum of Antarctic gravity waves from 35 to 105 km at McMurdo (77.8°S, 166.7°E), *J. Geophys. Res. Atmos.*, *120*, 2719–2737, doi:10.1002/2014JD022751.
- Lübken, F.-J. (1999), Thermal structure of the Arctic summer mesosphere, *J. Geophys. Res.*, *104*, 9135–9149.
- Lübken, F.-J., M. J. Jarvis, and G. O. L. Jones (1999), First in situ temperature measurements at the Antarctic summer mesopause, *Geophys. Res. Lett.*, *26*, 3581–3584.
- Lübken, F.-J., J. Lautenbach, J. Höffner, M. Rapp, and M. Zecha (2009), First continuous temperature measurements within polar mesosphere summer echoes, *J. Atmos. Sol. Terr. Phys.*, *71*, 453–463, doi:10.1016/j.jastp.2008.06.001.
- Lübken, F.-J., J. Höffner, T. P. Viehl, B. Kaifler, and R. J. Morris (2011), First measurements of thermal tides in the summer mesopause region at Antarctic latitudes, *Geophys. Res. Lett.*, *38*, L24806, doi:10.1029/2011GL050045.
- Lübken, F.-J., J. Höffner, T. P. Viehl, B. Kaifler, and R. J. Morris (2014), Winter/summer mesopause temperature transition at Davis (69°S) in 2011/2012, *Geophys. Res. Lett.*, *41*, 5233–5238, doi:10.1002/2014GL060777.
- Morris, R. J., D. J. Murphy, R. A. Vincent, D. A. Holdsworth, A. R. Klekociuk, and I. M. Reid (2006), Characteristics of the wind, temperature and PMSE field above Davis, Antarctica, *J. Atmos. Sol. Terr. Phys.*, *68*(3–5), 418–435, doi:10.1016/j.jastp.2005.04.011.
- Morris, R. J., J. Höffner, F.-J. Lübken, T. Viehl, B. Kaifler, and A. K. Klekociuk (2012), Experimental evidence of a stratospheric circulation influence on mesospheric temperatures and ice-particles during the 2010–11 austral summer at 69°S, *J. Atmos. Sol. Terr. Phys.*, *89*, 54–61, doi:10.1016/j.jastp.2012.08.007.
- Pan, W., and C. S. Gardner (2003), Seasonal variations of the atmospheric temperature structure at South Pole, *J. Geophys. Res.*, *108*(D18), 4564, doi:10.1029/2002JD003217.
- Placke, M., P. Hoffmann, R. Latteck, and M. Rapp (2015), Gravity wave momentum fluxes from MF and meteor radar measurements in the polar MLT region, *J. Geophys. Res. Space Physics*, *120*, 736–750, doi:10.1002/2014JA020460.
- Rapp, M., and F.-J. Lübken (2004), Polar mesosphere summer echoes (PMSE): Review of observations and current understanding, *Atmos. Chem. Phys.*, *4*, 2601–2633.
- Rienecker, M. M., et al. (2011), MERRA: NASA's modern-era retrospective analysis for research and applications, *J. Clim.*, *24*, 3624–3648, doi:10.1175/JCLI-D-11-00015.1.
- Rosenlof, K. H. (1996), Summer hemisphere differences in temperature and transport in the lower stratosphere, *J. Geophys. Res.*, *101*, 19,129–19,136.
- Senf, F., and U. Achatz (2011), On the impact of middle-atmosphere thermal tides on the propagation and dissipation of gravity waves, *J. Geophys. Res.*, *116*, D24110, doi:10.1029/2011JD015794.
- Singer, W., R. Latteck, and D. Holdsworth (2008), A new narrow beam Doppler radar at 3 MHz for studies of the high-latitude middle atmosphere, *Adv. Space Res.*, *41*(9), 1488–1494, doi:10.1016/j.asr.2007.10.006.
- Siskind, D. E., and J. P. McCormack (2014), Summer mesospheric warmings and the quasi 2-day wave, *Geophys. Res. Lett.*, *41*, 721–722, doi:10.1002/2013GL058875.
- Siskind, D. E., S. D. Eckermann, J. P. McCormack, M. J. Alexander, and J. T. Bacmeister (2003), Hemispheric differences in the temperature of the summertime stratosphere and mesosphere, *J. Geophys. Res.*, *108*(D2), 4051, doi:10.1029/2002JD002095.
- Smith, A. K., R. R. Garcia, D. R. Marsh, D. E. Kinnison, and J. H. Richter (2010), Simulations of the response of mesospheric circulation and temperature to the Antarctic ozone hole, *Geophys. Res. Lett.*, *37*, L22803, doi:10.1029/2010GL045255.
- Viehl, T. P., J. Höffner, F.-J. Lübken, J. M. C. Plane, B. Kaifler, and R. J. Morris (2015), Summer time Fe depletion in the Antarctic mesopause region, *J. Atmos. Sol. Terr. Phys.*, *127*, 97–102, doi:10.1016/j.jastp.2015.04.013.

Contribution to the Manuscripts

In accordance with §4 of the *Guidelines for making a cumulative dissertation at the Faculty of Mathematics and Natural Sciences, University of Rostock* in the version of 3 July 2012, the candidate's individual contributions to the manuscripts submitted in this thesis are detailed in the following.

Viehl et al. [2016a]

The photolysis of FeOH and its effect on the bottomside of the mesospheric Fe layer

Viehl, T. P., J. M. C. Plane, W. Feng, and J. Höffner *Geophys. Res. Lett.*, 43, 1373–1381, (2016)

The candidate set up the lidar experiments in Antarctica and the Arctic, performed most of the measurements in Antarctica, maintained the instrument, analysed the lidar data, contributed to analysing the model data, had a major share in discussing the results and drawing conclusions, created Figures 1, 2, and 4, wrote all of the manuscript with exception of Section 3, assisted with writing Section 3, submitted the manuscript, and addressed all reviewer comments.

Viehl et al. [2015]

Summer time Fe depletion in the Antarctic mesopause region

Viehl, T. P., J. Höffner, F.-J. Lübken, J. M. C. Plane, B. Kaifler, and R. J. Morris *J. Atmos. Solar-Terr. Phys.*, 127, 97–102, (2015)

The candidate set up the lidar experiment in Antarctica, performed most of the measurements, maintained the instrument, analysed the lidar data, had a major share in discussing the results and drawing conclusions, created all figures, wrote all of the manuscript with exception of the second half of Section 3.3, assisted with writing the second half of Section 3.3, submitted the manuscript, and addressed all reviewer comments.

Viehl et al. [2016b]

Corrigendum to: Summer time Fe depletion in the Antarctic mesopause region, by Viehl et al. [2015]

Viehl, T. P., J. Höffner, F.-J. Lübken, J. M. C. Plane, B. Kaifler, and R. J. Morris *J. Atmos. Solar-Terr. Phys.*, 142, (2016)

The candidate had a large share in discussing the results and drawing conclusions, jointly authored the text of the manuscript with J. M. C. Plane and J. Höffner, and submitted the manuscript.

Lübken et al. [2011]

First measurements of thermal tides in the summer mesopause region at Antarctic latitudes

Lübken, F.-J., J. Höffner, T. P. Viehl, B. Kaifler, and R. J. Morris *Geophys. Res. Lett.*, 38, L24806, (2011)

The candidate set up the lidar experiment in Antarctica, performed most of the measurements, maintained the instrument, had a minor share in discussing the results and drawing conclusions, and assisted with the data analysis. No contribution to the text of the manuscript.

Feng et al. [2015]

Diurnal variation of the potassium layer in the upper atmosphere

Feng, W., J. Höffner, D. R. Marsh, M. P. Chipperfield, E. C. M. Dawkins, T. P. Viehl, and J. M. C. Plane *GRL*, 42, (2015)

The candidate assisted with the analysis of lidar and model data shown in Figures 2 and 3 a, b, and had a minor share in discussing the results. Minor comments on the text of the manuscript.

Kaifler et al. [2015]

Lidar observations of gravity wave activity in the middle atmosphere over Davis (69°S, 78°E), Antarctica

Kaifler, B., Lübken, F.-J., J. Höffner, R. J. Morris, and T. P. Viehl *J. Geophys. Res.: Atmos.*, 120, 4506–4521, (2015)

The candidate set up the lidar experiment in Antarctica, maintained the instrument, and performed most of the lidar measurements excluding the winter months 05/2011 to 10/2011. No contribution to the data analysis, discussion of the results, or the text of the manuscript.

Morris et al. [2012]

Experimental evidence of a stratospheric circulation influence on mesospheric temperatures and ice-particles during the 2010–2011 austral summer at 69°

R. J. Morris, J. Höffner, F.-J. Lübken, T. P. Viehl, B. Kaifler, and A. R. Klekociuk *J. Atmos. Solar-Terr. Phys.*, 89, 54–61, (2012)

The candidate set up the lidar experiment in Antarctica, performed most of the lidar measurements, assisted with the analysis of lidar data, had a medium share in discussing the results, and assisted with the creation of Figure 3. No contribution to the text of the manuscript.

Lübken et al. [2014]

Winter/summer mesopause temperature transition at Davis (69°S) in 2011/2012

Lübken, F.-J., J. Höffner, T. P. Viehl, B. Kaifler, and R. J. Morris *Geophys. Res. Lett.*, 41, 5233–5238, (2014)

The candidate set up the lidar experiment in Antarctica, performed most of the lidar measurements, assisted with the analysis of lidar data, and had a minor share in discussing the results. Minor comments on the text of the manuscript.

Lübken et al. [2015]

Winter/summer transition in the Antarctic mesopause region

Lübken, F.-J., J. Höffner, T. P. Viehl, E. Becker, R. Latteck, B. Kaifler, D. J. Murphy, and R. J. Morris *J. Geophys. Res.: Atmos.*, 120, 12,394–12,409, (2015)

The candidate set up the lidar experiment in Antarctica, performed nearly all of the lidar measurements presented, assisted with the analysis of the lidar data, and performed a literature review. Some comments on the text of the manuscript. Medium contribution addressing reviewer comments.

Timo P. Viehl
October 2016

Prof. Dr. Franz-Josef Lübken
October 2016

Declaration

I declare that this thesis has been composed by myself and without outside help. I confirm that the work submitted is my own, except where work which has formed part of jointly-authored publications has been included. My contributions to the publications have been explicitly indicated on pages 141 and 142. I confirm that appropriate credit has been given within this thesis where reference has been made to the work of others. I declare that neither the opportunity for this doctoral research nor the completion of any tasks leading to the submission of this thesis have been arranged commercially.

I acknowledge that copyright of published works contained within this thesis resides with the copyright holder(s) of those works. The copyrighted material is reproduced in accordance with the licences on pages 61 and 62. As far as it does not infringe the rights of the original copyright holders, I give permission for the digital version of my thesis to be made available for fair use in scientific and educational context via the repositories, archives, and websites of the University Library of Rostock at the University of Rostock, Germany, the Leibniz-Institute of Atmospheric Physics at the University of Rostock in Kühlungsborn, Germany, and the German National Library in Frankfurt am Main and Leipzig, Germany and associated organisations. Please refer to the original copyright holders via the provided DOIs for personal copies of the full manuscripts submitted with this thesis.

Timo P. Viehl
October 2016

References

- Achatz, U. N. Grieger, and H. Schmidt (2008), Mechanisms controlling the diurnal solar tide: Analysis using a GCM and a linear model, *J. Geophys. Res.*, *113*, A08303, doi:10.1029/2007JA012967.
- Akmaev, R. A. (2011), Whole atmosphere modeling: connecting terrestrial and space weather, *Rev. Geophys.*, *49*, RG4004, doi:10.1029/2011RG000364.
- Allen, S. J., and R. A. Vincent (1995), Gravity wave activity in the lower atmosphere: Seasonal and latitudinal variations, *J. Geophys. Res.*, *100*(D1), 1327–1350, doi:10.1029/94JD02688.
- Alpers, M. (1993b), Untersuchung der mesosphärischen Eisenschicht in polaren und niedrigen geographischen Breiten mittels Lidar, *Dissertation*, University of Bonn, Germany.
- Alpers, M., J. Höffner, and U. von Zahn (1990), Iron atom densities in the polar mesosphere from lidar observations, *Geophys. Res. Lett.*, *17*(12), 2345–2348.
- Alpers, M., T. Blix, S. Kirkwood, D. Krankowsky, F.-J. Lübken, S. Lutz, and U. von Zahn (1993a), First Simultaneous Measurements of Neutral and Ionized Iron Densities in the Upper Mesosphere, *J. Geophys. Res.*, *98*(A1), 275–283.
- Alexander, M. J., and C. Barnett (2007), Using Satellite Observations to Constrain Parameterizations of Gravity Wave Effects for Global Models, *J. Atmos. Sci.*, *64*, 1652–1665, doi:10.1175/JAS3897.1.
- Alexander, S. P., A. R. Klekociuk, and D. J. Murphy (2011), Rayleigh lidar observations of gravity wave activity in the winter upper stratosphere and lower mesosphere above Davis, Antarctica (69°S, 78°E), *J. Geophys. Res.*, *116*, D13109, doi:10.1029/2011JD015164.
- Alexander, S. P., D. J. Murphy, and A. R. Klekociuk (2013), High resolution VHF radar measurements of tropopause structure and variability at Davis, Antarctica (69°S, 78°E), *Atmos. Chem. Phys.*, *13*, 3121–3132, doi:10.5194/acp-13-3121-2013.
- Anders, E., and M. Ebihara (1982), Solar-system abundances of the elements, *Geoch. Cosmoch. Acta*, *46*, 2363–2380.
- Baggaley, W. J. (2002), Radar Observations, in *Meteors in the Earth's Atmosphere*, ed. E. Murad and I. P. Williams, Cambridge University Press, 123–148, ISBN 978-0-521-80431-8.
- Bailey, S. M., A. W. Merkel, G. E. Thomas, and J. N. Carstens (2005), Observations of polar mesospheric clouds by the Student Nitric Oxide Explorer, *J. Geophys. Res.*, *110*, D13203, doi:10.1029/2004JD005422.
- Bailey, S. M., A. W. Merkel, G. E. Thomas, and D. W. Rusch (2007), Hemispheric differences in Polar Mesospheric Cloud morphology observed by the Student Nitric Oxide Explorer, *J. Atmos. Solar-Terr. Phys.*, *69*, 1407–1418, doi:10.1016/j.jastp.2007.02.008.
- Baumgarten, G., J. Fiedler, and M. Rapp (2010), On microphysical processes of noctilucent clouds (NLC): observations and modeling of mean and width of the particle size-distribution, *Atmos. Chem. Phys.*, *10*, 6661–6668, doi:10.5194/acp-10-6661-2010.
- Baumgarten, G., A. Chandran, J. Fiedler, P. Hoffmann, N. Kaifler, J. Lumpe, A. Merkel, C. E. Randall, D. Rusch, and G. Thomas (2012), On the horizontal and temporal structure of noctilucent clouds as observed by satellite and lidar at ALOMAR (69N), *Geophys. Res. Lett.*, *39*, L01803, doi:10.1029/2011GL049935.
- Baumgarten, G., and D. C. Fritts (2014), Quantifying Kelvin-Helmholtz instability dynamics observed in noctilucent clouds: 1. Methods and observations, *J. Geophys. Res. Atmos.*, *119*, 9324–9337, doi:10.1002/2014JD021832.
- Baumgarten, G., J. Fiedler, J. Hildebrand, and F.-J. Lübken (2015), Inertia gravity wave in the stratosphere and mesosphere observed by Doppler wind and temperature lidar, *Geophys. Res. Lett.*, *42*, 10,929–10,936, doi:10.1002/2015GL066991.

- Bautista, M. A., P. Romano, and A. K. Pradhan (1998), Resonance-averaged photoionization cross sections for astrophysical models, *Astrophys. J. Suppl. Ser.*, *118*, 259–265, doi:10.1086/313132.
- Becker, E. (2012), Dynamical Control of the Middle Atmosphere, *Space Sci. Rev.*, *168*(1), 283–314, doi:10.1007/s11214-011-9841-5.
- Becker, E., R. Knöpfel, and F.-J. Lübken (2015), Dynamically induced hemispheric differences in the seasonal cycle of the summer polar mesopause, *J. Atmos. Solar-Terr. Phys.*, *129*, 128–141, doi:10.1016/j.jastp.2015.04.014.
- Beig, G., P. Keckhut, R. P. Lowe, R. G. Roble, M. G. Mlynczak, J. Scheer, V. I. Formichev, D. Offermann, W. J. R. French, M. G. Shepherd, A. I. Semenov, E. E. Remsberg, C. Y. She, F. J. Lübken, J. Bremer, B. R. Clemesha, J. Stegman, F. Sigeres, and S. Fadnavis (2003), Review of mesospheric temperature trends, *Rev. Geophys.*, *41*, doi:10.1029/2002RG000121.
- Benze, S., C. E. Randall, B. Karlsson, V. L. Harvey, M. T. DeLand, G. E. Thomas, and E. P. Shettle (2012), On the onset of polar mesospheric cloud seasons as observed by SBUV, *J. Geophys. Res.*, *117*, D07104, doi:10.1029/2011JD017350.
- Berger, U., and F.-J. Lübken (2015), Trends in mesospheric ice layers in the Northern Hemisphere during 1961–2013, *J. Geophys. Res. Atmos.*, *120*, 11,277–11,298, doi:10.1002/2015JD023355.
- Bones, D. L., J. M. C. Plane, and W. Feng (2015), Dissociative Recombination of FeO⁺ with Electrons: Implications for Plasma Layers in the Ionosphere, *J. Phys. Chem. A*, doi:10.1021/acs/jPCA.5b04947.
- Brekke, A. (2013), *Physics of the Upper Polar Atmosphere*, 2nd ed., Springer-Praxis Books in Environmental Sciences, Springer-Verlag Berlin Heidelberg, ISBN 978-3-642-27400-8, doi:10.1007/978-3-642-27401-5.
- Bowman, M. R., A. J. Gibson, and M. C. W. Sandford (1969), Atmospheric Sodium measured by a Tuned Laser Radar, *Nature*, *221*, 456–457, doi:10.1038/221456a0.
- Butchart, N. (2014), The Brewer–Dobson circulation, *Rev. Geophys.*, *52*, 157–184, doi:10.1002/2013RG000448.
- Cepelcha, Z., J. Borovička, W. G. Elford, D. O. Revelle, R. L. Hawkes, V. Porubčan, and M. Šimek (1998) Meteor phenomena and bodies, *Space Science Reviews*, *84*, 327–471.
- Charney, J. G., and P. G. Drazin (1961), Propagation of planetary-scale disturbances from the lower into the upper atmosphere, *J. Geophys. Res.*, *66*(1), 83–109, doi:10.1029/JZ066i001p00083.
- Chu, X., C. Yamashita, P. J. Espy, G. J. Nott, E. J. Jensen, H.-L. Liu, W. Huang, and J. P. Thayer (2009), Responses of polar mesospheric cloud brightness to stratospheric gravity waves at the South Pole and Rothera, Antarctica, *J. Atmos. Solar-Terr. Phys.*, *71*, 434–445, doi:10.1016/j.jastp.2008.10.002.
- Chu, X, W. Huang, W. Fong, Z. Yu, Z. Wang, J. A. Smith, and C. S. Gardner (2011a), First lidar observations of polar mesospheric clouds and Fe temperatures at McMurdo (77.8°S, 166.7°E), Antarctica, *Geophys. Res. Lett.*, *38*, L16810, doi:10.1029/2011GL048373.
- Chu, X, Z. Yu, C. S. Gardner, C. Chen, and W. Fong (2011b), Lidar observations of neutral Fe layers and fast gravity waves in the thermosphere (110–155 km) at McMurdo (77.8°S, 166.7°E), Antarctica, *Geophys. Res. Lett.*, *38*, L23807, doi:10.1029/2011GL050016.
- Clemesha, B. R., D. M. Simonich, P. P. Batista, and V. W. J. H. Kirchhoff (1982), The diurnal variation of atmospheric sodium, *J. Geophys. Res.*, *87*(A1), 181–186, doi:10.1029/JA087iA01p00181.
- Collins, R. L., J. Li, and C. M. Martus (2015), First lidar observation of the mesospheric nickel layer, *Geophys. Res. Lett.*, *42*, 665–671, doi:10.1002/2014GL062716.
- Dawkins, E. C. M., J. M. C. Plane, M. P. Chipperfield, W. Feng, J. Gumbel, J. Hedin, J. Höffner, and J. S. Friedman, First global observations of the mesospheric potassium layer, *Geophys. Res. Lett.*, *41*, 5653–5661, doi:10.1002/2014GL060801.
- Dawkins, E. C. M., J. M. C. Plane, M. P. Chipperfield, W. Feng, D. R. Marsh, J. Höffner, and D. Janches, Solar cycle response and long-term trends in the mesospheric metal layers, *J. Geophys. Res. Space Physics*, *Accepted for publication*, doi:10.1002/2016JA022522.

- DeLand, M. T., E. P. Shettle, G. E. Thomas, and J. J. Olivero (2003), Solar backscattered ultraviolet (SBUV) observations of polar mesospheric clouds (PMCs) over two solar cycles, *J. Geophys. Res.*, *108*(D8), 8445, doi:10.1029/2002JD002398.
- DeLand, M. T., E. P. Shettle, G. E. Thomas, and J. J. Olivero (2006), A quarter-century of satellite polar mesospheric cloud observations, *J. Atmos. Solar-Terr. Phys.*, *68*, 9–29, doi:10.1016/j.jastp.2005.08.003.
- DeLand, M. T., E. P. Shettle, G. E. Thomas, and J. J. Olivero (2007), Latitude-dependent long-term variations in polar mesospheric clouds from SBUV version 3 PMC data, *J. Geophys. Res.*, *112*, D10315, doi:10.1029/2006JD007857.
- DeLand, M. T., and G. E. Thomas (2015), Updated PMC trends derived from SBUV data, *J. Geophys. Res. Atmos.*, *120*, 2140–2166, doi:10.1002/2014JD022253.
- Delaval, J. M., C. Dufour, and J. Schamps (1980), Rotational analysis of ultraviolet systems of FeCl, *J. Phys. B: Atom. Molec. Phys.*, *13*, 4757–4769, doi:10.1088/022-3700/13/24/010.
- Delgado, R., J. S. Friedman, J. T. Fentzke, S. Raizada, C. A. Tepley, and Q. Zhou (2012), Sporadic metal atom and ion layers and their connection to chemistry and thermal structure in the mesopause region at Arecibo, *J. Atmos. Solar-Terr. Phys.*, *74*, 11–23, doi:10.1016/j.jastp.2011.09.004.
- Dhadly, M. S., J. Meriwether, M. Conde, and D. Hampton (2015), First ever cross comparison of thermospheric wind measured by narrow- and wide-field optical Doppler spectroscopy, *J. Geophys. Res. Space Physics*, *120*, 9683–9705, doi:10.1002/2015JA021316.
- Dhomse, S. S., R. W. Saunders, W. Tian, M. P. Chipperfield, and J. M. C. Plane (2013), Plutonium-238 observations as a test of modeled transport and surface deposition of meteoric smoke particles, *Geophys. Res. Lett.*, *40*, 4454–4458, doi:10.1002/grl.50840.
- Drever, R. W. P., J. L. Hall, F. V. Kowalski, J. Hough, G. M. Ford, A. J. Munley, and H. Ward (1983), Laser Phase and Frequency Stabilization Using an Optical Resonator, *Appl. Phys. B*, *31*, 97–105.
- Dunker, T., U.-P. Hoppe, W. Feng, J. M. C. Plane, and D. R. Marsh (2015), Mesospheric temperatures and sodium properties measured with the ALOMAR Na lidar compared with WACCM, *J. Atmos. Solar-Terr. Phys.*, *127*, 111–119, doi:10.1016/j.jastp.2015.01.003.
- Eixmann, R., M. Gerding, J. Höffner, and M. Kopp (2015), Lidars with narrow FOV for spectral and daylight measurements, *Trans. Geo. Remote Sens.*, *53*(8), 4548–4553, doi:10.1109/TGRS.2015.2401333.
- England, S. L., S. Maus, T. J. Immel, and S. B. Mende (2006), Longitudinal variation of the E-region electric fields caused by atmospheric tides, *Geophys. Res. Lett.*, *33*, L21105, doi:10.1029/2006GL027465.
- Eska, V., and J. Höffner (1998), Observed linear and nonlinear K layer response, *Geophys. Res. Lett.*, *25*(15), 2933–2936.
- Feng, W., D. R. Marsh, M. P. Chipperfield, D. Janches, J. Höffner, F. Yi, and J. M. C. Plane (2013), A global atmospheric model of meteoric iron, *J. Geophys. Res.*, *118*, doi:10.1002/jgrd.50708.
- Feng, W., J. Höffner, D. R. Marsh, M. P. Chipperfield, E. C. M. Dawkins, T. P. Viehl, and J. M. C. Plane (2015)**, Diurnal variation of the potassium layer in the upper atmosphere, *Geophys. Res. Lett.*, *42*, 3619–3626, doi:10.1002/2015GL063718.
- Fentzke, J. T., and C. Janches (2008), A semi-empirical model of the contribution from sporadic meteoroid sources on the meteor input function in the MLT observed at Arecibo, *J. Geophys. Res.*, *113*, A03304, doi:10.1029/2007JA012531.
- Feofilov, A. G., and A. A. Kutepov (2012), Infrared Radiation in the Mesosphere and Lower Thermosphere: Energetic Effects and Remote Sensing, *Surv. Geophys.*, *33*, 1231–1280, doi:10.1007/s10712-012-9204-0.
- Fiedler, J., G. Baumgarten, U. Berger, A. Gabriel, R. Latteck, F.-J. Lübken (2015), On the early onset of the NLC season 2013 as observed at ALOMAR, *J. Atmos. Solar-Terr. Phys.*, *127*, 73–77, doi:10.1016/j.jastp.2014.07.011.
- Fleming, E. L., S. Chandra, J. J. Barnett, and M. Corney (1990), Zonal mean temperature, pressure, zonal wind and geopotential height as functions of latitude, COSPAR International Reference Atmospheres: 1986, Part II: Middle Atmosphere Models, *Adv. Space. Res.*, *10*(12), 11–59, doi:10.1016/0273-1177(90)90230-W.

- Flynn, G. J. (2002), Extraterrestrial Dust in the Near-Earth Environment, in *Meteors in the Earth's Atmosphere*, ed. E. Murad and I. P. Williams, Cambridge University Press, 77–94, ISBN 978-0-521-80431-8.
- Forbes, J. M., and H. B. Garrett (1979), Theoretical studies of atmospheric tides, *Reviews of Geophysics and Space Physics*, 17(8), 1951–1981, doi:10.1029/RG017i008p01951.
- Forbes, J. M., and D. Wu (2006), Solar Tides as Revealed by Measurements of Mesosphere Temperature by the MLS Experiment on UARS, *J. Atmos. Sci.*, 63, 1776–1797, doi:10.1175/JAS3724.1.
- Frankland, V. L., A. D. James, W. Feng, and J. M. C. Plane (2015), The uptake of HNO₃ on meteoric smoke analogues, *J. Atmos. Solar-Terr. Phys.*, 127, 150–160, doi:10.1016/j.jastp.2015.01.010.
- Fricke, K. H., and U. von Zahn (1985), Mesopause temperatures derived from probing the hyperfine structure of the D₂ resonance line of sodium by lidar, *J. Atmos. Terr. Phys.*, 47(5), 499–512.
- Fricke-Begemann, C., J. Höffner, and U. von Zahn (2002), The potassium density and temperature structure in the mesopause region (80–105 km) at low latitude (28°N), *Geophys. Res. Lett.*, 29(22), 2067, doi:10.1029/2002GL015578.
- Fricke-Begemann, C., and J. Höffner (2005), Temperature tides and waves near the mesopause from lidar observations at two latitudes, *J. Geophys. Res.*, 110, D19103, doi:10.1029/2005JD005770.
- Frisch, M. J., et al. (2009), *Gaussian 09, Revision A.1*, Gaussian Inc., Wallingford CT.
- Fritts, D. C., and R. A. Vincent (1987), Mesospheric Momentum Flux Studies at Adelaide, Australia: Observations and a Gravity Wave-Tidal Interaction Model, *J. Atmos. Sci.*, 44(3), 605–619.
- Fritts, D. C., and J. M. Alexander (2003), Gravity wave dynamics and effects in the middle atmosphere, *Rev. Geophys.*, 41(1), doi:10.1029/2001RG000106.
- French, W. J. R., and F. J. Mulligan (2010), Stability of temperatures from TIMED/SABER v1.07 (2002–2009) and Aura/MLS v2.2 (2004–2009) compared with OH(6–2) temperatures observed at Davis Station, Antarctica, *Atmos. Chem. Phys.*, 10, 11439–11446, doi:10.5194/acp-10-11439-2010.
- French, W. J. R., and A. R. Klekociuk (2011), Long-term trends in Antarctic winter hydroxyl temperatures, *J. Geophys. Res.*, 116, D00P09, doi:10.1029/2011JD015731.
- Fussen, D., F. Vanhellefont, C. Bingen, E. Kryölä, J. Tamminen, V. Sofieva, S. Hassinen, A. Sepälä, P. Verronen, J.-L. Bertraux, A. Hauchecorne, F. Dalaudier, J.-B. Renard, R. Fraisse, O. Fanton d'Andon, G. Barrot, A. Mangin, B. Théodore, M. Guirlet, R. Koopman, P. Snoeij, and L. Saavedra (2004), Global measurements of the mesospheric sodium layer by the star occultation instrument GOMOS, *Geophys. Res. Lett.*, 31, L24110, doi:10.1029/2004GL021618.
- Fussen, D., F. Vanhellefont, C. Tétard, N. Matheshvili, E. Dekemper, N. Loodts, C. Bingen, E. Kryölä, J. Tamminen, V. Sofieva, A. Hauchecorne, F. Dalaudier, J.-L. Bertraux, G. Barrot, L. Blanot, O. Fanton d'Andon, T. Fehr, L. Saavedra, T. Yuan, and C.-Y. She (2010), A global climatology of the mesospheric sodium layer from GOMOS data during the 2002–2008 period, *Atmos. Chem. Phys.*, 10, 9225–9236, doi:10.5194/acp-10-9225-2010.
- Garcia, R. R., and S. Solomon (1985), The Effect of Breaking Gravity Waves on the Dynamics and Chemical Composition of the Mesosphere and Lower Thermosphere, *J. Geophys. Res.*, 90(D2), 3850–3868.
- Garcia, R. R., F. Stordal, S. Solomon, and J. T. Kiehl (1992), A new numerical model of the middle atmosphere, 1, Dynamics and transport of tropospheric source gases, *J. Geophys. Res.*, 97, 12,967–12,991, doi:10.1029/92JD00960.
- García-Comas, M., M. López-Puertas, M. T. Marshall, P. P. Wintersteiner, B. Funke, D. Bermejo-Pantaleón, C. J. Mertens, E. E. Remsberg, L. L. Gordley, M. G. Mlynczak, and J. M. Russell III (2008), Errors in Sounding of the Atmosphere using Broadband Emission Radiometry (SABER) kinetic temperature caused by non-local-thermodynamic-equilibrium model parameters, *J. Geophys. Res.*, 113, D24106, doi:10.1029/2008JD010105.
- Gardner, C. S. (2004), Performance capabilities of middle-atmosphere temperature lidars: comparison of Na, Fe, K, Ca, Ca⁺, and Rayleigh systems, *Applied Optics*, 43(25), 4941–4956, doi:10.1364/AO.43.004941.



- Gardner, C. S., J. M. C. Plane, W. Pan, T. Vondrak, B. J. Murray, and X. Chu (2005), Seasonal variations of the Na and Fe layers at the South Pole and their implications for the chemistry and general circulation of the polar mesosphere, *J. Geophys. Res.*, *110*, D10302, doi:10.1029/2004JD005670.
- Gardner, C. S., X. Chu, P. J. Espy, and J. M. C. Plane, D. R. Marsh, and D. Janches (2011), Seasonal variations of the mesospheric Fe layer at Rothera, Antarctica (67.5°S, 68.0°W), *J. Geophys. Res.*, *116*, D02304, doi:10.1029/2010JD014655.
- Gardner, C. S., A. Z. Liu, D. R. Marsh, W. Feng, and J. M. C. Plane (2014), Inferring the global cosmic dust influx to the Earth's atmosphere from lidar observations of the vertical flux of mesospheric Na, *J. Geophys. Res.*, *119*, 7870–7879, doi:10.1002/2014JA020383.
- Geller, M. A. (1983), Dynamics of the middle atmosphere, *Space Sci. Rev.*, *34*, 359–375, doi:10.1007/BF00168828.
- Gerding, M., J. Höffner, J. Lautenbach, M. Rauthe, and F.-J. Lübken (2008), Seasonal variation of nocturnal temperatures between 1 and 105 km altitude at 54°N observed by lidar, *Atmos. Chem. Phys.*, *8*, 7465–7482, doi:10.5194/acp-8-7465-2008.
- Gibson, A. J., L. Thomas, and S. K. Bhattachacharyya (1979), Laser observations of the ground-state hyperfine structure of sodium and of temperatures in the upper atmosphere, *Nature*, *281*, 131–132, doi:10.1038/281131a0.
- Gómez-Martín, J. C., S. A. Garraway, and J. M. C. Plane (2015), Reaction Kinetics of Meteoric Sodium Reservoirs in the Upper Atmosphere, *J. Phys. Chem. A*, doi:10.1021/acs.jpca.5b00622.
- Gordley, L. L., M. E. Hervig, C. Fish, J. M. Russell III, S. Bailey, J. Cook, S. Hansen, A. Shumway, G. Paxton, L. Deaver, T. Marshall, J. Burton, B. Magill, C. Brown, E. Thompson, and J. Kemp (2009), The solar occultation for ice experiment, *J. Atmos. Solar-Terr. Phys.*, *71*, 300–315, doi:10.1016/j.jastp.2008.07.012.
- Grygalashvily, M., G. R. Sonnemann, F.-J. Lübken, P. Hartogh, and U. Berger (2014), Hydroxyl layer: Mean state and trends at midlatitudes, *J. Geophys. Res. Atmos.*, *119*, 12,391–12,419, doi:10.1002/2014JD022094.
- Gumbel, J., and L. Megner (2009), Charged meteoric smoke as ice nuclei in the mesosphere: Part 1—A review of basic concepts, *J. Atmos. Solar-Terr. Phys.*, *71*, 1225–1235, doi:10.1016/j.jastp.2009.04.012.
- Gumbel, J., and B. Karlsson (2011), Intra- and inter-hemispheric coupling effects on polar summer mesosphere, *Geophys. Res. Lett.*, *38*, L14804, doi:10.1029/2011GL047968.
- Gurubaran, S., R. Rajaram, T. Nakamura, and T. Tsuda (2005), Interannual variability of diurnal tide in the tropical mesopause region: A signature of the El Niño-Southern Oscillation (ENSO), *Geophys. Res. Lett.*, *32*, L13805, doi:10.1029/2005GL022928.
- Haldoupis, C., D. Pancheva, and N. J. Mitchell (2004), A study of tidal and planetary wave periodicities present in midlatitude sporadic E layers, *J. Geophys. Res.*, *109*, A02302, doi:10.1029/2003JA010253.
- Hansen, G., M. Serwazi, and U. von Zahn (1989), First detection of a noctilucent cloud by lidar, *Geophys. Res. Lett.*, *16*(12), 1445–1448, doi:10.1029/GL016i012p01445.
- Hagan, M. E., and J. M. Forbes (2002), Migrating and nonmigrating diurnal tides in the middle and upper atmosphere excited by tropospheric latent heat release, *J. Geophys. Res.*, *107*(D24), 4754, doi:10.1029/2001JD001236.
- Hagan, M. E., and J. M. Forbes (2003), Migrating and nonmigrating semidiurnal tides in the upper atmosphere excited by tropospheric latent heat release, *J. Geophys. Res.*, *108*, 1062, doi:10.1029/2002JA009466.
- Haynes, P. H., C. J. Marks, M. E. McIntyre, T. G. Shepherd, and K. P. Shine (1991), On the “Downward Control” of Extratropical Diabatic Circulations by Eddy-Induced Mean Zonal Forces, *J. Atmos. Sci.*, *48*(4), 651–678, doi:10.1175/1520-0469.
- Helmer, M., J. M. C. Plane, J. Qian, and C. S. Gardner (1998), A model of meteoric iron in the upper atmosphere, *J. Geophys. Res.*, *103*(D9), 10,913–10,925, doi:10.1029/97JD03075.
- Hervig, M., R. E. Thompson, M. McHugh, L. L. Gordley, J. M. Russell III, and M. E. Summers (2001), First confirmation that water ice is the primary component of polar mesospheric

- clouds, *Geophys. Res. Lett.*, 28(6), 971–974, doi:10.1029/2000GL012104.
- Hervig, M. E., L. L. Gordley, J. M. Russell III, and S. M. Bailey (2009), SOFIE PMC observations during the northern summer of 2007, *J. Atmos. Solar-Terr. Phys.*, 71, 331–339, doi:10.1016/j.jastp.2008.08.010.
- Hervig, M. E., and L. L. Gordley (2010), Temperature, shape, and phase of mesospheric ice from Solar Occultation for Ice Experiment observations, *J. Geophys. Res.*, 115, D15208, doi:10.1029/2010JD013918.
- Hervig, M. E., and M. H. Stevens (2014), Interpreting the 35 year SBUV PMC record with SOFIE observations, *J. Geophys. Res. Atmos.*, 119, 12,689–12,705, doi:10.1002/2014JD021923.
- Hervig, M. E., U. Berger, and D. E. Siskind (2016), Decadal variability in PMCs and implications for changing temperature and water vapor in the upper mesosphere, *J. Geophys. Res. Atmos.*, 121, 2383–2392, doi:10.1002/20015JD024439.
- Hildebrand, J., G. Baumgarten, J. Fiedler, U.-P. Hoppe, B. Kaifler, F.-J. Lübken, and B. P. Williams (2012), Combined wind measurements by two different lidar instruments in the Arctic middle atmosphere, *Atmos. Meas. Tech.*, 5, 2433–2445, doi:10.5194/amt-5-2433-2012.
- Hoffmann, P., E. Becker, W. Singer, and M. Placke (2010), Seasonal variation of mesospheric waves at northern middle and high latitudes, *J. Atmos. Solar-Terr. Phys.*, 72, 1068–1079, doi:10.1016/j.jastp.2010.07.002.
- Höffner, J. (1994), *Metallschichten in der Mesosphäre: Beobachtungen und Modellierung*, Dissertation, University of Bonn, Germany.
- Höffner, J. (2015), Method and device for determining and calculating a scattered radiation spectrum and method for compressing data, Patent, DE 102 012 221 862.9 (DE 10 2012 221 862 A1), PCT/EP2013/074781 (WO 2014/083014 A2), EP 13805791.4 (EP 2 926 163 A0), US 14/648,010 (US 2015/0323386 A1).
- Höffner, J., U. von Zahn, W. J. McNeil, and E. Murad (1999), The 1996 Leonid shower as studied with a potassium lidar: Observations and inferred meteoroid sizes, *J. Geophys. Res.*, 104(A2), 2633–2643, doi:10.1029/1998JA900063.
- Höffner, J., and J. S. Friedman (2004), The mesospheric metal layer topside: a possible connection to meteoroids, *Atmos. Chem. Phys.*, 4, 801–808, doi:10.5194/acp-4-801-2004.
- Höffner, J., and J. S. Friedman (2005), The mesospheric metal layer topside: Examples of simultaneous metal observations, *J. Atmos. Solar-Terr. Phys.*, 67, 1226–1237, doi:10.1016/j.jastp.2005.06.010.
- Höffner, J., and C. Fricke-Begemann (2005), Accurate lidar temperatures with narrowband filters, *Opt. Lett.*, 30(8), 890–892.
- Höffner, J., J. Lautenbach, C. Fricke-Begemann, and F.-J. Lübken (2006), Polar mesosphere temperature observations by lidar and falling sphere at 78°N, *Reviewed and Revised Papers Presented at the 23rd International Laser Radar Conference 24–28 July 2006, Nara, Japan, ISBN 4-9902916-0-3*.
- Höffner, J., and F.-J. Lübken (2007), Potassium lidar temperatures and densities in the mesopause region at Spitsbergen (78°N), *J. Geophys. Res.*, 112, D20114, doi:10.1029/2007JD008612.
- Höffner, J., and J. Lautenbach (2009), Daylight measurements of mesopause temperature and vertical wind with the mobile scanning iron Lidar, *Opt. Lett.*, 34, 1351–1353.
- Höffner, J., T. P. Viehl, and R. Eixmann (2016)**, Method and device for determining the wind speed, Verfahren und Vorrichtung zur Bestimmung der Windgeschwindigkeit, Patent pending EU/US/GER, DE 102 015 122 201.9, unpublished July 2016.
- Holton, J. R. (1982), The Role of Gravity Wave Induced Drag and Diffusion in the Momentum Budget of the Mesosphere, *J. Atmos. Science*, 39, 791–799.
- Holton, J. R. (1983), The Influence of Gravity Wave Breaking on the General Circulation of the Middle Atmosphere, *J. Atmos. Science*, 40, 2497–2507, doi:10.1175/1520-0469(1983)040<2497:TIOGWB>2.0.CO;2.
- Holton, J. R. (2004), *An Introduction to Dynamic Meteorology*, 4th ed., International Geophysics Series, Elsevier Academic Press, ISBN 978-0-12-354015-7.

- Houghton, J. T. (2002), *The Physics of Atmospheres*, 3rd ed., Reprinted 2005, Cambridge University Press, ISBN 0-521-01122-1.
- Huaman, M. M., and B. B. Balsley (1999), Differences in near-mesopause summer winds, temperatures, and water vapor at northern and southern latitudes as possible causal factors for inter-hemispheric PMSE differences, *Geophys. Res. Lett.*, 26(11), 1529–1532, doi:10.1029/1999GL00294.
- Huang, W., X. Chu, C. S. Gardner, J. D. Carrillo-Sanchez, W. Feng, J. M. C. Plane, and D. Nesvorny (2015), Measurements of the vertical fluxes of atomic Fe and Na at the mesopause: Implications for the velocity of cosmic dust entering the atmosphere, *Geophys. Res. Lett.*, 42, 169–175, doi:10.1002/2014GL062390.
- Hunten, D. M. (1954), A study of sodium in twilight. I. Theory, *J. Atmos. Terr. Phys.*, 5, 44–56, doi:10.1016/0021-9169(54)90006-9.
- Hunten, D. M., and W. L. Godson (1967), Upper-Atmospheric Sodium and Stratospheric Warmings at High Latitudes, *J. Atmos. Sci.*, 24, 80–87.
- Hunten, D. M., R. P. Turco, and O. B. Toon (1980), Smoke and Dust Particles of Meteoric Origin in the Mesosphere and Stratosphere, *J. Atmos. Sci.*, 37, 1342–1357, doi:10.1175/1520-0469.
- Jensen, D. E., and G. A. Jones (1974), Catalysis of radical recombination in flames by iron, *J. Chem. Phys.*, 60, 3421–3425, doi:10.1063/1.1681554.
- Jesse, O., (1896), Die Höhe der leuchtenden Nachtwolken, *Astron. Nachrichten*, 140(3347), 161–168.
- Johnson, K. S. (2001), Iron supply and demand in the upper ocean: Is extraterrestrial dust a significant source of bioavailable iron?, *Global Biogeochem. Cycles*, 15(1), 61–63, doi:10.1029/2000GB001295.
- Kaifler, B., (2014), Thermal Structure and Gravity Waves in the Antarctic Middle Atmosphere Observed by Lidar, *Dissertation*, University of Rosstock, Germany.
- Kaifler, B., F.-J. Lübken, J. Höffner, R. J. Morris, and T. P. Viehl (2015)**, Lidar observations of gravity wave activity in the middle atmosphere over Davis (69°S, 78°E), Antarctica, *J. Geophys. Res. Atmos.*, 120, doi:10.1002/2014JD022879.
- Kaifler, N., G. Baumgarten, J. Fiedler, and F.-J. Lübken (2013), Quantification of waves in lidar observations of noctilucent clouds at scales from seconds to minutes, *Atmos. Chem. Phys.*, 13, 11757–11768, doi:10.5194/acp-13-11757-2013.
- Kalashnikova, O., M. Horanyi, G. E. Thomas, and O. B. Toon (2000), Meteoric smoke production in the atmosphere, *Geophys. Res. Lett.*, 27(20), 3293–3296, doi:10.1029/1999GL011338.
- Karlsson, B., H. Körnich, and J. Gumbel (2007), Evidence for interhemispheric stratosphere-mesosphere coupling derived from noctilucent cloud properties, *Geophys. Res. Lett.*, 34, L16806, doi:10.1029/2007GL030282.
- Karlsson, B., C. E. Randall, T. G. Shepherd, V. L. Harvey, J. Lumpe, K. Nielsen, S. M. Bailey, M. Hervig, and J. M. Russell III (2011), On the seasonal onset of polar mesospheric clouds and the breakdown of the stratospheric polar vortex in the Southern Hemisphere, *J. Geophys. Res.*, 116, D18107, doi:10.1029/2011JD015989.
- Kiliani, J., G. Baumgarten, F.-J. Lübken, and U. Berger (2015), Impact of particle shape on the morphology of noctilucent clouds, *Atmos. Chem. Phys.*, 15, 12897–12907, doi:10.5194/acp-15-12897-2015.
- Kirkwood, S., I. Wolf, H. Nilsson, P. Dalin, D. Mikhaylova, and E. Belova (2007), Polar mesosphere summer echoes at Wasa, Antarctica (73°S): First observations and comparison with 68°N, *Geophys. Res. Lett.*, 34, L15803, doi:10.1029/2007GL030516.
- Kirkwood, S., H. Nilsson, R. J. Morris, A. R. Klekociuk, D. A. Holdsworth, and N. J. Mitchell (2008), A new height for the summer mesopause: Antarctica, December 2007, *Geophys. Res. Lett.*, 35, L23810, doi:10.1029/2008GL035915.
- Kinnison, D. E., G. P. Brasseur, S. Walters, R. R. Garcia, D. R. Marsh, F. Sassi, V. L. Harvey, C. E. Randall, L. Emmons, J. F. Lamarque, P. Hess, J. J. Orlando, X. X. Tie, W. Randel, L. L. Pan, A. Gettelman, C. Granier, T. Diehl, U. Niemeier, and A. J. Simmons (2007), Sensitivity of chemical tracers to meteorological parameters in the MOZART-3 chemical transport model, *J. Geophys. Res.*, 112(D20), 2156–2202, doi:10.1029/2006JD007879.
- Klekociuk, A. R., R. J. Morris, and J. L. Innis (2008), First Southern Hemisphere common-volume

- measurements of PMC and PMSE, *Geophys. Res. Lett.*, *35*, L24804, doi:10.1029/2008GL035988.
- Körnich, H., and E. Becker (2010), A simple model for the interhemispheric coupling of the middle atmosphere circulation, *Adv. Space Res.*, *45*, 661–668, doi:10.1016/j.asr.2009.11.001.
- Kopp, M., M. Gerding, J. Höffner, and F.-J. Lübken (2015), Tidal signatures in temperatures derived from daylight soundings above Kühlungsborn (54°N, 12°E), *J. Atmos. Solar-Terr. Phys.*, *127*, 37–50, doi:10.1016/j.jastp.2014.09.002.
- Langhoff, S. R., H.-J. Werner, and P. Rosmus (1986), Theoretical Transition Probabilities for the OH Meinel System, *J. Mol. Spectrosc.*, *118*(2), 507–529, doi:10.1016/0022-2852(86)90186-4.
- Langowski, M. P., C. von Savigny, J. P. Burrows, W. Feng, J. M. C. Plane, D. R. Marsh, D. Janches, M. Sinnhuber, A. C. Aikin, and P. Liebing (2015), Global investigation of the Mg atom and ion layers using SCIAMACHY/Envisat observations between 70 and 150 km altitude and WACCM-Mg model results, *Atmos. Chem. Phys.*, *15*, 273–295, doi:10.5194/acp-15-273-2015.
- Latteck, R., W. Singer, R. J. Morris, D. A. Holdsworth, and D. J. Murphy (2007), Observation of polar mesosphere summer echoes with calibrated VHF radars at 69° in the Northern and Southern hemispheres, *Geophys. Res. Lett.*, *34*, L14805, doi:10.1029/2007GL030032.
- Lautenbach, J., and J. Höffner (2004), Scanning iron temperature lidar for mesopause temperature observation, *Appl. Opt.*, *43*(23), 4559–4563, doi:10.1364/AO.43.004559.
- Lautenbach, J., J. Höffner, P. Menzel, and P. Keller (2005), The new scanning iron lidar, current state and future developments, *Proceedings of the 17th ESA Symposium on European Rocket and Balloon Programmes and Related Research*, Sandefjord, Norway, (ESA SP-590, August 2005).
- Lautenbach, J., J. Höffner, F.-J. Lübken, and M. Zeche (2008), The thermal structure at the topside and above of polar mesosphere summer echoes over Spitsbergen 78°N, *Ann. Geophys.*, *26*, 1083–1088, doi:10.5194/angeo-26-1083-2008.
- Lei, J., and P. J. Dagdigan (2000), Molecular beam study of the ${}^6\Pi-X^6\Delta$ electronic transition in FeCl, *J. Chem. Phys.*, *112*, 10221–10227, doi:10.1063/1.481664.
- Leslie, R. J. (1885), Sky glows, *Nature*, *33*, 245–246, doi:10.1038/032245a0.
- Lindzen, R. S. (1981), Turbulence and Stress Owing to Gravity Wave and Tidal Breakdown, *J. Geophys. Res.*, *86*(C10), 9707–9714, doi:10.1029/JCo86iC10p09707.
- Lindzen, R. S., and S. Chapman (1969), Atmospheric Tides, *Space Science Reviews*, *10*, 3–188.
- Lübken, F.-J. (1997), Seasonal variation of turbulent energy dissipation rates at high latitudes as determined by in situ measurements of neutral density fluctuations, *J. Geophys. Res.*, *102*(D12), 13,441–13,456, doi:10.1029/97JD00853.
- Lübken, F.-J. (1999), Thermal structure of the Arctic summer mesosphere, *J. Geophys. Res.*, *104*(D8), 9135–9149, doi:10.1029/1999JD900076.
- Lübken, F.-J. (2013), Turbulent scattering for radars: A summary, *J. Atmos. Solar-Terr. Phys.*, *107*, 1–7, doi:10.1016/j.jastp.2013.10.015.
- Lübken, F.-J., and U. von Zahn (1991), Thermal Structure of the Mesopause Region at Polar Latitudes, *J. Geophys. Res.*, *96*(D11), 20,841–20,857, doi:10.1029/91JD02018.
- Lübken, F.-J., and J. Höffner (2004), Experimental evidence for ice particle interaction with metal atoms at the high latitude summer mesopause region, *Geophys. Res. Lett.*, *31*, L08103, doi:10.1029/2004GL019586.
- Lübken, F.-J., A. Müllemann, and M. J. Jarvis (2004), Temperatures and horizontal winds in the Antarctic summer mesosphere, *J. Geophys. Res.*, *109*, D24112, doi:10.1029/2004JD005133.
- Lübken, F.-J., and U. Berger (2007), Interhemispheric comparison of mesospheric ice layers from the LIMA model, *J. Atmos. Solar-Terr. Phys.*, *69*, 2292–2308, doi:10.1016/j.jastp.2007.07.006.
- Lübken, F.-J., U. Berger, and G. Baumgarten (2009), Stratospheric and solar cycle effects on long-term variability of mesospheric ice clouds, *J. Geophys. Res.*, *114*, D00106, doi:10.1029/2009JD012377.

- Lübken, F.-J., and U. Berger (2011), Latitudinal and interhemispheric variation of stratospheric effects on mesospheric ice layer trends, *J. Geophys. Res.*, 116, D00P03, doi:10.1029/2010JD015258.
- Lübken, F.-J., J. Höffner, T. P. Viehl, B. Kaifler, and R. J. Morris (2011)**, First measurements of thermal tides in the summer mesopause region at Antarctic latitudes, *Geophys. Res. Lett.*, 38, doi:10.1029/2011GL050045.
- Lübken, F.-J., J. Höffner, T. P. Viehl, B. Kaifler, and R. J. Morris (2014)**, Winter/summer mesopause temperature transition at Davis (68°S) in 2011/2012, *Geophys. Res. Lett.*, 41, 5233–5238, doi:10.1002/2014GL060777.
- Lübken, F.-J., J. Höffner, T. P. Viehl, E. Becker, R. Latteck, B. Kaifler, D. J. Murphy, and R. J. Morris (2015)**, Winter/summer transition in the Antarctic mesopause region, *J. Geophys. Res. Atmos.*, 120, 12,394–12,409, doi:10.1002/2015JD023928.
- Lübken, F.-J., G. Baumgarten, J. Hildebrand, F. J. Schmidlin (2016), Simultaneous and co-located wind measurements in the middle atmosphere by lidar and rocket-borne techniques, *Atmos. Meas. Tech.*, 9, 3911–2919, doi:10.5194/amt-2016-106.
- Lübken, F.-J., R. Latteck, E. Becker, J. Höffner, and D. J. Murphy (2016), Using polar mesosphere summer echoes and stratospheric/mesospheric winds to explain summer mesopause jumps in Antarctica, *J. Atmos. Solar-Terr. Phys.*, *In Press*, *Corrected Proof*, available online 28 July 2016, doi:10.1016/j.jastp.2016.06.008.
- MacDougall, J. W., J. M. C. Plane, P. C. Jayachandran (2000), Polar cap Sporadic-E: part 2, modeling, *J. Atmos. Solar-Terr. Phys.*, 62, 1169–1176, doi:10.1016/S1364-6826(00)00092-4.
- Marsh, D. R., M. J. Mills, D. E. Kinnison, J.-F. Lamarque, N. Calvo, and L. M. Polvani (2013a), Climate Change from 1850 to 2005 Simulated in CESM1(WACCM) *J. Climate*, 26, 7372–7391, doi:10.1175/JCLI-D-12-00558.1.
- Marsh, D. R., D. Janches, W. Feng, and J. M. C. Plane (2013b), A global model of meteoric sodium, *J. Geophys. Res.*, 118, 11,442–11,452, doi:10.1002/jgrd.50870.
- Mayr, H. G., J. G. Mengel, E. R. Talaat, H. S. Porter, and K. L. Chan (2005a), Mesospheric non-migrating tides generated with planetary waves: I. Characteristics, *J. Atmos. Solar-Terr. Phys.*, 67, 959–980, doi:10.1016/j.jastp.2005.03.002.
- Mayr, H. G., J. G. Mengel, E. R. Talaat, H. S. Porter, and K. L. Chan (2005b), Mesospheric non-migrating tides generated with planetary waves: II. Influence of gravity waves, *J. Atmos. Solar-Terr. Phys.*, 67, 981–991, doi:10.1016/j.jastp.2005.03.003.
- McLandress, C. (1998), On the importance of gravity waves in the middle atmosphere and their parameterization in general circulation models, *J. Atmos. Solar-Terr. Phys.*, 60, 1357–1383, doi:10.1016/S1364-6826(98)00061-3.
- McLandress, C. (2002), The Seasonal Variation of the Propagating Diurnal Tide in the Mesosphere and Lower Thermosphere. Part I: The Role of Gravity Waves and Planetary Waves, *J. Atmos. Sci.*, 59(5), 893–906, doi:10.1175/1520-0469(2002)059<0893:TSVOTP>2.0.CO;2.
- Megner, L., and J. Gumbel (2009), Charged meteoric smoke as ice nuclei in the mesosphere: Part 2—A feasibility study, *J. Atmos. Solar-Terr. Phys.*, 71, 1236–1244, doi:10.1016/j.jastp.2009.05.002.
- Merkel, A. W., D. R. Marsh, A. Gettelman, and E. J. Jensen (2009), On the relationship of polar mesospheric cloud ice water content, particle radius and mesospheric temperature and its use in multi-dimensional models, *Atmos. Chem. Phys.*, 9, 8889–8901, doi:10.5194/acp-9-8889-2009.
- Mills, M. J., O. B. Toon, V. Vaida, P. E. Hintze, H. G. Kjaergaard, D. P. Schofield, and T. W. Robinson (2005), Photolysis of sulfuric acid vapor by visible light as a source of the polar stratospheric CN layer, *J. Geophys. Res.*, 110, D08201, doi:10.1029/2004JD005519.
- Morris, R. J., D. J. Murphy, I. M. Reid, D. A. Holdsworth, and R. A. Vincent (2004), First polar mesosphere summer echoes observed at Davis, Antarctica (68.6°), *Geophys. Res. Lett.*, 31, L16111, doi:10.1029/2004GL020352.
- Morris, R. J., M. B. Terkildsen, D. A. Holdsworth, and M. R. Hyde (2005), Is there a causal relationship between cosmic noise absorption and PMSE?, *Geophys. Res. Lett.*, 32, L24809, doi:10.1029/2005GL024568.

- Morris, R. J., D. J. Murphy, R. A. Vincent, D. A. Holdsworth, A. R. Klekociuk, and I. M. Reid (2006), Characteristics of the wind, temperature and PMSE field above Davis, Antarctica, *J. Atmos. Solar-Terr. Phys.*, *68*, 418–435, doi:10.1016/j.jastp.2005.04.011.
- Morris, R. J., A. R. Klekociuk, R. Latteck, W. Singer, D. A. Holdsworth, and D. J. Murphy (2009), Inter-hemispheric asymmetry in polar mesosphere summer echoes and temperature at 69° latitude, *J. Atmos. Solar-Terr. Phys.*, *71*, 464–469, doi:10.1016/j.jastp.2008.09.042.
- Morris, R. J., J. Höffner, F.-J. Lübken, T. P. Viehl, B. Kai-fler, and A. R. Klekociuk (2012)**, Experimental evidence of a stratospheric circulation influence on mesospheric temperatures and ice-particles during the 2010–2011 austral summer at 69°S, *J. Atmos. Solar-Terr. Phys.*, *89*, 54–61, doi:10.1016/j.jastp.2012.08.007.
- Mote, P. W., K. H. Rosenlof, M. E. McIntyre, E. S. Carr, J. C. Gille, J. R. Holton, J. S. Kinnersley, H. C. Pumphrey, J. M. Russell III, and J. W. Waters (1996), An atmospheric tape recorder: The imprint of tropical tropopause temperatures on stratospheric water vapor, *J. Geophys. Res.*, *101*(D2), 3989–4006, doi:10.1029/95JD03422.
- Murray, B. J., and J. M.C. Plane (2005), Uptake of Fe, Na and K atoms on low-temperature ice: implications for metal atom scavenging in the vicinity of polar mesospheric clouds, *Phys. Chem. Chem. Phys.*, *7*, 3970–3979, doi:10.1039/b508846a.
- Murphy, D. J., J. M. Forbes, R. L. Walterscheid, M. E. Hagan, S. K. Avery, T. Aso, G. J. Fraser, D. C. Fritts, M. J. Jarvis, A. J. McDonald, D. M. Riggan, M. Tsutsumi, and R. A. Vincent (2006), A climatology of tides in the Antarctic mesosphere and lower thermosphere, *J. Geophys. Res.*, *111*, D23104, doi:10.1029/2005JD006803.
- Murphy, D. J., S. P. Alexander, and R. A. Vincent (2012), Interhemispheric dynamical coupling to the southern mesosphere and lower thermosphere, *J. Geophys. Res.*, *117*, D08114, doi:10.1029/2011JD016865.
- Nahar, S. N., M. A. Bautista, and A. K. Pradhan (1997), Electron-ion recombination of neutral iron, *Astrophys. J.*, *479*, 497–503, doi:10.1086/303874.
- Neuber, R., P. von der Gathen, and U. von Zahn (1988), Altitude and temperature of the mesopause at 69°N latitude in winter, *J. Geophys. Res.*, *93*, D9, 11093–11101, doi:10.1029/JD093iD09p11093.
- Nesvorný, D., P. Jenniskens, H. F. Levison, W. F. Bottke, D. Vokrouhlický, and M. Gounelle (2010), Cometary origin of the zodiacal cloud and carbonaceous micrometeorites. Implications for hot debris disks, *Astrophys. J.*, *713*, 816–836, doi:10.1088/0004-637X/713/2/816.
- Nicolls, M. J., R. H. Varney, S. L. Vadas, P. A. Stamus, C. J. Heinselman, R. B. Cosgrove, and M. C. Kelley (2010), Influence of an inertia-gravity wave on mesospheric dynamics: A case study with the Poker Flat Incoherent Scatter Radar, *J. Geophys. Res.*, *115*(D3), D00N02, 2156–2202, doi:10.1029/2010JD014042.
- Noll, S., W. Kausch, S. Kimeswenger, S. Unterguggenberger, and A. M. Jones (2015), OH populations and temperatures from simultaneous spectroscopic observations of 25 bands, *Atmos. Chem. Phys.*, *15*, 3647–3669, doi:10.5194/acp-15-3647-2015.
- Noll, S., W. Kausch, S. Kimeswenger, S. Unterguggenberger, and A. M. Jones (2016), Comparison of VLT/X-shooter OH and O₂ rotational temperatures with consideration of TIMED/SABER emission and temperature profiles, *Atmos. Chem. Phys.*, *16*, 5021–5042, doi:10.5194/acp-16-5021-2016.
- Oberheide, J., Q. Wu, T. L. Killeen, M. E. Hagan, and R. G. Roble (2006), Diurnal nonmigrating tides from TIMED Doppler Interferometer wind data: Monthly climatologies and seasonal variations, *J. Geophys. Res.*, *111*, A10S03, doi:10.1029/2005JA011491.
- Pan, W., and C. S. Gardner (2003), Seasonal variations of the atmospheric temperature structure at South Pole, *J. Geophys. Res.*, *108*(D18), 4564, doi:10.1029/2002JD003217.
- Pancheva, D., et al. (2002), Global-Scale tidal structure in the mesosphere and lower Thermosphere during the PSMOS Campaign of June–August 1999 and Comparisons with the global scale wave model, *J. Atmos. Solar-Terr. Phys.*, *64*, 1011–1035, doi:10.1016/S1364-6826(02)00054-8.



- Pedatella, N. M., K. Raeder, J. L. Anderson, and H.-L. Liu (2014), Ensemble data assimilation in the Whole Atmosphere Community Climate Model, *J. Geophys. Res.*, *119*, 9793–9809, doi:10.1002/2014JD021776.
- Picone, J. M., A. E. Hedin, D. P. Drob, and A. C. Aikin (2002), NRLMSISE-00 empirical model of the atmosphere: Statistical comparisons and scientific issues, *J. Geophys. Res.*, *107*(A12), 1468, doi:10.1029/2002JA009430.
- Pignatelli, A., M. Pezzopane, and E. Zuccheretti (2014), Sporadic E layer at mid-latitudes: average properties and influence of atmospheric tides, *Ann. Geophys.*, *32*, 1427–1440, doi:10.5194/angeo-32-1427-2014.
- Plane, J. M. C. (1991), The chemistry of meteoric metals in the Earth's upper atmosphere, *Int. Rev. Phys. Chem.*, *10*(1), 55–106, doi:10.1080/01442359109353254.
- Plane, J. M. C., R. M. Cox, and R. J. Rollason (1999), Metallic Metal Layers in the Mesopause and Lower Thermosphere Region, *Adv. Space Res.*, *24*(11), 1559–1570, doi:10.1016/S0273-1177(99)00880-7.
- Plane, J. M. C. (2003), Atmospheric Chemistry of Meteoric Metals, *Chem. Rev.*, *103*(12), 4963–4984, doi:10.1021/cro205309.
- Plane, J. M. C. (2004), A time-resolved model of the mesospheric Na layer: constraints on the meteor input function, *Atmos. Chem. Phys.*, *4*(3), 627–638, doi:10.5194/acp-4-627-2004.
- Plane, J. M. C., B. J. Murray, X. Chu, and C. S. Gardner (2004), Removal of Meteoric Iron on Polar Mesospheric Clouds, *Science*, *304*, 16 April 2005, 426–428.
- Plane, J. M. C. (2012), Cosmic dust in the earth's atmosphere, *Chem. Soc. Rev.*, *41*, 6507–6518, doi:10.1039/c2cs35132c.
- Plane, J. M. C., W. Feng, E. M. C. Dawkins, M. P. Chipperfield, J. Höffner, D. Janches, and D. R. Marsh (2014), Resolving the strange behavior of extraterrestrial potassium in the upper atmosphere, *Geophys. Res. Lett.*, *41*(13), 4753–4760, doi:10.1002/2014GL060334.
- Plane, J. M. C., W. Feng, and E. M. C. Dawkins (2015), The Mesosphere and Metals: Chemistry and Changes, *Chem. Rev.*, *115*(10), 4497–4541, doi:10.1021/cr500501m.
- Raizada, S., M. Rapp, F.-J. Lübken, J. Höffner, M. Zecha, and J. M. C. Plane (2007), Effect of ice particles on the mesospheric potassium layer at Spitsbergen (78°N), *J. Geophys. Res.*, *112*, D08307, doi:10.1029/2005JD006938.
- Rapp, M., and F.-J. Lübken (2004), Polar mesosphere summer echoes (PMSE): review of observations and current understanding, *Atmos. Chem. Phys.*, *4*, 2601–1633, doi:10.5194/acp-4-2601-2004.
- Rapp, M., and G. E. Thomas, Modeling the microphysics of mesospheric ice particles: Assessment of current capabilities and basic sensitivities, *J. Atmos. Solar-Terr. Phys.*, *68*, 715–744, doi:10.1016/j.jastp.2005.10.015.
- Rapp, M., J. M. C. Plane, B. Strelnikov, G. Stober, S. Ernst, J. Hedin, M. Friedrich, and U.-P. Hoppe (2012), In situ observations of meteor smoke particles (MSP) during the Geminids 2010: constraints on MSP size, work function and composition, *Ann. Geophys.*, *30*, 1661–1673, doi:10.5194/angeo-30-1661-2012.
- Rees, M. H. (1989), *Physics and chemistry of the upper atmosphere*, Cambridge University Press, ISBN 0-521-32305-3.
- Ridder, C., G. Baumgarten, J. Fiedler, F.-J. Lübken, and G. Stober (2016), Analysis of small-scale structures in lidar observations of noctilucent clouds, *J. Atmos. Solar-Terr. Phys.*, submitted.
- Rienecker, M. M., et al. (2011), MERRA: NASA's Modern-Era Retrospective Analysis for Research and Applications, *J. Climate*, *24*, 3624–3648, doi:10.1175/JCLI-D-11-00015.1.
- Rietmeijer, F. J. M. (2001), Identification of Fe-rich meteoric dust, *Planet. Space Sci.*, *49*, 71–77, doi:10.1016/S0032-0633(00)00094-5.
- Rollason, R. J., and J. M. C. Plane (1998), A study of the reactions of Fe⁺ with O₃, O₂ and N₂, *J. Chem. Soc. Faraday Trans.*, *94*, 3067–3075, doi:10.1039/A805140B.
- Rollason, R. J., and J. M. C. Plane (2000), The reactions of FeO with O₃, H₂, H₂O, O₂ and

- CO₂, *Phys. Chem. Chem. Phys.*, 2, 2335–2343, doi:10.1039/B000877J.
- Rumminger, M. D., D. Reinelt, V. Babushok, and G. T. Linteris (1999), Numerical study of the inhibition of premixed and diffusion flames by iron pentacarbonyl, *Combust. Flame*, 116(1-2), 207–219, doi:10.1016/S0010-2180(98)00033-9.
- Russell III, J. M., S. M. Bailey, L. L. Gordley, D. W. Rusch, M. Horanyi, M. E. Hervig, G. E. Thomas, C. E. Randall, D. E. Siskind, M. H. Stevens, M. E. Summers, M. J. Taylor, C. R. Englert, P. J. Espy, W. E. McClintock, and A. W. Merkel (2009), The Aeronomy of Ice in the Mesosphere (AIM) mission: Overview and early science results, *J. Atmos. Solar-Terr. Phys.*, 71, 289–299, doi:10.1016/j.jastp.2008.08.011.
- Rutherford, J. A., and D. A. Vroom (1972), Formation of iron ions by charge transfer, *J. Chem. Phys.*, 57, 3091, doi:10.1063/1.1678724.
- Saunders, R. W., and J. M. C. Plane (2003), A laboratory study of meteor smoke analogues: Composition, optical properties and growth kinetics, *J. Atmos. Solar-Terr. Phys.*, 68, 2182–2202, doi:10.1016/j.jastp.2006.09.006.
- Saunders, R. W., O. Möhler, M. Schnaiter, S. Benz, R. Wagner, H. Saathoff, P. J. Connolly, R. Burgess, B. J. Murray, M. Gallagher, R. Wills, and J. M. C. Plane (2010), An aerosol chamber investigation of the heterogeneous ice nucleating potential of refractory nanoparticles, *Atmos. Chem. Phys.*, 10, 1227–1247, doi:10.5194/acp-10-1227-2010.
- Saunders, R. W., S. Dhomse, W. S. Tian, M. P. Chipperfield, and J. M. C. Plane (2012), Interactions of meteoric smoke particles with sulphuric acid in the Earth's stratosphere, *Atmos. Chem. Phys.*, 12, 4387–4398, doi:10.5194/acp-12-4378-2012.
- Scalmani, G., M. J. Frisch, B. Menucci, J. Tomasi, R. Cammi, and V. Barone (2006), Geometries and properties of excited states in the gas phase and in solution: Theory and application of a time-dependent density functional theory polarizable continuum model, *J. Chem. Phys.*, 124(9):094107, doi:10.1063/1.217325.
- Scharringhausen, M., A. C. Aikin, J. P. Burrows, and M. Sinnhuber (2008), Global column density retrievals of mesospheric and thermospheric Mg I and Mg II from SCIAMACHY limb and nadir radiance data, *J. Geophys. Res.*, 113, D13303, doi:10.1029/2007JD009043.
- Schmitz, S. (1994), Entwicklung eines schmalbandigen und durchstimmbaren Alexandrit Lasers für ein mobiles Na-Temperatur-Lidar, *Dissertation*, University of Bonn, Germany.
- Schmitz, S., U. von Zahn, J. C. Walling, and D. Heller (1995), Alexandrite lasers for temperature sounding of the sodium layer, *12th ESA Symposium on European rocket and balloon programmes and related research*, Edited by T. A. Blix.
- Schöch, A., G. Baumgarten, and J. Fiedler (2008), Polar middle atmosphere temperature climatology from Rayleigh lidar measurements at ALOMAR (69°N), *Ann. Geophys.*, 26, 1681–1698, doi:10.5194/angeo-26-1681-2008.
- Schröder, D. (2008), Gaseous Rust: Thermochemistry of Neutral and Ionic Iron Oxides and Hydroxides in the Gas Phase, *J. Phys. Chem. A*, 112, 13215–13224, doi:10.1021/jp8030804.
- Schumann, U. (Editor) (2012), *Atmospheric Physics, Research Topics in Aerospace*, Springer-Verlag Berlin Heidelberg, ISBN 978-3-642-30182-7, doi:10.1007/978-3-642-30183-4.
- Schwartz, M. J., et al. (2008), Validation of the Aura Microwave Limb Sounder temperature and geopotential height measurements, *J. Geophys. Res.*, 113(D15S11), 2156–2202, doi:10.1029/2007JD008783.
- Self, D. E., and J. M. C. Plane (2003), A kinetic study of the reactions of iron oxides and hydroxides relevant to the chemistry of iron in the upper mesosphere, *Phys. Chem. Chem. Phys.*, 5(7), 1407–1418, doi:10.1039/b211900e.
- Senf, F., and U. Achatz (2011), On the impact of middle-atmosphere thermal tides on the propagation and dissipation of gravity waves, *J. Geophys. Res.*, 116, D24110, doi:10.1029/2011JD015794.
- She, C. Y., J. R. Yu, and H. Chen (1993), Observed thermal structure of a midlatitude mesopause, *Geophys. Res. Lett.*, 20(7), 567–570, doi:10.1029/93GL00808.
- She, C. Y., B. P. Williams, P. Hoffman, R. Latteck, G. Baumgarten, J. D. Vance, J. Fiedler, P. Acott, D. C.

- Fritts, and F.-J. Lübken (2006), Simultaneous observations of sodium atoms, NLC and PMSE in the summer mesopause region above ALOMAR, Norway (69°N, 12°E), *J. Atmos. Solar-Terr. Phys.*, 68, 93–101, doi:10.1016/j.jastp.2005.08.014.
- Shepherd, M., and C. Fricke-Begemann (2004), Study of the tidal variations in mesospheric temperature at low and mid latitudes from WINDII and potassium lidar observations, *Ann. Geophys.*, 22, 1513–1528, doi:10.5194/angeo-22-1513-2004.
- Simonich, D. M., and B. R. Clemesha (1983), Resonant extinction of lidar returns from the alkali metal layers in the upper atmosphere, *Appl. Opt.*, 22(9), 1387–1389, doi:10.1364/AO.22.001387.
- Sinnhuber, M., H. Nieder, and N. Wieters. (2012), Energetic Particle Precipitation and the Chemistry of the Mesosphere/Lower Thermosphere, *Surv. Geophys.*, 33, 1281–1334, doi:10.1007/s10712-012-9201-3.
- Siskind, D. E., S. D. Eckermann, J. P. McCormack, M. J. Alexander, and J. T. Bacmeister (2003), Hemispheric differences in the temperature of the summertime stratosphere and mesosphere, *J. Geophys. Res.*, 108(D2), 4051, doi:10.1029/2002JD002095.
- Slipher, V. M. (1929), Emissions in the spectrum of the light of the night sky, *Publ. Astron. Soc. Pacific*, 41, 262–265.
- Smith, A. K. (2003a), The origin of stationary planetary waves in the upper mesosphere, *J. Atmos. Sci.*, 60, 3033–3041, doi:10.1175/1520-0469(2003)060<3033:TOOSPW>2.0.CO;2.
- Smith, A. K. (2012), Global Dynamics of the MLT, *Surv. Geophys.*, 33, 1177–1230, doi:10.1007/s10712-012-9196-9.
- Smith, A. K., D. R. Marsh, A. C. Szymczak (2003b), Interaction of chemical heating and tides in the mesosphere, *J. Geophys. Res.*, 108(D5), 4164, doi:10.1029/2002JD002664.
- Stevens, M. H., L. E. Deaver, M. E. Hervig, J. M. Russell III, D. E. Siskind, P. E. Sheese, E. J. Llewellyn, R. L. Gattinger, J. Höffner, and B. T. Marshall (2012), Validation of upper mesospheric and lower thermospheric temperatures measured by the Solar Occultation for Ice Experiment, *J. Geophys. Res.*, 117, D16304, doi:10.1029/2012JD017689.
- Suzuki, S., F.-J. Lübken, G. Baumgarten, N. Kaifler, R. Eixmann, B. P. Williams, T. Nakamura (2013), Vertical propagation of a mesoscale gravity wave from the lower to the upper atmosphere, *J. Atmos. Solar-Terr. Phys.*, 97, 29–36, doi:10.1016/j.jastp.2013.01.012.
- Teiser, G., and C. von Savigny (2016), Variability of OH(3-1) and OH(6-2) emission altitude and volume emission rate from 2003 to 2011, *submitted to J. Atmos. Solar-Terr. Phys.*.
- Thayer, J. P., and W. Pan (2006), Lidar observations of sodium density depletions in the presence of polar mesospheric clouds, *J. Atmos. Solar-Terr. Phys.*, 68, 85–92, doi:10.1016/j.jastp.2005.08.012.
- Thomas, G. E. (1991), Mesospheric clouds and the physics of the mesopause region, *Rev. Geophys.*, 29(4), 553–575, doi:10.1029/91RG01604.
- Thomas, G. E. (1996), Is the polar mesosphere the miner's canary of global change?, *Adv. Space Res.*, 18(3), (3)149–(3)158, doi:10.1016/0273-1177(95)00855-9.
- Tobiska, W. K., T. Woods, F. Eparvier, R. Viereck, L. Floyd, D. Bouwer, G. Rottman, and O. R. White (2000), The SOLAR2000 empirical solar irradiance model and forecast tool, *J. Atmos. Solar-Terr. Phys.*, 62, 1233–1250, doi:10.1016/S1364-6826(00)00070-5.
- Turco, R. P., O. B. Toon, R. C. Whitten, R. G. Keesee, and D. Hollenbach (1982), Noctilucent clouds: simulation studies of their genesis, properties and global influences, *Planet. Space Sci.*, 30(11), 1147–1181, doi:10.1016/0032-0633(82)90126-X.
- van de Hulst, H. C. (1981), *Light Scattering by Small Particles*, Dover Publications, Inc., unabridged corrected republication of the work originally published in 1957 by John Wiley & Sons, Inc., ISBN 0-486-64228-3.
- Viehl, T. P., (2010), Spektral hochaufgelöste Messungen von Aerosolen in der mittleren Atmosphäre, *Diplomarbeit*, University of Rostock, Germany.
- Viehl, T. P., J. Höffner, F.-J. Lübken, J. M. C. Plane, B. Kaifler, and R. J. Morris (2015)**, Summer time Fe depletion in the Antarctic mesopause region, *J. Atmos. Solar-Terr. Phys.*, 127, 97–102, doi:10.1016/j.jastp.2015.04.013.

- Viehl, T. P., J. M. C. Plane, W. Feng, and J. Höffner (2016a), The photolysis of FeOH and its effect on the bottomside of the mesospheric Fe layer, *Geophys. Res. Lett.*, *43*, 1373–1381, doi:10.1002/2015GL067241.
- Viehl, T. P., J. Höffner, F.-J. Lübken, J. M. C. Plane, B. Kaifler, and R. J. Morris (2016b), Corrigendum to “Summer time Fe depletion in the Antarctic mesopause region”, *J. Atmos. Solar-Terr. Phys.*, *142*, 150–151, doi:10.1016/j.jastp.2016.02.001.
- Vondrak, T., K. R. Woodcock, and J. M. C. Plane (2006), A kinetic study of the reactions of Fe⁺ with N₂O, N₂, O₂, CO₂ and H₂O, and the ligand switching reactions Fe⁺ · X + Y → Fe⁺ · Y + X (X=N₂, O₂, CO₂; Y=O₂, H₂O), *Phys. Chem. Chem. Phys.*, *8*, 503–512, doi:10.1039/B508922K.
- Vondrak, T., J. M. C. Plane, S. Broadley, and D. Janches (2008), A chemical model of meteoric ablation, *Atmos. Chem. Phys.*, *8*, 7015–7031, doi:10.5194/acp-8-7015-2008.
- von der Gathen, P. (1990), Sättigungseffekte bei Messungen mit einem Na-Temperatur-Lidar sowie Temperaturen und Schwerwellenaktivität in der polaren Hochatmosphäre, *Dissertation*, University of Bonn, Germany.
- von Zahn, U., and J. Höffner (1996a), Mesopause temperature profiling by potassium lidar, *Geophys. Res. Lett.*, *23*(2), 141–144, doi:10.1029/95GL03688.
- von Zahn, U., J. Höffner, V. Eska, and M. Alpers (1996b), The mesopause altitude: Only two distinctive levels worldwide?, *Geophys. Res. Lett.*, *23*(22), 3231–3234, doi:10.1029/96GL03041.
- von Zahn, U., and J. Höffner, and W. J. McNeil (2002), Meteor Trails as studied by ground-based Lidar, in *Meteors in the Earth's Atmosphere*, ed. E. Murad and I. P. Williams, Cambridge University Press, 149–187, ISBN 978-0-521-80431-8.
- Wilson, R., M. L. Chanin, A. Hauchercorne (1991), Gravity waves in the middle atmosphere observed by Rayleigh lidar: 2. Climatology, *J. Geophys. Res.*, *93*(D3), 5169–5183, doi:10.1029/90JD02610.
- Woodcock, K. R., T. Vondrak, S. R. Meech, and J. M. C. Plane (2006), A kinetic study of the reactions FeO⁺ + O, Fe⁺ · N₂ + O, Fe⁺ · O₂ + O and FeO⁺ + CO: Implications for sporadic E layers in the upper atmosphere, *Atmos. Chem. Phys.*, *8*, 7015–7031, doi:10.1039/b518155k.
- Woodman, R. F., B. B. Balsely, F. Aquino, L. Flores, E. Vazquez, M. Sarango, M. M. Huaman, and H. Soldi (1999), First observations of polar mesosphere summer echoes in Antarctica, *J. Geophys. Res.*, *104*(A10), 22,577–22,590, doi:10.1029/1999JA90226.
- Yamashita, C., X. Chu, H.-L. Liu, P. J. Espy, G. J. Nott, and W. Huang (2009), Stratospheric gravity wave characteristics and seasonal variations observed by lidar at the South Pole and Rothera, Antarctica, *J. Geophys. Res.*, *114*, D12101, doi:10.1029/2088JD011472.
- Yanai, T., D. Tew, and N. C. Handy (2004), A new hybrid exchange-correlation functional using the Coulomb-attenuating method (CAM-B3LYP), *Chem. Phys. Lett.*, *292*, 51–57, doi:10.1016/j.cplett.2004.06.011.
- Yu, Z., X. Chu, W. Huang, W. Fong, and B. R. Roberts (2012), Seasonal variations of the Fe layer in the mesosphere and lower thermosphere: Four season variability and solar effects on the layer bottomside at McMurdo (77.8°S, 166.7°E), Antarctica, *J. Geophys. Res.*, *117*, D22303, doi:10.1029/2012JD018079.
- Zhang, F. (2004), Generation of Mesoscale Gravity Waves in Upper-Tropospheric Jet-Front Systems, *J. Atmos. Sci.*, *61*, 440–457, doi:10.1175/1520-0469(2004)061<0440:GOMGWI>2.0.CO;2.
- Zhang, X., J. M. Forbes, and M. E. Hagan (2010), Longitudinal variation of tides in the MLT region: 2. Relative effects of solar radiative and latent heating, *J. Geophys. Res.*, *115*, A06317, doi:10.1029/2009JA014898.
- Zhou, Q., S. Raizada, C. A. Tepley, and J. M. C. Plane (2008), Seasonal and diurnal variation of electron and iron concentrations at the meteor heights above Arecibo, *J. Atmos. Solar-Terr. Phys.*, *70*, 49–60, doi:10.1016/j.jastp.2007.09.012.

Acknowledgment

The lidar observations and the expedition to Antarctica were funded by the Leibniz-Institute of Atmospheric Physics (IAP) and the Australian Antarctic Division (AAD) under projects No 2325 “VHF Radar Studies of the Antarctic Mesosphere, Stratosphere and Troposphere” and No 4025 “Gravity wave drag parameterization in climate models”. Analyses of lidar observations were co-funded by the Leibniz Association under project “Mixing and Transport in the Mesosphere/Lower Thermosphere” (MaTMELT). Publications were partly supported by Australian Antarctic science projects No 674 “Dynamical coupling in the Antarctic middle atmosphere” and No 737 “Lidar studies of atmospheric dynamics, composition and climatology”, the “Trends in the Middle Atmosphere” (TIMA) project of the BMBF research initiative “Role of the Middle Atmosphere in Climate” (ROMIC), and the “Processes and Climatology of Gravity Waves” (PACOG) project of the DFG. The modelling work was funded by ERC grant No 291332 “Cosmic Dust in the Terrestrial Atmosphere” (CODITA).

I thank Prof. Franz-Josef Lübken for offering and supervising my doctoral research position, for initiating the successful collaboration with the AAD under which most of the results presented in this thesis have been obtained and which enabled me to visit Antarctica twice for a total of 22 months, and for embedding IAP into a framework of national and international cooperations which allows to work in a stimulating environment among top researchers.

I am most grateful to have been closely working with Dr Josef Höffner, who has not only designed and built the main parts of our instrument, written most of the code to analyse the data, worked around the clock to keep the project going, and has always been an endless fountain of knowledge. He has also constantly been available to help solve urgent or not so urgent problems, especially while being on the other side of the world during my 2012 winter at Davis, answering the phone or emails even at 3 am on a Sunday morning. The measurement campaigns and this thesis would not have been possible without Josef. Thank you for all your work and friendship.

Science is a collaborative effort, and the contribution of those in the background is often overlooked. I thank all colleagues at IAP for a harmonious and productive work environment, scientific input, and long discussions at the lunch table. I especially thank all members of the Optical Soundings Department for their cooperative attitude and friendship. I want to emphasise the role of all technical and administrative staff, supporting the maintenance and further development of the instrument and prioritising yet another urgent order for spare parts placed at the last minute. I particularly thank Torsten Köpnick for years of developments on the mobile IAP Fe lidar’s electronics systems, and Michael Priester for helping out with all forgotten and unplanned tasks and errands.

The scientific campaign in Antarctica would not have been successful without the relentless efforts of many unsung heroes working in administrative and supportive roles at the AAD and on board the RSV Aurora Australis. I want to express my gratitude for all your contributions. I especially thank the members of the “Antarctica and the Global System” aka “Climate Processes and Change” aka “Atmospheric and Space Physics” group Dr Ray J. Morris, Dr Andrew R. Klekociuk, Dr Damian J. Murphy, Dr W. John R. French, and Dr Simon P. Alexander for welcoming us into their team, making the joint measurements possible, and for happily helping out with many smaller and larger problems. I also thank Dr Ray J. Morris and Dr Bernd Kailer for supporting and continuing the measurements throughout the 2011 winter.

I thank all expeditioners of the 64th – 66th Australian National Antarctic Research Expeditions who have made the campaign possible, helped out with uncountable little things, and have made Antarctica genuinely feel like home — especially Ashley Miskelly, Charmaine Alford, Hannah Taylor, and the 2012 winterers at Davis: Adam Christensen, Dr Alison Dean, Brigid Dwyer, Cathie Young, Chris Hill, Darryl Seidel, Emily, Greg Wilson, Dr Jan Wallace, Joseph Glacken, Jose Campos, Lincoln Mainsbridge, Mark Baker, Mark Coade, Melanie Ho, Dr Nick Chang, Rob Cullen, Scott Beardsley, Stephanie MacDonald, Steve Edwards, and Tom Luttrell. You truly became a second family during this memorable time. Let us also remember those who have suffered injury or died for the scientific expeditions to Antarctica, in particular our dear friends Bob Heath, Mike Denton, and Perry Anderson.

I thank Raimund Wörl, Rory MacDougall, and the staff of the Andøya Space Center in Andenes, Norway for their help in setting up the mobile IAP Fe lidar at ALOMAR. I thank the ALOMAR staff, Dr Josef Höffner, Raimund Wörl, and several summer students for their work to maintain the instrument and continue the measurements in the Arctic.

Science thrives from the exchange of knowledge and interdisciplinary approaches. I thank all members of Prof. John M. C. Plane's Atmospheric and Planetary Chemistry group at the University of Leeds for warmly welcoming me as their guest on several occasions. I further thank the School of Earth and Environment at the University of Leeds and the NCAS for hosting me during my stay. I especially thank Prof. John M. C. Plane and Dr Wuhu Feng for most valuable discussions about Fe chemistry and atmospheric modelling.

Any big pile of words comes with a bunch of errors and confusions. I thank Dr Josef Höffner, Dr Alison Dean, Dr Erin C. M. Dawkins, Mark Baker, Dr Jens Hildebrand, Dr Jeff Cumpston, Raimund Wörl, Dr Michael Gerding, and Dr Gerd Baumgarten for proofreading and valuable comments on this thesis. Peter Schubert and Dr Jens Hildebrand have developed the source code for the \LaTeX -layout. I further thank all co-authors as well as the anonymous reviewers at *Geophysical Research Letters*, the *Journal of Geophysical Research*, and the *Journal of Atmospheric and Solar-Terrestrial Physics* for their contribution and input to the papers of this thesis.

I am grateful for a very supportive family and a great mob of friends who have shared many adventures in Europe, Australia, and Antarctica. Thank you for helping me to keep my sanity with endlessly engaging discussions about sports, arts, gardening, good coffee, and all other truly meaningful things in life.

Finally, I am most grateful for my partner Anna-Christina who has borne nearly all of the weight of looking after our daughter Caroline while giving me as much time as possible to work on this thesis. Thank you for being the most supportive, mindful, and happy best friend anyone could hope for. And Caroline: your desire to explore the world and your boundless joy make me smile every single day.

Timo P. Viehl
October 2016